Breaking Barriers

Final Report Design Synthesis Exercise Spring 2024

AE3200: Design Synthesis Exercise

DSE Group 22

TUDelft

This page is intentionally left blank.

Breaking Barriers

Final Report Design Synthesis Exercise Spring 2024

by

DSE Group 22

Student Name	Student Number
Ebrahimi, Mohammad	5500117
Groen, Alexander	5246075
Lans, Joris	5078385
Lapidaire, Jasper	5088410
Margaritis, Christos	5271932
Oortwijn, Martijn	5248906
Poirier, Andrea	5482925
Rancaño Martinez, Mateo	5531519
Stomp, Tiago	5546796
Veerman, Tim	5279771

Version	Date	Changes
Version 1	19/06/2024	Initial Version
Version 2	26/06/2024	Feedback Implemented

Tutor:	M.C. Naeije
Coaches:	T. C. Darikwa and J. A. W. Poland
Project Duration:	04/2024 - 06/2024
Faculty:	Faculty of Aerospace Engineering, Delft
Date:	26/06/2024

TU Delft

Preface

Over the last few years, there has been a large increase in interest in the use of high-altitude pseudo-satellites (HAPS), operating in the stratosphere and higher. These mostly unused layers of the atmosphere offer a playground of endless possibilities and innovation. This report explores the detailed design of the EURUS, a HAPS platform with an optical communication terminal to achieve high-speed and secure data links. This configuration of novel concepts presents several exciting applications, and throughout this report, the challenges and opportunities in the EURUS design process are carefully analysed. This project was part of the design synthesis exercise that concludes the BSc cohort of 2024 in Aerospace Engineering at the TU Delft. This exercise challenges students to manage all facets of an engineering design project, and upon completion determines whether the students are eligible for a Bachelor of Science.

The project group would like to present our gratitude to our tutors, Marc Naeije, Tinashe Darikawa and Jelle Poland for their incessant guidance, involvement and support throughout the project. Additionally, we acknowledge our client Airbus Netherlands and specifically Lex Meijer and Remco den Breeje for their insight into the problem and assistance with the design of the system. Similarly, we would like to express gratitude to all parties who shared their knowledge and expertise in fields of science in which many group members lacked experience. Finally, the team would like to extend our gratitude to the OSCC and its teaching assistants, for steering the project in the right direction and aiding us along the way.

DSE Group 22
Delft, June 2024

Executive Overview

There is an ever-growing demand for high-speed and high-security digital communication services all around the world. This necessity is slowly creeping up to the limits that radio frequency-based communication provides in both data rates and availability. The use of free-space laser communication placed on airborne vehicles could become a new alternative or supplement to the existing radio frequency-based communication infrastructure by meeting this demand. In cooperation with the client, Airbus Netherlands, this DSE group aims to investigate this possible development under the following mission statement:

"Identify viable business cases for free-space laser communication networks with the use of high-altitude pseudo-satellites and design the necessary components to bring them to the market."

The aim of this report is to address this mission and start the development of the two required components implied by the objective. The first component is a High-Altitude Pseudo-Satellite (HAPS), a stratospheric long-endurance aerospace vehicle. The second component is the Laser Communication Terminal (LCT), which serves as the payload of the vehicle and allows for high-speed free-space laser communication. In this report, the HAPS is designed up to a subsystem detail, whereas the LCT is designed down to product selection for its components. This report builds on the previous work presented in the Group 22 midterm report [3], in which a final system concept was defined. Ultimately, this overview addresses and summarises the chapters presented in this report in the order that they are introduced.

Project Overview

Demarcating the accomplishments aimed to be realised at the end of the project, the following project objective statement was generated:

"Within 10 weeks, design a HAPS system that provides improved optical communication capabilities within 10 million euros, ensuring seamless integration within the Airbus environment."

The project logic is explained by recapitulating the work done previously. The N2 chart is generated and emphasis is made on the fact that the group treated the HAPS as a system composed of many related subsystems. The word related is essential and efforts were made to avoid subsystem isolation. Also, the updated requirements are presented.

LCT Design

The Laser Communication Terminal (LCT) serves as the payload of the HAPS. Free space optical communications provide high data rates and secure and versatile connection capabilities. The presented LCT design can create air-to-space links with LEO satellites, air-to-air links at a distance of 400 km and air-to-ground links to an altitude of 25 km. Data rates up to 10 Gbps can be achieved depending on link distance and atmospheric conditions using on-off keying and direct detection. This is achieved with an optical transmission power of 5 W. Even though the LCT has been designed in tandem with the HAPS, it is a standalone system featuring a global navigation satellite system, an inertial navigation unit and an independent power distribution system which allows it to be used in other aerial platforms or, if adapted, for ground or space use.

Furthermore, commercially available components were selected where possible, leading to a design that can be quickly realised without the need for fundamental R&D. The LCT cost per unit was projected to be approximately EUR 144,000 in the Fiscal Year of 2024 (FY24) with a power draw of 90 W and a mass of 8 kg. The size of the LCT is such that it can fit inside of the HAPS's wing thus minimising drag. The LCT is aligned through the use of a titanium coarse pointing assembly actuated with worm gear drives. These protrude out of the aerial platform and provide a wide field of regard. The coarse pointing assembly includes a custom telescope with an aperture diameter of 75 mm and an off-axis parabolic mirror that ensures that all of the available incoming light is captured. A second wide-FoV telescope ensures that the pointing acquisition and tracking procedure can be carried out even in challenging conditions.

Flight Performance

The first HAPS subsystem addressed is the flight performance, as it relates to various subsystems by determining the flight profile, power required, flight speeds and load factors. Herein, it was decided that the aircraft climb at constant IAS during the day from 15 to 24 km, glide back down to 15 km at the start of the night and then cruise at this altitude for the remainder of the night. This optimised the amount of energy used during the night. In this flight profile, designed for the longest night at 45° latitude, the maximum power required was found to be 2571.47 W. Additionally, the manoeuvre loading diagram and turning performance were found with the help of the airworthiness certification specifications for very light aeroplanes. It was determined that the biggest load factor is reached at take-off and is equal to 3.7. Take-off and landing operations were considered, and a stall

IAS of 4.66 m/s was found. Further development should consist of proving the compliance of the HAPS with aircraft authorities.

Aerodynamics

The Aerodynamics subsystem consists of the design of the aerodynamic platform optimised for maximum endurance. Firstly a trade-off was performed on airfoils with good low Reynolds number performance, high $C_L^{3/2}/C_D$ and C_L/C_D. To analyse the performance of the airfoils XFLR5 was used along with validation from literature. The best airfoil for this particular application was the FX 63-137, which is used on the main wing. A sensitivity analysis was included to show the robustness of the result. Furthermore, adapting the performance for a finite wing, induced drag and change in lift slope are considered. Secondly, the wing platform was sized. The wing area was selected using the minimal solar array area and is 100 m^2. The chord was determined by considering the highest aspect ratio possible as long as the Reynolds number over the wing does not go below 150,000. Ultimately, the chord length following this consideration is about 2 m, resulting in an aspect ratio of 25. Further work could be done to implement the use of different airfoils along the wing or varying taper for higher structural efficiency.

Propulsion

From the Flight Performance and Aerodynamics, the power required and drag value are used as the starting point for the propulsive design. The design starts by considering the propeller by selecting the airfoil resulting in the highest propeller efficiency. The SG 6043 airfoil is picked. Then, the propeller diameter and rotational speed are determined by optimising for the highest propeller efficiency. The result is two propellers with a diameter of 2.29 m and a rotational speed of 1312 RPM at 25km. The corresponding maximum thrust is 172.5 N at 25 km. A trade-off on the type of motor demonstrates that Brushless Direct Current Motors (BLDC) are the most suitable. An off-the-shelf motor, electric speed controller and gearbox are used. The robustness of the design is proven by considering headwind, mass increase and air density change. The overall efficiency of the subsystem is 0.77.

Stability & Control

The Stability & Control subsystem is responsible for ensuring that the HAPS is stable and controllable. The design starts by considering the longitudinal static stability, negative $C_{m,\alpha}$, by sizing the tail boom and horizontal tail. This resulted in a horizontal tail surface of 11.4 m^2 and a boom length of 7.9 m. With that in mind, the structural design of the boom is made where the outer diameter is found to be 13.8 cm. A sensitivity analysis was performed consisting of varying the mass and the minimum manufacturing thickness. Furthermore, the vertical tail volume is found following the horizontal tail volume, the vertical area surface is 6.33 m^2. Finally, the dihedral is determined through the lateral stability plot and is equal to 12°. This dihedral should lead to stable symmetric and asymmetric eigenmotions. These stability characteristics were not determined, however, an approach on how to address this in the future is mentioned.

Power

The Power subsystem is responsible for the sizing of the solar array and battery. The design starts by establishing the energy budget, it was found that for the longest night at 51 ° latitude, the energy to be delivered by the system to the components is 21.27 kWh during the day and 18.38 kWh during the night. With that in mind, the solar array is designed by first simulating the solar irradiance concerning the days in the year and latitude. Then, a trade-off is performed to select the best solar cell, Sharp Triple Junction cells are used with an efficiency of 32.1 %. The solar array can then be sized, the area is 99 m^2. Following that, the battery type chosen is lithium cobalt oxide. The battery is sized for the longest night at 45 ° latitude. It results that their mass is 51 kg and the capacity is 25.5 kWh. Sensitivity analysis is performed on the influence of solar panel coverage/shading and irradiation absorption.

Thermal Design and Analysis

The thermal analysis of the craft is made in the Simulink environment. The analysis takes into account the solar irradiance, the aerodynamic convection, albedo and planetary radiation. The wing, as it represents the majority of the aircraft volume, is considered. The result is that the temperature difference between the inside and outside is 1 $°C$ for the night and 11 $°C$ for the day. Therefore, it is concluded that passive thermal control is not sufficient. Further work should be done to expand the analysis to the entirety of the HAPS.

Structures

For the structure subsystem, the weight of all subsystems and the aerodynamic forces can be used to compute the forces on the craft. Carbon Fibre-Reinforced Polymer (CFRP) as material for the structural elements is chosen to ensure structural integrity whilst minimising the structural weight. For the layout of the structure, a single-spar solution is used with Hostaphan 87220 foil. This layout was used to compute the total weight of the

structural subsystem and thus the weight of the total HAPS, after the newly acquired total weight could be used to iterate over the other subsystems. The final weight of the wing structure is 111.8 kg with the total weight of the HAPS being 258 kg.

Command and Data Handling

The Command and data handling subsystem encompasses the computer systems onboard the HAPS, along with the TT&C sub-subsystem including the radio and ADS-B transceiver. Due to the unique consideration of the long duration of the mission along with the avionics needs of the aircraft, a split computer system was defined, with a mission computer handling the radio, LCT terminals and mission planning, and a flight computer handling the avionics and aircraft control. This split system provides redundancy and ensures the vehicle remains in control through any failures. To command the HAPS, S-Band RF communication was selected for its data rate, reliable links and the large amount of existing infrastructure. This system provides 10 to 100 Mbit/s up- and downlink performance in a full duplex manner to ensure the HAPS can be effectively controlled from the ground.

RAMS Analysis

A Reliability, Availability, Maintainability and Safety (RAMS) analysis is performed to prove requirements compliance and solidify the overall design. The reliability of the HAPS system is found to be 0.817 with the propulsion system being the driver. A maintenance plan is made for the 10-year operational lifetime. From that, the availability is calculated to be 99.6 %. Safety issues are addressed by first investigating the legislation on HAPS and then by investing in safety decisions made in the design as the use of an Automatic Dependant Surveillance-Broadcast (ADS-B) to avoid laser interference.

Manufacturing, Assembly & Integration Plan

The manufacturing plan of the HAPS is established. In particular, processes such as automated fibre placement and resin transfer moulding are proposed, for the manufacturing of the structural components, boasting reduced scrap rates and energy consumption. Furthermore, the assembly of the structural components was considered at a cost of EUR 100,000 (FY24). Finally, the integration of the subsystems to the HAPS system is divided into multiple steps: pre-integration, initial integration, electrical integration, communication and control integration and final assembly.

Operations and Logistic Concept Description

The network consists of multiple HAPS platforms able to perform links air-to-air, air-to-ground and air-to-space. Ground station support is required to control the system. Additionally, it was identified that the detailed design of the network would require significant work using graph theory methods. Therefore, only recommendations on how to proceed are given. The logistical implications of such a network are also considered through the HAPS deployment and landing procedure.

Risk

New risks arose from the final design. Five important risks per subsystem are identified and the likelihood of them happening is graded between 1 to 5 (Neglible to High) and their impact between 1 to 7 (Negligible to Extreme). For each of them, risk mitigation strategies are made to find the new reduced likelihood and impact. To conclude, a risk table is constructed to identify the most dangerous risk. It is found that the risks after mitigation with the highest severity (combination of likelihood and impact) are the overheating of the motors and the incorrect production of the structural spar.

Financial Analysis

The financial analysis is fourfold. The Strengths, Weaknesses, Opportunities and Threats (SWOT) analysis on the HAPS and LCT is made. The main conclusion is that the design is full of opportunities but lacks existing references. The three Business Cases (BC) for the application of the HAPS and LCT are briefly explained namely: disaster relief, radio-silent communication and providing small sat and cube sat communication coverage and support. The potential revenue for the year 2030 for the three BCs is found to be USD 945 million, 36 million and 5.6 respectively. Finally, the cost breakdown is made and it is found that the development cost for a HAPS is EUR 5,773,000, EUR 556,000 for the material manufacturing, EUR 234,000 for the operation and EUR 14,600,000 for one year of maintenance and EUR 213,000 per HAPS per year (FY24).

Sustainable Development Strategy

Firstly, social sustainability is addressed. It is identified the necessity to nurture healthy relations between group members and to ensure the moral origin of the product used in the design. Then, environmental sustainability is reviewed with careful attention to production and operational sustainability. The decommissioning of the aircraft is also studied. Finally, for each subsystem, efforts to design a sustainable system are presented alongside the points where improvement can be made. An example is the use of rare-earth magnets for electric motors.

Final Design

The integration, placement and configuration of the subsystems are determined by taking into account bending relief, centre of gravity placement and electric component interference. Particular attention is given to the placement of the LCT. The three most important relay modes are identified namely Space-HAPS-HAPS, HAPS-HAPS-Ground and HAPS-HAPS-HAPS, which helps in determining where the LCT shall be placed to be able to perform the links (without the aircraft interfering). It is concluded that the two LCTs shall be placed at the centre of the wing, one on the lower surface and the other one on the front of the craft. To ease the process, a CAD model is constructed and the isometric view (with render) is shown in Figure 1.

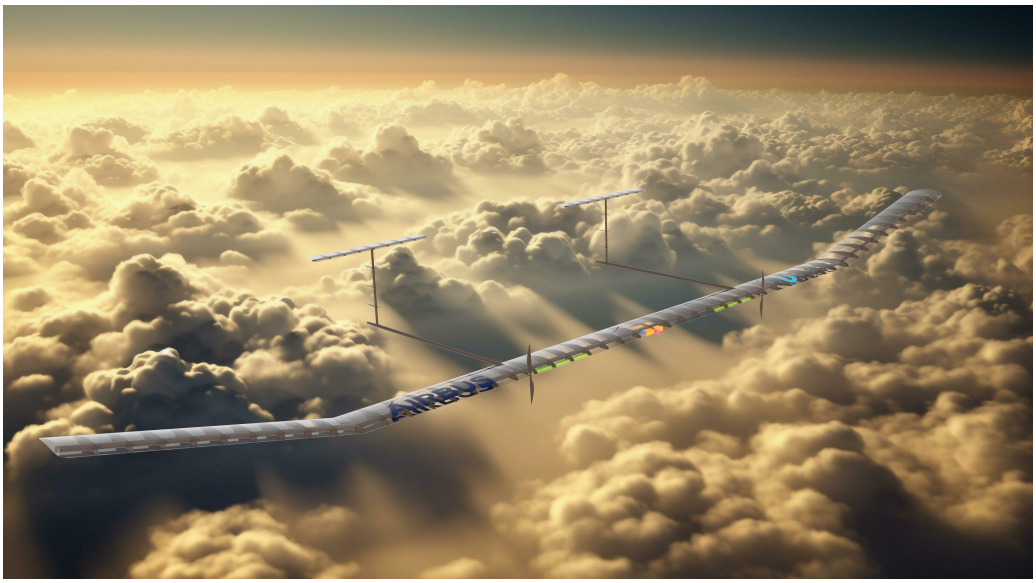

Figure 1: Final Design of the HAPS and LCT

To conclude, a performance analysis is done to summarise and evidentiate the most important design parameters.

Verification & Validation

Verification and Validation (V&V) are critical components of any engineering project, ensuring that the system meets its requirements and performs as expected. The verification procedures used are threefold. Code verification with the use of unit and integration testing. Calculation verification by performing convergence and sensitivity analysis. Product verification is done through the generation of the compliance matrix. It is found that all relevant requirements are answered. Some had to be eliminated as they are not relevant anymore and others are not checkable yet but mostly likely true. Finally, the validation procedure plan is defined by using experimental validation and real-world testing.

To be Continued

The considered project is ambitious and requires lots of work. However, the group is composed of only 10 students for 10 weeks. Consequently, more work remains to be done. A workflow and Gantt chart showing the future steps are shown. The first step is to finalise the detailed design. The validation and certification of the product is next with an estimated duration of 1 year. Following that, the manufacturing and assembly can start for 6 months. Finally, the operational and support work can begin for the remainder of the operational lifetime of 10 years.

TABLE OF CONTENTS

Nomenclature

Abbreviations

Abbreviation	Definition
AC	Alternative Current
AoA	Angle of Attack
AGL	Above Ground Level
BEMT	Blade Element Momentum Theory
BESS	Battery Energy Storage System
BLDC	Brushless Direct Current
CCD	Charge-Coupled Device
CCSDS	Consultative Committee for Space Data Systems
CDHS	Command and Data Handling System
CFRP	Carbon Fibre Reinforced Polymer
CMOS	Complementary Metal Oxide Semiconductor
CPA	Coarse Pointing Assembly
CPS	Coarse Pointing Sensor
CS-VLA	Certification Specification Very Light Aeroplanes
CTE	Coefficient of Thermal Expansion
DC	Direct Current
DRAM	Dynamic Random Access Memory
ESA	European Space Agency
ESC	Electric Speed Controller
ESTOL	ESA Specification for Terabit/sec Optical Links
FC	Flight Computer
FOG	Fibre Optic Gyro
FOV	Field of View
FSM	Fine Steering Mirror
FRAM	Ferroelectric Random Access Memory
FWHM	Full Width Half Maximum
GFRP	Glass Fibre Reinforced Polymer
GNSS	Global Navigation Satellite System
HAPS	High Altitude Pseudo-Satellite
HAPS	High Altitude Pseudo Satellite
HTA	Heavier Than Air
IAS	Indicated Air Speed
INS	Inertial Navigation System
ISA	International Standard Atmosphere
IMU	Inertial Measurement Unit
LCO	Lithium Cobalt Oxide
LCT	Laser Communication Terminal
LEO	Low Earth Orbit
LTA	Lighter Than Air
MC	Mission Computer
MNS	Mission Need Statement
MPPT	Maximum Power Point Tracker
NASA	National Aeronautics and Space Administration
NCA	Lithium Nickel Aluminium Cobalt Oxide
NUC	Next Unit of Computing
NMC	Lithium Nickel Manganese Cobalt Oxide
OS	Operating System
PAM	Point Ahead Mirror
PAT	Pointing, Acquisition and Tracking
POS	Project Objective Statement
PSD	Photo Sensitive Device
QPD	Quadrant Position Detector
RPM	Revolutions Per Minute
RF	Radio Frequency
RAM	Random Acess Memory
RTOS	Real Time Operating System
SDA	Space Development Agency
SNR	Signal to Noise Ratio
SPI	Serial Peripheral Interface
TT&C	Telemetry, Tracking and Command
UAV	Unmanned Air Vehicles
UC	Uncertainty Cone
UHF	Ultra High Frequency
VHF	Very High Frequency

Symbols

Symbol	Definition	Unit
a	Free Stream Speed of Sound	$[ms^{-1}]$
a_{albedo}	Albedo Coefficient	[-]
A_{solar}	Area of Solar Array	$[m^2]$
AR	Aspect Ratio	[-]
Ar	Area	$[m^2]$
b_{prpl}	Propeller Span	[m]
B	Number of Blades	[-]
c	Speed of Light	$[ms^{-2}]$
$\bar{c}$	Mean aerodynamic chord	[m]
c_h	Tail Chord	[m]
c_p	Isobaric Heat Capacity	[-]
C_{Y_β}	Dimensionless derivative Y-force w.r.t. sideslip angle β	[-]
$C_{Y_{\dot{\beta}}}$	Dimensionless derivative Y-force w.r.t. sideslip rate $\dot{\beta}$	[-]
C_L	Lift coefficient	[-]
C_{Y_p}	Dimensionless derivative Y-force w.r.t. roll rate p	[-]
C_{Y_r}	Dimensionless derivative Y-force w.r.t. yaw rate r	[-]
C_{ℓ_β}	Contribution of sideslip angle β to rolling moment coefficient C_ℓ	[-]
C_{ℓ_p}	Contribution of roll rate p to rolling moment coefficient C_ℓ	[-]
C_{ℓ_r}	Contribution of yaw rate r to rolling moment coefficient C_ℓ	[-]
C_{n_β}	Contribution of sideslip angle β to yawing moment coefficient C_n	[-]
C_{n_p}	Contribution of roll rate p to yawing moment coefficient C_n	[-]
C_{n_r}	Contribution of yaw rate r to yawing moment coefficient C_n	[-]
$C_{Y_{\delta_a}}$	Dimensionless derivative Y-force w.r.t. aileron deflection δ_a	[-]
$C_{Y_{\delta_r}}$	Dimensionless derivative Y-force w.r.t. rudder deflection δ_r	[-]
$C_{\ell_{\delta_a}}$	Dimensionless derivative rolling moment coefficient C_ℓ w.r.t. aileron deflection δ_a	[-]
$C_{\ell_{\delta_r}}$	Dimensionless derivative rolling moment coefficient C_ℓ w.r.t. rudder deflection δ_r	[-]
$C_{n_{\delta_a}}$	Dimensionless derivative yawing moment coefficient C_n w.r.t. aileron deflection δ_a	[-]
$C_{n_{\delta_r}}$	Dimensionless derivative yawing moment coefficient C_n w.r.t. rudder deflection δ_r	[-]
C_{X_u}	Dimensionless derivative X-force w.r.t. velocity u	[-]
C_{X_α}	Dimensionless derivative X-force w.r.t. angle of attack α	[-]
C_{Z_0}	Dimensionless Z-force in steady state	[-]
C_{Z_u}	Dimensionless derivative Z-force w.r.t. velocity u	[-]
C_{Z_α}	Dimensionless derivative Z-force w.r.t. angle of attack α	[-]
$C_{Z_{\dot{\alpha}}}$	Dimensionless derivative Z-force w.r.t. angle of attack rate of change $\dot{\alpha}$	[-]
C_{Z_q}	Dimensionless derivative Z-force w.r.t. pitch rate q	[-]
C_{m_u}	Contribution of velocity u to moment coefficient C_m	[-]
C_{m_α}	Contribution of angle of attack α to moment coefficient C_m	[-]
$C_{m_{\dot{\alpha}}}$	Contribution of rate of change of angle of attack $\dot{\alpha}$ to moment coefficient C_m	[-]
C_{m_q}	Contribution of pitch rate q to moment coefficient C_m	[-]
$C_{X_{\delta_e}}$	Dimensionless derivative X-force w.r.t. elevator deflection δ_e	[-]
$C_{Z_{\delta_e}}$	Dimensionless derivative Z-force w.r.t. elevator deflection δ_e	[-]
$C_{m_{\delta_e}}$	Dimensionless derivative moment coefficient C_m w.r.t. elevator deflection δ_e	[-]
δ_e	Elevator deflection	[deg]
C_d	Airfoil Drag Coefficient	[-]
$C_{d_{min}}$	Minimum Airfoil Drag Coefficient	[-]
C_D	Drag Coefficient	[-]
$C_{D_{min}}$	Minimum Drag Coefficient	[-]
C_l	Airfoil Lift Coefficient	[-]
$C_{l_{max}}$	Max Airfoil Lift Coefficient	[-]
C_{lo}	Free Stream Lift Coefficient	[-]
C_L	Wing Lift Coefficient	[-]
$C_{L_{max}}$	Maximum Wing Lift Coefficient	[-]
$C_{L_{w_\alpha}}$	Wing Lift Coefficient Gradient	[-]
$C_{L_{h_\alpha}}$	Horizontal Tail Lift Coefficient Gradient	[-]
$C_{L_{hmax}}$	Maximum Horizontal Stabilizer Lift Coefficient	[-]
C_{L_α}	Wing Lift Gradient	[-]
$C_{m_{ac}}$	Wing Moment Coefficient About Aerodynamic Center	[-]
C_m	Airfoil Moment Coefficient	[-]
C_{M_α}	Aircraft Longitudinal Pitching Moment Gradient	[-]
C_{M_δ}	Elevator Effectiveness Coefficient	[-]
C_{spiral}	Spiral Spacing	[rad]
d	Day of the Year	[-]
d_{slant}	Slant Range	[-]
D	Drag	[N]
D_i	Inner Diameter Spar	[m]
D_in	Inner Diameter Boom	[m]
D_o	Outer Diameter Spar	[m]
D_{out}	Outer Diameter Boom	[m]

Symbol	Definition	Unit
D_{prpl}	Propeller Diameter	[m]
D_{hub}	Hub Diameter	[m]
D_{wind}	Drag with Headwind	[N]
D_b	Dimensionless differential operator (asymmetric flight)	[-]
D_c	Dimensionless differential operator	[-]
e	Span efficiency factor	[-]
e_{pnt_eph}	Ephemeris Pointing Error	[-]
e_{pnt_t}	Pointing Error due to Timing Accuracy	[-]
e_{along}	Position Error Along Satellite Track	[m]
e_{GNSS}	GNSS Position Sensing Error	[m]
e_{out}	Position Error Perpendicular to Both Satellite Track and Link	[m]
E	Young's modulus	[GPa]
$E_{handshake}$	Energy Required for Handshake Protocol	[s]
f	Tip Loss Exponential	[-]
F	Tip Loss Factor	[-]
F_d	Drag Force	[N]
g	Gravitational Acceleration	$[ms^{-2}]$
Gr	Grashoff Number	[-]
G_{Rx}	Receiver Gain	[-]
G_{Tx}	Transmitter Gain	[-]
h	Altitude	[m]
h_{conv}	Convection Coefficient	[-]
H_{HAPS}	Height Above Ground Level of HAPS Platform	[m]
H_{SAT}	Height Above Ground Level of Satellite	[m]
I_{CPA_rem}	Remaining Mass Moment of Inertia of the CPA	$[kgm^2]$
I_{gimbal}	Mass Moment of Inertia of the Gimbal	$[kgm^2]$
I_{max}	Maximum Solar Irradiance	$[Wm^{-2}]$
I_{out}	Amperage Output of Analog-Digital	[C]
I_{Rx}	Laser Irradiance at Receiver	$[Wm^{-2}]$
I_{sc}	Standard Solar Constant	$[Wm^{-2}]$
I_{total}	Total Mass Moment of Inertia of the CPA	$[kgm^2]$
J	Advance Ratio	[-]
k	Thermal Conductivity Coefficient	[-]
k_b	Buckling Coefficient	[-]
K_X	Dimensionless moment of inertia about the X-axis	[-]
K_{XZ}	Dimensionless product of inertia about X and Z axes	[-]
K_Z	Dimensionless moment of inertia about the Z-axis	[-]
K_Y	Dimensionless moment of inertia about the Y-axis	[-]
l_{boom}	Boom Length	[m]
L	Lift	[N]
Lat	Degrees Latitude	[°]
L_{atmo}	Atmospheric Loss	[-]

Symbol	Definition	Unit
$L_{coupling}$	Coupling Loss	[-]
L_{FS}	Free Space Loss	[-]
L_{max}	Maximum Horizontal Tail Load	[N]
$L_{point_{Rx}}$	Pointing Loss at Receiver	[-]
$L_{point_{Tx}}$	Pointing Loss at Transmitter	[-]
$L_{trans_{Rx}}$	Transmission Loss at Receiver	[-]
$L_{trans_{Tx}}$	Transmission Loss at Transmitter	[-]
L_{sys}	System Loss	[-]
m_{prop}	Propeller Mass	[kg]
M	Moment Force	[Nm]
M_{int}	Internal Bending Moment	[Nm]
M_a	Mach Number	[-]
M_{anom}	Mean Anomaly of the Sun	[°]
n	Load Factor	[-]
n_{max}	Maximum Load Factor	[-]
n_{prop}	Propeller Rotational Speed	[rps]
n_{spar}	Safety Factor of Spar	[-]
NU	Nusselt Number	[-]
Pr	Prandtl Number	[-]
P_{cr}	Cruise Power	[W]
P_{dec}	Descent Power	[W]
$P_{elec,climb}$	Electric Power Required for Climb	[W]
$P_{elec,cruise}$	Electric Power Required for Cruise	[W]
$P_{elec,descent}$	Electric Power Required for descent	[W]
P_{Loss}	Power Loss at Converter	[W]
P_{max}	Maximum Propulsive Power	[W]
P_{prpl}	Propeller Power	[W]
P_{req}	Required Propulsive Power	[W]
P_{Rx}	Incident Power at Receiver	[W]
P_{Tx}	Power Emitted at Transmission	[W]
P_{Total_Loss}	Total Power Lost of Converters	[W]
Q	Propeller Torque	[Nm]
Q_{cond}	Heat Flow to Conduction	[W]
$Q_{conv,static}$	Heat Flow to Convection in Static Air	[W]
$Q_{conv,dynamic}$	Heat Flow to Convection in Flowing Air	[W]
$Q_{rad,albedo}$	Heat Flow to Albedo Radiation	[W]
$Q_{rad,Earth}$	Heat Flow to Earth Radiation	[W]
$Q_{rad,2bodies}$	Heat Flow to Radiation from Another Body	[W]
dr	Blade Infinitesimal Element	[m]
r	Position on Blade	[-]
r_{spiral}	Spiral Radius	[rad]
R	Blade's Radius	[m]
R_{min}	Minimum Turn Radius [m]	
R_{series}	Series Reliability	[-]
$R_{parallel}$	Series Reliability	[-]
R_t	Turn Radius	[m]
RC	Rate of Climb	$[ms^{-1}]$
RC_s	Steady Rate of Climb	$[ms^{-1}]$
Re	Reynolds number	[-]
RE	Radius Earth	[km]
S	Total Lifting Surface Area	$[m^2]$
S_w	Wing Surface Area	$[m^2]$

Symbol	Definition	Unit
S_h	Horizontal Stabilizer Surface Area	$[m^2]$
S_s	Solar Irradiance	$[Wm^{-2}]$
t	Time	[s]
t_{climb}	Climb Time	[s]
t_{cr}	Cruise Time	[s]
t_{day}	Time of One Earth Day	[s]
t_{dec}	Descent Time	[s]
$t_{handshake}$	Time Required for Handshake Protocol	[s]
t_{min}	Minimum Turn Time	[s]
t_{plate}	Plate Thickness [m]	
T	Thrust	[N]
T_{day}	Time of Daylight	[hrs]
T_{max}	Maximum Thrust	[N]
T_{spiral}	Time for Spiral Search	[s]
UC	Uncertainty Cone Half Angle	[rad]
$\hat{u}$	Dimensionless velocity	[-]
v	Poisson's ratio	[-]
v_t	Velocity of Link Partner at Time t	$[ms^{-1}]$
V	Velocity	$[ms^{-1}]$
V_h	Horizontal Tail Volume	[-]
V_v	Vertical Tail Volume	[-]
V_{nmax}	Airspeed at Maximum Load Factor	$[ms^{-1}]$
V_{out}	Voltage Out of the Analog-Digital Converter	[v]
V_s	Shear force	[N]
V_{spiral}	Radial Velocity of Spiral Search	$[rads^{-1}]$
$V_{surface}$	Angular Velocity at Earth's Equator	$[ms^{-1}]$
V_{wind}	Wind velocity	$[ms^{-1}]$
V_∞	Free stream velocity	$[ms^{-1}]$
w	Shear Loading	$[Nm^{-1}]$
w_{char}	Characteristic Length	[m]
W	Weight	[N]
x_{cg}	Longitudinal position of center of gravity	[m]
$x_{w_{ac}}$	Longitudinal position of main wing aerodynamic center	[m]
$x_{h_{ac}}$	Longitudinal position of horizontal stabilizer aerodynamic center	[m]
x_{spiral}	X-axis Coordinate During Spiral Search	[rad]
y_{spiral}	Y-axis Coordinate During Spiral Search	[rad]
α	Angle of Attack	[deg]
α_{abs}	Absorptivity Coefficient	[-]
α_{accel}	Angular Acceleration	$[rads^{-2}]$
α_t	Thermal Expansion Coefficient	$[mK^{-1}]$
α_i	Blade Local Angle of attack	[deg]
β	Blade's Twist	[deg]
β_{therm}	Coefficient Thermal Expansion	[-]
β	Sideslip angle	[deg]
γ	Flight Path Angle	[deg]
γ_{air}	Heat Capacity Ratio	[-]
γ_{gain_1}	Predominance of the Natural Convection	[-]
γ_{gain_2}	Predominance of Thermal Diffusivity	[-]
δ	Solar Declination Angle	[deg]
Δ_{timing}	Timing Accuracy	[s]
δ_a	Aileron deflection	[deg]
δ_r	Rudder deflection	[deg]
ϵ	Emissivity Coefficient	[-]
ϵ_{obl}	Angle of Obliquity	[deg]
η_{ssf}	Structural Safety Factor	[-]
$\eta_{battery}$	Battery Efficiency	[-]
$\eta_{cabling}$	Electric Cabling Efficiency	[-]
η_{camber}	Efficiency due to Camber Geometry	[-]
η_{cells}	Solar Cell Efficiency	[-]
η_{conv}	Efficiency of Analog to Digital Converter	[-]
η_{grb}	Gearbox Efficiency	[-]
η_{motor}	Motor Efficiency	[-]
η_{mppt}	Maximum Power Point Tracking Efficiency	[-]
η_{pro}	Propulsive Efficiency	[-]
η_{prpl}	Propeller Efficiency	[-]
η_{ESC}	ESC Efficiency	[-]
θ_{FWHM}	Full Width Half Maximum Angle	[-]
θ_{PA}	Point Ahead Angle	[rad]
θ_{spiral}	Total Revolved Angle during Link Acquisition	[rad]
θ	Pitch angle	[deg]
λ	Wavelength	[-]
$\Lambda_{\frac{1}{4}}$	Sweep Angle at Quarter Chord	[-]
μ	Absolute Viscosity	$[kgm^{-1}s^{-1}]$
μ_b	Dimensionless mass (asymmetric flight)	[-]
μ_c	Dimensionless mass	[-]
μ_{orb}	Orbital Velocity	$[m^1s^{-1}]$
ν	Kinematic Viscosity	$[m^2s^{-1}]$
σ	Boltzmann Constant	[-]
σ_{cr}	Critical Stress	[MPa]
σ_{max}	Minimum of Tensile or Compressive Strengths	[MPa]
σ_{pnt_eph}	Ephemeris Pointing Error	[-]
$\sigma_{pnt_{GNSS\_A-to-A}}$	GNSS Air-to-Air Pointing Error	[-]
$\sigma_{pnt_{GNSS\_A-to-G}}$	GNSS Air-to-Ground Pointing Error	[-]
σ_{total}	Total Standard Deviation	[-]
σ_y	Yield Stress	[MPa]
τ	Torque Force	[Nm]
τ_{motor}	Torque Force of the Motor	[Nm]
τ_{motor_adj}	Adjusted Torque Force of the Motor	[Nm]
ρ	Air Density	$[kgm^{-3}]$
ϕ	Bank Angle	[deg]
ϕ_i	Inflow Angle	[deg]
ϕ_{sun}	Azimuth Angle of the Sun	[deg]
ϕ_t	Tip Inflow Angle	[deg]
φ	Bank angle	[deg]

1. Project Overview

A project of this scale requires a comprehensive and detailed overview to outline its scope and execution. This chapter begins by defining the project's objective and mission in section section 1.1, revisiting and refining the previous definitions. This step is crucial to ensure all parties involved have a clear as well as up to date understanding of the project's goals

Next, throughout this phase of the project, an extensive iterative process is conducted, involving the collaboration of different subsystems to achieve the final design configuration.

The logic of this design process is defined in section 1.2. A comprehensive list of requirements was previously established and is presented again in section 1.3. Additionally, new requirements derived/identified during the subsystem design are included in their respective chapters.

1.1. Project Objective

The first step in defining a clear project is establishing a central and unified vision between all project members and other relevant parties. This is achieved through a Mission Need Statement (MNS) and a Project Objective Statement (POS). The need for the mission is described as follows:

"Identify viable business cases for free space laser communication networks with the use of high altitude pseudo-satellites and design the necessary components to bring them to the market."

The identification of viable business cases of the mission need statement has mainly been covered in the business case report [2] as the main focus of this report is the detailed design of the LCT and HAPS. Although some relevant parts are briefly mentioned in chapter 15.Next to a mission need, the project's exact objective is equally importantThis is defined as follows:

"Within 10 weeks, design a HAPS system that provides improved optical communication capabilities within 10 million euros, ensuring seamless integration within the Airbus environment."

These statements form the backbone of the project and are crucial parameters for all design choices and specifications. However, a structured system is still necessary to guide the process from the conceptual phase to the detailed design.

1.2. Project Logic

Next to a clear mission need and project objective statement, the design of the HAPS and LCT systems need a clear process and logic flow in order to arrive at a convergent solution to the problem. This section describes this logic. The gross part of this report describes the detailed design of the LCT and the detailed subsystem design of the HAPS. Naturally, all the payload and all subsystems are heavily integrated into each other, with the design of one influencing the other greatly. After the Midterm Review on the 21st of May, the HAPS design was continued from a conceptual state. The detailed design focuses on the concept of a twin-boom high aspect ratio low sweep slender wing solar-powered aircraft. The design will carry two of the aforementioned LCTs as payload. This concept was selected from five conceptual designs: Two lighter-than-air (LTA) vehicles, namely a controllable balloon and a rigid zeppelin, and three heavier-than-air (HTA) vehicles, which were mainly differentiated by their wing configuration. They were described as a flying wing, a canard/tandem wing and a twin-boom wing configuration. The twin-boom wing configuration was selected to be the most optimal design choice as it performed well in nearly all qualitative trade-off metrics, such as performance, sustainability and safety.

The values that were found in the preliminary concept design were used as a starting point for the detailed design. The detailed design focuses on a large-scale iterative process to converge to a possible design solution. Here, all subsystem departments started with the preliminary values and created a subsystem that would fit with the current design state. From this, new values were extracted that the other subsystems would use to further iterate on their subsystem design. For example, if the structural group decides that the mass needs to be increased, then consequently an increase in wing surface area is needed, which in turn increases the mass, creating a loop. This iterative procedure was continued until the loop converged to final values. This was mainly done by the use of an N2-diagram, which is shown in Figure 1.1. This chart shows the relation between the inputs and outputs of each subsystem. It is important to note that not all outputs of each subsystem are noted here since not every output is used as an input to another subsystem.

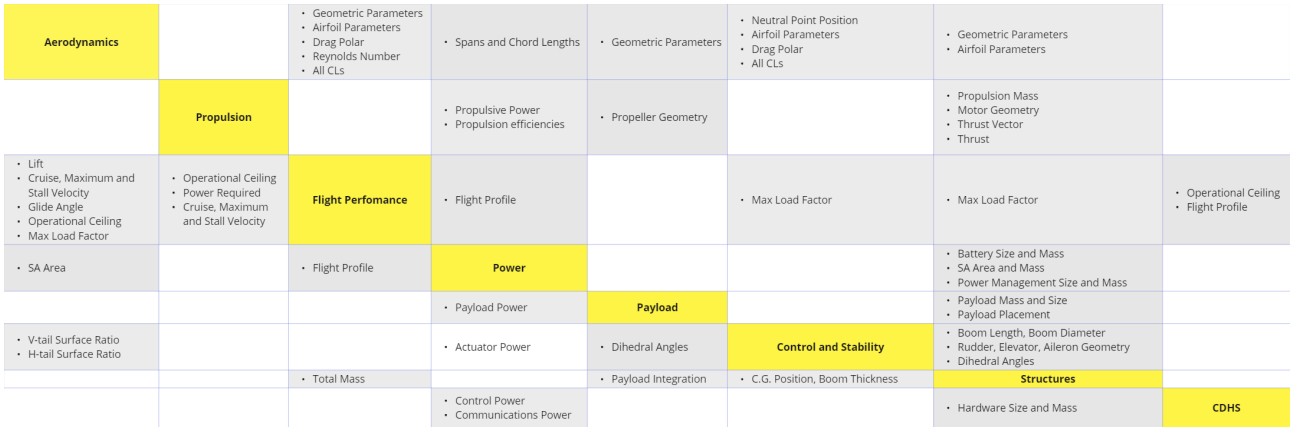

Figure 1.1: Project Detail Design N2-Diagram

With such extensive interconnectedness of all subsystems, the team should keep a clear overview of how and which different values, parameters and numbers are used. The team decided on a method of organising this using a variable checkbook. This book comprises of a large list of every variable that is used in the design process. For each of these values, a specific subsystem is assigned to be responsible for that value. The responsible team member imposes a value that all other subsystems should adhere to. When it is found that a subsystem cannot adhere to this value, it should confer with the imposing subsystem to change the used value. The checkbook keeps up with which subsystem is using which values, and which values being used are outdated. The imposing subsystem is most often the subsystem that calculates or defines this value (e.g. the lift coefficient is imposed by the aerodynamics subsystem, and the total mass is imposed by the structures subsystem). The combination of the integration of the N2-chart and the close maintenance of the variable checkbook creates a comprehensive but easy-to-use and -understand process that guides the detailed design of the HAPS and LCT.

1.3. Project Requirements

Over the course of the design of the system, a large number of requirements have been identified. All of the conceptually identified requirements are shown below in Table 1.1. Over the course of the design of the different subsystems, new requirements for these subsystems were identified. In each chapter, the relevant requirements for that subsystem that were either found before or created new are shown.

Table 1.1: Project Requirements

Code	Description
Technical Requirements	
Maintenance	
REQ-TEC-MAI-1	The system, including all components, shall be smartly positioned in the design to ensure ease of access for (dis)assembly.
REQ-TEC-MAI-2	The system shall be designed to allow for efficient repair of components in case of failure.
REQ-TEC-MAI-3	The system shall provide inspection capabilities to facilitate routine checks.
Linking Performance	
REQ-TEC-LIN-1	The LCT system shall have the capability to establish and maintain an air-to-ground communication link over distances ranging from 15 km to 25 km
REQ-TEC-LIN-2	The LCT system shall have the capability to establish and maintain an air-to-air communication link up to a distance of 1000 km.
REQ-TEC-LIN-3	The LCT system shall have the capability to establish and maintain an air-to-space communication link up to a distance of 2000 km.
Data Processing	
REQ-TEC-DAP-1	The LCT system shall support data transmission rates ranging from 1 Gbps to 10 Gbps.
REQ-TEC-DAP-2	The LCT system shall be able to complete amplitude modulation of a signal.
REQ-TEC-DAP-3	The LCT system shall be able to complete amplitude demodulation of a signal.
REQ-TEC-DAP-4	The optical communication link shall transmit 1 bits per symbol.
REQ-TEC-DAP-5	The optical communication link shall transmit 1Gbaud to 10Gbaud symbols per second.
REQ-TEC-DAP-6	The LCT system shall be able to encode a transmission.
REQ-TEC-DAP-7	The LCT system shall be able to decode a transmission.
Integration	
REQ-TEC-INT-1	The LCT system shall have a maximum drag impact of 0.5 N.
REQ-TEC-INT-2	All LCT subsystems shall be configured in the design to fit within the designated housing.
Laser Sensing	

REQ-TEC-LSN-1	The LCT system shall be able to focus the laser beam onto the receiving sensor.
REQ-TEC-LSN-2	The LCT sensor shall detect optical signals of less than -56dBm of power.
REQ-TEC-LSN-3	The LCT sensor analogue to digital converter shall have a resolution less than 13 mV.
REQ-TEC-LSN-4	The LCT sensor shall have a noise figure of less than 45.3dB.
REQ-TEC-LSN-5	The LCT sensor shall have a 10 GSPS sampling rate.
REQ-TEC-LSN-6	The LCT sensor shall operate in a wavelength between 1535nm and 1565nm.
Laser Generation	
REQ-TEC-LSR-1	The laser optical components shall be capable of any polarisation.
REQ-TEC-LSR-2	The laser shall transmit no more than 5 W.
REQ-TEC-LSR-3	The beam shall have an M2 factor less than 1.1.
REQ-TEC-LSR-4	The beam shall have a full divergence angle greater than 26 µrad.
REQ-TEC-LSR-5	The beam pulse shall have a duration of no more than 100ps.
REQ-TEC-LSR-6	The beam shall have an irradiance of at least 5.2 $\mu W/m^2$ at the receiver aperture.
REQ-TEC-LSR-7	The laser shall operate in a wavelength between 1535nm and 1565nm.
Optical Tracking	
REQ-TEC-OPT-1	The LCT shall have a field of regard of $N \cdot 360$ degrees azimuth and 190 degrees elevation in relation to its reference system.
REQ-TEC-OPT-2	The LCT shall have a slew rate of 1.88 degrees/second.
REQ-TEC-OPT-3	The LCT pointing system shall cause no more than 3dB loss (3σ) assuming a Gaussian beam.
REQ-TEC-OPT-4	The LCT shall perform acquisition patterns in accordance with the SDA standard.
REQ-TEC-OPT-5	The LCT terminal shall complete the acquisition process in no more than 60 seconds.
REQ-TEC-OPT-6	The LCT shall initiate link acquisition in a cone of 360 degrees azimuth and 190 degrees elevation in relation to its reference system.
REQ-TEC-OPT-7	The LCT shall acquire a link from an initial offset angle of 0.3 degrees.
REQ-TEC-OPT-8	The system shall acquire links from aerial, space and ground platforms.
Sensing	
REQ-TEC-SEN-1	The platform shall be able to determine its altitude.
REQ-TEC-SEN-2	The platform shall be able to determine its attitude.
REQ-TEC-SEN-3	The platform shall be able to determine its airspeed.
REQ-TEC-SEN-4	The platform shall be able to determine environmental conditions for navigation.
REQ-TEC-SEN-5	The LCT shall be able to determine its position to within 2 m (1σ).
REQ-TEC-SEN-6	The LCT shall be able to determine its attitude to within 0.03 degrees on all axes (1σ).
Propulsion	
REQ-TEC-PRO-1.1	The platform propulsion system shall provide thrust to get to and sustain the service altitude at all times.
REQ-TEC-PRO-1.2	The platform propulsion system shall provide thrust for minimum climb rate at service altitude.
REQ-TEC-PRO-2	The platform propulsion system shall provide thrust for one-engine-off take-off and landing.
Structures	
REQ-TEC-STR-1.1	There shall be a structure to provide thermal insulation for internal systems.
REQ-TEC-STR-1.2	There shall be a structure to provide radiation protection for internal systems.
REQ-TEC-STR-1.3	The systems shall employ anti-icing techniques.
REQ-TEC-STR-1.4	There shall be a structure to provide waterproofing for the internal systems.
REQ-TEC-STR-1.5	There shall be a structure to provide humidity protection for the internal systems.
REQ-TEC-STR-2.1	The platform structure shall sustain mission start and finish.
REQ-TEC-STR-2.2	The platform structure shall sustain climb and descent to flight service altitude.
REQ-TEC-STR-2.3	The platform structure shall handle manoeuvre loads at service altitude.
Aerodynamics	
REQ-TEC-AE-1	The platform aerodynamics shall be optimized for endurance.
REQ-TEC-AE-2	The platform shall provide sufficient lift at service altitude.
REQ-TEC-AE-3	The platform shall have controlled boundary layer separation.
Stability & Control	
REQ-TEC-SC-1	The platform shall be operating at level 4 autonomy.
REQ-TEC-SC-2.1	The platform shall be longitudinally statically stable.
REQ-TEC-SC-2.2	The platform shall be laterally statically stable.
Power	
REQ-TEC-PW-1	The platform shall be capable of delivering the required power to LCT.
REQ-TEC-PW-2	The platform shall be capable of delivering the required power to the propulsion system.
REQ-TEC-PW-3	The platform shall be capable of delivering the required power to the sensing system.
REQ-TEC-PW-4	The platform shall be capable of generating power to an energy storage system from the operating environment equal to that of the drawn power at mission end-of-life.
REQ-TEC-PW-5	The platform shall be capable of enduring intermittent periods where no power generation is possible.
Operational Requirements	

Network Robustness	
REQ-MOP-NWR-1	The Network shall remain operational in the event of platform failure.
REQ-MOP-NWR-2	The Network shall have a defined product maintenance philosophy.
REQ-MOP-NWR-3	The Network shall have a 24/7 operational uptime.
REQ-MOP-NWR-4	The system shall provide status telemetry.
Deployment	
REQ-MOP-DEP-1	The Network shall be globally deployable.
REQ-MOP-DEP-2	The Network shall be deployable within 72 hours.
Coverage	
REQ-MOP-COV-1.1	The Network shall ensure ground link distance within LCT capacity.
REQ-MOP-COV-1.2	The Network shall ensure that the platform is available for user connectivity.
REQ-MOP-COV-2	The Network shall have coverage which is still to be determined.
REQ-MOP-COV-3.1	The Network shall ensure that network adjacent platforms are within LCT to air-to-air link distance.
REQ-MOP-COV-3.2	For air-space communication, the Network shall ensure that platform-to-satellite distance is smaller than 2000 km
REQ-MOP-COV-4	The system shall operate up to 2 optical links simultaneously.
Command Network	
REQ-MOP-CNW-1.1	There shall be a mission start system.
REQ-MOP-CNW-1.2	There shall be a mission retrieval system.
REQ-MOP-CNW-1.3.1	There shall be storage infrastructure for the network.
REQ-MOP-CNW-1.3.2	There shall be trained mission support personnel.
REQ-MOP-CNW-1.3.3	There shall be trained system maintenance personnel.
REQ-MOP-CNW-2	The Network shall be operated via RF link.
REQ-MOP-CNW-3	There shall be an intra-platform coordination system.
REQ-MOP-CNW-4	The Network shall communicate network status for monitoring.
REQ-MOP-CNW-5	During linking with a satellite network, the HAPS network shall be able to get the positions of the satellites
Constraint Requirements	
Cost	
REQ-CON-CST-1	The recurring cost of the HAPS platforms shall be less than 10M Euro.
REQ-CON-CST-3	The recurring cost of the LCT shall be less than 100k Euro.
REQ-CON-CST-4	The cost per bit shall be better than $0.04/Gbit.
Legal	
REQ-CON-LGL-1	The platform shall be compliant with air and space authorities.
REQ-CON-LGL-2	The LCT shall be compliant with SDA and ESTOL regulations.
REQ-CON-LGL-3	The system shall adhere to European and North American governmental regulations.
REQ-CON-LGL-4	The system shall be compliant with the SDA.
REQ-CON-LGL-5	The system shall be CE certified.
Use of Resources	
REQ-CON-RSC-1	The LCT shall utilise Off-the-shelf components when possible and not in conflict with cost and standardization requirements.
REQ-CON-RSC-2	Materials used shall be sustainably procured when possible.
REQ-CON-RSC-3	Recycle material shall be used when possible.
REQ-CON-RSC-4	Design effort shall be made to use TRLs better than 5.
Safety	
REQ-CON-SFT-1	The platform design shall include redundancies for safety-critical systems.
REQ-CON-SFT-2	The platforms shall be compliant with Aerospace Safety Standards.
REQ-CON-SFT-3	The system shall be compliant with safety regulations TBC.
Compatibility Payload	
REQ-CON-CMP-1	The platforms shall be structurally supportive for the LCT.
REQ-CON-CMP-2	The platform shall be able to communicate with the payload.
REQ-CON-CMP-3	There shall be compatibility with ground station communication systems.
REQ-CON-CMP-4	There shall be compatibility with control systems.
Engineering Budget	
REQ-CON-ENB-1	The LCT shall have a volume of no more than 150x300x1000 mm^3
REQ-CON-ENB-2	The LCT shall have a mass of no more than 5 kg.
REQ-CON-ENB-3	The LCT shall use no more than 50 W of power.
Reliability	
REQ-CON-REL-1	The system shall operate with 95% reliability within its operational lifetime.
REQ-CON-REL-2	The operational lifetime of the HAPS shall be 10 years.
REQ-CON-REL-3	The operational lifetime of the LCT shall be 5 years.
Organisational Requirements	
Schedule	

REQ-CON-SCL-1	Concept design shall be finished within 3 weeks time.
REQ-CON-SCL-2	The final concept design shall be made within 5 weeks.
REQ-CON-SCL-3	The project shall be completed by 10 Full-Time upcoming Bachelor Engineers.

2. LCT Design

This chapter addresses the design and configuration principles of the Laser Communication Terminal (LCT) to set up high-speed and reliable communication links between ground stations, high-altitude platforms, and satellites. Free space optical communications provide high data rates and secure and versatile connection capabilities. The proposed system is to be mounted on the HAPS and therefore was developed in tandem with the platform that carries it. Therefore the relationship between the LCT and the HAPS should be considered. The LCT mass and power draw were considered during the HAPS design while the dimensions of the LCT optical bench were dictated by the HAPS wing size. Additionally, the LCT's field of regard, the HAPS shape and the dihedral angle make it so that links can be formed from various angles and allow it to serve the business cases. The LCT is stand-alone however and includes all necessary components for its operation, allowing it to be transferred to another aerial platform or adapted for ground and/or space operations.

In the following sections, a system overview showing all system components, cost, mass and power draw will be presented. Afterwards, the system's link budget and link capabilities will be analysed. With this known, the layout of the optical bench and the pointing acquisition and tracking procedure will be discussed followed by a presentation of the design of the coarse pointing assembly which includes the design of the primary and wide Field-of-View (FoV) telescopes. The selection of mirrors and pointing sensors will be discussed, followed by control and power management.

2.1. System Overview

The LCT system comprises two integrated parts, the optical bench and the coarse pointing assembly (CPA). These two parts consist of several subsystem components which work together to ensure efficient communication. As depicted in Figure 2.1, the optical bench houses both the optical transmission and the optical reception subsystem of the LCT. The optical transmission subsystem's origin is characterised by the laser diode generating the carrier wave. The signal is then modulated by the Mach-Zehnder modulator after which the laser beam is reshaped before being amplified, and directed through collimators. The Point Ahead Mechanism (PAM) directs the beam towards the target, with fine-pointing adjustments made by the Fine Steering Mirror (FSM) and the primary telescope.

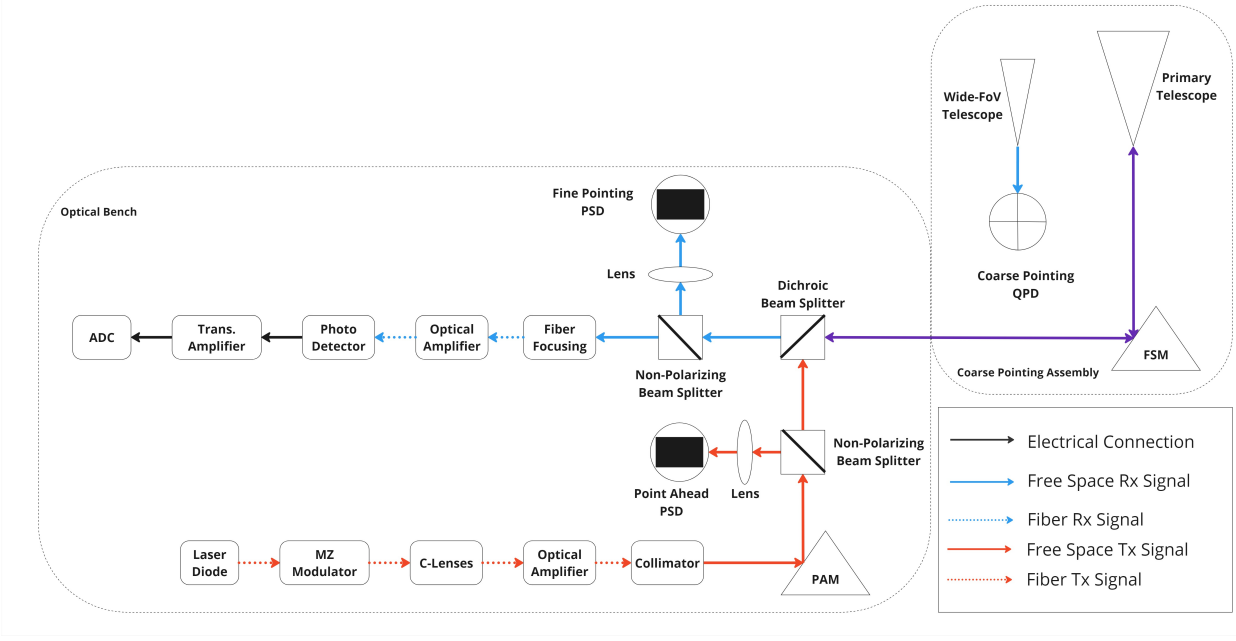

Figure 2.1: LCT General Block diagram Depicting Critical LCT Components and the Electrical, Fiver and Free Space Paths.

The receiving subsystem collects incoming signals via the primary telescope, directing these, through the FSM,

into the optical bench. The signals are amplified, converted to electrical signals by the photodetector, further amplified, and finally digitised by the analog-to-digital converter. The optical bench houses these components, ensuring precise alignment and minimal signal loss. Furthermore, the CPA, featuring a Wide-FoV Telescope and coarse pointing Quadrant Position Detector (QPD), aids in initial signal acquisition and coarse alignment, whereas the fine-pointing Photo Sensitive Device (PSD) ensures precise tracking.

Table 2.1: LCT Engineering Budget: total cost is rounded up to nearest k€

LCT Engineering Budget			
Component	Cost Estimate (€) FY24	Power Estimate (W)	Mass Estimate (kg)
Transmitter			
Laser Diode [1]	995	0.13	0.015
Laser Diode Driver [2]	4,795	13.80	0.500
Mach-Zender Modulator [3]	1,468	0.05	0.311
C-lens (2x) [4]	208	-	0.006
Amplifier [5]	5,931	24.00	0.650
Collimator [6]	291	-	0.040
Receiver			
Amplifier [7]	5,962	20.00	0.350
Photo Detector [8]	6,051	-	0.204
Trans. Amplifier [9]	13	-	-
AD Converter [10]	3,059	6.00	0.110
Optics			
Telescope	15,000	-	1.00
Gimbal	5,000	2.00	2.880
PAM (Same as FSM) [93]	25,000	0.64	0.061
FSM [93]	25,000	0.64	0.061
Lenses (4x) [11]	1,456	-	0.080
Non-Polarizing Beam Splitter (2x) [12]	374	-	0.040
Dichroic Beam Splitter [13]	188	-	0.020
PSD (2x) [14]	3,840	1.00	0.050
QPD [15]	200	-	-
Folding Mirrors (8x) [16]	524	-	0.160
Other			
FPGA [17]	1,840	0.17	-
GNSS-INS [18]	5,000	3.00	0.155
Power Distributor	500	3.10	0.100
Results			
Total	€113,000	75W	6.79kg
Total (20% Margin)	€135,000	89W	8.15kg

[3]Laser Diode: https://www.aerodiode.com/wp-content/uploads/2020/05/1550-nm-laser-diode-Model-1-Datasheet-5.pdf
[4]Laser Diode: https://www.aerodiode.com/product/low-noise-laser-diode-driver/
[5]Modulator: https://www.optilab.com/products/1550-nm-10-ghz-intensity-modulator-pm-fc-apc
[6]Collimator: https://www.thorlabs.com/thorproduct.cfm?partnumber=F810APC-1550
[7]Rx Amplifier: https://www.optilab.com/products/low-noise-high-gain-pre-amp-edfa-module-40-db-wideband-gain
[8]Photo Detector: https://nl.mouser.com/ProductDetail/508-VPDV2120VFFA
[9]Transimpedance Amplifier: https://nl.mouser.com/ProductDetail/595-ONET2804TLPY
[10]Analogue to Digital Converter: https://nl.mouser.com/ProductDetail/584-AD9213BBPZ-10G
[11]Lenses: https://www.thorlabs.com/thorproduct.cfm?partnumber=ASL10142-C
[12]Non-Polarizing Beam Splitter: https://www.thorlabs.com/thorproduct.cfm?partnumber=BS072
[13]Dichroic Beam Splitter: https://www.thorlabs.com/thorproduct.cfm?partnumber=DMSP1500T
[14]PSD: https://www.newport.com/p/CONEX-PSD10GE
[15]QPD: https://specs.marktechopto.com/pdf/products/datasheet/MTPD4346T38-300%20v112123%20prelim.pdf
[16]Folding Mirrors: https://www.thorlabs.com/thorproduct.cfm?partnumber=MRA10-G01
[17]FPGA: https://nl.mouser.com/ProductDetail/Altera/5AGTFC7H3F35I5G?qs=u16ybLDytRZb1msz04ArEQ%3D%3D
[18]GNSS-INS: https://www.advancednavigation.com/inertial-navigation-systems/mems-gnss-ins/certus-evo/

A Field Programmable Gate Array (FPGA) which is not included in the overview for clarity is also used to act as a modem, converting from ethernet protocol to the protocol specified by the relevant Space Development Agency (SDA) standard [60] as well as control the fine pointing, coarse pointing and point ahead control loops. Amplitude modulation and direct detection are selected as the modulation and demodulation method as opposed to coherent methods since they are widely used, and demanded by both the SDA and ESTOL specification for Terabit/sec Optical Links (ESTOL) standards [60] [54] and simple. Therefore an On-off-Keying modulation scheme is chosen with the possibility of using Manchester-Encoding as required from SDA [60] although the transmission rate might decrease in that case.

Beam splitting is done on a wavelength basis and not on a polarisation basis in order to comply with REQ-TEC-LSR-1 and the relevant ESTOL standard [54]. Only a single diode is used per LCT and therefore the Tx and Rx wavelength of the LCT need to be selected before deployment so that the correct diode and dichroic beam splitter can be selected. The wavelength should be separated sufficiently to ensure efficient separation in the dichroic beam splitter. Figure 2.1 provides a foundation for understanding the detailed operations of each subsystem, which will be addressed and elaborated upon in detail in the following sections. An overview of the LCT engineering budget including cost, power and mass estimates can be found in Table 2.1. A 20% margin is included for all results, the cost margin is included to account for price uncertainties in the price estimates and future price fluctuations. The power margin is included in order to account for non-calculated losses and the power draw of the non-analysed thermal management system. The mass margin includes non-modelled structural elements such as the optical bench housing. For more information on the components in Table 2.1, and the corresponding design, please refer to the Midterm Report [3].

2.2. Link Budget

To ensure the successful creation and operation of the communication link, a link budget needs to be created so that it can be ensured that the required signal power is delivered to the receiver. Link budgets are used extensively in radio communications and the same principles can be translated to laser communications. The link can be described by Equation 2.1, where P_{RX} is the received power, P_{TX} is the transmitted power, G_{TX} is the transmitter gain, G_{RX} is the receiver gain, L_{FS} is the free space loss, L_{atmo} is the atmospheric loss due to absorption and scintillation and L_{sys} is the system loss. For more information about the derivation of this relation please refer to the Midterm Report [3].

$$P_{RX} = P_{TX} \cdot G_{TX} \cdot G_{RX} \cdot L_{FS} \cdot L_{atmo} \cdot L_{sys} \tag{2.1}$$

In the following subsections, Equation 2.1 will be broken down and ultimately the link budget finalised. Herein, the product of free space loss and atmospheric loss is treated as a single variable and forms the basis from which the capabilities of the link will be determined. To simplify computation, the wavelength is assumed constant and equal to 1550nm, being the centre of the C-band. This is acceptable since according to REQ-TEC-LSR-7 the wavelength shall be between 1535 nm and 1565 nm which varies by ±1% from the centre wavelength.

2.2.1. Loss

As a laser travels through the atmosphere, it suffers from atmospheric absorption and scattering, as well as aerosol absorption and scattering. These effects can be modelled by a set of equations based on the effective visibility, range and wavelength to determine the path loss. These equations were drawn from the writings of Roberto Sabatini et al.[121] and were then incorporated into the overall loss model. This led to a set of loss values for each possible angle of elevation in both the Earth and space use case. Additionally, the beam was subjected to scintillation[64], which is "the random optical-power fluctuations caused by atmospheric turbulence"[115]. This is a function of the receiver aperture diameter, fading loss probability and turbulence intensity. The receiver aperture is 75 mm as discussed in subsection 2.5.3. The turbulence intensity is expressed in terms of the index-of-refraction structure coefficient which is related to altitude based on the model proposed by Fried [61]. For more details please refer to the Midterm report [3].

The system loss comprises multiple factors; transmission losses on both the transmitter side, pointing losses on both the transmitter and receiver side, fibre coupling losses and beam splitting losses on the receiver side. Therefore, the system loss is described by Equation 2.2, where $L_{trans_{TX}}$ and $L_{trans_{RX}}$ are the transmission losses on the transmission and receiver side, $L_{point_{TX}}$ and $L_{point_{RX}}$ are the pointing losses on the transmission and receiver side and $L_{coupling}$ is the fibre coupling loss on the receiver side.

$$L_{sys} = L_{trans_{TX}} + L_{point_{TX}} + L_{trans_{RX}} + L_{point_{RX}} + L_{coupling} \tag{2.2}$$

From the paper by Remco den Breeje et al.[40] reasonable values for the tracking and transmission losses can be found.

$$L_{trans_{TX}} = L_{trans_{RX}} = -1dB \tag{2.3}$$

$$L_{point_{TX}} = L_{point_{RX}} = -3dB \tag{2.4}$$

With respect to coupling and splitting loss, coupling loss according to [38] can reach a maximum of $-0.9dB$ while beam splitters of a ratio of 92:8 are available. The addition of the coupling loss and loss due to the beam splitter results in a total loss of -1.26 dB. However, faced with a lack of further analysis capability, a more reasonable -7.5dB is chosen based on the thermal and mechanical operational environment as demonstrated in the paper by Breeje et al.[40].

2.2.2. Noise

Another major aspect within the link budget is the determination of the signal-to-noise ratio (SNR) which represents the bit error rate of the signal at a given data rate. This SNR can be used to determine the minimum required received power and thus the data rate the system can sustain during operation. Based on the requirements from SDA and ESTOL standards[60][54] a minimum bit error rate of $1 \cdot 10^{-6}$ was imposed, leading to a design minimum SNR of approximately 19.5 dB at the receiver.

Table 2.2: Noise Factors

Source of Noise	Amount of Noise (NF)
Transmitter Thermal Noise	2.7 dB
Transmitter Amplifier	6 dB
Shot Noise	47.55 dB
Receiver Amplifier	6 dB
Receiver Thermal Noise	33.3 dB
Receiver Electrical Amplifier	6 dB

This SNR serves as the preliminary signal-to-noise ratio for the link budget. Table 2.2 indicates a prospective noise budget based on supporting 1 Gbps data rate. For information about how these noise figures were derived please refer to the Midterm report [3]. Based on this SNR ratio and the summation of the noise figures for the system's components presented in Table 2.2, the received power requirement can then be determined. This received power is -56.1 dBm, in order to ensure sufficient SNR at the receiver.

2.2.3. Results and Requirement Compliance

Table 2.3: Link Budget Requirements from SDA and ESTOL

Name	Description	Origin
REQ-TEC-LKB-1	The Bit Error Rate shall be less than 1e-6	SDA
REQ-TEC-LKB-2	The link margin shall be no less than 3dB	SDA
REQ-TEC-LKB-3	The irradiance at 5500km shall be no less than 25 µW m^{-2} at Full-Width-Half-Maximum angle in the absence of atmospheric effects.	SDA
REQ-TEC-LKB-4	The FWHM beam diameter shall be no less than 1.5m at a range of 100km	SDA
REQ-TEC-LKB-5	The irradiance at the receiver aperture shall be no less than 5.2 µW m^{-2}	ESTOL
REQ-TEC-LKB-6	A transmission loss of no less than 1dB shall be included in both receiver and transmitter sides.	ESTOL
REQ-TEC-LKB-7	A pointing loss of no less than 2dB shall be included in both receiver and transmitter sides.	ESTOL

Table 2.4: Link Budget

Name	Unit	Value
Tx Power		
Laser Power	[dBm]	37.0
Tx Antenna		
Antenna Gain	[dB]	108.3
Tx Margins		
Transmission Loss	[dB]	-1.0
Tracking Loss	[dB]	-3.0
Medium Losses		
Free Space & Atmo Loss	[dB]	-286.5
Rx Margins		
Transmission Loss	[dB]	-1.0
Tracking Loss	[dB]	-3.0
Rx Antenna		
Antenna Gain	[dB]	103.6
Rx Optical		
Coupling and Splitting Loss	[dB]	-7.5
Results		
Received Power	[dBm]	-53.1
Required Power	[dBm]	-56.1
Margin	[dB]	3.0
Coding Gain	[dB]	5.0
Margin with FEC	[dB]	8.0

In order to create the link budget, the system will be studied at its most strained conditions. REQ-TEC-DAP-1 specifies the expected data transfer rate between 1 Gbps and 10 Gbps. For the link budget, a data rate of 1 Gbps will be used. This way it is ensured that if the conditions are more favourable, a higher data rate will be achieved. Due to high uncertainty, the link will be designed so that it operates according to the specifications without forward error correction. An achievable coding gain of 5dB is assumed [40] acting as an additional margin. However, it should be noted that pointing acquisition and tracking conditions have not been considered at this point. Furthermore, to ensure compliance with the relevant ESTOL and SDA standards[54][60] the link budget requirements in Table 2.3 were identified.

It should be noted that REQ-TEC-LKB-4 describes the required beam diameter at 100km leading to REQ-TEC-LSR-4 which defines the requirement for the minimum beam divergence. By requiring a beam diameter at Full Width Half Maximum (FWHM) of 1.5m at 100km the minimum required $1/e^2$ angle is 13 µrad. The Full Width Half Maximum (FWHM) angle represents the beam width angle at which the delivered power is half in comparison to the maximum while the $1/e^2$ angle represents the half angle at which the delivered power is equal to $1/e^2 \approx 0.135$ in comparison to the maximum, which is a common measure of beam divergence. They are related

according to $\theta_{FWHM} = \sqrt{2\ln 2} \cdot \theta_{1/e^2}$. By complying with this requirement compatibility with other terminals is ensured.

Additionally, another relevant requirement constraining the link budget is REQ-TEC-LSR-2 which constrains the transmitted power to a maximum 37 dBm (5 W) which will be used in this study. The receiver power was discussed above in subsection 2.2.2, determining a required power of -56.1dBm. A 75 mm aperture diameter is selected as discussed in subsection 2.5.3. The resulting link budget is presented in Table 2.4.

Regarding compliance with the requirements set forth in Table 2.3, REQ-TEC-LKB-1 that requires the Bit Error Rate to be less than $1 \cdot 10^{-6}$ is satisfied by setting the fading loss probability to $1 \cdot 10^{-6}$ and by calculating the required power as discussed in subsection 2.2.2. REQ-TEC-LKB-2 is satisfied based on Table 2.4 while FEC provides extra margin. By taking the transmitted power into account, the FWHM angle and the link distance for the irradiance at half power can be calculated at range based on Equation 2.5.

$$\frac{1}{2} I_{RX} = \frac{1}{2} P_{TX} \frac{2}{1 - cos(\frac{\theta_{FWHM}}{2})} \frac{1}{4\pi d_{slant}^2} \tag{2.5}$$

Based on this, the irrradiance at 5500 km is 451 µW m^{-2} thus complying with REQ-TEC-LKB-3. The irradiance at the aperture being an arbitrary distance away is calculated by Equation 2.6. This results in an irradiance at the receiver aperture at an arbitrary distance based on the medium loss of 6.4 µW m^{-2} thus complying with REQ-TEC-LKB-5. Lastly based on Equation 2.3 and Equation 2.4 compliance with REQ-TEC-LKB-6 and REQ-TEC-LKB-7 is ensured.

$$I_{RX} = P_{TX} G_{TX} L_{trans_{TX}} L_{point_{TX}} L_{FS} L_{atmo} L_{trans_{RX}} L_{point_{RX}} \left(\frac{2\sqrt{\pi}}{\lambda}\right)^2 \tag{2.6}$$

The product of free space loss and atmospheric loss needs to produce less loss than -286.5 dB for the product of the link budget components to produce a link margin of more than 3dB and meet all the requirements as can be seen in Table 2.4. By taking this limit into account, the link capabilities can be investigated. The results are presented in Figure 2.2 and Figure 2.3.

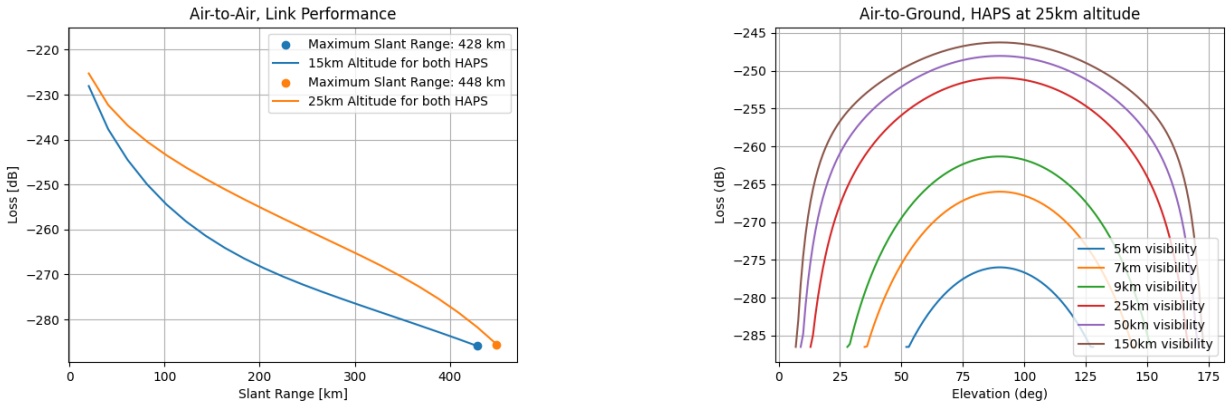

(a) Air-Air Performance

(b) Air to Ground Performance

Figure 2.2: Overview of the Air-Air and Air-to-Ground Link Performance .

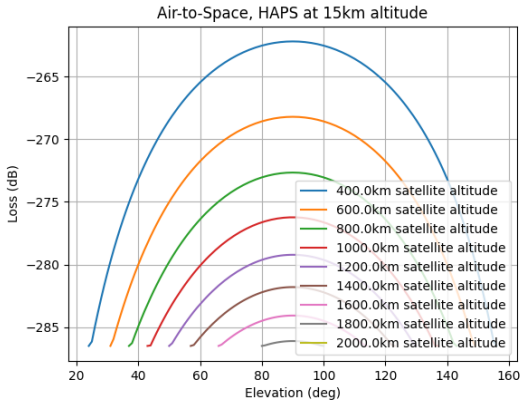

(a) Air to Space Performance with the HAPS at 15km.

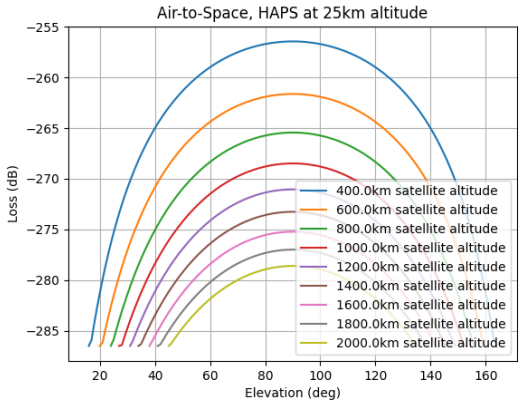

(b) Air to Space Performance with the HAPS at 25km.

Figure 2.3: Overview of the Air to Space Performance.

Based on Figure 2.2b it can be seen that REQ-TEC-LIN-1 is met since an Air-to-Ground link can be established with a HAPS altitude of 25km. The range of this link is heavily dependent on the present weather conditions. In case the HAPS flies at a lower altitude, the ranges at which the link can be established increase.

With respect to Air-to-Air performance the 1000 km link distance set by REQ-TEC-LIN-2 is not met. Due to atmospheric loss and the curvature of the earth, such links are not easily realisable since the beam would have to travel close to the ground and would therefore be even more susceptible to atmospheric losses. The client has been informed about the Air-to-Air performance and it has been deemed reasonable.

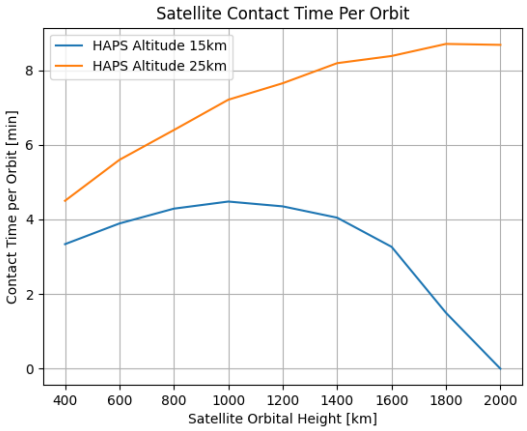

Figure 2.4: Satellite Contact Time with Respect to Orbital Height and HAPS Height.

Air-to-Space performance depends on the flight height of the HAPS. Assuming circular orbits REQ-TEC-LIN-3 is met, since links can be formed with all of Low Earth Orbits (LEOs) for a high HAPS altitude as shown in Figure 2.3. The satellite contact time per orbit with respect to both orbital height and HAPS height can be seen in Figure 2.4. Generally, a higher orbital height leads to an increase in contact time. However, due to the atmospheric effects when the HAPS is at low altitude, contact time with higher LEOs is diminished.

2.3. Optical bench

This section looks into the critical components and design considerations that comprise the optical bench of LCT. The design and selection of optical elements are crucial for achieving optimal performance and meeting the requirements. In the following section, compliance of the optical bench elements selected in the Midterm Report [3] with the requirements is discussed. Afterwards, the layout of the optical bench will be addressed.

2.3.1. Optical Bench Requirement Compliance

During the Midterm Report, numerous components of the laser beam transmitter and receiver were selected. In this section, an overview of the performance of these components will be presented in order to ensure their compliance with the requirements. For more information regarding the selection of these components please refer to the Midterm Report [3].

Starting from the transmitter design, it was ensured that the selected diode [19] complies with REQ-TEC-LSR-7 which specifies the allowable transmission wavelength between 1535nm and 1565nm. Careful consideration was put to ensure that the transmitted optical power of 5 W can be achieved while allowing for tunable output power so that the maximum optical power of 5W specified by REQ-TEC-LSR-2 is not exceeded [3]. Through the selection of high-quality components, the required beam M2 factor of less than 1.1 specified by REQ-TEC-LSR-3 is also achieved [3].

Due to the fact that amplitude modulation either through the use of On-Off-Keying-NRZ or Manchester encoding is required by the relevant SDA[60] and ESTOl[54] standard, a Mach-Zender modulator with a modulation rate

[19] https://www.aerodiode.com/wp-content/uploads/2020/05/1550-nm-laser-diode-Model-1-Datasheet-5.pdf

of 12.5 GHz for digital modulation was selected [20] therefore complying with REQ-TEC-DAP-2 that specifies that amplitude modulation shall be supported and REQ-TEC-LSR-5 that specifies the required pulse duration shall be less than 100 ps while the modulator provides a pulse width of 80 ps.

The selected Analogue to Digital converter [21]has a resolution of 1.37 mV therefore complying with REQ-TEC-LSN-3 that specifies the required resolution to be 13 mV.

Preliminary since the trans-impedance amplifier [22] input-referred RMS noise and the photodetector's [23]dark current (2 µA and −200 nA respectively) and the amplifier [24] noise figure is small it is expected that the detector meets REQ-TEC-LSN-4 that specifies that the detector noise figure shall be bellow 45.3dB. Further analysis shall be performed if deemed necessary.

Through the use of a photodiode for direct signal detection amplitude demodulation can be achieved therefore complying with REQ-TEC-DAP-3. At the same time, all selected receiver components have a bandwidth of more or equal to 10GHz and therefore the detector sampling rate requirement of 10Gsps imposed by REQ-TEC-LSN-5 is achieved. The selected photodiode is compatible with the C-band and therefore complies with REQ-TEC-LSN-6 which specifies that the detector shall operate between 1535nm and 1565nm.

The receiver components synergises in such a way that the analogue signal reaches the analogue to digital converter which has a resolution of 1.37 mV is high enough for detection if the received optical power is -56.1dBm. An overview of the receiver signals can be found in Table 2.5.

Table 2.5: Detector Stages, Gains and Outputs

Stage	Gain	Output
Input	-	-56.1dBm
Optical Amplifier	40dB	16.1dBm
Photo-Detector	0.4 A/W	24.6 µA
Trans-impedance Amplifier	7.5 kΩ	184 mV

2.3.2. Optical Bench Configuration

For the configuration of the optical bench, all components are strategically placed to optimise performance while adhering to spatial constraints. The optical bench is housed within the wing of the platform, which increases the importance of a compact and efficient optical bench layout. This bench makes use of shock absorbers to reduce the negative effect that platform vibration might have on the platform.

The order and arrangement of different components are identical to the block diagram of the LCT presented earlier in this chapter. The layout is presented in Figure 2.5. In Figure 2.6, the top view of the same optical bench is presented, where a space-optimised arrangement is featured. The red lines refer to the transmitting laser while the blue lines refer to the receiving laser.

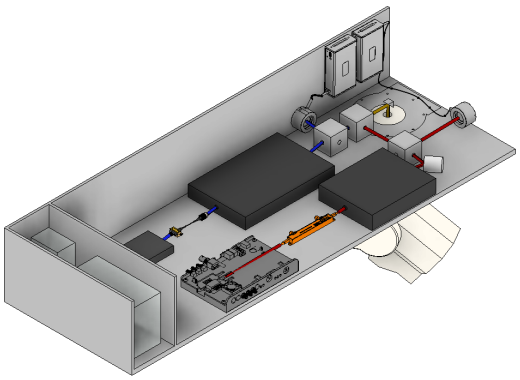

Figure 2.5: Optical Bench of the LCT

To optimise the layout and ensure smooth operation, components that do not directly interact with the light path as shown in Figure 2.6. Parts such as voltage converters, controllers and the control computer are placed at the end of the optical bench. This arrangement ensures that the optical components have a clear, unobstructed path for the laser signals. Furthermore, by keeping the electronic components separate from the optical components, the design reduces the risk of electromagnetic interference which could affect the laser communication performance. The dimensions of the current layout and design of the optical bench of the LCT, as shown in Figure 2.6, is 900 mm by 300 mm by 150 mm, which satisfies REQ-CON-ENB-1.

[20] https://www.optilab.com/products/1550-nm-10-ghz-intensity-modulator-pm-fc-apc
[21] https://nl.mouser.com/ProductDetail/584-AD9213BBPZ-10G
[22] https://nl.mouser.com/ProductDetail/595-ONET2804TLPY
[23] https://nl.mouser.com/ProductDetail/508-VPDV2120VFFA
[24] https://www.optilab.com/products/low-noise-high-gain-pre-amp-edfa-module-40-db-wideband-gain

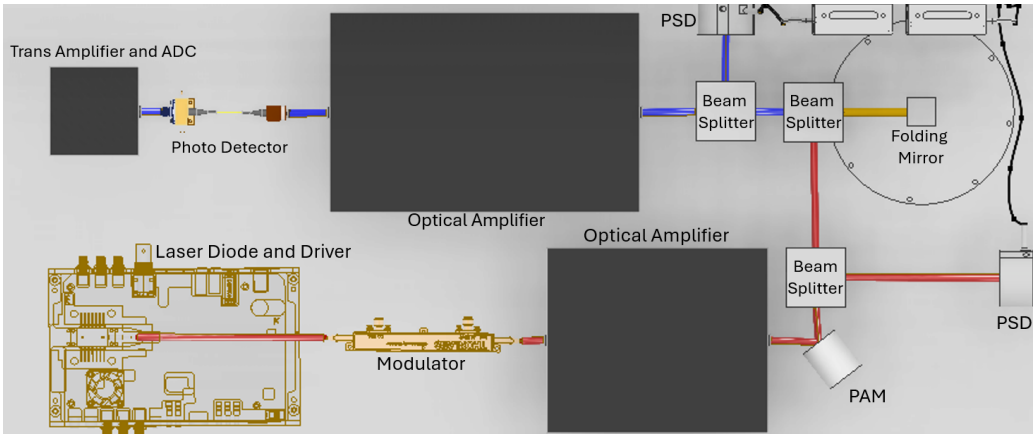

Figure 2.6: Top View of the Optical Bench Layout, Showing the Main Components.

2.4. Pointing Acquisition and Tracking (PAT)

Pointing Acquisition and Tracking usually referred to as PAT in laser communication terminals is the process of initial pointing of the laser using the coarse pointing assembly followed by performance of the acquisition patterns and finally the achievement of a stable track and therefore communication link. According to REQ-TEC-OPT-4 the PAT strategy must comply with the relevant SDA standard [60] which describes a beacon-less acquisition strategy meaning that the communication beam is used for PAT as well. In addition to this REQ-TEC-OPT-5 which stems from the relevant ESTOL standard [54] states that the acquisition process shall take no more than 60 seconds. In order to perform an analysis on the PAT, an estimation of the uncertainty cone in various conditions will be performed followed by an analysis of the acquisition pattern under platform vibrations and finally a summary of the performance of the PAT process.

2.4.1. Uncertainty Cone

A critical aspect of the PAT is the size of the uncertainty cone. Due to the imperfect positional and attitude knowledge of the two LCTs to be connected, it is not possible to spatially align the communication beams directly on the receivers' apertures. From the perspective of the primary LCT, the location of the target LCT is uncertain and therefore it is located within an uncertainty cone.

Uncertainty of this type has many sources which are split into three categories. Namely, jitter/vibrations, pointing accuracy and pointing error due to attitude and positional knowledge errors. All errors are assumed to follow a Gaussian distribution and be independent. This serves as a good approximation of the error environment [89]. Therefore the standard deviation of all errors combined according to Kaushal et al. [89] can be expressed as seen in Equation 2.7 where σ_{total} is the standard deviation of the total error and $\sigma_1^2 + \sigma_2^2 + \cdots + \sigma_n^2$ is the summation of the variances of all the individual errors.

$$\sigma_{total} = \sqrt{\sigma_1^2 + \sigma_2^2 + \cdots + \sigma_n^2} \tag{2.7}$$

The acquisition process according to [60] consists of three phases. An overview of this process can be found in Figure 2.7. During the first phase, the "lead" LCT scans the initial uncertainty cone this cone is therefore referred to as UC1A while the "follow" LCT detects the direction of the incoming beam and positions itself. This follow LCT then scans the new uncertainty cone, referred to as UC1B. After phase 1 is completed phase two of acquisition can be started, in which either one of both of the terminals scan the new uncertainty cone. Since the links need to be bidirectional according to [54] both terminals scan the UC referred to UC2. Finally, fine acquisition can commence and the uncertainty cone at this time is called UC3.

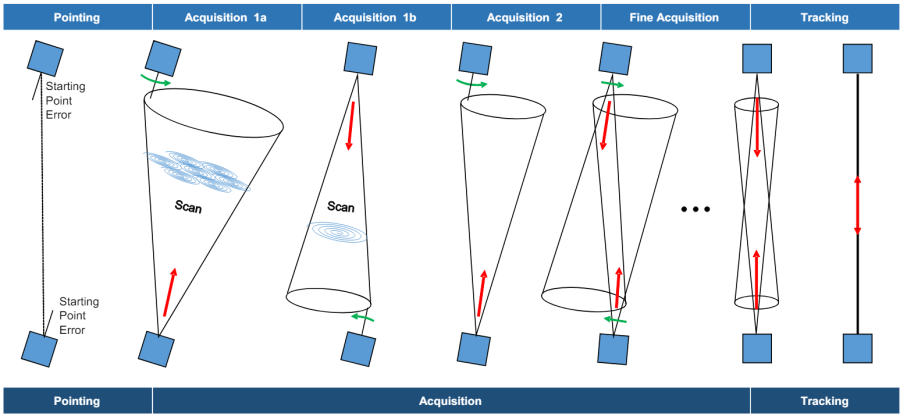

Figure 2.7: Spatial Acquisition Process Diagramming the Sub-states of Pointing Acquisition, and Tracking as Defined within the PAT State Machine. [60]

The initial uncertainty cone UC1A is influenced by pointing and positional errors since the LCT needs to slew the CPA at an uncertain target attitude. However, UC1B and UC2 are not directly influenced by position errors since the attitude information originated from the CPS (Coarse Pointing Sensor) which in turn introduces uncertainty. Additionally, UC1B and UC2 are assumed to be equal. Finally, UC3 is assumed to be half of UC2 for ease of analysis and as a conservative estimate.

Uncertainties related to pointing accuracy are of high importance. Due to the fact that the link has not been established, closed-loop tracking can not be utilised and therefore open-loop pointing must be used which is therefore influenced by pointing accuracy. Pointing accuracy is influenced by both the FSM and PAM as well as the CPA. For the CPA a commercially available magnetic encoder is used as a reference for the accuracy. For the CPS a Quadrant Photodiode is used whose accuracy is estimated in subsection 2.5.3. A summary of the pointing accuracy both including and excluding the CPS can be found in Table 2.6. The accuracy of the FSM and PAM is 100 µrad and needs to be scaled based on the angle of the beam in relation to the angle of the FSM, with that being 6.67 based on Figure 2.16 that will be discussed in subsection 2.5.3 where a 2 degrees FSM deflection produces a 0.3° beam deflection.

Attitude and Positional errors should also be estimated. Attitude errors are affected by the attitude knowledge errors of the LCT while positional errors are affected by positional knowledge errors of the LCT, ephemeris errors, point ahead angle errors and timing errors [134]. The attitude error remains constant in all link types and according to the chosen GNSS-INS unit (Global Navigation Satellite System - Inertial Navigation System)[26] the standard deviation is maximum for the pitch/roll at 524 µrad (assuming a GNSS receiver separation of more than 2 m). In addition to this, the GNSS-INS unit provides a standard deviation of 2 m positions accuracy to the LCT. The angle error caused by positional errors varies per link type. The angle errors caused by the positioning errors will be investigated in Air-to-Space, Air-to-Air, and Air-to-Ground link types.

Table 2.6: Pointing Errors due to Accuracy.

	σ[µrad]
FSM [93]	15
PAM [93]	15
CPA [25]	698
CPS [95]	123
σ_{accu}	698
$\sigma_{accu_{CPS}}$	709

Starting with Air-to-Space Links circular orbits are assumed. The along track, e_{along}, and out-of-plane, e_{out} ephemeris errors shall be investigated. The impact of ephemeris errors and positional errors, e_{GNSS}, can be seen in Figure 2.8 with H_{HAPS} and H_SAT being the HAPS and Satellite height accordingly.

[26]Advanced Navigation Certus Evo `https://www.advancednavigation.com/inertial-navigation-systems/mems-gnss-ins/certus-evo/`

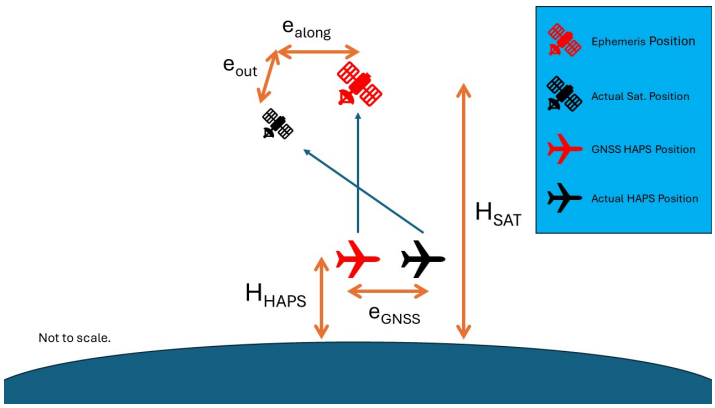

Figure 2.8: Overview of Ephemeris Errors.

Therefore the pointing error due to ephemeris and positional errors, e_{pnt_eph}, is defined in Equation 2.8.

$$e_{pnt\_eph} = \arctan\left(\frac{\sqrt{e_{along}^2 + e_{out}^2} + e_{GNSS}}{H_{SAT} - H_{HAPS}}\right) \tag{2.8}$$

An estimate of the along-track and out-of-plane errors based on a Two-line element set for LEO satellites can be obtained from Flohrer et al. [59] taken as 500 m and 150 m respectively. The satellite orbital height is assumed to be 400 km as according to the World Meteorological Organisation [27] most of the lowest orbiting satellites do not orbit bellow that height and by taking the minimum orbital height the errors is maximised thus making it a conservative estimate. By realising the GNSS error is small it can be neglected and by assuming small angles Equation 2.8 can be expressed as Equation 2.9.

$$\sigma_{pnt\_eph} = \frac{\sqrt{e_{along}^2 + e_{out}^2}}{H_{SAT} - H_{HAPS}} \tag{2.9}$$

With respect to the point ahead angle's impact on the uncertainty cone the angle calculated in subsection 2.7.3 will simply be added as another error source for the sake of simplicity. The point ahead angle is negligible in comparison to the ephemeris error however it is included.

Lastly, the timing error is caused by incorrect calculation of the satellite position due to erroneous knowledge of the current time. This phenomenon can be visually contextualised in Figure 2.9, with v_t being the satellite velocity projected perpendicularly to the line of sight and Δt_{timing} being the timing accuracy. The effects of the HAPS speed on the timing error are negligible due to the low speed. The pointing angle error, σ_{pnt_t}, assuming small angles can be calculated based on Equation 2.10.

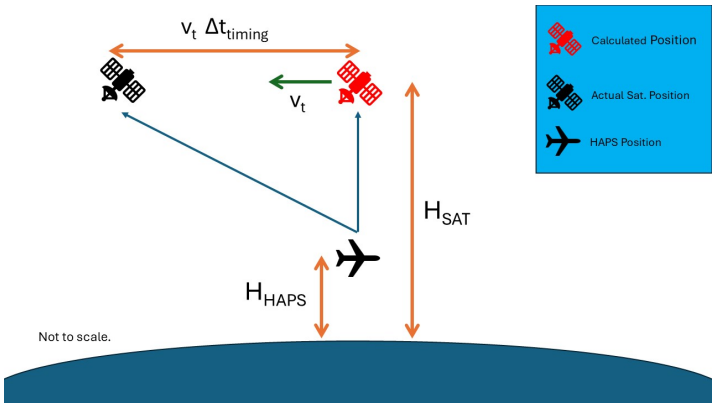

Figure 2.9: Overview of Timing Errors

[27] https://tools.wmo.int/satellites

$$\sigma_{pnt\_t} = \frac{v_t \Delta_{t_{timing}}}{H_{SAT} - H_{HAPS}} \tag{2.10}$$

Using Equation 2.31 the tangential speed can be calculated. The GNSS-INS receiver provides a timing accuracy of 20 ns and therefore for an orbital height of 400 km the angle error is 434 prad which is negligible and therefore not included.

For Air-to-Air applications the point ahead angle is not relevant. Timing errors are also not relevant due to the low speeds involved. Therefore only positional errors are relevant. With both LCTs using the same GNSS-INS receiver providing 2 m positional accuracy the pointing error due to positional error knowledge, $\sigma_{pnt_{GNSS\_A-to-A}}$, can be calculated assuming small angles based on Equation 2.11 with d_{slant} being the slant range. A slant range of 100km will be assumed as the minimum slant range. Air-to-Air links at smaller ranges impose stringent requirements on the field of regard of the LCTs and therefore are not considered at this point.

$$\sigma_{pnt_{GNSS\_A-to-A}} = \frac{\sqrt{e_{GNSS}^2 + e_{GNSS}^2}}{d_{slant}} = \sqrt{2}\frac{e_{GNSS}}{d_{slant}} \tag{2.11}$$

For Air-to-Ground links the situation is the same as for Air-to-Air links however perfect positional knowledge of the ground station is assumed and therefore the pointing error due to positional inaccuracies, $\sigma_{pnt_{GNSS\_A-to-G}}$, can be expressed by Equation 2.12.

$$\sigma_{pnt_{GNSS\_A-to-G}} = \frac{e_{GNSS}}{d_{slant}} \tag{2.12}$$

An overview of the pointing errors originating from attitude and positional knowledge errors for all link types can be found in Table 2.7.

Table 2.7: Pointing Errors due to Attitude and Positional Errors.

Error Source	Pointing Error [µrad]		
	Air-to-Space	Air-to-Air	Air-to-Ground
Attitude Error	524	524	524
Positional Error	1339	28	133
$\sigma_{att-pos}$	1438	525	541

In order to achieve 3σ acquisition probability when excluding platform vibrations the UC is taken to have a radius of 3σ. Therefore the uncertainty cones are reported for each link type in Table 2.8.

Table 2.8: Radius of the Uncertainty Cone for all Link Types.

	Uncertainty Cone Radius [µrad]		
Cone	Air-to-Space	Air-to-Air	Air-to-Ground
UC1A	4797	2620	2649
UC1B	2128	2128	2128
UC2	2128	2128	2128
UC3	1064	1064	1064

2.4.2. Acquisition Pattern

The acquisition pattern in accordance with the relevant SDA standard [60] should be a constant velocity Archimedes spiral starting from the centre. As discussed in subsection 2.5.3 the entire uncertainty cone can be covered by a single spiral. The spiral in polar coordinates can be described by Equation 2.13 [97] and in Cartesian coordinates by Equation 2.14 and Equation 2.15.

$$r_{spiral} = \frac{C_{spiral}}{2\pi}\theta_{spiral} \tag{2.13}$$

$$x_{spiral} = r_{spiral}\cos(\theta_{spiral}) \tag{2.14}$$

$$y_{spiral} = r_{spiral}\sin(\theta_{spiral}) \tag{2.15}$$

[27] Artos Magnetic Encoder: `https://www.rls.si/eng/artos-dhr-rotary-absolute-magnetic-encoder-system`

Where C_{spiral} is the spiral spacing. The spiral spacing dictates the power delivered to the points in between the spiral "arms". Since this is a constant velocity spiral, with spiral velocity V_{spiral} the rate of change of θ_{spiral} is described by Equation 2.16.

$$\frac{d}{dt}\theta_{spiral} = \frac{V_{spiral}}{\frac{C_{spiral}}{2\pi}\sqrt{1+\theta_{spiral}^2}} \tag{2.16}$$

From Table 2.4 it can be seen that the pointing accuracy is -3dB while at the same time the relevant ESTOL standard [54] demands a -3dB acquisition margin. Therefore C_{spiral} must be chosen such that no less than half power is delivered to the uncertainty cone. This corresponds to $C_{spiral} = \theta_{FWHM} = \sqrt{2\ln(2)} \cdot \theta_{1/e^2}$. In this case as will be discussed in subsection 2.5.3 with diffraction limited performance $\theta_{1/e^2} = 13.16\,\mu\text{rad}$ and therefore $C_{spiral} = 18.24\,\mu\text{rad}$. The spiral pattern continues until $r_{spiral} \geq UC + C_{spiral}$ with the extra C_{spiral} term ensuring that the entirety of the uncertainty cone is covered.

A beam kernel of a Gaussian beam is overlaid over the spiral pattern to calculate the power delivered in the uncertainty cone area. The beam kernel can be seen in Figure 2.10a while an example spiral pattern can be seen in Figure 2.10b. When the beam kernel is overplayed over the spiral, the total received energy and the maximum received power at the uncertainty cone can be computed. An overview of this can be seen in Figure 2.11.

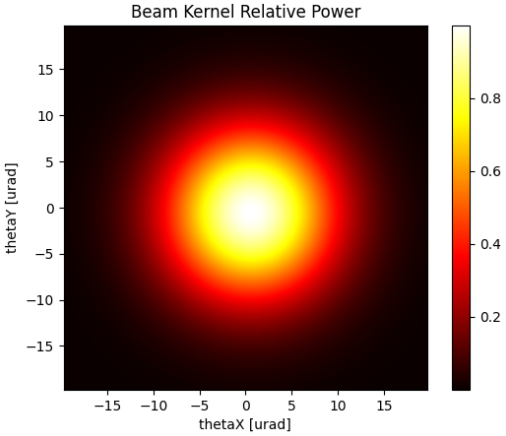

(a) Beam Kernel Relative Power.

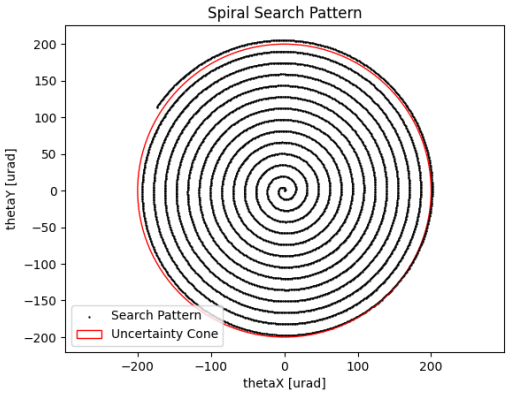

(b) Spiral Pattern

Figure 2.10: Beam Kernel and Spiral Search Pattern.

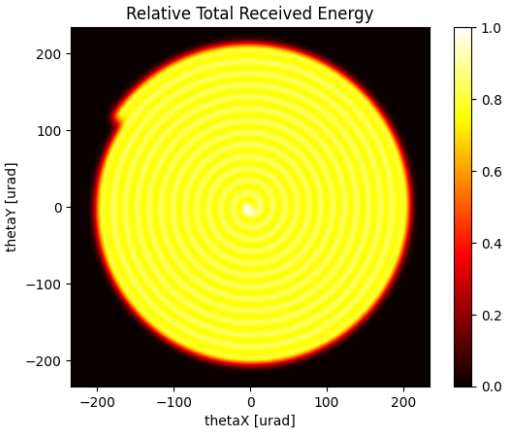

(a) Relative Energy Delivered at the Uncertainty Cone.

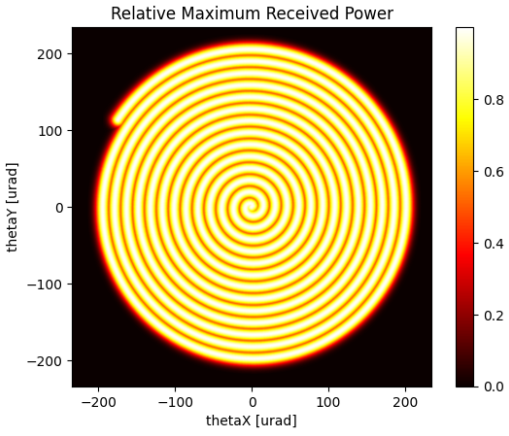

(b) Maximum Power Delivered at the Uncertainty Cone.

Figure 2.11: Relative Total Energy and Maximum Power Received at the Uncertainty Cone.

In order to study the effects of platform vibrations, a typical aeroplane rotational vibrations power spectral density is assumed as well as a dampener [76]. Dampening can be achieved by either mechanical dampeners or active dampening based on the measurements of the INS or preferably a combination of both. The phase spectrum of the Fourier transform is randomised and then an inverse fast Fourier transform is performed

to obtain a time series. The vibrations on the two axes are assumed to be independent. An overview of the vibration's power spectral density and time series can be seen in Figure 2.12. The effect of these vibrations on the search pattern can be seen in Figure 2.13.

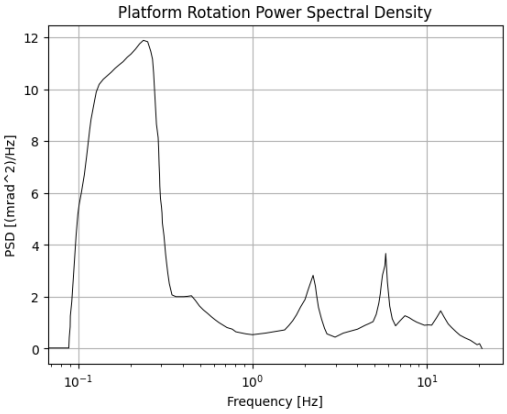

(a) Rotational Vibrations Power Spectral Density [76]

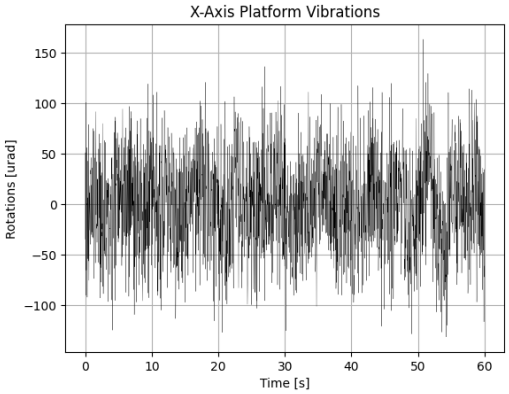

(b) Rotational Vibrations Time Series with -20dB Dampener.

Figure 2.12: Rotational Vibrations Power Spectral Density [76] and its corresponding Example Time-series.

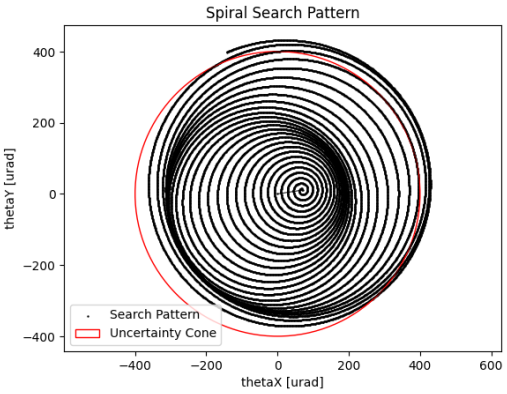

(a) Spiral Search Pattern Affected by platform vibrations.

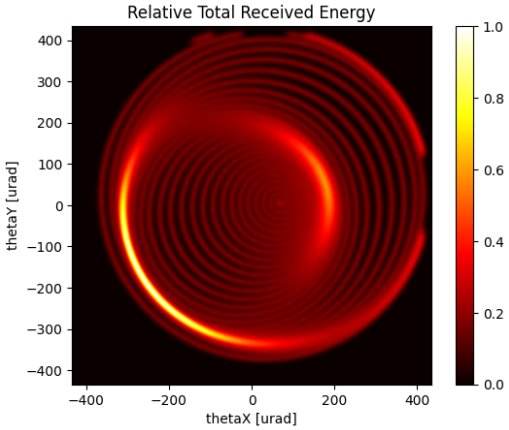

(b) Total relative delivered energy affected by platform vibrations

Figure 2.13: Example Effects of Platform Vibrations on the Acquisition Pattern.

2.4.3. Performance

In accordance to EQ-TEC-OPT-5 the PAT sequence shall not take more than 60s. The time required to perform a spiral, T_{spiral}, can be analytically calculated according to Equation 2.17[60].

$$T_{spiral} = \pi \frac{C_{spiral}}{V_{spiral}} \left(\frac{UC}{C_{spiral}} \right)^2 \tag{2.17}$$

The spiral time is therefore dependent on the radius of the uncertainty cone, the spiral spacing and the spiral velocity. Therefore for the various link types heat maps representing the total PAT time with respect to spiral spacing and spiral speed can be created. Spiral spacing up to θ_{FWHM} is considered as discussed in subsection 2.4.2 since above that spiral spacing the coverage drops below 100% even with no vibrations. These heat maps for Air-to-Space and Air-to-Air can be found in Figure 2.14. Air-to-Ground is omitted as it is very similar to Air-to-Air since the uncertainty cone radii are approximately the same as seen in Table 2.8.

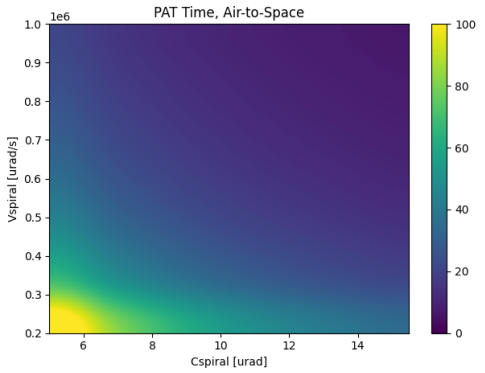

(a) PAT Time Air-to-Space. (Time in Seconds)

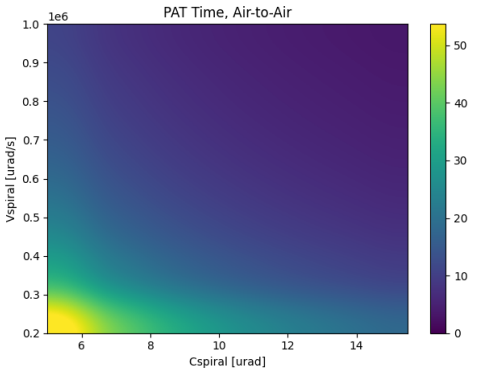

(b) PAT time Air-to-Air. (Time in seconds)

Figure 2.14: PAT time for Air-to-Space and Air-to-Air Links with Respect to Spiral Spacing and Speed.

Therefore appropriate combination of spiral speed and spiral spacing needs to be selected in order for the PAT process to take less than 60 seconds. In case vibrations are not an issue, the spiral spacing shall be taken as θ_{FWHM} to ensure complete coverage and the spiral velocity shall be selected as the minimum velocity that achieves the 60s requirement. This way the demand on the FSM that traces the spirals and the QPD that detects the incoming signals is minimised. The SDA standard states that the PAT process should take 30s, and therefore if the hardware permits this a faster spiral speed can be selected in order to decrease that PAT time. An estimate of these spiral speeds can be found in Table 2.9.

Table 2.9: Selected Spiral Speeds in Absence of Vibrations.

PAT Time [s]	Spiral Speed [µrad/s]		
	Air-to-Space	Air-to-Air	Air-to-Ground
60	113717	58332	58870
30	227434	116664	117741

When vibrations are considered, the selection of spiral spacing and speed is not trivial. The effects of platform vibrations will be investigated by inspecting the UC1A scan of the Air-to-Air link type. The scan coverage under various vibration conditions can be seen in Figure 2.15.

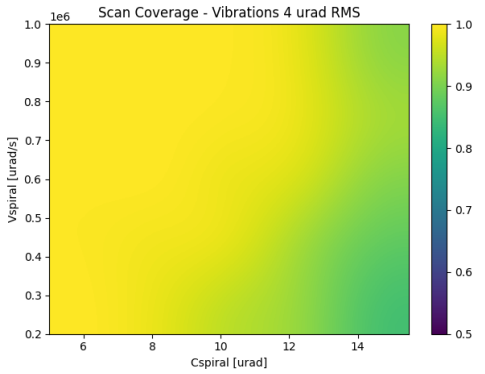

(a) Coverage with 4 µrad RMS vibrations.

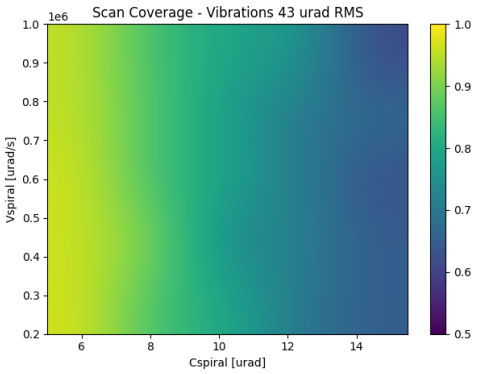

(b) Coverage with 43 µrad RMS vibrations.

Figure 2.15: Effects of Vibrations on Spiral Coverage.

It can be seen that in this case, spiral spacing has a higher effect on the spiral coverage. It is therefore recommended to start the optimisation procedure from θ_{FWHM} and the spiral speeds presented in Table 2.9 after which the spiral spacing shall be reduced while the spiral speed should be increased in order to maintain the total PAT time target. This way spiral speed is kept at a minimum.

Further analysis of what the maximum spiral velocity is and the vibrations of the HAPS should be carried out in the future in order to fully characterise the PAT procedure of the LCT/HAPS combination.

2.4.4. Global Navigation Satellite System - Inertial Navigation System (GNSS-INS)

In order for the LCT to be able to conduct the PAT procedure, its position and attitude needs to be known. While these could theoretically be provided by the platform that it is installed on it would be preferable if the LCT acted as a stand-alone system.

Therefore a GNSS-INS unit needs to be included in the LCT. These combined units provide positional information through the GNSS component and attitude information based on both the GNSS and INS components. With regards to the INS unit, two gyroscope technologies are identified: Micro-ElectroMechanical System (MEMS) and FOG. A selection of GNSS-INS units from Xsense and Advanced Navigation is presented in Table 2.10.

Table 2.10: Overview of Examined GNSS-INS Units Performance.

Name	Gyro Technology	Accuracy RMS				Power [W]	Mass [g]
		Pitch/Roll [deg]	Heading [deg]	Horizontal [m]	Vertical [m]		
MTi-670 [28]	MEMS	0.2	0.8	1	N/A	0.5	8.9
Certus Evo [29]	MEMS	0.03	0.05	1.2	2	2.9	155
Spatial FOG [30]	FOG	0.01	0.01	0.8	1.5	6.1	740
Spatial [31]	MEMS	0.1	0.2	2	3	0.5	5
MTi-G-710 [32]	MEMS	0.2	0.8	1	N/A	0.66	58

While the performance of the unit utilising FOG technology is superior in terms of attitude determination there is a considerable power and mass penalty as well as a cost-benefit not presented in Table 2.10 due to the lack of cost values available. At the same time since the accuracy of the CPA is approximately 698 mrad as discussed in subsection 2.4.1, the benefit of a much more accurate GNSS-INS unit is diminished. Therefore from the presented GNSS-INS units, the Certus Evo from advanced navigation is selected. It should be noted that if the GNSS antenna separation of more than 2m the heading accuracy of the Certus Evo is less significant than the Roll/Pitch accuracy.

2.5. Coarse Pointing

The gimbal design used for the coarse pointing of the LCT is of great importance. In this section, the detail will be given with regards to the mechanical drive of the gimbal in subsection 2.5.1. This is followed by the material selection of the overall assembly in subsection 2.5.2 and subsequently the design of the telescope, in subsection 2.5.3, which will be placed on the coarse pointing assembly. Before delving deeper into the detailed design of the coarse pointing, it is important to mention that for the sake of minimising the optical aberrations, which is crucial, especially given the requirement for long-distance links, no glass bulb or any other curved-shaped glass is utilised for protection. Meaning the coarse pointing assembly will be in direct contact with the outside environment.

2.5.1. Mechnical Drive System Configuration

To minimise the protruding volume of the Laser Communication Terminal (LCT), a coarse pointing assembly, namely a gimbal, is used to re-direct the light into as well as out of the optical bench. For this, the design requires a hollow shaft to provide an optical path from the outside into and out of the optical bench. Two primary options for achieving this are using hollow shaft motors and incorporating a Ring Gear which is derived with a motor on the outer side, allowing for the shaft rotation axis of the ring gear to be hollow.

- Hollow Shaft Motors: These motors, which are typically Frameless Brushless DC motors, are designed with a hollow shaft which makes them optimal for applications where an unobstructed optical pathway is needed, such as directing the light into and out of the LCT. This configuration is advantageous due to their low weight and their ability to provide smooth and precise control. However, these motors require a robust feedback system, especially critical in environments with unpredictable forces, such as those encountered during high-altitude flights. This will be discussed in more detail in the following paragraphs.
- Ring Gear: The ring gear drive configuration consists of a large ring gear, driven by a smaller gear. For this configuration, there are two options available, namely ring gear in combination with a normal gear or a worm gear, among which the focus will be on the worm gear in this section due to the self-locking feature of the worm gear combination which does not allow any back driving. This ensures the motor gear

[28]MTi-670: https://www.movella.com/products/sensor-modules/xsens-mti-670-gnss-ins
[29]Certus Evo: https://www.advancednavigation.com/inertial-navigation-systems/mems-gnss-ins/certus-evo/
[30]Spatial FOG https://www.advancednavigation.com/inertial-navigation-systems/fog-gnss-ins/spatial-fog-dual/
[31]Spatial https://www.advancednavigation.com/inertial-navigation-systems/mems-gnss-ins/spatial/
[32]MTi-G-710: https://www.movella.com/products/sensor-modules/xsens-mti-g-710-gnss-ins

can rotate the main shaft/ring but the ring gear cannot drive the motor gear. Similar to the hollow shaft motors, the ring gear configuration can provide a hollow shaft by making use of a bearing in the centre of the turning gear, providing an unobstructed optical path.

As mentioned earlier, the usage of a glass bulb was avoided. This means the gimbal will be in direct contact with the environment, including continuous aerodynamic force during flight and turbulent/gust pockets of air hitting the assembly from all directions. Additionally, the movements of the aircraft itself contribute to these forces. These factors affect the selection procedure for the driver system, as explained below.

When using a hollow shaft motor, most probably a Frameless Brushless DC motor, which is going to be in direct contact with air, resulting in a continuous aerodynamic force during cruise, there is a need for continuous power to maintain its attitude in the right direction. Even when there's no need for establishing a link, there is still a need for continuous power to prevent the assembly from swinging around as a result of the continuous aerodynamic force experienced by the gimbal. As the power needed for maintaining position is not that significant it is not considered a notable drawback for hollow shaft motors, but the need for this power is still present. In the case of the ring gear which uses a worm gear configuration, there is no additional power required to maintain attitude thanks to the self-locking feature of the worm gears preventing back driving. As mentioned earlier, this ensures the motor is able to easily rotate the shaft/ring gear but the shaft/ring gear is not able to rotate the motor.

Furthermore, the gimbal will be exposed to an unpredictable environment characterized by varying aerodynamic forces. These forces can change in direction and magnitude due to factors such as gusts, turbulence, and the aircraft's movement. The chosen drive system must maintain the gimbal's position against these unpredictable forces without excessive power consumption. The worm gear's self-locking property addresses this challenge by ensuring the gimbal remains stationary without needing active power to counteract aerodynamic forces. On the other hand, a brushless frameless DC motor must be paired with a rapid and responsive feedback system to function properly. This system would require continuous high-resolution sensors, to monitor the position constantly. Additionally, the feedback loop must be quick enough to detect and correct any deviations caused by external forces. The need for a sophisticated and high-bandwidth feedback system increases the complexity and power consumption of using a brushless frameless motor. Therefore, the ring gear with a worm gear is the best option for this use case, as it simplifies the system without introducing additional complexity.

The main reliable options for powering the shaft in the case of the worm gear-ring gear combination are stepper motors and brushless motors, since they are capable of rotating without limits, unlike most servo motors. With regards to picking the specific motor for the worm gear-ring fear combination, there is a lot of freedom available. This is mainly because the resolution is not a limiting factor in this case. This is due to the gear ratio that this drive is going to have. The high gear ratios of this configuration will mean that even a lot more rotations are needed from the motor side to achieve only one rotation of the ring gear/shaft, meaning even stepper motors which would have rather big steps can still mostly be used in this case. The motor selection for powering the shafts will be discussed and presented in subsection 2.5.5.

2.5.2. Material

Selecting the appropriate material for the coarse pointing assembly is crucial, especially given the challenging environmental conditions encountered at high altitudes. The CPA must operate reliably at low temperatures and in continuous contact with air while maintaining structural integrity and performance. This section outlines the key considerations and the justification for picking the suitable material for CPA.

When selecting the material, several important aspects were considered:

- **Mechanical Properties:** The material must provide high strength and especially stiffness to ensure the CPA can withstand various mechanical loads and stresses during operation.
- **Thermal Properties:** The Coefficient of Thermal Expansion (CTE) must be low to minimise thermal deformation, ensuring stable alignment of optical components under temperature variations.
- **Physical Properties:** The density of the material impacts the overall weight of the CPA. Lightweight materials are preferred to reduce the payload weight.
- **Environmental Resistance:** The material should resist corrosion and moisture to maintain performance and longevity, especially under harsh environmental conditions in high altitudes.
- **Cost:** Material cost and manufacturability are important to keep the overall project within budget while ensuring ease of fabrication and assembly.

For picking the best material, common materials used in the precision engineering and aerospace engineering fields were considered. Due to the limited room for exploring different options, only the three materials that were chosen as the best option will be presented. These three materials are Aluminium Silicon Carbide (AlSiC),

Titanium Alloy (Ti-6Al-4V), and Aluminium Alloy (7075-T6). The main properties of the aforementioned material are given in Table 2.11:

Table 2.11: Comparison of Material Properties for Gimbal Design

Property	**Aluminum Silicon Carbide (AlSiC)**	**Titanium Alloy (Ti-6Al-4V)**	**Aluminum Alloy (7075-T6)**
Mechanical	High stiffness, good strength	High strength, excellent fatigue resistance	High strength, good fatigue resistance
Thermal	CTE: $\sim 6 - 8 \times 10^{-6}$/°C	CTE: $\sim 8.6 \times 10^{-6}$/°C	CTE: $\sim 23.5 \times 10^{-6}$/°C
Physical	Density: ~ 3.0 g/cm^3	Density: 4.43 g/cm^3	Density: 2.81 g/cm^3
Environmental Resistance	Excellent corrosion resistance	Excellent corrosion resistance	Good corrosion resistance (requires surface treatment)

When cost is not a primary concern, Titanium Alloy (Ti-6Al-4V) stands out as the best material for the gimbal design. It offers a great combination of high strength, excellent fatigue resistance, and outstanding corrosion resistance, making it ideal for high-altitude conditions. Aluminium Silicon Carbide (AlSiC) is a strong contender due to its low thermal expansion and good stiffness, but it doesn't quite match the strength of Ti-6Al-4V. On the other hand, Aluminium Alloy (7075-T6) is the lightest option and has good mechanical properties, but its higher thermal expansion and the need for additional corrosion protection make it less suitable for this particular use.

2.5.3. Telescope

The telescope of the LCT serves two main purposes, it needs to transmit the outgoing beam with a divergence angle according to the specifications as well as gather the incoming beam and reduce its diameter so that it can be transferred into the optical bench for processing. Many telescope types are available which fall under three categories, namely refractor, reflector and catadioptric telescopes. For this application a reflector telescope is selected, providing a size advantage over the refractor telescope and being simpler than the catadioptric telescope. Additionally, it was decided to make the main mirror off-axis as to avoid placing any optical components at the aperture of the telescope, thus maximising the amount of incoming light. Focusing the laser to a small volume is also avoided so that no ionisation of the air occurs.

According to REQ-TEC-LSR-4, the outgoing beam shall have a full beam divergence of more than 26 µrad and therefore θ_{1/e^2} shall be greater than 13 µrad. If a Gaussian diffraction-limited beam is assumed this would correspond to a primary mirror diameter of approximately 75 mm [33] resulting in a $\theta_{1/e^2} = 13.16$ µrad > 13 µrad. After consulting with a TNO expert, it was discussed that this assumption is reasonable for a surface flatness of $\lambda/20$ at 1550 nm wavelength and therefore the common surface flatness of $\lambda/10$ defined at 632.8 nm[34] would be sufficient to meet REQ-TEC-LSR-3 which specifies that the M2 factor shall be less than 1.1.

Another consideration for the telescope is the ability to perform the acquisition pattern. As mentioned in subsection 2.4.2 the entire uncertainty cone is covered with a single spiral drawn by the FSM to avoid using the CPA during the scan. From Table 2.8 it can be seen that the maximum uncertainty cone radius is 4797 µrad. This cone can be covered if the telescope in combination with the FSM has a field of regard of 0.3°. This results in the decision to place the FSM as close to the primary mirror as possible to allow the 2° of movement of the FSM to draw the 0.3° spiral. This is made possible due to the compact and lightweight nature of the TNO FSM that has been selected allowing it to be placed in the CPA. An overview of the configuration of the primary telescope can be seen in Figure 2.16 made using OpticalRayTracer 9.6 [35].

[33] Propagation of Gaussian beams: `https://www.rp-photonics.com/gaussian_beams.html`
[34] Surface flatness: `https://www.edmundoptics.com/knowledge-center/application-notes/optics/optical-flats/`
[35] OpticalRayTracer: `https://arachnoid.com/OpticalRayTracer/`

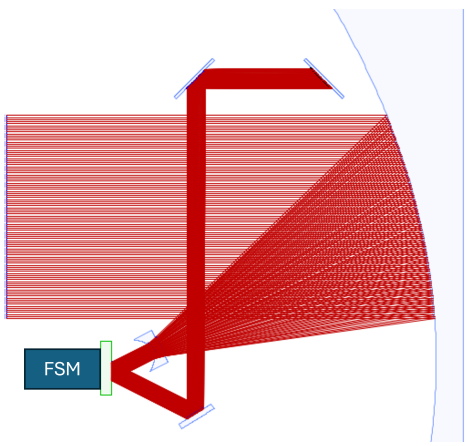

(a) 0° Outgoing Beam, 0° FSM Deflection

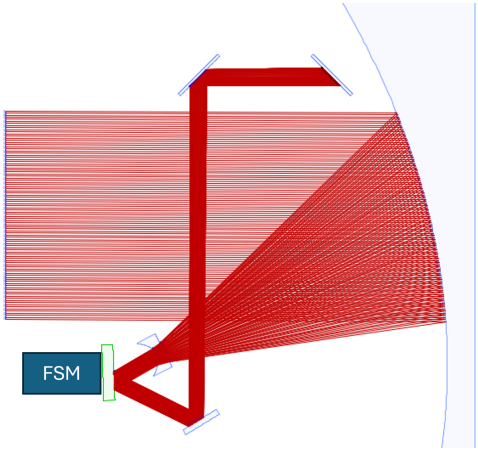

(b) 0.3° Outgoing Beam, 2° FSM Deflection

Figure 2.16: Overview of the Primary Telescope.

The primary telescope's primary mirror of an off-axis parabolic mirror. The light is collimated using collimator optics and therefore turned into a low divergence beam, in this case, a singlet parabolic lens is used for simplicity but it should be replaced with a configuration providing achromatic characteristics and potentially a custom lens shape. The presented telescope magnifies a 7 mm beam to a 75 mm beam providing a magnification factor of 10.71.

While the field of regard has a radius of 0.3° in practice this is only usable when transmitting. When receiving an offset signal, the FSM needs to be tilted to a specific orientation in order to redirect the incoming light into the arm of the CPA and the optical bench. This is not possible due to the fact the fine pointing sensor is located behind the FSM and into the optical bench. For this reason, a second wide-FOV telescope is used which focuses the light directly onto the coarse pointing sensor. An overview of the wide-FoV telescope made in OpticalRayTracer 9.6 can be seen in Figure 2.17.

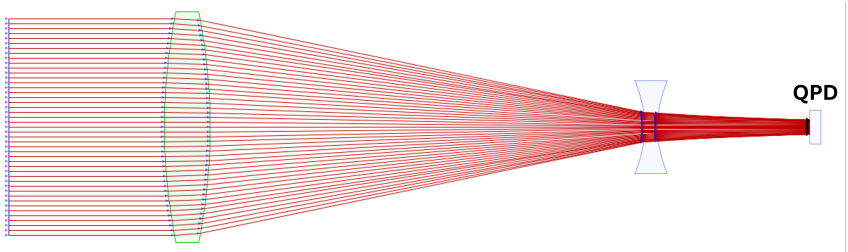

(a) 0° incoming beam

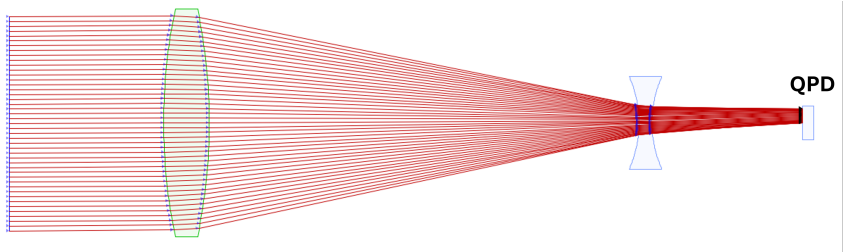

(b) 0.3° incoming beam

Figure 2.17: Overview of the Wide-FoV Telescope.

The wide-FoV Telescope consists of two parabolic lenses other configurations are also possible. The selected QPD from section 2.6 has a radius of 1.5mm. The aperture of this telescope is 20 mm. The spot radius is approximately 0.6 mm and at an incoming beam off-set angle of 0.3° it moves by 0.6 mm. By assuming the spot moves linearly with the incident angle and assuming a spot centre error of 0.01 mm [143] the accuracy (1σ) of the coarse pointing sensor is calculated as 123 µrad.

This analysis of the telescopes is severely limited. Limitations are imposed by time constraints and constraints from the software available to the design team. A more in-depth analysis of the telescopes is required taking

into account varying wavelengths, surface flatness, coating and positional tolerance. However, the analysis presented in this section allows for a first estimate of the shape and size of the selected telescopes.

2.5.4. Configuration

The configuration of the CPA gimbal is an important aspect of the LCT design. The main design focused on the structure and functionality of the gimbal arms. These arms not only provide mechanical support but also serve as pathways for the laser beams. Therefore, their design must balance both structural integrity while also providing an optical path.

The primary design decision involved the overall configuration of the gimbal arms. As mentioned earlier, their design had to accommodate both mechanical stability and optical efficiency. They are responsible for providing an unobstructed optical path. For this, the cross-section of the arms needs to be sufficiently thick to house the optical pathway. This can be seen on the right. In this design, the right arm in the picture was used as the optical path. Inside, there exist a total of three folding mirrors inside the arm that direct the light into and out of the optical bench. This design is capable of providing $n \cdot 360°$ rotation in azimuth and an elevation angle of at least 190° (±5° on each end) which satisfies REQ-TEC-OPT-1.

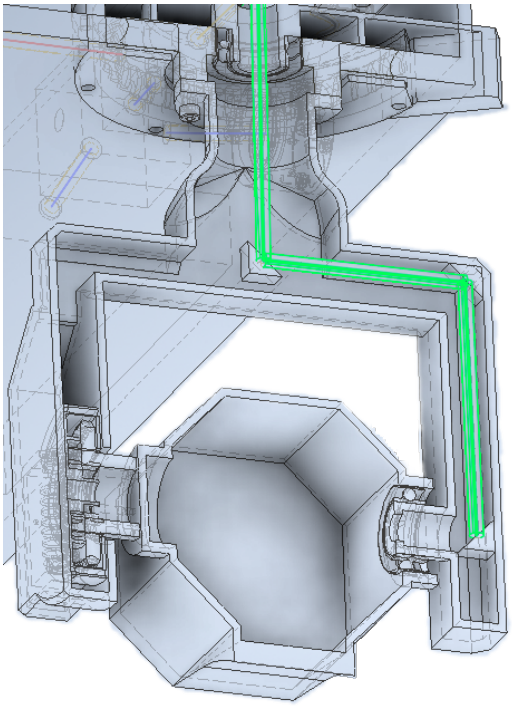

Figure 2.18: Section View of the Coarse Pointing Showing the Optical Path

Furthermore, the gimbal was designed in such a way that the bottom part of the gimbal (arm and telescope) can be disconnected from the ring gear of the azimuth as shown in Figure 2.18. This modular design, which allows the arms to be easily connected and disconnected from the azimuth axis, significantly simplifies the removal of the assembly for maintenance or upgrades. This feature is beneficial when replacing or upgrading the telescope and arm for a larger model. Additionally, this modularity enhances maintenance efficiency enabling quick replacement of non-functional telescopes or arms with functional ones without the need to remove the optical bench or disconnect the azimuth axis from the aircraft. This streamlined process reduces downtime and ensures the system can be swiftly restored to optimal operation.

2.5.5. Powering the Gimbal and Agility

The configuration of the azimuth axis as well as the elevation axis for the CPA in the LCT requires careful consideration of the motor selection to ensure optimal performance. This section outlines the process of calculating the required torque, considering the total mass, moments of inertia, desired angular velocity, gear ratio, and worm gear efficiency. The information available from previous parts and derived from some requirements are presented below:

- Moment of Inertia of the arm and the telescope housing(I) which are made out of Titanium Ti-6Al-4V: 0.006249 kg·m^2 (this is the maximum I possible which happens when the telescope is pointed orthogonal to the axis of the azimuth shaft)
- Moment of Inertia of the primary mirror of the telescope, folding mirrors, and remaining components (in total): 0.00125 kg · m2
- Desired Angular Velocity: 180 degrees in 10 seconds. This number was derived by looking at the 60-second budget (requirement REQ-TEC-OPT-5) available for establishing a link. Since there is a lot of room for improving the performance and agility by picking better motors, it was decided to set a low time budget of 10 seconds for the gimbal to point in the right direction starting from the exact opposite direction, meaning a 180-degree turn.
- Gear Ratio: 40:1 (worm gear and ring gear setup). This was picked by looking at initial size estimations of the CPA. Given that smooth slow rotations will be needed for tracking and the fact that it is easy to achieve a high gear ratio when using worm gears, the gear ratio of 40:1 was picked. This means 40 rotations of the worm gear will result in one full rotation of the ring gear.
- The efficiency of worm gears reported in the literature varies, with estimates ranging from approximately 50% to approximately 70%[136] for a gear ratio of 40. However, to ensure a conservative approach in our initial calculations, we use the lower bound efficiency of 50% (0.5).

The exact total moment of inertia of the upper part of the CPA, which will rotate relative to the HAPS platform via

the azimuth shaft, was obtained by looking at the assembly file in the computer-aided design (CAD) software[36] directly. The total moment of inertia is obtained using Equation 2.18.

$$I_{\text{total}} = I_{\text{gimbal}} + I_{\text{CPA\_rem}} = 0.007499\,\text{kg} \cdot \text{m}^2 \tag{2.18}$$

Desired Angular Velocity

The angular velocity to turn 180 degrees (π radians) in 10 seconds is calculated in Equation 2.19.

$$\text{Angular Velocity} = \frac{\pi\,\text{radians}}{10\,\text{seconds}} = 0.314\,\text{rad/s} \tag{2.19}$$

With a gear ratio of 40:1, the motor actually needs to turn 40 times for the ring gear to turn once. Therefore, the angular velocity and the Rotations Per Minute (RPM) at which the motor itself has to turn is calculated by using Equation 2.20 and Equation 2.21.

$$\text{Motor Angular Velocity} = 0.314\,\text{rad/s} \times 40 = 12.56\,\text{rad/s} \tag{2.20}$$

$$\text{Motor RPM} = 12.56 \cdot 9.5493 = 119.9\ \text{RPM} \tag{2.21}$$

This means the RPM of the motor shall simply be more than 120 RPM.

Calculating the Required Torque

For calculating the torque required, the agility of the CPA will be considered. First, the formula for calculating the torque will be given in Equation 2.22.

$$\tau = I_{total}\alpha_{accel} \tag{2.22}$$

where $I_{total} = 0.007499kg \cdot m^2$.

Angular Acceleration (α): To find α, we need to know how quickly the system is supposed to reach the desired angular velocity. Given no strict requirements are set for this specific part, we assume it should reach the desired velocity in 1 second for simplicity and to ensure responsive performance. This assumption provides a practical basis for calculating the necessary torque while ensuring a quick response from the CPA for establishing the link quickly. α can be calculated as shown in Equation 2.23.

$$\alpha = \frac{\text{Angular Velocity}}{\text{Time}} = \frac{0.314\,\text{rad/s}}{1\,\text{s}} = 0.314\,\text{rad/s}^2 \tag{2.23}$$

Torque Calculation: Having the angular acceleration, the required torque can be calculated as done in Equation 2.24.

$$\tau = 0.007499\,\text{kg} \cdot \text{m}^2 \times 0.314\,\text{rad/s}^2 = 0.00235\,\text{Nm} \tag{2.24}$$

It should be noted the torque calculated is not equal to the torque which the motor has to provide. Due to the gear ratio, the torque required by the motor should be calculated as shown in Equation 2.25.

$$\tau_{\text{motor}} = \frac{\tau}{40} = \frac{0.00235\,\text{Nm}}{40} = 0.00005875\,\text{Nm} = 0.05875\text{mNm} \tag{2.25}$$

Accounting for Worm Gear Efficiency

Given the worm gear efficiency (η) of 50% (0.5) which is a conservative estimate the actual required torque which should be used for selecting the motor can be calculated as done in Equation 2.26.

$$T_{\text{motor\_adjusted}} = \frac{T_{\text{motor}}}{\eta} = \frac{0.05875\,\text{mNm}}{0.5} = 0.1175\,\text{mNm} \tag{2.26}$$

Motor Selection

For picking a suitable motor the criteria used, concerning torque and agility which were addressed and calculated above will be summarised below:

- Motor Torque Rating: Ensuring the motor can provide at least 0.1175 mNm of continuous torque.
- Speed Requirements: The motor should achieve the calculated speed of 12.56 rad/s.

[36] https://www.autodesk.com/products/inventor/

- The size should be optimal to fit inside the coarse pointing assembly for both the azimuth and elevation.

Motor selected: A suitable motor for this application which was picked is the following:

- Motor Model: Maxon DCX 10 S Ø10 mm, Precious Metal Brushes CLL, sintered sleeve bearings[37]
- Torque: Continuous torque of 0.905 mNm (provides a significant safety margin).
- Speed: Up to 12500 rpm RPM (approximately 1309 rad/s, sufficient for 12.56 rad/s needed with a gear ratio of 40:1).
- Voltage: 12 V
- Power consumption: 1 W

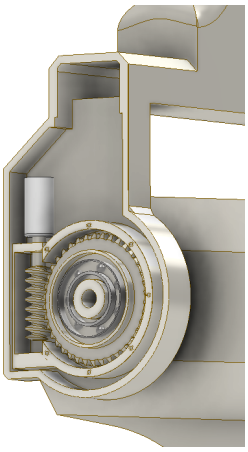

Figure 2.19: Section View of the Arm of the CPA, Housing the Worm and Ring Gear along with the Selected Motor.

Furthermore, the chosen motor integrated into the gimbal can be seen in Figure 2.19, which shows the optimal size of the motor compared to the gimbal size. As shown in this section, the motor not only meets but exceeds the agility and torque requirements necessary for the coarse pointing assembly. Its optimal size and configurability which is offered by Maxon makes it a suitable choice for this specific application. Although it may seem overpowered, its adherence to the size constraints and its reasonable power consumption justifies its selection. Additionally, the high quality and reliability of Maxon products ensure that this motor is a dependable choice for this use case. Additionally, it should be noted that encoders will be used to ensure the gimbal is pointing in the right direction as expected.

2.5.6. Aerodynamic Analysis

In this section, we analyze the aerodynamic drag acting on the gimbal of the laser communication terminal mounted on an aeroplane flying at altitudes between 15 and 25 km. Due to limitations in manpower and time, in-depth aerodynamic simulations were not feasible. Therefore, a reverse engineering approach will be utilised. All parameters required for calculating the drag will be determined, leaving the drag coefficient (C_d) as the only variable. We will then identify the C_d value that results in the client's specified drag force. Subsequently, we will evaluate if this C_d aligns with the estimated drag coefficient for the gimbal, considering its design is not fully aerodynamically bluff.

Drag Force Calculation

The drag force (F_d) acting on an object moving through a fluid can be calculated using the drag equation by using Equation 2.27.

$$F_d = \frac{1}{2} \cdot \rho \cdot V^2 \cdot C_d \cdot Ar \tag{2.27}$$

where ρ is the air density at the operating altitude, V is the velocity of the airplane, C_d is the drag coefficient and Ar is the reference area.

Parameters:

- **Reference Area (Ar)**: The gimbal can have different orientations. The reference area of the gimbal when it's the largest (this is when e.g. the gimbal on the bottom of the HAPS is pointing directly down) is 0.021146 m^2. The orientation with the smallest reference area has a reference area of 0.021146 m^2. For a conservative approach, the maximum reference area will be taken into account.
- **Velocity (V)**: The top operational speed of the airplane is 27.15 m/s, which is at 25km.
- **Altitude**: The HAPS operates at altitudes between 15 and 25 km. The dynamic pressure given the cruise speeds at 15km and 25km, using the air densities at those altitudes [38] are as follows: 15.302 Pa at 15km and 14.54 Pa at 25km. For a conservative approach, the altitude of 25km and its corresponding air density and dynamic pressure will be used.

By substituting these values into the drag equation, Equation 2.28 can be obtained.

$$F_d = \frac{1}{2} \cdot 0.03946\,\mathrm{kg/m^3} \cdot (27.15\,\mathrm{m/s})^2 \cdot C_d \cdot 0.026076\,\mathrm{m^2} \tag{2.28}$$

To meet the client's requirement of a maximum drag force of 0.5 N, namely requirement REQ-TEC-INT-1, we need to determine the corresponding C_d. By substituting the required drag force into the drag equation and

[37] https://www.maxongroup.com/maxon/view/product/motor/dcmotor/DCX/DCX10/DCX10S01EBSL550
[38] http://www.braeunig.us/space/atmos.htm

solving for C_d Equation 2.29 can be obtained.

$$C_d = \frac{0.5 \cdot 2}{0.03946 \cdot (27.15)^2 \cdot 0.026076} \tag{2.29}$$

Figure 2.20 shows the drag force as a function of C_d, highlighting the level where the drag force is 0.5 N. The intersection point on the graph indicates that a C_d value around ≈ 1.3 adheres to the maximum allowable drag force of 0.5 N. This C_d value is typically associated with bluff bodies[77], but given the design and operational context, the gimbal design meets the drag force requirement set by the client. Again, as mentioned earlier for more reliable results an in-depth aerodynamic simulation shall be performed with the gimbal geometry, which was not possible given the limited manpower and time available.

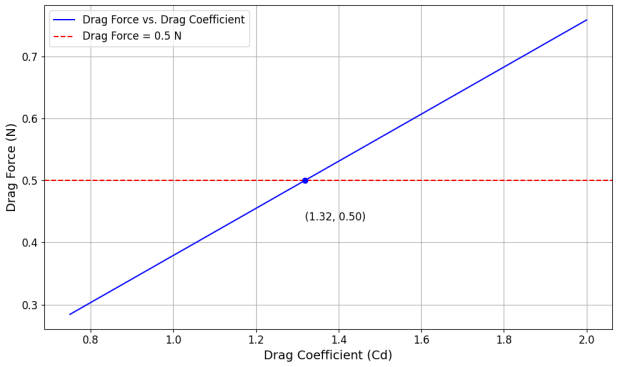

Figure 2.20: Drag Force as a Function of Drag Coefficient

2.6. Pointing Sensors

When designing an LCT that will be placed on a moving HAPS platform, the choice of sensors for coarse and fine alignment becomes crucial for achieving precise and reliable beam positioning/alignment. The primary options considered for these tasks include Quadrant Photo Detectors (QPDs), Position Sensitive Detectors (PSDs), Charge-Coupled Devices (CCDs), and Complementary Metal-Oxide-Semiconductor (CMOS) sensors. This section looks into these options and justifies their selection for this specific context.

When selecting the detectors, special attention had to be paid to the spectrum in which these detectors can operate optimally, namely the infrared spectrum. Knowing this, two of the options were deemed infeasible. These two options were namely the CCDs and CMOS sensors.[39] The performance of CCDs at the 1535 nm wavelength is sub-optimal without significant modifications. Similarly, CMOS sensors, have higher noise levels and are not inherently optimised for the near-infrared spectrum around 1535 nm. These factors make both CCDs and CMOS sensors less ideal compared to QPDs and PSDs, which provide superior sensitivity, fast response, and better suitability for precise alignment tasks in the infrared range.

Coming to QPDs, special attention should be paid to the material used. The two main options which divided the detectors into two groups are namely the Silicon-based detectors and Indium gallium arsenic (InGaAs) based detectors. The differences between these are summarised in Table 2.12.

Table 2.12: Summary of Silicon vs InGaAs

Material	Wavelength Range	Application
Silicon	400 nm - 1100 nm	General-purpose, visible to near-infrared
InGaAs	900 nm - 1700 nm	Infra-red detection, laser alignment

As shown in Table 2.12, InGaAs-based detectors are only sensitive to bigger wavelengths that exceed the range of the silicon ones. Additionally, the elements deemed infeasible earlier also mostly make use of silicon for sensing (for example CCD silicon-based arrays), hence why they were not optimal for these wavelengths. Although there are some optimised versions, these become costly and complicated to use.

For the design of the LCT on a HAPS, integrating both QPDs and PSDs were picked to optimise the performance for coarse and fine pointing. For coarse alignment of the LCT, QPDs are selected due to their high sensitivity and fast response, which is ideal for quickly capturing and centring the beam. Furthermore, their ease of use, simplicity, and low cost led to this detector being picked as the coarse pointing detector. The specific quadrant detector is namely MTPD4346T38-300 [40] with peak performance at 1600 nm wavelength, speed response of 1 GHz, and suited for optical communication, manufactured by Marktech Optoelectronics.

Furthermore, PSDs were chosen for fine alignment because they provide continuous, high-resolution feedback, allowing for precise and stable beam adjustments over a larger range. Overall, This combination ensures accurate and reliable beam alignment necessary for effective Air-to-Ground, Air-to-Air, and Air-to-Space communication. the specific power picked is namely CONEX-PSD10GE [41] manufactured by Newport.

[39] https://ibsen.com/resources/detector-resources/detector-selection-guide
[40] https://specs.marktechopto.com/pdf/products/datasheet/MTPD4346T38-300%20v112123%20prelim.pdf
[41] https://www.newport.com/p/CONEX-PSD10GE

2.7. Mirrors

Mirrors are essential in the Laser Communication Terminals for redirecting the laser beam into and out of the optical bench. The mirrors used are named folding mirrors. Mirrors are also used to fine-steer the laser to ensure that the laser is received perfectly inside the LCT as well as ensuring the transmitted laser goes to where the other partner terminal will be in case of fast-moving partner terminal, namely in case of the air-to-space links. These powered mirrors capable of mechanical motions for steering the laser beam are namely the Fine Steering Mirrors (FSM) and Point Ahead Mirrors (PAM).

2.7.1. Folding Mirrors

Folding mirrors redirect to mirrors used to redirect the light. In this context, a number of folding mirrors will be utilised to redirect the laser into and out of the optical bench. These mirrors make it possible to have a more compact design and ensure the laser travels the intended path. There are three main options available for folding mirrors, namely Flat, Parabolic, and, Elliptical mirrors. In this case, for the sake of simplicity and there being no need to use a non-flat mirror, only flat folding mirrors will be used.

2.7.2. Fine Steering Mirror

The most common fine-pointing mirror in free space optics is done by making use of FSMs [107]. These mirrors can be pointed with accuracy in the range of micro radians, which is required to obtain the optical link. The FSM is crucial for maintaining the alignment of the optical beam coming from both the transmitter and the receiver. Based on any sort of disturbances or changes, the mirror can quickly react to this to make sure the optical communication link is maintained. Due to its precision, it is also able to optimise the quality of the signal.

Even though in most cases mechanical-driven FSMs are used, there also exist non-mechanical approaches such as liquid-crystal-based actuators, liquid lenses, vertical cavity surface emitting lasers, and chip scale beam steering arrays which is discussed in a review paper about different options for FSMs, authored by Milaševičius and Mačiulis [107]. Even though there are some strong points, for the application of the HAPS and keeping requirements such as technical readiness, thermal control and power consumption in mind this means that the non-mechanical FPMs are not suitable for this mission.

Mechanical fine steering mirrors can be categorised into three main groups based on what pointing mechanism they use. There are FSMs mirrors that could be driven electro-statically, electro-magnetically or using the piezo-electric effect. Some brief information with regard to the options available are given below[107]:

- **Electrostatically Driven Mirrors**
  - **Electrostatic MEMS Mirrors**: These mirrors are characterised by low mass, small size, low cost, and ease of manufacturing. However, they have limited actuator force, resulting in a small stroke and bandwidth, making them suitable for smaller applications.
- **Electromagnetically Driven Mirrors**
  - **Electromagnetic MEMS Mirrors**: Similar to electrostatic MEMS but provides more actuator force and better stability. They can interfere with other magnetic fields, which can be a drawback.
  - **Voice Coil Mirrors**: These mirrors offer strong actuator forces and reliability at an affordable cost. They handle thermal management better than MEMS but may still struggle with it due to producing heat more compared to others.
  - **Magnetic Reluctance Mirrors**: Utilise both coils and permanent magnets, providing higher efficiency and linearity than voice coils. They offer large strokes and high bandwidth, making them ideal for long-distance communication.
- **Piezoelectrically Driven Mirrors**
  - **Piezo-Stack Mirrors**: Use stacked layers of piezoelectric material for actuation, offering high accuracy but limited pointing range due to small deflections.
  - **X-Y Piezo-Stage Mirrors**: Similar limitations as piezo-stack mirrors with respect to range and SWaP (size, weight, and power consumption) efficiency.
  - **Piezoelectric MEMS Mirrors**: Optimised for SWaP but have lower actuator resolution and smaller possible mirror sizes compared to other piezoelectric options.

Fine Steering Mirror Trade off

To perform a proper trade-off, several critical performance metrics that are important for meeting the requirements and achieving a feasible design were made. For each of these performance metrics, a weight was assigned. The specifics with regards to the metrics and their weights used along with their in-depth justifications can be found in [3].

The trade-off table is presented below in Table 2.13. The weights are scaled from 1 to 3, with a colour assigned to each metric.

Table 2.13: Trade-off Analysis for Different FSM Technologies along with the Colour Scheme Used.

	Weights	Electrostatic MEMS FSM	Electromagnetic MEMS FSM	Piezoelectric MEMS FSM	Voice Coil FSM4	Magnetic Reluctance FSM	PiezoStack FSM	X-Y Piezo Stage FSM
Size and Weight	10%							
Steering Angles	10%							
Thermal handling	15%							
Pointing Accuracy	15%							
Cost	10%							
Operational Bandwidth	15%							
Actuator Resolution	15%							
Mirror Size	10%							
Total ranking		1.95	1.8	1.85	2.25	2.4	2.15	2.00

Good (3)
Moderate (2)
Poor (1)

As can be seen above, the best available type is Magnetic Reluctance FSM, due to its comprehensive balance of performance metrics. Despite its higher cost, the Magnetic Reluctance FSM's robust performance and proven reliability make it ideal for maintaining precise and stable laser communication links, essential for Air-to-Air, Air-to-Ground, and Air-to-Space connections. Potential magnetic interference is something that has to be considered during the design of the rest of the pointing mechanism.

FSM Selection

The main available magnetic-reluctance FSM that exist is the one developed by TNO and Demcon[42]. Some specifications and prices are not publicly available and experts were restricted from disclosing the pricing details, which adds to the challenge of obtaining comprehensive information about these high-precision devices. However, there are a few literature reviews where an indication of mass, power consumption, and range are given [107]. The main characteristics are given in Table 2.14.

Table 2.14: Indication of Budgets for FPM [107][24]

	Mass [g]	Power Consumption [W]	Pointing Range [deg]	Housing dimensions
TNO Magnetic Reluctance	61	0.64	+-2	diameter ± height, H in mm Ø27 × H30

2.7.3. Point Ahead Mirror

The Point Ahead Mirror (PAM) is crucial for ensuring that the transmitting laser beam is directed to where the partner terminal will be, rather than where it is currently located. This is mainly relevant and important in air-to-space communication, where the high speed of the space terminal is significantly greater compared to the terminal on the HAPS. The PAM uses the calculated point-ahead angle to deflect the laser light accordingly, ensuring accurate and effective communication between the rapidly moving terminals is maintained.

Point Ahead Angle Estimation

The PAM angle can be calculated by taking into account the speed of light and the rotational speed of the satellite orbit. The speed of light will be assumed to be constant, the orbit is assumed to be circular and the HAPS is assumed to be located at 25km above ground level with a speed that matches the Earth's surface speed at the equator which is 465 m s^{-1}[43]. Therefore the PAM angle is expressed by Equation 2.30 and Equation 2.31 [71].

$$\theta_{PA} = \frac{2v_t}{c} \tag{2.30}$$

$$v_t = \sqrt{\frac{\mu_{orb}}{c}} + V_{surface} \tag{2.31}$$

For an orbital height of 0m, thus representing the worst case, this results in a point ahead angle of 55.8 µrad.

[42]https://hts.demcon.com/showcases/fine-steering-mirror/
[43]Rotational Speed of Earth: `https://www.unitarium.com/earth-speed`

PAM Selection

The PAM functions in a similar manner to the FSM while fulfilling a different role. Since the PAA does not have high frequency components the operational bandwidth of the PAM does not need to be high. At the same time since the required PAA does not exceed 55.8 µrad for the current application the requirements for steering angle range can be loosened. Generally speaking, FSMs can be used as PAMs and therefore the same trade-off used for the FSM can be used for the PAM but with altered weights. Weight is decreased in the "Steering Angle" and "Operational Bandwidth" criteria while increased in the "Thermal Handling", "Pointing Accuracy" and "Actuator Resolution" in a uniform manner since these were the remaining most dominant criteria.

Magnetic reluctance FSM remains the top option for PAM as well and therefore the TNO magnetic reluctance FSM is selected for the PAM. This choice is enforced based on the fact that the TNO FSM was designed for both FSM and PAM usage [93].

2.8. Control

The control system of the LCT plays a crucial role in establishing as well as painting accurate beam alignment and stability. this section will focus on the feedback loops for the coarse pointing, fine steering mirror, and point ahead mirror. Furthermore, the functional block diagrams of different operations, such as the spiral search algorithm will be given. A simplified version is given below in Figure 2.21.

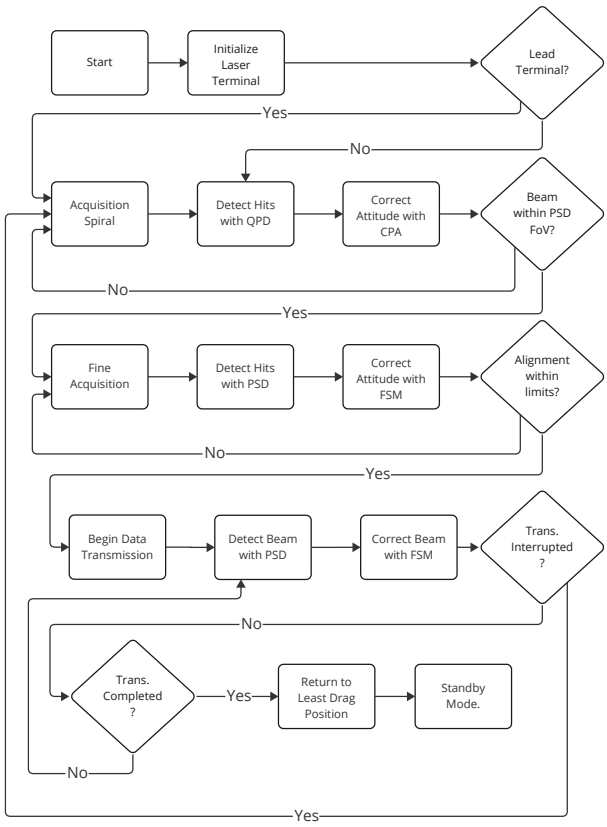

Figure 2.21: LCT Operational Block Diagram.

The LCT is first initiated and receives information about the target LCT's position and information about the PAT procedure in accordance with the relevant SDA standard [60]. If it is the lead terminal the spiral pattern is drawn, if not, PAT hits are detected. During coarse alignment, the attitude is corrected with the CPA. If the beam is within the PSD FoV then fine alignment commences, otherwise coarse alignment continues. During fine alignment, both terminals scan and detect hits at the same time. If the alignment is within the tracking loss limit then data transmission can begin, otherwise fine alignment continues. During data transmission, the beam is directed with the PSD and the FSM. If the transmission is interrupted for any reason coarse acquisition is resumed. If the transmission is completed, the CPS is tilted so that it produces minimum drag and the LCT enters standby mode where non-necessary elements are shut down to save power. The Point Ahead procedure is not included here for the sake of clarity. If a point ahead angle is needed then it is calculated based on the target's positional data and it is added with the point ahead mirror before coarse alignment and then further corrected during fine alignment.

The existing feedback loops which shall be used can be grouped into the following:

Coarse Pointing: The Coarse Pointing Assembly (CPA) handles large-scale adjustments to align the LCT toward the target. Essential during the initial link establishment phase, the CPA is responsible for locating and locking onto the communication partner. It operates within a broad field of regard, using GNSS/INS data for initial orientation (while using inertial measurement units and encoders to know its actual orientation) and a QPD sensor for accurate positioning.

Fine Pointing: After the coarse pointing is done, the FSM takes over for fine alignment. It does so by performing a spiral search as many times as needed to cover the uncertainty cone as explained in section 2.4. It should be noted in case of too big of an uncertainty cone [for the FSM to cover], the CPA will come to help and make further minor adjustments to aid the Fine Steering Mirror (FSM), to enable the mirror to cover the whole uncertainty cone, as again detailed in section 2.4. This will operate by using continuous and high-precision feedback from the PSD sensor.

Pointing Ahead: Point ahead mirror is responsible for ensuring the transmitting laser goes to where the target will be when the laser arrives, which is mostly relevant when trying to establish a communication link between

HAPS and LEO satellites. The PAM makes use of the calculated point ahead angle by using the available information about the speed and location of both the HAPS and the partner terminal. In this sense, this part is an open-loop system. In this case, an additional PSD sensor was utilised to ensure that the mirror is providing the actual needed point ahead angle.

2.9. Power Management

Power management is of crucial importance which ensures the system operates efficiently and reliably. In this context, the LCT power management system must address two key challenges. These are as follows:

- Diverse Voltage Requirements of different components
- Battery Dependency of the system

in addition to the above two challenges, one should also keep in mind that the system shall remain as efficient especially since the power available is rather limited. The above two challenges are addressed in the following two sub-sections.

2.9.1. Battery Management

When using batteries to power a system, it is crucial to install a battery management system (BMS) to monitor the voltage and current provided by the battery as well as the temperature of the battery. This is to ensure a safe and efficient operation, preventing cases such as over-charging or over-discharging and the battery going over its safe temperature. Since the LCT is powered by the main batteries of the HAPS platform, there is no need to go into details in this sub-section.

2.9.2. Converters

Providing the correct voltage to different components inside the LCT is crucial for ensuring optimal performance and reliability. This section discusses the method used to ensure different components with different voltage requirements meet their needs.

To do the aforementioned task and ensure that each component receives the required voltage, buck converters and boost buck converters will be used. The working principle of these components is rather simple. A simple representation of these components is shown in Figure 2.22:

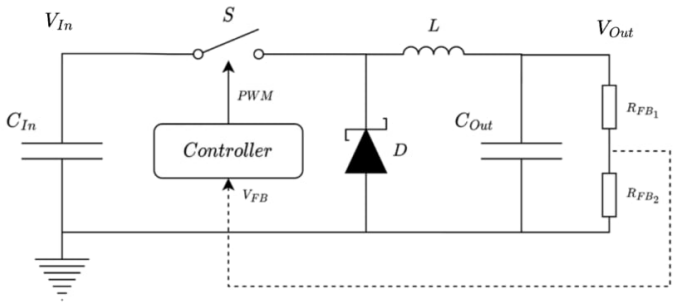

Figure 2.22: Working of Converters [44]

As shown (Figure 2.22), these converters consist of four main elements. These are namely the input voltage source, a switching element (e.g., transistor), an inductor, a diode, and control circuitry for Pulse Width Modulation regulation.

The advantage of using converters is the control circuit inside each unit which continuously monitors the input voltage and adjusts the PWM signal accordingly to regulate the output voltage. As this is changed, the duty cycle of the PWM signal is modified to compensate for any input voltage variances, which enables the converter to ensure that the output voltage remains stable.

The two types of converters are namely buck converters and boost converters, which both operate with roughly the same overall working principle as explained above. Buck converters step down the input voltage to a lower output voltage, while boost converters step up the input voltage to a higher output voltage. As mentioned earlier, these converters are crucial since they ensure that stable voltage is available in case of fluctuations in the input voltage, thus providing power conversion and minimising power loss and heat generation. It's by utilising these converters that the LCT will be able to provide the needed voltage to its diverse components while maximising efficiency and stability, which is essential for the reliable operation of all the components in the LCT.

To ensure that different components receive their needed voltage, a variety of main converters will be utilised.

[44] https://resources.altium.com/p/buck-converter-component-sizing

The main voltage groups identified within the LCT, along with examples for components within each group are given in Table 2.15.

Table 2.15: Voltage Groups and Components

Voltage Group	Example of components	Purpose
3.3V	Most digital circuits, low power sensors and micro-controllers, etc.	Commonly required by low-power and signal processing tasks.
5V	Certain micro-controllers, logic circuits, certain amplifiers, etc.	Essential for components in the low to medium power range but higher than 3.3V
12V	Higher-power components such as motors, actuators, some high-power sensors, certain amplifiers, etc.	Components which perform mechanical work or require higher power levels for operation
24V	Certain Laser drivers, actuators for possible high-demand mechanical tasks, etc.	Reserved for components that will require substantial power levels to operate

For all these conversions, components had to be picked. After research, the following converters were picked, shown in Table 2.16. When selecting these, special attention was paid to the reliability of the manufacturer, efficiency, the Temperatures they can operate in, and the maximum power they can output. The last point is of special importance since failing to provide enough output power to all the components connected to a specific converter will cause problems. It should be ensured that components can draw the current they need to operate properly. For these, the number of components in each voltage group and the current they draw were looked at and were taken into consideration when picking the following components.

Table 2.16: The Converters (Buck and Booster) Selected for the LCT

Type	Vin	Vout	Max Power out (W)	Max I out (A)	Efficiency	Temperature (C)	Product Name
Buck Converter	12	3.3	12	3.64	83.5%	-40 to 85	NCS12S1203C[45]
	12	5	75	15	90%	-40 to 85	UWE-5/15-Q12P-C[46]
Boost Converter	12	24	120	5	92%	-40 to 85	IRE-24/5-Q12N-C[47]

As mentioned earlier, efficiency is one of the important factors taken into account when picking the components. Adding these converters to the system brings some consequences which in this case is namely the power loss they bring. This makes it important to consider when adding these converters to the system. The power loss as a result of a converter is by the following equation, namely Equation 2.32, where η stands for the efficiency of the converter:

$$P_{Loss} = \frac{(1 - \eta_{conv})}{\eta_{conv}}(V_{out} \cdot I_{out}) \tag{2.32}$$

Using the above formula, Equation 2.32, the total power loss of the system as a consequence of using boost and buck converters for providing the required voltages was calculated to be roughly 3 Watts.

2.10. LCT Conclusions and Recommendations

In this chapter, the design of the LCT has been presented. The LCT is capable of acquiring Air-to-Space, Air-to-Air, and Air-to-Ground links. It should be noted that the presented LCT link performance assumed no forward error correction which adds additional margin and also assumed a 1 Gbps transmission rate. If the medium loss is reduced, the transmission rate can be increased or the optical power can be reduced. Therefore in case the available power that can be delivered to the LCT is reduced, link distances can be reduced or the transmission rate can be reduced to ensure that the link can be formed. It should also be noted that the link performance is highly sensitive to environmental conditions. Link establishment capabilities should be investigated based on the current weather.

The feasibility of placing the FSM in the CPA should also be investigated. With the current FSM placement, the distance between the FSM and the Rx fibre is long which might cause the coupling performance to decrease due to FSM resolution and vibrations. If this is deemed to be an issue it can be mitigated by adding another

[45]https://www.murata.com/en-eu/products/productdetail?partno=NCS12S1203C
[46]https://www.murata.com/en-eu/products/productdetail?partno=UWE-5/15-Q12P-C
[47]https://www.murata.com/en-eu/products/productdetail?partno=IRE-24/5-Q12N-C

FSM inside the optical bench closer to the Rx fibre and potentially replacing the FSM in the CPA with a less performant alternative in order to reduce cost. The maximum spiral speed should also be investigated further in order to fully characterise the PAT performance.

3. Flight Performance

With the detailed design of the LCT system clearly defined, it is now possible to move on to a detailed design of the HAPS Platform as well. The next number of chapters describe the design of the HAPS system on a per-subsystem basis, with this chapter starting with the flight performance of the HAPS Platform. By the use of the equations of motion and graphical analysis first level estimates for the required power, flight profiles and maximum load factors are made, which the other subsystems use for their design process, from which new values for the flight performance are created. It is important to note that the entire design is an iterative loop, thus the values used in this section are already synthesised with the other subsystems. Firstly, section 3.1 defines the HAPS flight performance requirements. Secondly, section 3.2 defines the flight of the craft during cruise using the simplified equations of motion. From this, section 3.3 and section 3.4 use these equations to find flight profiles and manoeuvre loading diagrams. Additionally, section 3.5 discusses the take-off and landing of the HAPS. Finally, section 3.6 verifies the previous calculations and code by use of a sensitivity analysis.

3.1. Requirements

To investigate the flight performance of the HAPS, some requirements need to be established for it. These requirements originate mainly from the mission requirements and other subsystem requirements. These requirements are shown in Table 3.1.

Table 3.1: Flight Performance Requirements

Flight Performance		
ID	**Requirement**	**Derived from**
REQ-FP-01	The HAPS design ceiling shall be 25km.	-
REQ-FP-02	The HAPS operational ceiling shall be 24km.	-
REQ-FP-03	The HAPS cruise altitude shall be 15km.	-
REQ-FP-04	The HAPS shall be able to climb from 15 to 24km within the duration of the winter solstice day at 45° latitude.	-
REQ-FP-05	The HAPS shall be able to perform an assisted take-off.	-
REQ-FP-06	The HAPS shall be able to perform a controlled landing.	-
REQ-FP-07	The HAPS shall be able to perform horizontal coordinated turns.	-
REQ-FP-08	The HAPS shall operate at the minimum power required flight condition.	-

3.2. Cruise

To get started with the design of the HAPS Platform, it is easiest to first look at the simplest flight condition: cruise. The equations of motion for an aircraft in symmetric flight can be derived from the kinetic diagram shown in Figure 3.1. For cruise conditions, symmetric flight is assumed. The equations of motion are then defined in Equation 3.1 and Equation 3.2 in the velocity direction and the lift direction respectively.

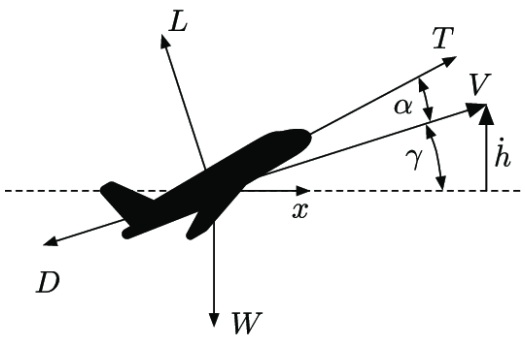

Figure 3.1: Symmetric Flight Kinetic Diagram [83]

$$T\cos\alpha - D - W\sin\gamma = \frac{W}{g}\frac{dV}{dt} \tag{3.1}$$

$$L - W\cos\gamma + T\sin\alpha = \frac{W}{g}V\frac{d\gamma}{dt} \tag{3.2}$$

In the case of cruise, two assumptions are made: Firstly, next to flying symmetrically, the HAPS is also assumed to fly steady and straight. Therefore dV/dt and $d\gamma/dt$ reduce to zero. Secondly, the HAPS is designed to have a very long endurance, therefore its L/D ratio should be very high. This consequently means its rate of descent/climb is very low compared to its cruise speed. In other words, $V >> RC = Wsin\gamma$. Thus γ is sufficiently small and by small-angle approximation $sin\gamma \approx \gamma$ and $cos\gamma \approx 1$. Finally, α is often also quite small in cruise conditions and therefore the same small-angle approximation is applied to it. This reduces Equation 3.1 and Equation 3.2 to the well-known simple cruise flight equations shown in Equation 3.3.

$$T - D = 0 \qquad\qquad L - W = 0 \tag{3.3}$$

From these simplified equations it is possible to perform a performance analysis using the aerodynamic data from the aerodynamics subsystem and the common relations shown in Equation 3.4.

$$L = \frac{1}{2} C_L \rho V^2 S \qquad\qquad D = \frac{1}{2} C_D \rho V^2 S \tag{3.4}$$

With the drag coefficient C_D defined by the drag polar in Equation 3.5.

$$C_D = C_{D,0} + \frac{C_L^2}{\pi A e} \tag{3.5}$$

The aerodynamic data found in chapter 4 applies a varying C_L and $C_{D,0}$ for a specific altitude, true airspeed and altitude. It is then found for which of these values the load factor is set to be approximately one ($L = W$). With these coefficients, the drag is calculated and plotted against its corresponding airspeed. These data points are quadratically extrapolated (since $D \sim V^2$) to create a complete drag curve. The power required is then found by multiplying this curve by the airspeed. The power available is assumed to be constant over airspeed for a propeller, and the thrust relates inversely to the airspeed from Equation 3.6.

$$P_a = T \cdot V \qquad\qquad P_r = D \cdot V \tag{3.6}$$

The HAPS is designed to have an absolute maximum flight altitude of 25km. Additionally, in order to have the best possible endurance the craft shall operate at the minimum required power per altitude. This gives a value for the maximum available power of the HAPS vehicle, which the propulsion and power groups use to size their respective subsystems. The maximum required power is found to be about 2570W. For three different important altitudes (0km, 15km and 25km) the drag and power are plotted in Figure 3.2. Here it can be clearly seen that the excess power is zero at the minimum power required at 25km, as is designed. With the maximum power, the climb and descent of the craft can be analysed.

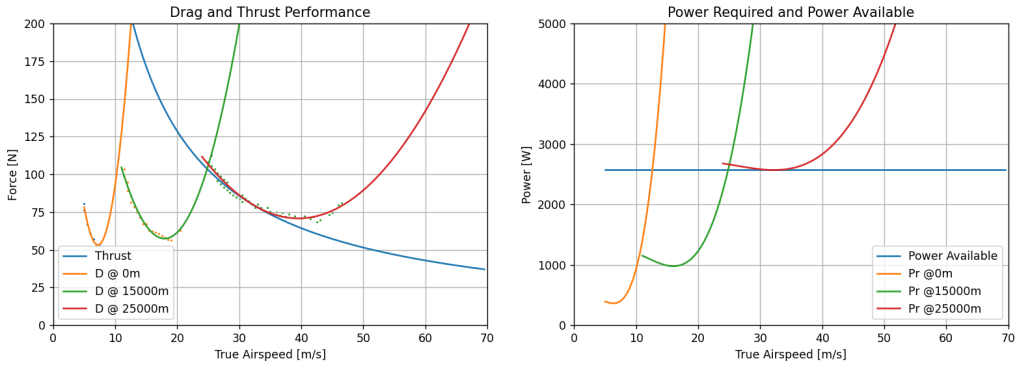

Figure 3.2: Flight Performance Diagrams for 0km, 15km and 25km.

3.3. Climb and Descent

The climb and descent of the aircraft consist of two important parts: Climbing to and from operational altitude and manoeuvres during operation. The first part is quite self-explanatory: The HAPS needs to be able to climb

from 0km to 15km without issues. Secondly, when the HAPS is operating it performs a climbing and descending manoeuvre where it climbs up to 25km while charging the batteries during the day and descends back down to 15km using a powered descent or glide in order to save power. Manoeuvres like this can also be found in various other HAPS vehicles [73]. The rate of climb at a certain altitude can be found by multiplying the equations of motion with the velocity, with the rate of climb defined as the $RC = Vsin\gamma$. Thus Equation 3.1 becomes Equation 3.7, and the steady rate of climb follows from this in Equation 3.8.

$$T \cdot V - D \cdot V - V \cdot Wsin\gamma = 0 \tag{3.7}$$

$$RC_s = Vsin\gamma = \frac{P_a - P_r}{W} \tag{3.8}$$

The model to evaluate the rate of climb at different altitudes uses a discrete height-step iteration, which makes it so that the steady rate of climb closely approximates the actual rate of climb because $dV/dH \approx 0$. Next to that, the time to climb between two altitudes can then also be approximated by the form of a Riemann sum with n amount of height steps as shown in Equation 3.9.

$$t_c = \int_{h1}^{h2} \frac{1}{RC} dh \approx \sum_{i=1}^{n} \frac{1}{RC_i} dh = \sum_{i=1}^{n} \frac{W}{P_a - P_{req,i}} dh \tag{3.9}$$

In order to define the flight profile throughout a day it needs to be known what kind of descent manoeuvre will be performed and what amount of power equates to it. The nighttime descent manoeuvre is divided into two parts: a descent and a cruise. During the night, the HAPS descends with a specific amount of propeller power in order to have the descent last a specific amount of time. This supplied power can vary between zero power, which makes the descent a glide; or the power required at 15km altitude, since any higher supplied power would mean the aircraft starts going up again at 15km altitude. When the HAPS reaches 15km during the descent, the propellers provide the power required again to continue cruising at 15km throughout the rest of the night. At the start of the day, the HAPS starts climbing again. For the flight profile, an operational ceiling of 24km is assumed, in order to not operate at the aircraft's design limits.

For each different descent profile the batteries can be sized differently due to the different power and energy needs as the time to descend increases as more power is supplied to the propellers. To find the best power supply to descend it is needed to evaluate the power usage and consequently the energy usage during the nighttime. The maximum power output of the propellers is 2571.47 W, which means that the maximum energy output (which would equate to cruising at 25km during the entire night) is equal to 61.7 kWh, since $E_{tot,n} = P \cdot t_n$. The value that needs to be maximised is the total excess energy surplus throughout the entire night, with the required propeller energy during the night as the summation of the energy during the descent and the energy during the night cruise. This is defined in Equation 3.10.

$$E_{exs,n} = E_{tot,n} - E_{req,n} = P_{max}t_n - P_{req,n}t_n = P_{max}t_n - (P_{dec}t_{dec} + P_{cr}t_{cr}) \tag{3.10}$$

Here the descent and cruise times are related to each other by $t_n = t_{dec} + t_{cr}$ and the cruise power is simply the required power at 15km, which is found to be 976.85 W. From Equation 3.9 it can be seen that the time to descend is inversely related to the required power. When plotting the time to descend and energy surplus against the power supplied during the descent against each other, as shown in Figure 3.3, it can be seen that the maximum power surplus occurs when there is no power supplied to the propellers; in other words, a gliding descent is the most energy-efficient way to perform the operations manoeuvre. This is likely due to the increase in aerodynamic performance, and therefore power efficiency, at lower altitudes associated with an increase in Reynolds number. These effects are discussed in more detail in **??**

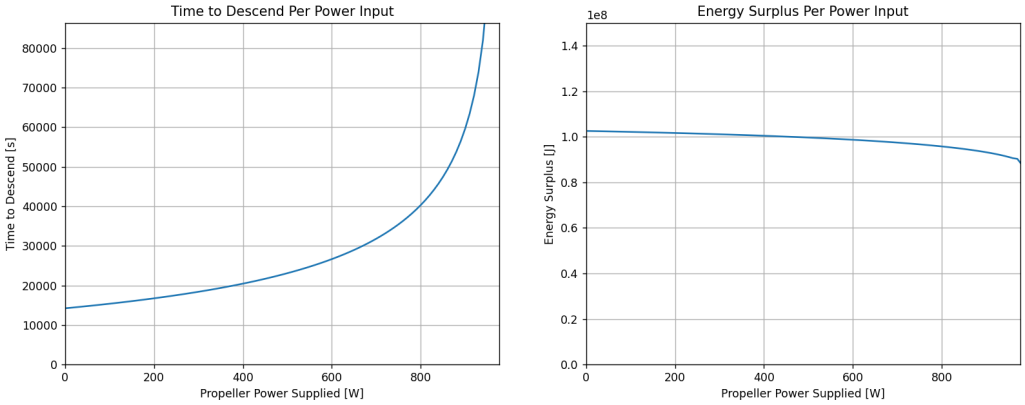

Figure 3.3: Time to Descend and Energy Surplus Per Power Supplied

Using the aforementioned equations, several significant mission operation times are found. These times, along with their required power supply to the propellers are shown in Table 3.2. Next to that, a mission profile for consecutive days is shown in Figure 3.4. In this case, the day and night time are assumed to be for the worst-case design scenario, which is during the winter solstice around a latitude of 45°. The HAPS can also cruise for a short time during the day since it is not climbing to its maximum design altitude of 25km, but only to the operational ceiling of 24km. The take-off climb and landing descent do not take into account the actual take-off and landing procedure, which is discussed in section 3.5.

Table 3.2: Flight Manoeuvre Times and Power Around the Winter Solstice at 45° Latitude

Manoeuvre	h_{start} [km]	h_{end} [km]	Duration [hrs]	Power Supplied [W]
Take-Off Climb	0	15	4.75	2571.47
Landing Descent	15	0	17.84	0
Cruise (day)	15	15	1.65	976.85
Cruise (night)	15	15	11.48	976.85
Climb (day)	15	24	6.91	2571.47
Descent (night)	24	15	3.96	0

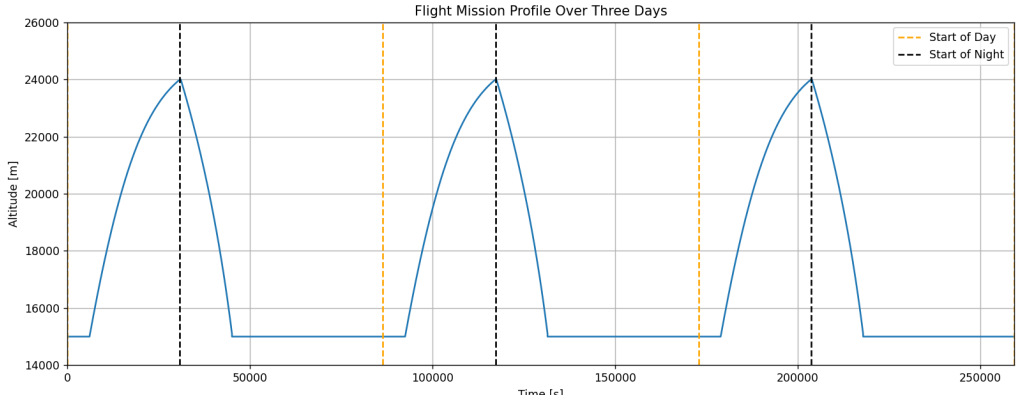

Figure 3.4: Flight Profile for Three Consecutive Days Around the Winter Solstice at 45° Latitude

3.4. Turning

With the flight profile defined, it is now possible to look at the next flight performance characteristic, the turning performance. The HAPS platform will operate by essentially loitering around an area for long periods of time, with it only flying straight if it needs to change altitude or needs to go to a new location. It is therefore crucial that the HAPS has excellent turning performance throughout the mission. For horizontal turning flight, the aircraft can be described by the lateral and frontal kinetic diagram in Figure 3.5. This gives the equations of motions shown in Equation 3.11 to Equation 3.13.

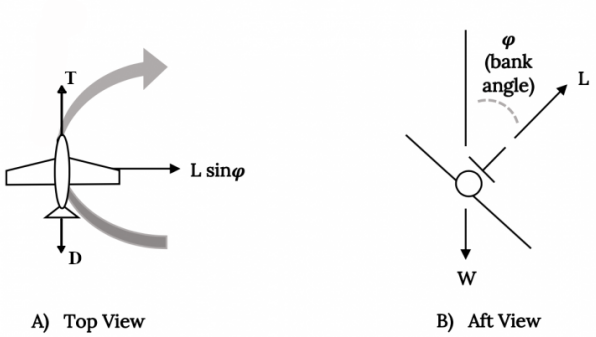

Figure 3.5: Turning Flight Kinetic Diagrams [103]

$$\frac{W}{g}\frac{dV}{dt} = T - D \qquad (3.11) \qquad \frac{W}{g}\frac{V^2}{R_t} = Lsin\phi \qquad (3.12) \qquad \frac{W}{g}V\frac{d\gamma}{dt} = Lcos\phi - W \qquad (3.13)$$

Where dV/dt and $d\gamma/dt$ equal to zero for a steady, coordinated turn and the load factor n being defined by Equation 3.13 as $n = L/W = 1/cos\phi$, with ϕ as the bank angle For the maximum turning performance, it is first needed to know the maximum load factor at certain altitudes, as this relates directly to the maximum bank angle at that altitude, and therefore the steepest turn that the HAPS can perform. With this maximum load factor, the minimum turn radius and turn time can also be computed. Because $L = nW$, the drag and airspeed of the HAPS will increase when the load factor is increased. This is shown in Equation 3.14 and Equation 3.15 using the relations from Equation 3.4.

$$D = \frac{D}{L}L = \frac{D}{L}nW = \frac{C_D}{C_L}nW \qquad (3.14) \qquad V = \sqrt{\frac{2L}{\rho C_L S}} = \sqrt{\frac{2nW}{\rho C_L S}} \qquad (3.15)$$

Therefore, as the load factor doubles, the drag also doubles and the related airspeed increases by a factor $\sqrt{2}$. The V-D performance diagrams from Figure 3.2 shift up and to the right as the load factor is increased. By examining the intersections of the drag performance curves with the thrust curve for different load factors, the maximum load factor for different airspeeds at different altitudes can be found. For 0, 15 and 24km this gives the load factor diagrams shown in Figure 3.6. Because there is no excess power at the maximum design altitude of 25km the maximum load factor here is equal to one, meaning a turn is not possible at this altitude as the HAPS would immediately stall. This further strengthens the maximum operational ceiling of 24km. The maximum load factor is described by either stall, shown by the left, nearly straight section of the graph, or by engine limitations, shown by the right part of the graph.

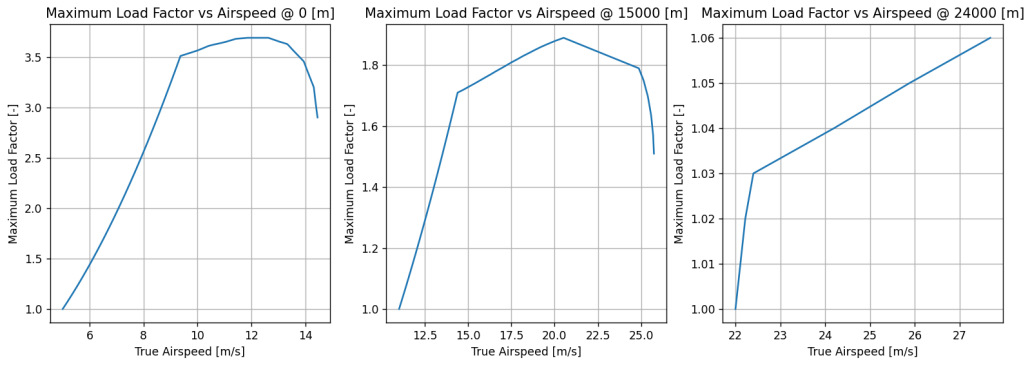

Figure 3.6: Maximum Load Factor Against Airspeed at 0, 15 and 24km

From these figures, the minimum turn radius and turn time can be computed. The turn radius and turn time are described by the equations of motion, dynamics and geometry in Equation 3.16 and Equation 3.17.

$$R_t = \frac{WV^2}{gLsin\phi} = \frac{Lcos\phi V^2}{gLsin\phi} = \frac{V^2}{gtan\phi} = \frac{V^2}{g\sqrt{n^2-1}} \qquad (3.16) \qquad T = \frac{2\pi R_t}{V} = \frac{2\pi V}{g\sqrt{n^2-1}} \qquad (3.17)$$

This gives a minimum turn radius and turn time graph, an example for 15km shown in Figure 3.7. For 0, 15 and 24km, all relevant values are shown in Table 3.3.

Table 3.3: Turning Performance for 0,15 and 24km altitude

h [km]	n_{max} **[-]**	V_{nmax} **[m/s]**	R_{min} **[m]**	T_{min} **[s]**
0	3.70	12.44	2.66	1.78
15	1.90	21.19	15.21	6.64
24	1.06	30.39	207.25	50.43

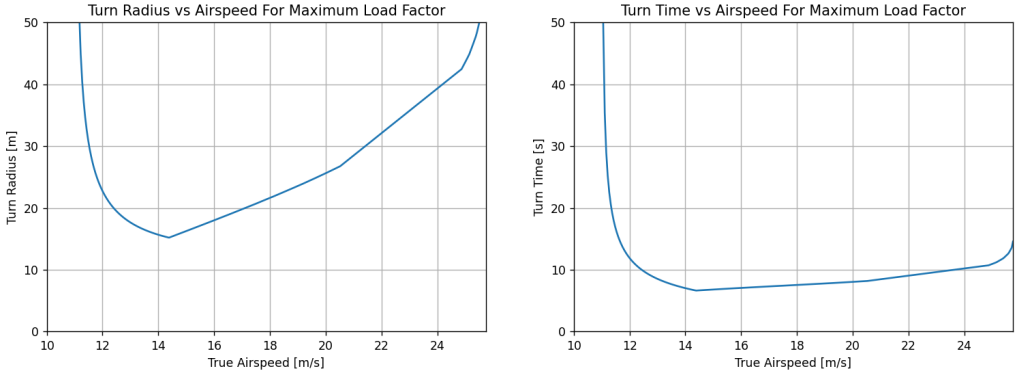

Figure 3.7: Minimum Turn Radius and Turn Time For a Turn at 15km Altitude

Finally, for a given altitude a manoeuvre loading diagram can be set up. Since the HAPS only weighs 230kg, the certification specification CS-VLA [7] is used. This specifies maximum loading specifications and also what kinds of gusts the aircraft should sustain. The loading diagram for a flight at an altitude of 15km is shown in Figure 3.8. It shows that gusts are not a limiting factor at most altitudes, only at very high altitudes. These maximum loads are still, however, much less than the maximum loads at sea and are therefore not a limiting factor. The structural subsystem then uses this maximum load factor to design the structure of the HAPS.

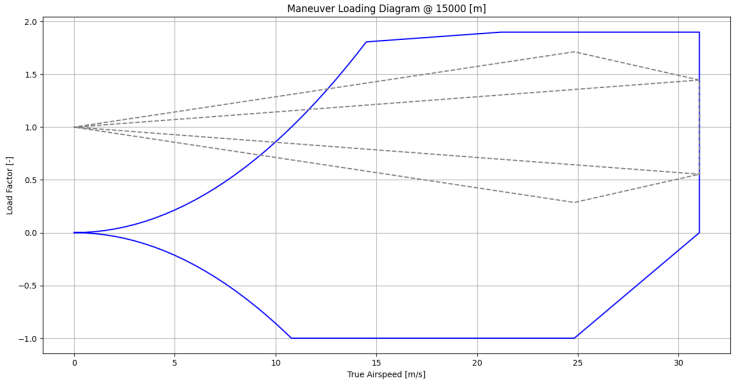

Figure 3.8: Manoeuvre Loading Diagram at 15km Altitude

3.5. Take-Off and Landing

As the final part of the flight performance of the HAPS Platform the take-off and landing of the HAPS needs to be discussed. Because of the very high L/D of the HAPS, it demonstrates very excellent take-off performance, with it being able to take off at a very low speed. The minimum velocity required to take-off is found from the stall speed at sea level using Equation 3.4. This was identified to be 4.66 m/s. This extremely low take-off speed means it can virtually take off from any location without the need for extensive infrastructure such as runways and airports. However, due to the lightweight structure of the HAPS the environment and weather might play a significant role during take-off and landing procedures. Additionally, the HAPS can only generate power in sunny weather which is another reason to only perform take-off and landing in good weather conditions. To reduce the mass of the HAPS proper landing gear such as wheels is not used. Therefore it is proposed to launch the HAPS Platform using an assisted launch. This can be done in many different ways. For example, the HAPS could be simply put onto another moving vehicle such as a car or truck which accelerates the HAPS to the required take-off velocity. A speed of 4.66 m/s (about the speed of a bicycle) can be reached by a car in a matter of 1-2 seconds, meaning the distance it travels in that time is also very minimal, being equivalent to around ten meters. The most important part that does have to be taken into account is the wide wingspan of 50 meters. At zero velocity, the wings will produce a large downward bending moment due to their weight. This might cause problems during take-off because the wings would be very close to the ground. A way to circumvent this is to

add loose wheels under the wings, similar to the 'pogo wheels' of the Lockheed Martin U2[1], which are not fixed to the aircraft and fall on the ground during take-off. Next to the wings bending downward, the slender boom will also bend downward under its weight when the tail is not generating lift yet. To make sure that the tails do not scrape the runway during take-off a small wheel is added to the bottom of both tails for it to rest on.

The landing procedure shares similarities with the take-off procedure in its unconventional nature. The absence of dedicated landing gears means that for a traditional aircraft landing there would need to be some form of implemented design or infrastructure that accommodates for it. Two possibilities are identified. Either the HAPS has some sort of way to not get damaged by landing, for example, a skid on the underside of the HAPS; or when it lands it would need to land using dedicated landing infrastructure, such as a net or a cushion for the HAPS to land on. Since the HAPS will already have small wheels on the underside of the tail to aid in take-off, these can also be used for landing as a point of first contact. This, combined with a replaceable landing skid on the belly of the HAPS should be enough to properly land the HAPS on a runway or other flat surface. The skid should be easily attached and detached from the craft, as it will regularly get damaged during landing.

3.6. Sensitivity Analysis

In order to verify that the flight performance models created in this chapter are properly implemented a sensitivity analysis of the model is performed. Firstly, the model is heavily dependent on the analysis of graphs in order to find the desired performance parameters. This consequently means that a natural discretisation error will arise in the found values. There are four different values which are discretised and are used for calculation: the altitude h, the airspeed V, the angle of attack α and the load factor n. The airspeed and angle of attack are used iteratively in the aerodynamics model to find the optimal combination of both at a certain altitude for the minimum power required. This is done at a mesh size for $dV = 0.5m/s$ and $d\alpha = 0.5°$ respectively. Next, the altitude is once iterated over in order to perform the Riemann sum specified in Equation 3.9. This is done at a mesh spacing $dh = 100m$. Finally to calculate the maximum load factors the V-D diagram is multiplied by the load factor iteratively, at a very fine mesh of $dn = 0.01$. In order to verify that the meshes are fine enough, calculations are performed for one finer and one coarser mesh, while keeping the other mesh sizes constant. The results of the calculations for some parameters are shown in Table 3.4. Unfortunately, the model that was created to calculate aerodynamic coefficients did not allow for a change in the mesh size of α, as it would break its calculation. Therefore this mesh was kept constant.

Table 3.4: Mesh Size Variation

		Velocity Mesh Size	
Parameter	dV = 0.25 m/s	dV = 0.5 m/s	dV = 1 m/s
Power Required (25km) [W]	2581.62	2571.47	2582.44
Power Required (15km) [W]	969.05	976.85	988.45
Cruise Speed (15km) [m/s]	16.00	16.00	16.00
Drag (15km) [N]	60.57	61.05	61.78
		Altitude Mesh Size	
Parameter	dh = 50 m	dh = 100 m	dh = 200 m
Climb (Day) [hrs]	6.83	6.91	7.07
Descent (Night) [hrs]	3.95	3.96	3.97
Cruise [hrs]	13.21	13.13	12.95
		Load Factor Mesh Size	
Parameter	dn = 0.005	dn = 0.01	dn = 0.02
Maximum Load Factor (15km) [-]	1.91	1.90	1.90
Maximum Load Factor Airspeed (15km) [m/s]	21.83	21.19	21.18
Minimum Turn Radius (15km) [m]	15.21	15.21	15.25
Minimum Turn Time (15km) [s]	6.64	6.64	6.68

It can be seen from the table that there is less than 1% variance in the values of the parameters, therefore the mesh sizes are valid. Next to the mesh sizing, some assumptions were also made throughout the model that would need to be verified to be valid. The assumptions made were *small-angle approximations* and *steady* flight for all conditions, *straight and horizontal* flight for cruise and *horizontal and coordinated* turns. The small-angle assumption is applied to both the angle of attack α and the flight path angle γ. The flight path angle can be found from the sine of the airspeed and the rate of climb $sin\gamma = RC/V$. For 15km altitude, the rate of climb is maximal at 0.98 m/s. With a true airspeed of 16m/s, $sin\gamma = 0.06125$ and $arcsin(0.06125) = 0.06129$, thus

[1]https://www.blackbirds.net/u2/c_bennett/bbird-06.html

$sin\gamma \approx \gamma$. The small-angle approximation for the angle of attack follows from the results of the aerodynamics, which showed that α rarely goes higher than 8°. The impact of neglecting the most extreme 8° results in an assumption that 0.99 is 1 for these calculation, so it introduces 1% of inaccuracy. This only occurs in extreme cases of maximum power configurations, such as flying at the maximum design altitude or maximum lift. In the same sense accelerations throughout the mission profile are very low since the true airspeed varies between about 10 - 40 m/s, compared to for example traditional commercial airlines which can reach speeds up to 200 - 300 m/s. All of the values found in this chapter can now be used to work out all of the subsystems in more detail.

3.7. Summary and Conclusion

Now that the mission profile of the HAPS is clearly defined and has actual numbers associated with it, it is possible to further develop each subsystem in more detail. It was shown that the HAPS required a maximum propeller power of 2571.47W, which the propulsion and power subsystems will use to size the propellers, electric motors and batteries. Next, a climb and descent mission profile was specified throughout the day, showing that the HAPS should fly by the use of a powered climb and an unpowered glide during the night to save as much power as possible to reduce the battery size. The manoeuvre loading diagram and turning performance were found with the help of the airworthiness certification specifications for very light aeroplanes [7]. Finally, the take-off and landing procedures were shortly discussed. A sensitivity analysis was performed for all parts, to ensure that they were properly implemented. In the further development of the HAPS, it should be looked at that all certifications set by airworthiness authorities are adhered to, to make sure that the performance derived is actually reachable. Next to that, the exact procedures for all of the flight manoeuvres should be specified in more detail, especially the take-off and landing. Finally, cases where the aforementioned assumptions would not hold, such as non-horizontal turns.

4. Aerodynamics

The aerodynamic design of the HAPS is developed and presented in this chapter. The scope of this subsystem is the geometric design of the main wing as well as the development of a general aerodynamic model of the aircraft to predict the performance under various flight conditions. With this in mind, the chapter starts by laying out the subsystem requirements in section 4.1. After this, the process of selecting an airfoil begins in section 4.2 which involves an analysis of the flow characteristics of the HAPS operating environment in subsection 4.2.1, this lays the groundwork for the remainder of the aerodynamic performance discussion. The airfoil options are presented in subsection 4.2.2 after which the methods for evaluating each airfoil are elaborated in subsection 4.2.3. Finally, the trade-off is performed in subsection 4.2.4, this involves a validation of the airfoil performance results with wind tunnel data before the final selection takes place. Once the airfoil is selected the 3D wing is modelled in Section 4.3. The model and its results are presented in Section 4.4 after which a sensitivity analysis is performed on the airfoils and the geometric parameters in Section 4.5. Finally, the chapter is wrapped up in Section 4.6.

4.1. Requirements

Before going into the aerodynamic design, the requirements on the aerodynamic subsystem will first be discussed in this section and are listed in Table 4.1. These requirements follow from the high altitude long endurance mission profile and from the solar panel area requirements established by the power subsystem in chapter 7. They can be said to give a direction or vision to the aerodynamic design by specifying the important considerations and performance targets.

Table 4.1: Aerodynamic Requirements

Aerodynamics		
ID	**Requirement**	**Derived from**
REQ-TEC-AE-1	The platform aerodynamics shall be optimised for maximum ${C_l}^{3/2}/C_d$.	Section 1.3
REQ-TEC-AE-2	The aerodynamics shall provide sufficient lift at service altitude.	Section 1.3
REQ-TEC-AE-3	The aerodynamics shall have controlled boundary layer separation.	Section 1.3
REQ-AE-1	The surface of the main wing and horizontal tails shall be at least 110 m^2.	Chapter 7
REQ-AE-2	The aerodynamics shall be designed for a minimum Reynolds number of 10^5.	-

4.2. Airfoil Selection

In this section, the airfoil design for the main wing of the HAPS is picked and validated by performing an elaborate trade-off.

4.2.1. Reynolds Number Considerations

The aerodynamics of the HAPS are characterised by relatively low Reynolds numbers (Re). This has significant implications on the aerodynamic design, in particular about the airfoil performance. Below Re of 10^5 conventional airfoils experience performance decreases and less predictable behaviour [146]. In particular, decreases are seen in $C_{l_{max}}$ and maximum ${C_l}^2/{C_d}^2$ values which are combined with significant non-linear drag polar changes. Physical testing of conventional airfoils at low Re has been historically unreliable due to large performance variations with small Re changes [146].

For a given chord length and velocity the Reynolds number decreases with altitude because the density decreases much more drastically than the dynamic viscosity. As such the operating ceiling for the HAPS (25km) will give the lowest nominal Reynolds number. This value is placed at around 1.2×10^5. During cruise at the standard operating floor (15km) the value is around 2.7×10^5. During sea-level take-off the value is around 5.6×10^5.

At these Reynolds numbers the performance degrades compared to higher Re flows due to the presence of laminar separation bubbles along the top layer of the airfoil (see Figure 4.1). In particular, these laminar separation bubbles cause an increase in pressure drag, with the larger bubbles causing more drag. The laminar separation bubble directly precedes the transition of the flow from laminar to turbulent and it is through inducing this transition early that the "bubble drag" can be minimised. This early transition is promoted via the use of turbulators on the surface near the front of the airfoil or via a transition ramp. This transition ramp works by generating an adverse pressure gradient over the top surface of the airfoil which separates the airflow allowing it to transition and then reattach creating a smaller bubble in the process. A well-designed low Re airfoil will have a geometry that maintains the low drag benefits of the transition ramp over a large range of C_l values, or in other words, over a larger angle of attack range [125]. A key distinction between high and low Re airfoils is usually how much emphasis is placed on this performance characteristic.

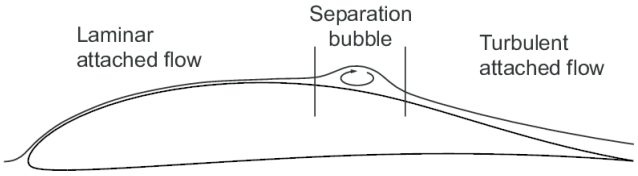

Figure 4.1: Laminar Separation Bubble [1]

4.2.2. Airfoil Options

To make the next step in the selection process of the airfoil for the wing, a literature study was performed resulting in a number of potentially suitable airfoils for the HAPS. The main focus was on airfoils being selected in designs for similar HAPS vehicles or already applied airfoils on high lift, low Reynolds number vehicles as sailplanes [39] and gliders. In this section, these identified airfoils will be discussed.

FX 63-137 Airfoil: Sakib et al.[27] describe an application of the FX 63-137 airfoil on a HAPS as operating in the lower part of the stratosphere, very similar to the HAPS design in this report. The airfoil is specifically designed for a maximum lift-to-drag ratio and a maximal lift coefficient for low speeds at low Reynolds numbers. The airfoil is used in a high-aspect ratio, polyhedral wings which is generally a characteristic of HAPS vehicles with a single main wing.

SG6042 Airfoil: J. Kimmons et al. describe [26] the application of the SG6042 airfoil in a HAPS design. The airfoil is originally used in small horizontal axis wind turbines [65] at Reynolds numbers from $1 \cdot 10^5 - 5 \cdot 10^5$. The airfoil is designed in a way that it optimises its lift-to-drag performance. Its thickness-to-chord (t/c) ratio is 0.1. The high lift-over-drag Reynolds number range for the airfoil is between $2.5 \cdot 10^5 - 5 \cdot 10^5$ in the HAPS application, a smaller range than in wind turbine application, related to lifting coefficients between 0.6 and 1.2.

GOE 523 Airfoil: The GOE 523 airfoil is mentioned in the same paper as the SG60642 airfoil [26] being used in the design for a HAPS. It is an airfoil that also has high lift-to-drag performance and a maximum (t/c) ratio of 0.165 and overall is a solid option for a HAPS design.

S1223 Airfoil: The S1223 airfoil is a low Reynolds number airfoil and is optimised in [29] to have high lift-to-drag performance for near-space vehicles in the stratosphere. The Reynolds number range is similar to the other airfoils at about $2 \cdot 10^5 - 5 \cdot 10^5$. In this paper, they optimize the airfoil for a couple of parameters such as a high lift-to-drag ratio, endurance factor and high $C_{l_{max}}$ which they do not succeed in successfully making the airfoil a good option for the HAPS.

[1] https://www.researchgate.net/figure/Laminar-separation-bubble-13_fig6_307087525

Ishii Airfoil: The Ishii airfoil is an ultra-low Reynolds number airfoil and is designed for maximum lift-to-drag ratios below Re 70,000 [33]. It was originally designed to be used for a hand-launched glider, hence the low Reynolds number focus. In particular, the airfoil is said to behave similarly regardless of the Reynolds number at very low Re (below 50,000) [34]. Potential applications have included the Japanese Mars Airplane [33].

NACA 63-412: The NACA 63-412 airfoil was taken as the candidate airfoil for a HAPS by Silva de Mattos et al. [105]. They note that the low Re conditions require the wing to be operating at high lift coefficients and therefore there is a need for an airfoil with low drag properties under these conditions. They provide a Reynolds number range of 150,000 to 200,000 and use it to justify the selection of this airfoil describing it as "laminar" and with a wide drag bucket [105].

SD7003: The SD7003 is similar to the Ishii airfoil albeit with a focus on marginally higher Reynolds numbers. Designed by Michael Selig it was originally used for radio control soaring competitions where the focus was its low drag characteristics [125]. As mentioned in subsection 4.2.1 the main culprit at low Reynolds numbers for deteriorating airfoil performance is pressure drag due to laminar separation bubbles. This airfoil is characterised by being able to generate a "long and quite shallow transition ramp" minimising the "bubble drag" for the airfoil [125]. These properties could make it a desirable airfoil for the HAPS being designed.

SD2030: Similarly to the SD7003 the SD2030 was designed by Michael Selig for the soaring competitions. However, the design approach was radically different to that of the SD7003. Instead of making use of the long transition ramp, the SD2030 features a shorter ramp near the end of the airfoil [125]. The value in this is to take advantage of "extended runs of laminar flow" in order to reduce drag (albeit at the expense of larger separation bubbles aft of the airfoil) [125].

4.2.3. Performance Evaluation Methodology and Trade-off Approach

In this subsection, the method of measuring the airfoil performance is described and the approach to the airfoil trade-off is explained.

First, the most important methods and relevant performance parameters for describing the performance of the wing will be discussed. During operation, the main goal of the HAPS is to stay in the air for as long as possible. During powered flight, this means that there should be optimised for maximum endurance, which can be done by optimising the parameter $C_L{}^{3/2}/C_D$, this is the optimal ratio for minimum power flight for propeller aircraft and will be referred to as the endurance parameter.[2] Then during unpowered flight, it is important to optimise for the gliding ratio and this can be done by optimising the gliding ratio which is defined as C_L/C_D. The stall characteristics will also be important during the design of the HAPS in the form of $C_{L_{max}}$. Especially during take-off or loitering manoeuvres and for robustness in general against e.g. disturbances in the form of gusts.

To assess the performance of each considered airfoil, a combination of literature studies specifically looking at wind-tunnel data and an analysis tool in the form of XFLR5 will be used. In XFLR5 it is very easy to plot aerodynamic properties of airfoils and visualize and analyze these properties. Some options allow for a comparison of a batch of airfoils which allows for easy and quick comparison of a larger number of potential airfoil profiles.

There are some limitations to XFLR5, it is for example not able to accurately describe stalling characteristics, in other words, $C_{l_{max}}$ and V_{stall}, and the region close to these values [87]. XFLR5 makes use of the panel method which is also only valid for compressible boundary layer regions of airfoils and wings. Sometimes XFLR5 over- or underpredicts drag and lift values and this needs to be taken into account during the use of it. In XFLR5 it is also very easy to model the effects of the angle of attack and Reynolds number, which will vary quite a lot in the operating region of the HAPS. Finally, the last relevant limitation of XFLR5 is that it sometimes has difficulty modelling viscous effects. For the design of the HAPS, which operates at relatively low Reynolds numbers compared to conventional aircraft, this means that the viscous effects and especially the effects of the laminar separation bubble will not be modelled perfectly and this should be taken into account.

Then to complement and correct the comparing results of XFLR5 a literature study is performed on each airfoil where the focus will lie on finding the stall characteristics for each airfoil considering XFLR5 is not able to. Then the shape of the drag bucket will be checked, especially for the lower Reynolds numbers for which it can be inaccurately approximated by XFLR5. Finally, an overall sanity check is done in terms of values for the gliding ratio and endurance optimisation validating the characteristics of the airfoils. In the literature study there will be specifically looked for wind tunnel and experimental data, since this will significantly add value to the results of the simulation of XFLR5.

Having discussed the relevant parameters and important limitations and strengths of the methods to analyse the airfoils the approach will be to start analysing all airfoils in XFLR5. Then data is extracted on the trade-off criteria and a preliminary airfoil is selected and communicated to the other subsystems. Then a literature study

[2]https://people.clarkson.edu/ pmarzocc/AE429/AE-429-11.pdf

focused specifically on wind tunnel data is performed, the weights are revisited and the last values are extracted. Then a final winning airfoil is selected and the design of the rest of the wing can start.

4.2.4. Trade-off

In this subsection, the airfoil trade-off is performed but before performing the trade-off all required preparation is done by determining criteria, weights, scoring and revisiting and validating of the scoring.

Trade-off Criteria and Weights

The performance of the main wing will greatly influence the performance of the whole HAPS and can reduce requirements for other subsystems such as propulsion, structures and power. The most important characteristics of the airfoil have already been mentioned in subsection 4.2.3. Therefore ,$C_l{}^{3/2}/C_d$, C_l/C_d and $C_{l_{max}}$ will form three of the selected criteria. The HAPS will spend the longest time in powered flight and endurance is the most important airfoil characteristic resulting in a 40% weight for $C_l{}^{3/2}/C_d$. Maximising this parameter will also greatly reduce the required power and will thus help out the power and propulsion subsystem a lot. Then for unpowered flight, C_l/C_d has been assigned a weight of 25%. $C_{l_{max}}$ is assigned 10% weight since it is an important parameter but will not come into play too often except for a few specific situations.

Next to these, the thickness to chord ratio (t/c) will also be considered as criteria and has an assigned weight of 15%. The (t/c) is very important for resisting bending moment and consideration of the required high aspect ratio of the wing stresses the importance of this parameter [69]. Finally, the minimal drag coefficient will also be taken into account as this will enable the propulsion subsystem to have more freedom during the design. This criterion is also assigned a weight of 10%. The C_m of an airfoil is important for the longitudinal stability of an aircraft as it is the longitudinal pitching moment coefficient, but it has been decided to neglect this parameter in the airfoil trade-off since the battery and payload masses are a large part of the total mass and their placement can thus be used to make the HAPS longitudinally stable. The definition of the scoring of each criterion in the trade-off can be seen in Table 4.2.

Table 4.2: Airfoil Criteria and Weights Table

Criteria	1	2	3	4	5
$C_l{}^{3/2}/C_d$ (40%)	Insufficient performance in operating range of Reynolds numbers	Limited performance in operating range of Reynolds numbers	Decent performance in operating range of Reynolds numbers	High performance in operating range of Reynolds numbers	Very high performance in operating range of Reynolds numbers
C_l/C_D (25%)	Insufficient performance in operating range of Reynolds numbers	Limited performance in operating range of Reynolds numbers	Decent performance in operating range of Reynolds numbers	High performance in operating range of Reynolds numbers	Very high performance in operating range of Reynolds numbers
t/c_{max} (15%)	Very thin airfoil	Thin airfoil	Medium thick airfoil	Thick airfoil	Very thick airfoil
$C_{l_{max}}$ (10%)	Very limiting in take-off Reynolds numbers	Limited in take-off Reynolds numbers	Decent in take off Reynolds numbers	High in take-off Reynolds numbers	Very high in take-off Reynolds numbers
$C_{d_{min}}$ (10%)	Very high in operating range of Reynolds numbers	High in operating range of Reynolds numbers	Decent in operating range of Reynolds numbers	Low in operating range of Reynolds numbers	Very low in operating range of Reynolds numbers

XFLR5 Results and Initial Scoring

To score the criteria using the analysis of XFLR5, a couple of definitions are defined to ensure consistent scoring and proper comparison of the airfoils. For the $C_l{}^3/C_d{}^2$, $C_l{}^3/C_d{}^2$ and minimal C_d values, the best-performing value is selected for the relevant Re ranges and the related AoA is also documented. Then to ensure stability over multiple AoA, the values at 1 degree increase and decrease from the optimal AoA are also documented and taken into account in the scoring. For the drag values, the width of the bucket was noted using an increase of 10% as a boundary but still, sanity checking by visual inspection of the drag bucket.
The XFLR5 values for the parameters can be found in Table 4.3 and Table 4.4. Please do note that the $C_{l_{max}}$ values are included in this table but are results from the literature study.

Table 4.3: $C_l{}^{3/2}/C_d$, C_l/C_d, t/c, and Max C_l

Airfoil	$C_l{}^{3/2}/C_d$ (Re = 300,000)	$C_l{}^{3/2}/C_d$ (Re = 100,000)	C_l/C_d (Re = 300,000)	C_l/C_d (Re = 100,000)

FX 63-137	130 at 6.5° (129-125)	78 at 8° (76-76)	106 at 5° (104-105)	61 at 8° (61-59)
SG6042	103 at 4.5° (97-97)	66 at 6° (56-62)	105 at 4° (100-100)	63 at 6° (56-58)
GOE 523	103 at 2° (101-103)	64 at 6° (63-62)	88 at 1° (87-87)	50 at 5° (49-49)
S1223	117 at 8° (117-116)	69 at 4° (68-68)	85 at 4.5° (84-85)	55 at 3° (54-54)
Ishii	62 at 7° (68-59)	35 at 7° (33-33)	63 at 6.5° (59-59)	40 at 2° (24-37)
NACA 63-412	85 at 5.5° (74-64)	56 at 6.5° (46-39)	89 at 5.5° (82-65)	57 at 6.5° (49-39)
SD7003	64 at 7.5° (62-62)	39 at 6.5° (38-38)	67 at 5.5° (66-66)	43 at 5° (42-43)
SD2030	74 at 3.5° (64-71)	51 at 5° (37-46)	89 at 3.5° (82-81)	56 at 5° (45-49)

Table 4.4: t/c, Max C_l, and Min C_d

Airfoil	t/c	Max C_l at Re=500,000	Min C_d (Re=300,000)	Min C_d (Re=100,000)
FX 63-137	0.137	1.7	0.011 (0.45-1.15)	0.026 (0.3-1.65)
SG6042	0.100	1.52	0.008 (0.45-0.95)	0.017 (0.1-1.15)
GOE 523	0.166	0.9	0.013 (0.9-1.25)	0.030 (0.9-1.65)
S1223	0.121	2.25	0.016 (0.9-1.35)	0.022 (0.9-1.25)
Ishii	0.072	N/A	0.009 (-0.15-0.4)	0.011 (0.2-0.5)
NACA 63-412	0.120	N/A	0.009 (-0.1-0.9)	0.018 (-0.25-1)
SD7003	0.085	1.25	0.007 (-0.1-0.45)	0.011 (-0.2-0.4)
SD2030	0.086	1.20	0.008 (0.2-0.75)	0.014 (-0.1-0.85)

Value Correction and Validation with Literature

Now that the initial scoring is completed with the use of XFLR5 the values are compared to the literature on wind tunnel experiments and values for $C_{l_{max}}$ can be added to Table 4.4. First, the literature study on each airfoil will briefly be described below.

FX 63-137: Wind tunnel measurements at various Reynolds numbers suggest the following discrepancies with the XFLR5 predictions.

The $C_{l_{max}}$ at a Reynolds number of 500,000 is experimentally around 1.7 at an AoA of around 10 degrees, XFLR5 predicts at that angle of attack a value of around 1.75 [124]. However, while XFLR5 can predict the soft stall characteristic of the airfoil it fails to identify the actual stall which should be kept in mind when using the polars from the software for this airfoil.

For the minimum drag, the predictions are overall quite accurate at higher Reynolds numbers with an experimental value of between 0.010 for Re 350,000 which when compared with the simulated 0.011 for Re 300,000 lines up with the expected performance drop associated with decreasing the Re number [124].

At Re 100,000, this accuracy degrades significantly, since, at a Reynolds number of 100,000 at low AoA the flow separates from the airfoil and does not reattach until the angle of attack is around 4° at which point the drag performance improves again [124]. However, at these low Re and low angles of attack, the rise in drag as a result is significant. This would be relevant either at high altitudes where the density decreases the Reynolds number, however, the aircraft is likely flying at a high C_L (therefore the high angle of attack) since this would be one of the limiting design cases. At lower altitudes, the Re tends to increase but care must be taken to ensure that the aircraft does not slow so much as to decrease the Re during low angle of attack flight. The minimum experimental Cd is 0.032 with two small drag buckets whereas the prediction was 0.026 with a larger drag bucket, although the software did predict two minimums for this larger bucket.

The aforementioned discrepancies will no doubt have impacts on the ${C_l}^{3/2}/C_d$ and C_l/C_d values but these will be minimal for Re 300,000. For Re 100,000 the drag is significantly affected up to around 4° as was mentioned, above this angle of attack, the predictions are still off but by around 20% at the minimum drag point. This takes place at a Cl of 1.6 which corresponds to an angle of attack of 8° which is the value for maximum ${C_l}^{3/2}/C_d$ and C_l/C_d hence suggesting a similar degree of accuracy for these values.

SG6042: To be able to compare with the XFLR5 simulation, the main important aerodynamic properties of the SG6042 airfoil are described in [130]. The $C_{l_{max}}$ at Re $5 \cdot 10^5$ is 1.52, the C_l/C_d for Re $1 \cdot 10^5$ is 55.6 and for Re $3 \cdot 10^5$ 77.8. The C_l/C_d for Re $1 \cdot 10^5$ is overestimated by XFLR5 by a bit and for Re $3 \cdot 10^5$ it overestimates it more than 30%.
The minimal C_d is about 0.01 for Re $3 \cdot 10^5$, but the values of the drag significantly increase and the shape of the drag bucket gets significantly worse for Re $1.5 \cdot 10^5$ or lower. For Re $1 \cdot 10^5$, the minimal C_d is in the range of 0.025 but as mentioned before a bit difficult to quantify due to the more complicated shape of the drag bucket. Comparing this to the XFLR5 it seems that the XFLR5 underestimates the drag slightly for both Re.

GOE 523: In an article by Kimmons et al. [26] results of wind tunnel data of the GOE 523 airfoil are presented for Re of $2.5 \cdot 10^5$. Here $C_{l_{max}}$ is around 0.9 at Re $2.5 \cdot 10^5$ and this paper also compares this data to XFOIL simulation data and for the simulation data, the $C_{l_{max}}$ is overestimated significantly. In the paper, the minimal drag is found to be around 0.01 for Re $2.5 \cdot 10^5$ and around 0.02 for Re $1 \cdot 10^5$. Comparing this with the XFLR5 analysis results it seems that XFLR5 overestimates the drag, especially for the low Re $1 \cdot 10^5$ the drag is overestimated in XFLR5 by about 50%.

S1223: For the S1223 airfoil there is some wind tunnel data on several Reynolds numbers in [3] with a value of 2.25 for Re $2.5 \cdot 10^5$. In an article by Selig et al. [28] the drag characteristics for the S1223 airfoil are tested in a wind tunnel and discussed. The minimal C_d is about 0.024 for Re $1 \cdot 10^5$ and about 0.017 for Re $3 \cdot 10^5$. Compared to the XFLR5 data this is very similar and thus all seems to be correct.

Ishii: As mentioned in the description of the Ishii airfoil in subsection 4.2.2, the airfoil was designed for extremely low Reynolds numbers, this is reflected in the lack of wind tunnel data for this airfoil at the Reynolds numbers of interest. The existing wind tunnel data is for Reynolds numbers up to 60,000 [33]. However, although it is not possible to compare experimental data with the simulation, the confirmation that the airfoil is designed for lower Reynolds numbers backs up the below-average performance of the airfoil (given it is operating outside of its design range).

NACA 63-412: As mentioned in the description of this airfoil in subsection 4.2.2, the NACA 63-412 is a laminar airfoil with a drag-bucket covering a large C_l range. The main applications are for higher-speed flight so the existing data corresponds to Reynolds numbers above 10^6. As such validation of the simulation results is made difficult, the approach of previous literature is to adapt the simulation results with data from higher Reynolds numbers, however, it is not made clear at all how this is done (and how reliable it is) so attempting a similar approach is not deemed reliable [106].

SD7003: The maximum C_l predicted by the simulation at Re 500,000 for the SD 7003 is around 1.34 while the experimental results place the value at around 1.25 [125]. The minimum C_d for the simulation at Re 300,000 was 0.007, experimentally at Re 350,000 the value is also 0.007, showing a good match but hinting at a slight under-prediction of the drag by the model as it is expected that the performance would get worse for increasing Re. Experimentally at Re 200,000, the value is 0.008, this is also predicted by the software [125]. Unfortunately, the value at Re 100,000 could not be found in the available experimental data but the value of 0.011 predicted is coherent with the expected decrease in performance and represents a large enough jump (when compared to between 350,000 and 200,000) to give confidence that the value is not being severely under-predicted (perhaps a similar order error is encountered as with the FX 137-63 airfoil). The relatively acceptable accuracy should also translate to the ${C_l}^{3/2}/C_d$ and C_l/C_d values considering drag is usually the main source of inaccuracies and is well predicted for this airfoil.

SD2030: The maximum C_l predicted by the simulation at Re 500,000 for the SD2030 is around 1.30 while the experimental results place the value at around 1.20 [125]. The minimum C_d for the simulation at Re 300,000 was 0.008, experimentally at Re 350,000 the value is 0.007, this under-prediction matches the expected performance drop with increasing Reynolds number. The value at Re 100,000 experimentally was 0.015, the simulated value is 0.014 which is a slight under-prediction of the drag [125]. For this airfoil, the simulation performed accurately but as per usual care should be taken with the drag polar for low Reynolds number conditions (referring to experimental data where possible). The acceptable accuracy should also translate to the ${C_l}^{3/2}/C_d$ and C_l/C_d values considering drag is usually the main source of inaccuracies and is well predicted for this airfoil.

Final Scoring and Trade-off Results

Using Table 4.2.4 a couple of changes were made to the scoring, so before going into the final results of the trade-off these are briefly mentioned. It was noticeable that the S1223 airfoil had by far the highest $C_{l_{max}}$ value compared to the other airfoils. For the FX 63-137 airfoil, the scoring for ${C_l}^{3/2}/C_d$ is decreased for Re $1 \cdot 10^5$ to account for an underestimation, while the airfoil already had the worst drag performance of the batch. Then for the SG 6042 airfoil, the C_l/C_d scoring was reduced for Re $3 \cdot 10^5$ since the prediction of XFLR5 was significantly higher than the wind tunnel data. There also was an underestimation of the drag for Re $1 \cdot 10^5$ which resulted in a decrease in scoring for the minimal C_d.

For the GOE 523, XFLR5 seemed to overpredict the drag for Re $1 \cdot 10^5$ leading to an increased score for the C_d. Also in Re $3 \cdot 10^5$, the drag was overestimated leading to an increase in the corresponding C_d. The S1223 airfoil results from the wind tunnel and XFLR5 matched quite well, so no scores were changed for this airfoil. Then during the literature study for the Ishii and NACA 63-412 airfoils absence of experimental data in the relevant Re numbers led to the elimination of these airfoils in the trade-off. Some time was spent on researching the applications of these airfoils and the Re range where these airfoils perform well is even lower than relevant for

[3] https://mselig.ae.illinois.edu/uiuc_lsat/s1223/s1223_liftcm.html

the HAPS. Both the SD airfoils results were also matched between the wind tunnel data and XFLR5 data leading to no changes in scoring.

Now all scores are completed, re-evaluated and validated the final trade-off results can be seen in Figure 4.2 where the FX 63-137 airfoil is the selected airfoil for the HAPS wing.

Figure 4.2: Final Results for the Airfoil Trade-off

		Score					
Criterion	**Weight**	**FX 63-137**	**GOE 523**	**S1223**	**SD2030**	**SD7003**	**SG6042**
Cl^3/Cd^2 Re = 0.3	0,20	5	3	4	2	1	3
Cl^3/Cd^2 Re = 0.1	0,20	4	4	4	3	1	4
Cl/Cd Re = 0.3	0,13	4	3	3	3	2	3
Cl/Cd Re = 0.1	0,13	4	3	3	3	2	4
Cl max Re = 0.5	0,10	3	1	5	2	2	3
Cd min Re = 0.3	0,05	3	3	1	5	5	5
Cd min Re = 0.1	0,05	1	2	2	4	5	2
t/c	0,15	3	4	3	2	2	2
Total (Unweighted)	1	3,38	2,88	3,13	3,00	2,50	3,25
Total (Weighted)		3,75	3,10	3,45	2,70	1,90	3,23

Having selected the airfoil, it is now useful to return to the wind tunnel data and performance discussions obtained for the FX 63-137 from Selig's VKI lecture series in consideration of REQ-TEC-AE-3 [125]. This requirement establishes the need for "controlled" boundary layer separation. This requirement aims to ensure that within the operational range of the angle of attacks, the point at which the boundary layer separates and its behaviour is well understood. As discussed extensively in subsection 4.2.1, at these Reynolds numbers the flow tends to form laminar separation bubbles which can result in large drag increases if the airfoil is not designed for the given conditions (both in Re and angle of attack). For the FX 63-137 this behaviour is properly controlled by a geometry designed to incite a "gradual adverse pressure gradient" which transitions the flow gradually to minimise the associated pressure drag [125]. This property is the transition ramp of the airfoil and for the FX 63-137 enables maintaining low drag performance for a large range of angles of attack (-2° to 10°) and therefore for a large range of C_l [125]. Throughout this range the reattachment point of the now turbulent flow onto the airfoil moves from the trailing edge of the airfoil to around the quarter chord point (from low to high angles of attack) [125]. In this way ensuring that REQ-TEC-AE-3 is met.

4.3. From Airfoil to Wing

With the FX 63-137 airfoil selected for the HAPS wing, there is now a basis from which to design and model the performance of the 3D wing. The wind tunnel data for this airfoil confirmed that the XFLR5 predictions for the lift are of acceptable accuracy up to an angle of attack of 10° for the Reynolds numbers in question. The drag predictions are generally of similar accuracy unless the Reynolds number is around 10^5 and the angle of attack is below four degrees at which point the drag is severely under-predicted. Fortunately, this situation is not one that can readily take place in the flight profile. The reasons for this are that such low Re only occur at the highest operational altitudes (25km) which are the limiting design case for the propulsion system. As such, cruising at these altitudes involves the optimal endurance factor angle of attack, 8°, and any decrease in this angle would immediately cause the aircraft to lower the altitude and gain speed, increasing the Reynolds number over the wing improving drag performance.

With this in mind and in order to have a higher resolution view of the performance of the airfoil under various conditions, the XFLR5 analysis was performed again just for the FX 63-147. This was done with an angle of attack resolution of 0.1 degrees and for Reynolds Numbers from Re $1 - 5 \cdot 10^5$ with a resolution of $0.25 \cdot 10^5$ between Re $1 - 3 \cdot 10^5$ and of $0.5 \cdot 10^5$ up to Re $4 \cdot 10^5$.

The goal is to be able to predict the lift and drag of the wing for a given altitude, airspeed and angle of attack. For the lift, the relationship between the lift coefficient of the airfoil and that of the wing depends on a modification to the lift slope based on the aspect ratio and the assumption that the zero lift angle of attack is the same between the wing and airfoil. Equation 4.1 contains the formula for this lift slope modification which applies to high-aspect ratio straight wings [31]. Since the HAPS falls into this category the formula is a reasonable estimate. For the zero lift angle of attack, the XFLR5 prediction is not used because it falls at a very low angle of attack where the simulation starts to behave erratically. Since the lift slope for the airfoil is calculated from two points in the simulation for which there is confidence in the validity, the zero lift angle is extrapolated from the

line drawn between these two points (so that the linear model of the airfoil is accurate at the relevant angles of attack). Only two points are needed because the lift slope is very well-behaved in the linear range for the XFLR5 simulation. With the modified lift slope and the zero lift angle of attack, the wing lift coefficient is established.

$$C_{L_\alpha} = \frac{C_{l_\alpha}}{1 + \frac{C_{l_\alpha}}{\pi AR}} \tag{4.1}$$

For the wing drag the prediction follows the standard drag polar seen in Equation 4.2. The first term is the sum of the skin friction drag and the pressure drag. This is taken to be the drag coefficient value for the airfoil at the given Re and angle of attack (C_d), an assumption that is backed by Anderson's *Fundamentals of Aerodynamics* for moderate angles of attack [31]. The second term is the lift-induced drag, which is modelled by the following parameters. The lift coefficient (C_L), which has already been determined from the lift slope (C_{L_α}), and angle of attack α. The aspect ratio (AR) for which higher values promote lower induced drag. Due to the low Reynolds numbers for the mission, the flight takes place at higher lift coefficients, making the induced drag contribution significant. As such, the aspect ratio is an important design parameter for lowering the drag. The final term is the span efficiency factor for the wing (e). This is minimised for elliptical lift distributions (or closely approximated by taper ratios of around 0.3). However, the Reynolds numbers for the root are already on the order of $1 \cdot 10^5$, if the taper ratio were 0.3, the Re at the tip would decrease by that factor. This would drastically increase the pressure drag of the airfoil as the laminar separation bubble stops re-attaching, undoing the positive effects of a more optimal lift distribution. Due to the wing being rectangular then, the span efficiency factor is taken to be 0.7 [4]. Taper could be considered for structural reasons, at the expense of aerodynamic performance.

$$C_D = C_d + \frac{C_L^2}{e\pi AR} \tag{4.2}$$

These coefficients allow for the calculation of the lift and drag of the main wing for different spans, aspect ratios, velocities, altitudes and angles of attack. By looping over the velocity for a given angle of attack and altitude it is possible to find the minimum velocity for a load factor of 1. By performing this loop for the operational angles of attack it is possible to confirm the angle of attack for minimum power at the various altitudes. These were found to match well with those determined for the airfoil during the trade-off.

For the Reynolds number range the HAPS will be operating in, the magnitude of the induced and viscous drag are comparable as can be seen in Figure 4.3. Here the wing is analysed in XFLR5 and the purple drag represents the viscous drag and the yellow drag represents the induced drag. The drag is analysed at the lowest Reynolds number of $1 \cdot 10^5$.

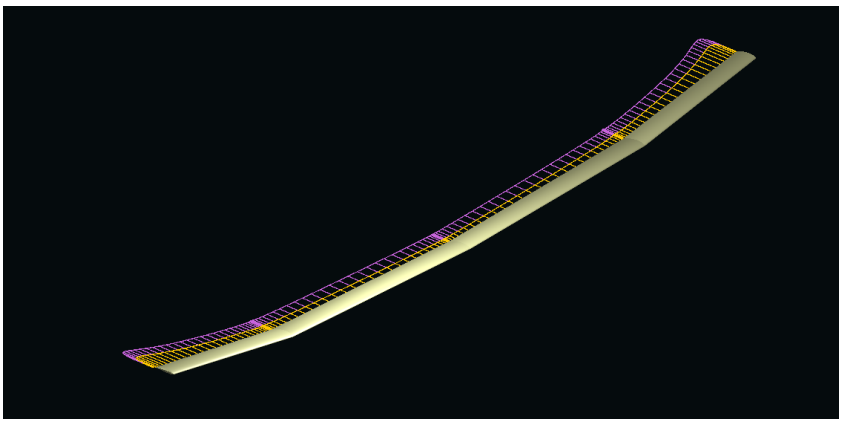

Figure 4.3: Visualisation of Ratio of Viscous and Induced Drag in XFLR5

4.4. Simulation and Results

The methodology presented in the previous sections is integrated into a simulation that takes an altitude a velocity and an angle of attack and uses the XFLR5 airfoil simulation data to predict the lift and drag for the entire aircraft. Initially, this simulation only predicted the performance as if the wing was the only lifting surface, carrying all the subsystem masses. This was necessary as the stabilising surfaces were not sized at that point and the preliminary results were crucial for getting the ball rolling on the design of various other subsystems giving realistic but preliminary estimates for crucial values. The values used by each system are laid out later on in this section. Once the subsystems were more defined and the tails had selected airfoils and were sized

[4] https://www1.grc.nasa.gov/beginners-guide-to-aeronautics/induced-drag-coefficient/

these aerodynamic surfaces were included in the model. The horizontal tail was modelled in the same way as the main wing with the vertical tail assumed to only contribute profile drag, the drag of the booms was not estimated, and that of the LCT is discussed in Section 2.5.6.

By looping over the simulation, the airspeed can be found at which the load factor is one, i.e. the minimum cruising speed. The results of these loops are presented in Table 4.5 for sea-level, 15 km and 25km. Sea level is presented to consider take-off conditions. 15km is presented as it is the altitude the vehicle will spend the most time at during the nighttime cruise. 25km is the design altitude which as mentioned earlier sets the maximum required power values. It should be noted that performance values can be obtained for any altitude below 25km. These results are for the optimal angle of attack of the main wing for minimum power, ensuring that the endurance requirement is met. Likewise, with a load factor of 1 at the maximum operational altitude, 25 km, such that REQ-TEC-AE-2 is met. The lower limit Reynolds number requirement, REQ-SUB-AE-1, is met by considering the performance of the airfoil at low Re during the trade-off.

Table 4.5: Aerodynamic Simulation Results at Different Altitudes

Parameter	Altitude = 0 m	Altitude = 15000 m	Altitude = 25000 m
Reynolds Number [Re] (-)	691,442.85	342,314.33	147,813.28
Velocity [TAS] (m/s)	5.05	12.57	27.15
Velocity [IAS] (m/s)	5.05	5.00	4.87
Angle of Attack (°)	5.3	6.0	7.0
Airfoil Drag Coefficient [cd] (-)	0.0112	0.0140	0.0202
Airfoil Lift Slope [C_{l_α}] (1/°)	0.0956	0.0933	0.0998
Wing Lift Slope [C_{L_α}] (1/°)	0.0955	0.0932	0.0997
Wing Lift Coefficient [C_L] (-)	1.4347	1.4755	1.5494
Wing Drag Coefficient [C_D] (-)	0.0486	0.0536	0.0639
Total Surface Area of Wing (m^2)	100.00	100.00	100.00
Total Span (m)	50.00	50.00	50.00
Total Chord (m)	2.00	2.00	2.00
Lift (N)	2,240.72	2,255.72	2,252.20
Drag (N)	75.95	81.96	92.89
Lift-to-Drag	29.50	27.52	24.25
Power Required (W)	383.48	1,029.96	2,521.70
Endurance Parameter (-)	35.34	33.43	30.18
Load Factor (-)	1.007	1.016	1.008

The results presented in this table are of great interest to many of the following subsystems and are used extensively in the design-wide iteration process. For example, the drag is given to the propulsion subsystem in order to verify the thrust needed from which the propeller and engines are sized (see chapter 6). The power required is given to the power subsystem which applies the necessary efficiencies and solar angle considerations to size the solar panels. This value of solar panel area ended up being the driving constraint for the wing sizing, leading to the 50-meter wing span to fulfil the 100 m^2 area needed (with the tail which is designed in chapter 5). The highest value of power required which corresponds to the maximum altitude is also an important parameter for the flight performance analysis. In particular in relation to determining the flight profile, as the power available corresponds to this maximum power required value and flight at lower altitudes requires less power. Part of the excess power is used for determining the rate of climb and as such defining the day-night flight profile discussed in chapter 3.

4.5. Sensitivity Analysis

In this section, a sensitivity analysis will be performed on the aerodynamic design discussed in this chapter. Typically this is done by changing design parameters and looking at the performance changes of the subsystem, but since a large part of this chapter is a trade-off first a sensitivity analysis is performed on this trade-off. After this, the effect of increased aspect ratio and mass on the ${C_L}^3/{C_D}^2$ will be investigated.

4.5.1. Trade-off Sensitivity Analysis

The results of the trade-off sensitivity analysis can be seen in Table 4.6.

Table 4.6: Weight Sensitivity Analysis of the HAPS Concept Trade-off

Criterion	Change	New winner
${C_L}^3/{C_D}^2$	infinite	No new winner
C_L/C_D	infinite	No new winner
C_{Lmax}	+150%	SD1223
C_{Dmin}	+400%	SG 6042
(t/c)	+500%	GOE 523

From the sensitivity analysis, it is clear that the FX 63-137 is a very convincing winner, excelling in endurance and in gliding properties. The runner-up from the trade-off, the SD1223, needed "only" 150% increase of weight for the C_{Lmax} which is by far the smallest change of weights to get a different winner from the trade-off.

4.5.2. Design Parameter Sensitivity Analysis

Once there is confidence in the airfoil choice it is wise to vary some of the important design parameters that the aerodynamics department is responsible for choosing, namely the aspect ratio of the wing, to see its effects on the performance of the wing. Likewise, seeing how the subsystem responds to imposed changes in general design parameters such as the total mass can give insight into how flexible the final design is to design changes from other subsystems. The best parameter to evaluate the performance of the wing under these changes is the endurance parameter (${C_L}^3/{C_D}^2$) as it measures how power efficient the aerodynamics are.

Aspect Ratio: For the majority of aircraft, increasing the aspect ratio free from structural limitations increases the efficiency of the aerodynamics. Usually, the balance is between the increased structural weight required to support a more slender wing and the aerodynamic improvements from such a wing. For the HAPS being designed another consideration limits the aspect ratio. This is the decrease in Reynolds number across the wing cross-section with an increase in aspect ratio due to the decrease in chord length. As can be seen in Figure 4.4a the endurance parameters for the higher altitude plots are much lower than those for the lower altitudes due to the lower Reynolds numbers at those altitudes. Given that aerodynamic performance degrades significantly below 100k Re, an increase in the aspect ratio would pose issues for flight at the highest operational altitude.

Looking more closely at Figure 4.4a it is clear that the Reynolds effect is not enough to cause a direct decrease in performance for the selected aspect ratio range. However, there is a significant drop in performance gain at the highest altitudes with the increase in aspect ratio. Given that the lowest Re for the current design operational profile is around 150k, just decreasing the chord from 2m to 1.5m (i.e. increasing the aspect ratio to 50) would decrease this lower limit to 100k. At which point, as discussed in Table 4.2.4 the simulation starts to significantly under-predict the drag for the airfoil in question, this would lead to a much worse actual endurance value than the one predicted by the aerodynamic model.

Total Mass: Figure 4.4b shows the effect of the total mass of the vehicle on the endurance parameter of the main wing. The expected result should be no change in the endurance parameter since it is a ratio of dimensionless coefficients, however, there is a marginal increase in the endurance parameter as the mass of the vehicle increases. Although it is becoming repetitive, this increase is due to Reynolds number effects. As the mass increases the aircraft has to fly faster to produce the same lift, this increases the Reynolds number which improves the drag properties of the airfoil improving the endurance parameter.

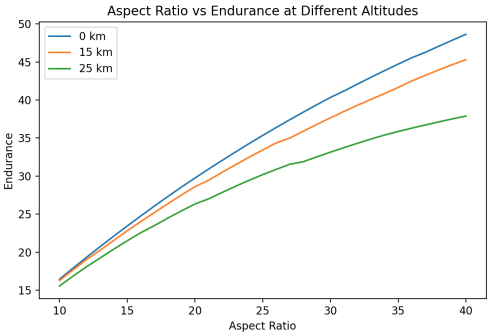

(a) Effect of Aspect Ratio on Endurance

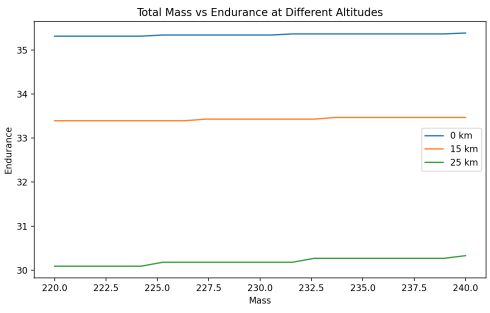

(b) Effect of Total Mass on Endurance

Figure 4.4: Effect of Aspect Ratio (left) and Mass (right) on Endurance

4.6. Summary and Recommendations

In this section, the design of the aerodynamics subsystem is summarised and then further recommendations are given for future design. The cost and mass budget for the wing generally refers to the structures that make up the wing. The structural masses to make the aerodynamic design a reality are calculated in chapter 9 and the associated costs are estimated in chapter 15 and refined further in chapter 12.

Summary In this chapter, before starting the design of the aerodynamics, first, the main relevant aerodynamic theory is quickly discussed. Then a selection of possible airfoils fitting the requirements is considered and briefly described. This is followed by a discussion on trade-off criteria and weights, and using XFLR5 preliminary scoring of all airfoils is done. Then these scores are revisited and corrected with wind tunnel data found in literature together resulting in the FX 63-137 airfoil as the winner. Then the step from airfoil to wing is discussed and basic design decisions as not using sweep are mentioned and explained. Finally, a sensitivity analysis concluded that the FX 63-137 is the best choice out of the airfoil batch and that it is aerodynamically beneficial for endurance performance to keep the operating Reynolds number range above $1 \cdot 10^5$ to avoid negative effects of the laminar separation bubble.

Recommendations Finally, it is recommended to look into the possibility of selecting a different airfoil for the outer wing, with a lower Reynolds number airfoil that will allow for taper. Taper could bring advantages such as an improved lift distribution, a higher Oswald efficiency factor resulting in lower induced drag and better stall characteristics for the wing with the tip stalling later than the root. As well as an increase in structural efficiency. It is also recommended to keep iterating with the other subsystems with the main constraint of the wing design now coming from minimal required solar surface area. A final recommendation is to investigate the effects of a trip-wire on the wing which will trigger the boundary layer to become turbulent and might increase aerodynamic performance by avoiding the laminar separation bubble on the wing.

5. Stability & Control

The goal of this chapter is to design aspects of the EURUS influencing stability such as the tail, dihedral and boom length. The analysis of the eigenmodes is conceptually described, as applied as possible but not executed due to time constraints. The chapter starts with the revised stability and control requirements which are discussed in section 5.1. Then the tail and boom are designed in section 5.2 followed by eigenmode considerations and equations in section 5.3. Then the methodology for performing the analysis is discussed in section 5.4 and the section is concluded by a sensitivity analysis in section 5.5 and a summary including recommendations in section 5.6.

5.1. Requirements

To provide a frame for the design of the stability and control subsystem, the requirements for this subsystem are extended as can be seen in Table 5.1.

Table 5.1: Stability and Control Requirements

Stability and Control		
ID	**Requirement**	**Derived from**
REQ-TEC-SC-1	The platform shall be operating at level 4 autonomy.	Section 1.3
REQ-TEC-SC-2.1	The platform shall be longitudinally statically stable.	Section 1.3
REQ-TEC-SC-2.2	The platform shall be laterally statically stable.	Section 1.3
REQ-SC-1	The platform shall be dynamically longitudinally stable.	-
REQ-SC-2	The symmetric eigenmotions of the platform shall be stable.	REQ-SC-1
REQ-SC-3	The platform shall be directionally statically stable.	-
REQ-SC-4	The asymmetric eigenmotions of the platform shall be stable.	-
REQ-SC-5	The platforms shall have redundant sensors for all stability-dependent controllers.	Section 1.3

5.2. Tail and Boom Design

In this section, the tail is sized and the boom length is determined based on the static and dynamic longitudinal stability requirements.

5.2.1. Horizontal Tailplane and Boom Design

There are several stability coefficients crucial in determining longitudinal static stability for aircraft, and relevant for the Eurus HAPS platform. These are $C_{M\alpha}$, describing the aerodynamic moment with relation to the angle of

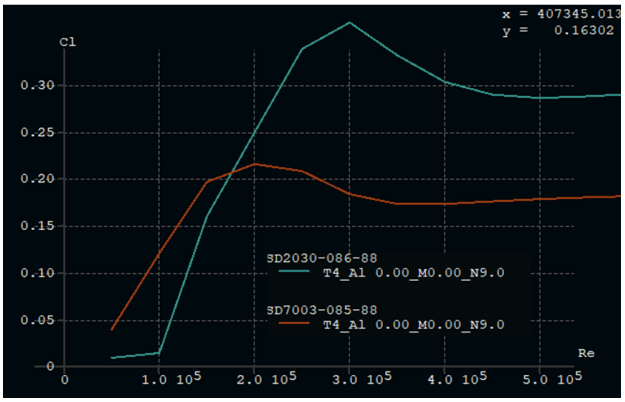

Figure 5.1: CL-Re Curves for the SD2030 and SD7003 in XLFR5

attack, and $C_{M\delta_e}$, describing the elevator effectiveness. $C_{M\alpha}$ needs to be negative to counteract any disturbance to the pitch. $C_{M\delta_e}$ also needs to be negative to be able to create a nose-down moment and reduce the angle of attack when using the elevator in situations close to stall for example.

Horizontal Tailplane Airfoil Selection

The horizontal tailplane first needs an airfoil selected before the sizing of the surface area can take place. There are a couple of important characteristics that are relevant to the horizontal control surfaces, namely: The C_L at deg AoA is small, The airfoil has low drag, the airfoil has high C_L/C_D and the airfoil has these characteristics for Re $1 \cdot 10^5 - 5 \cdot 10^5$

During the airfoil selection for the wing in 4.2, 2 airfoils, the SD2030 and SD7003, boasted extremely low drag, low C_L and performed adequately in the expected range for Reynolds numbers. Hence, they are very well suited for the horizontal tailplane. For control surfaces typically symmetric airfoils are used to have them not produce lift nor downforce at 0° AoA. It is possible to have the elevator set at a standard trim angle, but for conventional aircraft, the tail is usually required to produce downforce which is not desired. In this case, the aerodynamic centre of the wing of the HAPS will be in front of the c.g. meaning the tail will need to produce lift. A symmetric airfoil is therefore not required and an airfoil with non-zero C_L at 0° AoA can be used in the form of the SD airfoils.

To select between these 2 airfoils they are compared in XFLR5, specifically analysing at the behaviour of C_L at the specific Re range. The compared airfoils can be seen in Figure 5.1. In Figure 5.1 it can be seen that the overall lift of the SD2030 is better and it reaches almost twice the value of the SD7003 at Re $3 \cdot 10^5$. The control surface airfoil must generate lift for the entire range of Reynolds numbers, as the platform requires control throughout climb and descent. In the CL-Re plot, there is a steep decline of the SD2030 when approaching Re $1 \cdot 10^5$ due to the laminar separation bubble and it has thus been decided that the airfoil is not reliable enough to use in these conditions. The SD7003 airfoil is reliable in this region and will thus be used for the horizontal tail. Furthermore, at low angles of attack, which correspond to a more nominal operational condition, the drag is extremely low even at the lowest Reynolds numbers.

Horizontal Tail Surface and Boom Length

The sizing of the horizontal tail and the boom are strongly linked. The approach for designing with these parameters presents an interesting consideration, a larger boom shifts the centre of gravity back increasing the tail load required to balance the moment generated by the main wing (in the case of static stability). Similarly, the required thickness of the boom is different for different values of boom outer diameter. Larger boom diameters result in thinner booms, as more area is placed further away from the centre line of the structure, increasing the area moment of inertia. Note that there is a critical value for thickness where manufacturing considerations for CFRP become limiting. Finally, dynamic stability must also be ensured. The approach taken to tackle these criteria will be deliberated in the following subsections.

Maximum Static Load

The largest load the horizontal tail will have to produce to achieve static equilibrium corresponds to the largest moment generated by the main wing and sets one of the minimum values for the horizontal tail surface. This serves as the most limiting design case for the boom thickness by setting the largest internal bending load. For the horizontal tail surface sizing this takes place when the main wing is at maximum lift coefficient. For the boom, it is the actual load that matters and so the limiting case is the maximum load factor (i.e. maximum lift coefficient at take-off). The dimensionless moment is calculated following Equation 5.1, which can be rearranged to solve for the horizontal tail surface (S_h) as a function of the aerodynamic and geometric parameters. The aerodynamic parameters are $C_{L_{h_{max}}}$, $C_{m_{ac}}$ and $C_{L_{max}}$ which are the maximum lift coefficient for the tail, the moment around the aerodynamic centre of the main wing and the maximum lift coefficient of the main wing

respectively. The geometric parameters are S_h and S_w which are the surface of the horizontal tail and the surface of the wing respectively. The values x_{cg}, $x_{w_{ac}}$, $x_{h_{ac}}$ and $\bar{c}$ are the longitudinal positions of the centre of gravity, measured from the nose of the craft. Respectively these refer to the aerodynamic centre of the main wing, the aerodynamic centre of the horizontal tail and respectively.

$$C_{m_{max}} = C_{L_{h_{max}}} \frac{S_h}{S_w} \frac{x_{cg} - x_{h_{ac}}}{\bar{c}} = C_{m_{ac}} + C_{L_{max}} \frac{x_{cg} - x_{w_{ac}}}{\bar{c}} \tag{5.1}$$

To calculate the dimensional maximum lift that needs to be produced by the tail Equation (5.2) is used, where m_{total} is the total mass of the vehicle, n_{max} is the maximum load factor, g is the standard gravitational acceleration and a safety factor of 1.5 is included to compensate for uncertainties in the lengths of the moment arms.

$$L_{max} = m_{total} \cdot n_{max} \cdot g \frac{x_{cg} - x_{w_{ac}}}{x_{h_{ac}} - x_{cg}} \cdot 1.5 \tag{5.2}$$

Boom Thickness Calculation

The boom thickness calculation is divided into two parts. The first represented by Equation 5.3 calculates the internal moment at the front of the beam due to the maximum tail load calculated in Equation 5.2. Where each tail produces half the maximum tail load affecting each boom. This assumes a fixed support boundary condition at the front of the boom.

$$M_{int} = \frac{L_{max}}{2} \cdot (l_{boom} + 0.25 \cdot c_h) \tag{5.3}$$

Then, from the internal moment, it is possible to calculate the maximum stress in a ring cross-section of arbitrary outer and inner diameters. Using the tensile and compressive strengths of a CFRP product for use in primary aircraft products, it is possible to formulate an expression for the inner diameter given an outer diameter value. [1] In Equation 5.4 σ_{max} is the minimum of the tensile or compressive strengths of the material, η_{ssf} is the structural safety factor which is usually taken as 2. Finally D_{in} and D_{out} are the inner and outer diameters of the boom respectively.

$$D_{in} = \sqrt[4]{D_{out}^4 - \frac{M_{int} \cdot \eta_{ssf} \cdot 32 \cdot D_{out}}{\sigma_{max} \pi}} \tag{5.4}$$

As before, the boom cross-section, the boom length and the tail surface are interrelated and require iterations to converge to a valid parameter combination. Additionally, constraints are placed to take into account manufacturing considerations and longitudinal dynamic stability. Furthermore, to not overcomplicate the boom sizing the safety factor was doubled to 4 in order to take into account a combined maximum load from the vertical and horizontal tails. This makes the conservative assumption that the maximum load generated by the vertical tail is the same as that generated by the horizontal tail and that both occur at the same time. That is, effectively the internal moment is doubled for the combined load case and then a safety factor of two is applied.

Longitudinal Static Stability

The for the sizing of the horizontal tail surface the value of C_{M_α} can also be constraining. It is required that this value is negative so that a disturbance in the angle of attack is met with a counteracting pitching moment, returning the aircraft to its original equilibrium. This value can be determined following Equation 5.5.

$$C_{m_\alpha} = C_{L_{w_\alpha}} \frac{x_{cg} - x_{w_{ac}}}{\bar{c}} - C_{L_{h_\alpha}} \frac{S_h}{S_w} \frac{x_{h_{ac}} - x_{cg}}{\bar{c}} \tag{5.5}$$

The terms $C_{L_{w_\alpha}}$ and $C_{L_{w_\alpha}}$ are the lift slope of the main wing and the horizontal tail respectively. The rest of the terms are defined as in the previous expressions. Furthermore, the effects of down-wash are neglected due to the combination of the T-tail configuration, the low speed of the vehicle and the large span which places the wing tip vortices at a greater lateral distance from the horizontal surfaces.

Integration

In the following paragraphs, the approach to integrate prior considerations is described. First, it is useful to establish the objective parameter, which is the horizontal tail surface which is minimised in order to reduce the trim drag as much as possible. With this in mind, the iteration will take place over the boom lengths and outer diameter. A constant parameter through the iterations is the minimum value for the horizontal tail surface for dynamic stability. This value is used to check for dynamic stability for a given boom length before determining

[1] https://www.matweb.com/search/datasheet.aspx?MatGUID=a34a1841aa0a44db8412b38d2e01436c&ckck=1

if the static case is valid. The result will be for each combination a value of the horizontal tail surface, the boom cross-section geometry and the mass of the booms. The boom sizing includes a consideration for manufacturing constraints that place the minimum thickness of the boom at 2 mm.

Determining the surface of the horizontal tail from the static case involves the position of the centre of gravity of the vehicle which is affected by the boom mass. This effect is destabilising as it shifts the centre of gravity back increasing the lift moment arm and decreasing the moment arm of the tail. To ensure the effect of the boom is taken into account the boom and tail surfaces are sized initially for an assumed boom mass of 10kg before the centre of gravity is recalculated and the boom and tail surfaces are sized again. During each iteration, it is checked if the static horizontal tail surface is less than the minimum surface for dynamic stability. Consequently, the larger required surface area is chosen to ensure that the boom is sized to the most constraining scenario and that the resulting increase in boom mass is taken into account in the sizing of the static case. Convergence generally takes place in less than 5 iterations so the loop is run 20 times at most.

Finally, once the tail has been sized for both static and dynamic stability, the results are stored for that boom length and outer diameter combination. The convergent parameter combination for the is selected that results in the lowest horizontal tail surface. This makes it possible to plot the minimum horizontal tail surface for each value of the boom outer diameter as shown in Figure 5.2a.

The point for the minimum tail surface value corresponds to the boom and tail values shown in Table 5.2 and are the selected values for the design. Interesting characteristics of the chart that correspond to the constraints imposed through the method include the linear increase in tail surface after the minimum tail surface point, this is a result of the 2mm manufacturing constraint. Booms with larger outer diameters theoretically would go below this constraint but are prevented from doing so and so have a larger mass resulting in a larger tail surface.

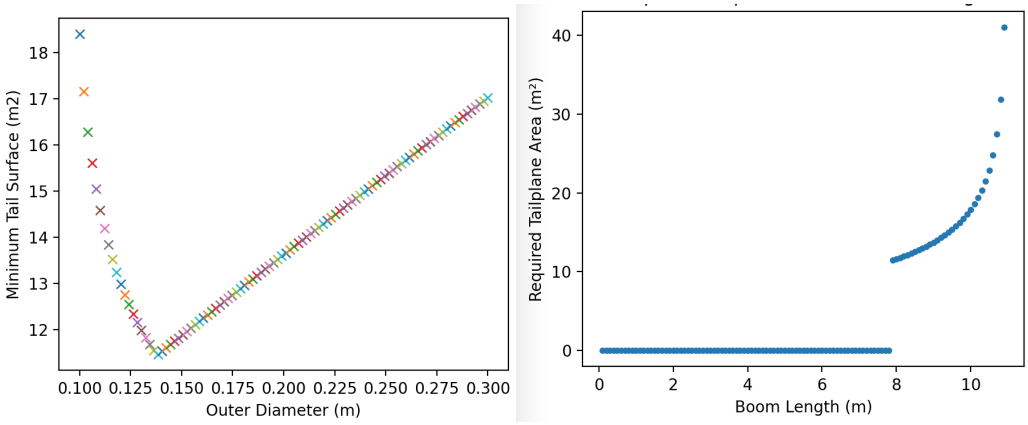

(a) Minimum Tail Surface with Boom Outer Diameter

(b) Required Tailplane Area with Boom Length

Plotting the tail surface values against the boom length, in Figure 5.2b, for the chosen outer diameter also gives insights into how the optimal design point is reached. The zero values below the chosen boom length correspond to static unstable configurations for the provided minimum tail surface. The points to the right of the chosen boom length correspond to the increase in the tail area required for longitudinal moment equilibrium as the boom length is increased. The reason for this increase is that at a certain point increasing the boom length, and thus mass, moves the centre of gravity back enough to give more moment arm to the wing lift under the maximum factor than the tail gains from the extra boom length. This leads to a need for a larger horizontal tail surface.

Table 5.2: Parameters for the Horizontal Tail

Parameter	**Value**
Boom Outer Diameter	13.8 cm
Boom Thickness	2 mm
Horizontal Tail Surface Area	11.4 m^2
Aspect Ratio	12.5
Mass of Booms	6.75 kg
Tail Volume Coefficient	0.45
Boom Length	7.9 m

Validation for Horizontal Tail Surface and Boom Length Sizing

To validate that the final combination of boom length and the horizontal tail is dynamically longitudinally stable an analysis for the wing and tail was run in XFLR5 and the C_{M_α}-curve is shown in Figure 5.3.

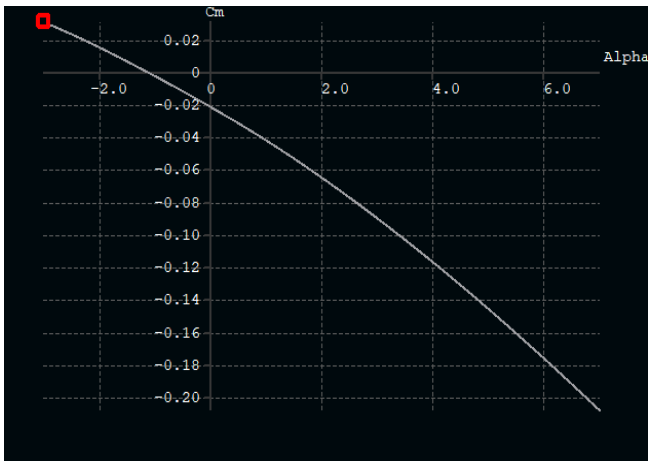

Figure 5.3: Validation of Stable $C_{M\alpha}$ Curve for the HAPS

Figure 5.3 demonstrated that the $C_{M\alpha}$ curve has a negative slope for the lowest Re number of $1 \cdot 10^5$ for a relevant AoA range from −3°-7°. This result validates the dynamic longitudinal stability of the boom length and horizontal tail surface sizing.

5.2.2. Vertical Tail Sizing

The sizing for the vertical tail was performed in a preliminary fashion as a result of time constraints. As such the approach follows from a comparison of tail volume coefficients, taking advantage of the considerations taken during the sizing of the horizontal tail.

The volume coefficient for the horizontal tail can be determined following Equation 5.6 where S_h is the horizontal tail surface area, l_h is the moment arm of the aerodynamic centre of the horizontal tail to the centre of gravity, S is the sum of the wing and horizontal tail surface areas and $\bar{c}$ is the mean aerodynamic chord of the main wing.

$$V_h = \frac{S_h l_h}{S\bar{c}} \tag{5.6}$$

The value for this coefficient is 0.45 for the optimal design point, this lines up pretty closely with Raymers' value for horizontal volume coefficients for sailplanes in Aircraft Design: A Conceptual Approach which is 0.5 [117]. This gives confidence that a preliminary value for the vertical tail surface can follow from Raymer's value for vertical tails. However, this value must be modified in two ways to more accurately match this specific vehicle. Firstly, since the horizontal tail volume coefficient is around 90% predicted by Raymer for sailplanes, the vertical tail volume coefficient will also be multiplied by this value. Secondly, the formula for the vertical tail volume coefficient (see Equation 5.7) includes the span as opposed to the chord.

$$V_v = \frac{S_v l_h}{Sb} \tag{5.7}$$

The HAPS has a main wing aspect ratio of 25 which is around half of that for sailplanes, for the given chord. A sailplane would therefore have double the span of the HAPS. Therefore, the vertical tail volume coefficient should also be corrected by 50% compared to the Raymer value. Raymers value is 0.02, applying the 50% and 90% corrections the tail surface is estimated at around 6.33 m^2.

5.2.3. Contribution to Mass and Cost Budgets

The cost and mass budget for the control and stability systems include the structures that make up the horizontal and vertical tail as well as the actuators needed for the control. The structural costs are estimated in chapter 12. The actuators and structures are the only global mass budget contribution for this chapter. The cost of the actuators are already taken into account in chapter 15. Given that the ailerons and rudder have not been sized yet, the choice of the actuator for reference is based on a conservative estimate for the actuator needed to deflect the horizontal tail surfaces which also act as elevators. There are eight actuators, four for the elevators, two for the rudders and two for the ailerons. Each of them weighs 1.04 kg so the conservative estimate for the total actuator mass is 8.32 kg [2]. The mass of the tail surface is calculated using the full wing structural mass proportional to area. The surface of the vertical and horizontal surfaces adds up to 17.93 m^2 which corresponds to 17.93% of the main wing surface, resulting in a tail structural mass of 20.01 kg.

[2]https://www.hiwin.cz/download/6083334a42c47d6fe1adb3f7468ccc56

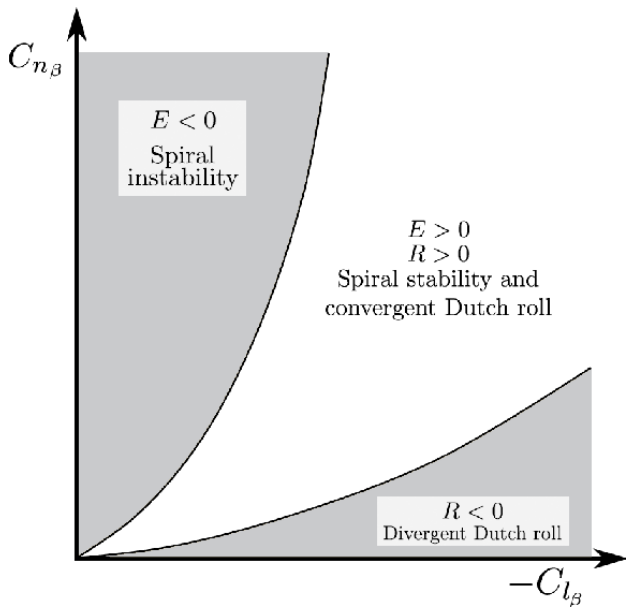

Figure 5.4: Lateral Stability Diagram Presenting the Balance of a Stable Spiral and Dutch Roll [70]

5.3. Eigenmodes and Equations of Motion

Since the design of the HAPS is still quite preliminary the execution of the eigenmotion assessment is outside of the scope of this project, but the methodology and application of methodology for this stability assessment will be discussed in this section and the rest of the chapter.

To assess the stability of the eigenmotions, an analysis can be made based on the equations of motion making use of the specific stability coefficients for the HAPS. These stability coefficients are used to describe the dimensionless equations of motion and describe relationships between angles, angular rates and moments of the HAPS. The eigenmotions, dimensionless equations of motion and these stability coefficients will be discussed below.

5.3.1. Symmetric and Asymmetric Eigenmotions

Within dynamic stability, the eigenmotions are the best indication of natural dynamic stability of an aircraft, or a HAPS, and thus they will be discussed here. Whether the aircraft can counteract the disturbance and stabilise determines whether it is dynamically stable or not. There are five eigenmotions of which two are symmetric: short-period motion and phugoid and three are asymmetric: A-periodic roll, spiral and Dutch roll

The symmetric eigenmotions are mainly relevant for longitudinal stability and the asymmetric eigenmotions are relevant for lateral stability. The eigenmotions are split up into symmetric and asymmetric, as it is common that these modes are assumed to be uncoupled making the analysis of the eigenmotions significantly easier. Even though one can compensate for an unstable HAPS with a controller using feedback loops, there are two main advantages to having a naturally stable HAPS (stable without use of controllers). Firstly, the HAPS will not be dependent on its control system and thus also not on the functioning of it. It is always possible that the controller itself, the computer or something as the power source fails and the reliability of the HAPS is then much higher when it is stable in a natural way. Secondly, the HAPS controller will consume less power, since it does not have to continuously correct for disturbances of the HAPS [30].

5.3.2. Dihedral Sizing and the Lateral Stability Plot

Lateral Stability Plot: For the asymmetric eigenmodes, the stability of the Dutch roll and the spiral are very closely related. The Routh-Hurwitz stability criterion is used to assess the stability of both eigenmodes with the weathervane stability coefficient, $C_{N\beta}$, and the effective dihedral coefficient, $C_{L\beta}$, being the most important for this stability. When these two coefficients are plotted against each other as seen in Figure 5.4 $C_{L\beta}$ should be as negative as possible for a stable spiral, but if it becomes too negative the Dutch roll will become divergent. A very positive $C_{N\beta}$ typically results in a stable Dutch roll but, especially combined with a not very negative $C_{L\beta}$, this may result in an unstable spiral.

Dihedral Sizing: Concerning the discussion with regards to Figure 5.4, the balance between spiral and dutch roll is rather important. One of the most important manoeuvres is loitering since the HAPS should be able to stay around the same area when required. It is then attractive to make the spiral as stable as possible, but the Dutch roll still needs to be taken into account.

The deflection of the wing due to lift naturally results in an effective dihedral angle, but throughout the flight

profile, this is not constant. The C_{L_β} is especially important for spiral stability so the need for a dihedral angle in the wing is clear.

To make the HAPS have constant stable behaviour, the goal is to keep effective dihedral as constant as possible. The deflection of the wing increases quadratically with the distance from the root and inspired by [30] it is decided to define the wing in two parts, the inner wing and the outer wing. Two different dihedral angles can now be applied to the wing and to make it more effective, the dihedral will only be applied to the outer wing. To achieve a constant effective dihedral the induced deflection of the dihedral will be minimised with the help of the split of the wing. For a wing without taper, such as the HAPS, the optimal place would be at the middle of the half span [30] and the dihedral is defined to be 12°.

5.3.3. Equations of Motion

Equation of motions of symmetrical Flight: The symmetrical flight can be described by Equation 5.8[48].

$$\begin{bmatrix} C_{X_u} - 2\mu_c D_c & C_{X_\alpha} & C_{Z_0} & 0 \\ C_{Z_u} & C_{Z_\alpha} + \left(C_{Z_{\dot{\alpha}}} - 2\mu_c\right) D_c & -C_{X_0} & C_{Z_q} + 2\mu_c \\ 0 & 0 & -D_c & 1 \\ C_{m_u} & C_{m_\alpha} + C_{m_{\dot{\alpha}}} D_c & 0 & C_{m_q} - 2\mu_c K_Y^2 D_c \end{bmatrix} \begin{bmatrix} \hat{u} \\ \alpha \\ \theta \\ \frac{q\bar{c}}{V} \end{bmatrix} = \begin{bmatrix} -C_{X_{\delta_e}} \\ -C_{Z_{\delta_e}} \\ 0 \\ -C_{m_{\delta_e}} \end{bmatrix} \begin{bmatrix} \delta_e \end{bmatrix} \tag{5.8}$$

Where C_{m_u} is the contribution of the velocity to the moment coefficient, $C_{m_{\delta_e}}$ is the contribution of δ_e to C_m, μ_c is the dimensionless mass, D_c is the dimensionless differential operator, $\mu_c K_Y^2$ is the dimensionless moment of inertia about the Y-axis, $\hat{u}$ is the dimensionless velocity, α is the angle of attack, θ is the pitch angle, $\frac{q\bar{c}}{V}$ is the dimensionless yaw rate, δ_e is the elevator deflection, and δ_t is the engine setting. All the other parameters on the left side of the equation are stability derivatives, and the remaining parameters on the right side of the equation are control derivatives.

Equation of motions of asymmetrical Flight: The asymmetrical flight is characterised by Equation 5.9[48].

$$\begin{bmatrix} C_{Y_\beta} + \left(C_{Y_{\dot{\beta}}} - 2\mu_b\right) D_b & C_L & C_{Y_p} & C_{Y_r} - 4\mu_b \\ 0 & -\frac{1}{2} D_b & 1 & 0 \\ C_{\ell_\beta} & 0 & C_{\ell_p} - 4\mu_b K_X^2 D_b & C_{\ell_r} + 4\mu_b K_{XZ} D_b \\ C_{n_\beta} + C_{n_{\dot{\beta}}} D_b & 0 & C_{n_p} + 4\mu_b K_{XZ} D_b & C_{n_r} - 4\mu_b K_Z^2 D_b \end{bmatrix} \begin{bmatrix} \beta \\ \varphi \\ \frac{pb}{2V} \\ \frac{rb}{2V} \end{bmatrix} = \begin{bmatrix} -C_{Y_{\delta_a}} & -C_{Y_{\delta_r}} \\ 0 & 0 \\ -C_{\ell_{\delta_a}} & -C_{\ell_{\delta_r}} \\ -C_{n_{\delta_a}} & -C_{n_{\delta_r}} \end{bmatrix} \begin{bmatrix} \delta_a \\ \delta_r \end{bmatrix} \tag{5.9}$$

Where $C_{Y_{\dot{\beta}}}$ is the rate of change of C_{Y_β} w.r.t time, μ_b is the dimensionless mass, D_b is the dimensionless differential operator, $\mu_b K_X^2$ or any other subscript by the K is the dimensionless moment of inertia about that axis, β is the angle of sideslip, ϕ is the roll angle, $\frac{pb}{2V}$ is the dimensionless roll rate, $\frac{rb}{2V}$ is the dimensionless yaw rate, δ_a is the aileron deflection, and δ_r is the rudder deflection. All the other parameters on the left side of the equation are stability derivatives, and the remaining parameters on the right side of the equation are control derivatives.

Acquiring the Stability Coefficients: The general dimensionless equations of motion are described above and apply to any aircraft. The combination of all coefficients together describes the stability behaviour of the HAPS and to perform the stability analysis is thus needed for the analysis. One way to get hold of these coefficients is with the specific USAF stability and control DATCOM method, "A method that provides a systematic summary of methods for estimating stability and control characteristics in preliminary design applications" [47]. The concept of HAPS vehicles was not invented yet when this method was developed and during the process of this method, it is important to compare the vehicle to aircraft groups with similar characteristics such as sailplanes or gliders.

Another way to acquire these stability coefficients is with a simulation/analysis program such as Flow5 or XFLR5 [4]. These programs can be used for estimating performance of the selected airfoils and determining their polars. Then the geometry of the aircraft can be put into the program and then 3D analysis can be run to assess the performance of all aerodynamic surfaces operating together. XFLR5 has limits in terms of Reynolds numbers and is mainly capable of analysis up until Re $1 \cdot 10^5$ so for analysis of the HAPS Flow5 will be more suited. These programs can plot the poles of the eigenmodes and then the geometry of the control surfaces can be tuned to make sure all eigenmotions are stable. More details on the analysis of the polar plot will be discussed later.

5.4. Stability Analysis

In this section, the methodology for performing stability analysis, designing controllers and tuning controllers is explained.

5.4.1. Polar Plots

To use the matrices of the symmetric and asymmetric motions for analysis of the HAPS, the eigenvalues of the matrices need to be calculated. These eigenvalues can be plotted in a pole plot and tell a lot about the stability of the eigenmodes. The imaginary axis is an indication of oscillatory behaviour and the further the poles are positioned from the real-axis the larger the oscillatory behaviour of that eigenmode will be. For the HAPS it is expected that the phugoid and Dutch roll will especially show high oscillatory behaviour and thus their poles will have larger values on the imaginary axis. An example of a polar plot can be seen in Figure 5.5b.

Ultimately, the real axis is the most important, as it will determine whether the motion is converging back to steady flight or diverging to an uncontrollable state of the HAPS. For a naturally stable HAPS, it will be important that all real values of the eigenmodes are negative and the more negative the values, the faster the HAPS will return to its steady state from before the disturbances.

Finally, it is important to take into account that for aircraft design in general there will always be a trade-off between stability and manoeuvrability. The more stable your aircraft, the harder it becomes to manoeuvre it out of its stable motion into the desired motion. For the HAPS vehicle, the main manoeuvres will be related to loitering and possible collision avoidance and both will not require a very high manoeuvrability. For the HAPS, the design should be aiming at very high stability and thus very negative real values of the poles.

5.4.2. Controllers

When an eigenmode is not or only just stable it luckily is still possible to operate the HAPS vehicle stably. This is done with all kinds of sensors giving feedback on parameters such as angles, forces and pressures. Since the equations of motion discussed earlier in this chapter are linearised, a linear controller will be most appropriate. This controller will then be giving feedback to all control surfaces and in that way the HAPS will be able to operate stable without naturally being stable. The equations of motion will typically be described in state space and are represented by four matrices A, B, C and D. Here matrix A is the state matrix and contains the aerodynamic stability derivatives, B is the input matrix and contains the control derivatives, C is the output matrix and describes how the current state affects the changes and D is the feedthrough matrix and gives potential direct feedback from the input to the output but is usually zero.

Then with the equations of motion in state space, a simple linear controller can be used to give feedback on the pitch for example as can be seen in Figure 5.5a. A linear controller here means that the output can linearly be described by the input.

In Figure 5.5a one can see the orange block K, representing the gain of the controller. This gain can be tuned to optimise the working of the controller and stabilise the HAPS even faster. This is typically done with a root-locus plot and is discussed in Section 5.4.3.

5.4.3. Root-locus

When the controller is defined it is possible to tune the gains and optimise the stability of the HAPS. There is not a physical meaning behind a gain so it is difficult to change this value, but a good tool to do this is a root-locus plot. The root-locus plot describes the displacement path of the poles of the eigenmodes for increases and decreases of gain. In this way, controllers can be tuned until all eigenmodes are stable or if that is not possible a different controller can be selected that is more suitable to ensure stability.

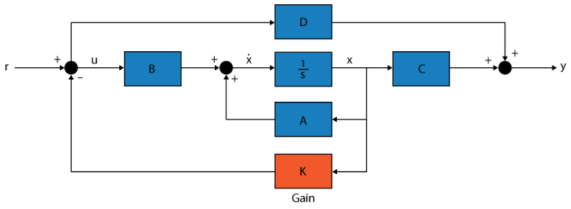

(a) Example of a Linear Pitch Controller [104]

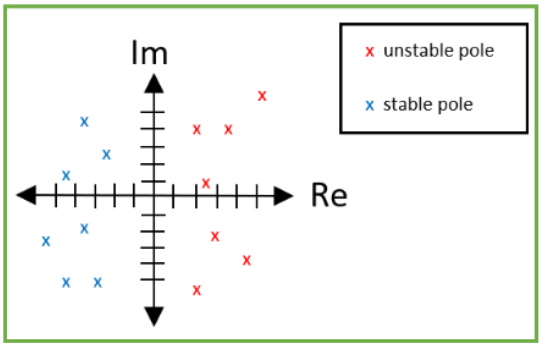

(b) Example of Polar Plot

5.5. Sensitivity Analysis

The aim of the sensitivity analysis for the tail surfaces will be to explore how changes to aircraft parameters and assumptions affect the optimal design choice.

Table 5.4: Mass and Cost of Actuators and Structures Proposed for Stability and Control System (FY24)

Contribution	Mass (kg)	Cost (€)
Actuators	8.32	1441.5
Structures	20.01	4199
Total	**28.33**	**6065**

Total Mass
Varying the total mass of the vehicle by 10kg leads to the values for the optimal tail design presented in Table 5.3. This seems to suggest that the extra bending load from the mass increase or decrease mostly affects the boom diameter and their mass while having less effect on the tail surfaces nor any significant effect on the length of the booms.
Minimum Manufacturing Thickness
Varying the minimum value for the thickness of the boom by 1 mm leads to the values for the optimal tail design presented in Table 5.3. This parameter has a significant effect on the horizontal tail design. The reason for this is that booms with larger outer diameters have lower thicknesses for carrying the same moment. The lower weight of these (even with a larger outer diameter) also results in a smaller static load case, due to shifting the c.g. back much less, which allows them to increase in length while maintaining a relatively constant horizontal tail surface area. The increase in boom length for thinner booms increases the tail volume coefficient which through the vertical tail sizing method increases the surface of the vertical tail.

Parameter	Original Values	Min t = 3 mm	Min t = 1 mm	ΔM = 10 kg	ΔM = -10 kg
D_{out}	13.8 cm	10.9 cm	19.8 cm	14.1 cm	13.3 cm
t_{boom}	2 mm	3 mm	1 mm	2 mm	2 mm
S_h	11.4 m^2	11.75 m^2	10.71 m^2	11.55 m^2	11.3 m^2
m_{booms}	6.75 kg	7.3 kg	5.0 kg	7.20 kg	6.22 kg
$\frac{V_h l_h}{S\bar{c}}$	0.45	0.41	0.50	0.46	0.44
l_{boom}	7.9 m	6.9 m	9.65 m	7.9 m	7.9 m
S_v	6.40	5.77	7.04	6.33	6.28

Table 5.3: Parameters for the Horizontal Tail

Implications on Other Subsystems
The stabilising surfaces, namely, the horizontal and vertical tails are significant for some of the other subsystems of the aircraft. The aerodynamic modelling of the aircraft must include the drag and lift produced by the horizontal and vertical tails. Another affected subsystem is the structures subsystem which must ensure that the tail loads are transferred correctly from the boom to the structure of the main wing. Further, it must ensure that the boom is sized to carry any additional loads that may affect the aircraft. For the CDHS system the tails are relevant for the functioning of the autopilot within the flight computer. Finally, the power subsystem has to take into account the (marginal) power consumption of the actuators that will be present for control in the tails.

5.6. Summary and Recommendations

In this section, the design of the stability and control subsystem is summarised and then further recommendations are given for feature designing.

Summary: First the static longitudinal stability of the HAPS was made stable by sizing of horizontal tail surface area together with the length of the boom with the latter influencing both the distance between c.g. and horizontal tail surface and the position of the c.g. itself. To this required static stability, requirements for a negative $C_{M\alpha}$ were added to also ensure dynamic longitudinal stability. Then basic structure requirements for the boom were taken into account to in the end size of the boom and horizontal tailplane. Based on the sizing of the horizontal tailplane, the vertical tailplane was also sized based on the tail volume coefficient and this tail volume coefficient was acquired from literature using a lot of reference aircraft.

Then the methodology for eigenmotion stability analysis was described starting with sizing of the dihedral and discussion on the spiral and dutch roll stability. After this the eigenmodes were described and the equations of motion were set up. Finally, the inspection of polar plots is discussed with a short controller description ending with the conceptual tuning of the controller with a root-locus plot.

The cost and mass budget for this system, combining the structures and actuators can be seen in Table 5.4.

Recommendations: It is recommended that looking forward a more refined method is found for sizing the vertical tail. This will also be intertwined with actually performing the eigenmotion analysis, for which an

analysis program is recommended for validation together with performing the USAF stability and control DATCOM method which together will provide these required stability coefficients. Then suited linear controllers can be selected and tuned based on the root locus plots making sure the eigenmotions of the HAPS are stable. Finally there still are all the control surfaces that can be designed in depth so this is the next thing to look into for this subsystem.

6. Propulsion

The Propulsion subsystem is responsible for providing thrust to the HAPS in varying conditions. The different conditions will generate requirements on the propulsive sub-system that are presented in Section 6.1. The goal of this chapter will be to design a subsystem that meets these requirements while optimising for mass, cost and power consumption, with careful attention to the latter. The physical relation between the subsystem components is shown in Figure 6.1. The current is delivered by the power sub-system to the Electric Speed Controller (ESC) that regulates the voltage and current for the motor. The electric power is transformed into mechanical power by the motor. Following that, the gearbox regulates the rotational speed. Finally, the power is transmitted via the shaft to the propeller which generates thrust. The goal will be to maximise the product of the components' efficiencies.

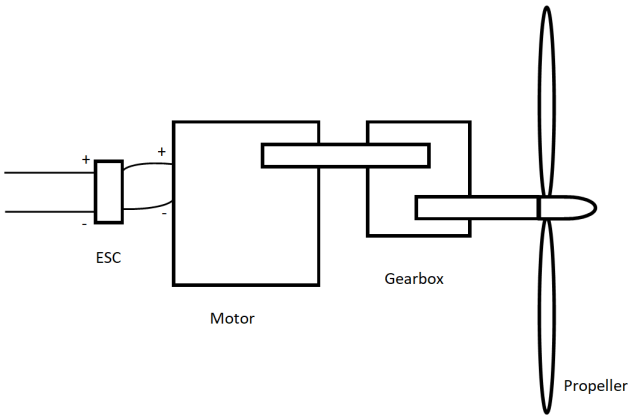

Figure 6.1: Propulsion Sub-system Components Diagram

6.1. Requirements

Requirements on propulsion were previously generated and are shown in Table 6.1. Additionally, new requirements were created relating to the propulsion subsystem originating from the Aerodynamics and Flight Performance sub-systems, as presented in Chapter 4 and Chapter 3 respectively. The power required was determined for the entire flight envelope. The climb is done at constant IAS, consequently, the dynamic pressure is constant. Therefore, the highest drag value is determined by the drag coefficient which as seen in chapter 4 increases with altitude. Therefore, the biggest drag (and power required) is at maximum altitude. Furthermore, the available power and thrust of the propeller are lowest at high altitudes as the density decreases. Therefore, the constraining conditions are at 25km, which are translated into requirements in Table 6.1.

Table 6.1: Propulsion Requirements

Propulsion		
ID	**Requirement**	**Derived from**
REQ-TEC-PRO-1.1	The platform propulsion system shall provide thrust to get to and sustain the service altitude at all times.	Section 1.3
REQ-TEC-PRO-1.2	The platform propulsion system shall provide thrust for minimum climb rate at service altitude.	Section 1.3
REQ-TEC-PRO-2	The platform propulsion system shall provide thrust for one-engine-off take-off and landing.	Section 1.3
REQ-PRO-1	The available thrust shall be at least 101 N at 25 km (under ISA conditions)	Chapter 3 and 4
REQ-PRO-2	The available power shall be at least 2874 W at 25 km (under ISA conditions)	Chapter 3 and 4

6.2. Design of Propeller

Propellers are rotating wings that generate thrust by creating a pressure differential. Similar to wings, their geometry can be defined by their chord, span, twist and airfoil type. In this section, the goal will be to design the blade of the propeller of the HAPS.

Propellers have been used since the beginning of powered flight. Therefore, their design is well understood [14]. However, the design of propellers for low-speed and high-altitude conditions, that the HAPS platform faces, is less developed. The main reason is that the Reynolds number over the blades at such conditions is significantly lower (in the orders of 10^5). In such a range the viscosity effect can not be neglected in the aerodynamic analysis, increasing the complexity of the problem and reducing the airfoil performance [46]. Further explanation of the influence on the flow of low Reynolds number can be found in subsection 4.2.1. However, thanks to growing interest in HAPS, research has been conducted on this topic, which will be used as a foundation for the design process.

The design process starts by identifying well-performing airfoils for the application. Note that the criteria for suitability will be expanded on later. Then in subsection 6.2.2, using the Blade Element Momentum Theory, the performance of each airfoil will be compared for a given chord and twist distribution. After that, one airfoil will be chosen and the corresponding optimal rotational speed, blade number and diameter will be chosen.

6.2.1. Airfoil Identification

As mentioned before the chosen airfoil must be able to operate at low Reynolds numbers. In Chapter 4, a series of airfoils were identified to be used on the wing. Such airfoils are not necessarily suited for propellers as the encountered angle of attack may be higher along the blades than for wings (due to varying twist). Therefore, a literature study on high-altitude propeller airfoils was conducted and five airfoils were identified: S1223 [96], E387 [45], DAE 51 [19], NACA 4412 [8] and SG6043 [126]. Their relevant aerodynamic performance was computed with XFLR 5 and is shown in Figure 6.2.

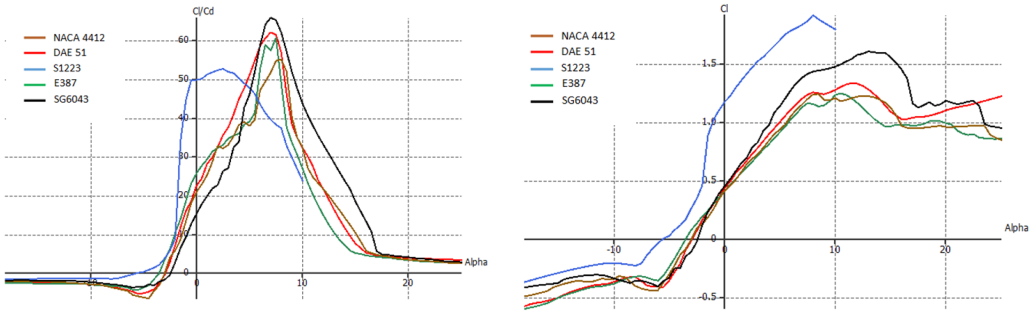

(a) $\frac{C_L}{C_D}$ vs α for the Five Airfoils at Re = 10^5

(b) C_L vs α for the Five Airfoils at Re = 10^5

Figure 6.2: Relevant Aerodynamic Performance of the Five Airfoils at Re = 10^5

Figure 6.2 demonstrates that all 5 airfoils present high $\frac{C_L}{C_D}$ values, which is desired. Note that the performance of the airfoil would significantly vary between Reynolds numbers, but is analysed at the best estimate of 10^5.

6.2.2. Blade Element Momentum Theory

The Blade Element Momentum Theory (BEMT) will be used to calculate the theoretical thrust and efficiency of the propeller for the five airfoils. It was derived by Glaubert [66] and shows satisfactory results [142]. The theory radially separates the blade into many elements (dr). For each element, the torque and the thrust are calculated. The thrust of one propeller is given as the sum of each element's contribution by Equation 6.1.

$$T = \int_0^R \frac{1}{2}\rho V_\infty^2 b_{prpl} dr C_L B \frac{cos(\gamma + \phi_i)}{sin^2(\phi_i) \cdot cos(\gamma)} \tag{6.1}$$

In Equation 6.1, T is the thrust, R is the blade radius, ρ is the air density, V_∞ is the free stream velocity, b_{prpl} is the spanwise distribution of the chord, C_L is the lift coefficient, B the number of blades, γ is the reaction force angle defined in Equation 6.3, ϕ_i is the inflow angle given as the ratio of free stream and rotational speed as defined in Equation 6.2.

$$\phi_i = \arctan\left(\frac{V_\infty}{2\pi n_{prp} r}\right) \tag{6.2}$$

$$\gamma = \arctan\left(\frac{C_D}{C_L}\right) \tag{6.3}$$

$$\alpha_i = \beta - \phi_i \tag{6.4}$$

In Equation 6.3, C_D is the drag coefficient and in Equation 6.2 n_{prp} is the rotational speed in revolutions per second, and r is the ratio of the distance to the centre of the propeller with the radius. To compute C_L and C_D, the local angle of attack α_i can be calculated according to Equation 6.4, where β is the local twist angle.

$$Q = \int_0^R \frac{1}{2}\rho V_\infty^2 r b_{prpl} dr C_L B \frac{sin(\gamma + \phi_i)}{sin^2(\phi_i) \cdot cos(\gamma)} \tag{6.5}$$

The second step in BEMT is to compute the torque of the propeller with Equation 6.5. Computing the torque allows for the determination of the efficiency of the propeller for these conditions with Equation 6.6.

$$\eta_{prpl} = \frac{TV_\infty}{2\pi\omega Q} \tag{6.6}$$

An important limitation of the BEMT method is that tip losses are not accounted for in this model. Prandtl proposes to correct this inaccuracy by multiplying the torque and thrust by a loss factor F given by Equation 6.7 and Equation 6.8 [142]. Where $\phi_{i,t}$ is the inflow angle at the tip. Note that the tip losses do not affect the efficiency but only the force and torque.

$$F = \frac{2}{\pi} cos^{-1}(e^{-f}) \tag{6.7}$$

$$f = \frac{B}{2}\frac{1-r}{sin(\phi_{i,t})} \tag{6.8}$$

6.2.3. Airfoil Selection

To select the best airfoil, the theoretical propeller efficiency for a given twist and chord distribution will be computed using BEMT with a 10-point numerical integration [1]. The computation will be made for a range of advance ratios. The advance ratio, J represents all the flight conditions by relating speed and propeller characteristics and is given in Equation 6.9[46].

$$J = \frac{V_\infty}{n_{prp} D_{prpl}} \tag{6.9}$$

where D_{prpl} is the propeller diameter. Furthermore, the twist and chord distribution is given, respectively, by Equation (6.10) and Equation (6.11). Equation (6.10) and Equation (6.11) were taken from Liu and He [96], where a propeller blade geometry was optimised for stratospheric use.

$$\beta = 20.9387 + (0.3040r - 3.9616r^2 + 5.1180r^3 - 1.6284r^4 - 0.3244r^5)\frac{180}{\pi} \tag{6.10}$$

$$b_{prpl} = (0.084241 - 0.85789r + 4.7176r^2 - 9.6225r^3 + 8.5004r^4 - 2.7959r^5)D_{prpl} \tag{6.11}$$

The results are given in Figure 6.3. The maximum efficiency is reached by SG6043 around J = 0.53. On top of that, it presents the highest efficiency between J = 0.3 and J = 0.65 which as seen later will be the operating advance ratio. Overall, the SG6043 present good performance throughout the conditions, therefore it is the airfoil that will be used.

[1] https://planetcalc.com/5494/

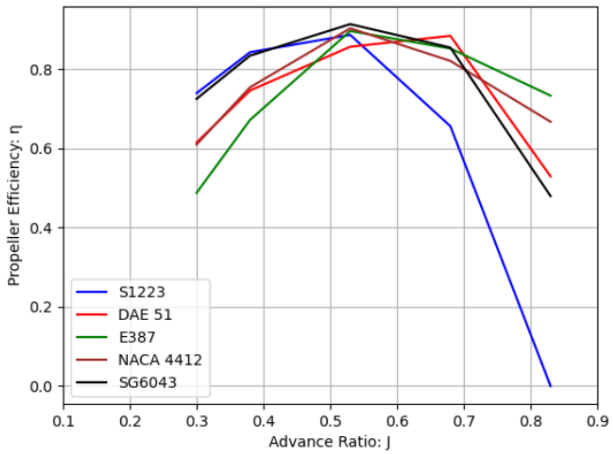

Figure 6.3: Propeller Efficiency of the Five Airfoils with Advance Ratio

6.2.4. Propeller Sizing

With the airfoil selected, it is now possible to size the propeller. The design of a high-altitude propeller is a complex problem that requires the correct combination of many parameters including geometry, speed and others. Each one of them and their influence will be discussed here and design decisions will be made.

Number of Blades:
Increasing the number of blades increases the thrust provided as seen in Equation 6.1. However, it has been observed that generally the more blades, the lower the efficiency of the propeller [96]. As efficiency is the driving design parameter, 2 blades per propeller will be chosen.

Fixed vs Variable Pitch Propeller:
Variable pitch propellers are used to increase the propeller efficiency over the range of operational conditions by regulating the pitch during flight to reach the optimal angle of attack [2]. They are particularly useful for aircraft that operate at varying speeds and densities. However, they add complexity and mass [112]. In the case of UAVs, variable-pitch propellers are not used as the relative increase of weight is bigger than for larger aircraft [46]. Therefore, they are not used on HAPS as seen in many designs, such as NASA's Pathfinder ([46]). Consequently, fixed-pitch propellers will be used.

Rotations Per Minute (RPM):

The rotational speed of the propeller greatly influences its efficiency. Increasing the rotational speed will increase the Reynolds numbers over the blade, resulting in better C_L/C_D performance of the airfoil as seen in Figure 6.4. Consequently, the propulsive efficiency will increase. However, at really high RPM, the efficiency might decrease as the local angle of attack is too low (see Equation 6.4 and 6.2).

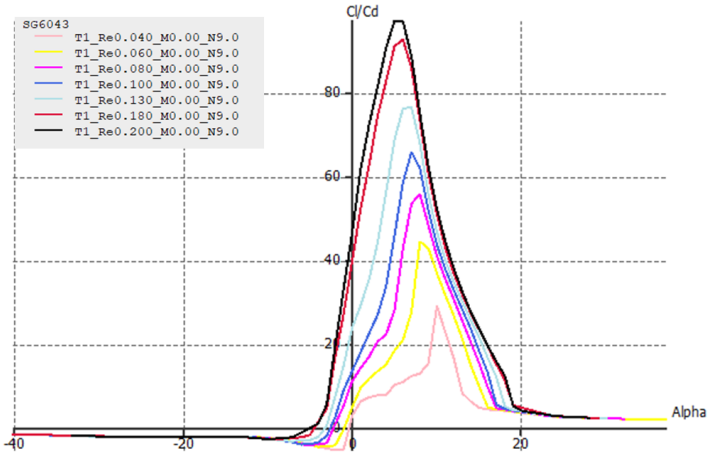

Figure 6.4: $\frac{C_L}{C_D}$ vs α for the SG-6043 airfoil for Increasing Re

[2]https://skybrary.aero/articles/variable-pitch-propeller

Therefore, the goal will be to run the propeller at the highest possible RPMs while remaining in acceptable ranges of angle of attack. The maximum values for the RPM are set by structural considerations: as the centrifugal force and torque cause a great amount of stress on the blades. However, in-depth analysis on this topic is considered outside the scope of the project but can be found in Dahal et al [10].
Additionally, increasing the RPM may cause supersonic flow over the blade creating shock waves, reducing the propeller performance [46]. Therefore, the flow of the tip may not surpass Ma = 0.75, which is mathematically translated by Equation 6.12 [96].

$$0.75 \geq \frac{\sqrt{V_0^2 + (n_{prp} D_{prpl} \pi)^2}}{a} \tag{6.12}$$

where a is the free stream speed of sound.

Blade Diameter and Hub:
Longer blades will generate more thrust and power. Generally speaking, HAPS have large blade diameters to generate enough thrust at high altitudes [46]. As with the RPM, the diameter is constrained by the blade tip velocity and structural considerations. The hub is the centre part of the propeller connecting the blades together. The torque from the shaft is distributed to the hub which in return transfers it to the blades. The comprise is that it shall be big enough to carry the loads and avoid wake interference while not being too large which reduces the thrust-generating surface. Typical values for its diameter is 10 % of the propeller diameter [96].

Take off and Landing Considerations
The diameter of the propeller leads to operational complications, as the blades might touch the ground at landing and take off. Solutions to overcome this might come from the use of multiple propellers with different diameters. Some would be used for low altitudes and others for high altitudes. According to Gonzalo et al [46], variable diameter propellers fix this issue. The diameter would increase as the altitude increases. However, this technology similar to variable pitch propellers does not lend itself toward use on a lightweight HAPS. Therefore, propeller locks were preferred that block the blades horizontally at landing.

Propeller Mass:
The mass of the propeller is a small part of the total aircraft mass, but must still be computed. Hall et al [11] and Keidel [90] use Equation 6.13, which will be used here.

$$m_{prop} = 0.12 B^{0.391} \left(D_{prpl} \frac{P_{prpl}}{1000} \right)^{0.782} \tag{6.13}$$

,where m_{prop} is the mass of one propeller and P_{prpl} the power of the propeller.

Final Propeller Design

To determine the combination of rotational speed and propeller diameter with the highest propeller efficiency, a Python code was constructed that iterated through the values that respected the REQ-PRO-1 and REQ-PRO-2 and the tip speed conditions. The change in rotational speed affected the Reynolds number hence the drag polar. This was taken into account in the code. The combination with the highest efficiency was used as the design. The final design values of the propeller can be found in Table 6.2.

The maximum thrust that can be achieved is constrained by the maximum propeller rotational speed that must meet the tip velocity requirement. Using Equation 6.12, it is found that for the current design, the maximum rotational speed is 32 rps leading to a total thrust of 172.5 N. Note that the propeller efficiency is slightly lower (0.86) since the local angle of attack on the blades are different. For close-to-ground operations (assuming h = 0), the maximum rotational speed is 35.46 rps. Since the drag at take-off is 76 N for a speed of 5 ms^{-1}(chapter 3), the thrust needs to be 76 N which is achieved for a rotational speed of 5 rps. Therefore, the propulsive system can generate enough thrust for take-off. One engine take-off is also possible.

Overall, the results are satisfactory. Typical efficiencies for propeller efficiencies are in the range of 0.85 [112]. The diameter length is considerable but in the range of comparable aircraft, such as the Zephyr and Helios.

Table 6.2: Propeller Design

(a) Relevant Numbers

Variable	Value
Max Thrust (25km) (T_{max})	172.5 [N]
Propeller Efficiency (η_{prpl})	0.91 [-]
Rotational Speed (n_{prp})	1312 [RPM]
Propeller Diameter (D_{prpl})	2.29 [m]
Blade Number (B)	2 [-]
Hub Diameter (D_{hub})	0.229 [m]
Propeller Mass (m_{prpl})	0.68 [kg]

(b) General Characteristics

Characteristics	Design Choice
Airfoil	SG 6043
Pitch	Fixed
Twist (β)	Equation 6.11
Chord (b)	Equation 6.10

6.3. Design of Motor

Electrical motors convert electrical energy into mechanical energy. They are divided into three main types namely: Brushed DC Motors (BDC), Brushless DC Motors (BLDC) and Alternating Current (AC) Motors. BDC motors use brushes to pass the current to the coils, whereas BLDC does not [3]. The main difference between DC and AC is that DC motors are the type of current they use. Batteries often operate at DC therefore, they are normally preferred in UAV applications [112]. However, a trade-off for the considered mission needs is still made to choose the most suitable type, shown in Table 6.3.

The criteria and their weights can be found in Table 6.3. The HAPS is to be optimised for power and weight and is ensured by a highly efficient propulsive system as it is the biggest power-consuming subsystem. Therefore, the efficiency criteria were deemed to receive a weight of 40% of the final grade. Similarly, a bigger aircraft mass leads to more lift required, meaning more drag and therefore more power consumption. For these reasons, the specific power was also awarded a weight of 40 %. Finally, how often maintenance is required is important as mission duration is in order of months and years. Therefore, Maintenance was given a weight of 20%. The grades were awarded based on the performed literature study, they can be found in Table 6.4.

Table 6.3: Motor Trade-off Criteria

Criteria	1: Poor	2: Moderate	3: Nominal	4: Good	5: Excellent
Efficiency (40 %)	≤ 0.6	0.6-0.7	0.7-0.8	0.8-0.9	≥ 0.9
Specific Power (40 %)	≤ 1 kW/kg	1-2 kW/kg	2-3 kW/kg	3-4 kW/kg	≥ 4 kW/kg
Maintenance (20 %)	Frequently	Often	Occasionally	Rarely	Never

Table 6.4: Motor Trade-off Grades

Criteria	Brushed DC Motor	BLDC Motor	AC Motor
Efficiency (40 %)	3 [144]	4	4
Specific Power (40 %)	1 [112]	4 [122]	1 [122]
Maintenance (20%)	1 [112]	4	4
Weighted Average	1.8	4	2.8

The conclusively best option is the BLDC Motor. This result was expected, but the choice of the motor is such a critical decision in the design process, that making a trade-off was deemed necessary. Performing a sensitivity analysis is not needed as by a simple observation one would see that the BLDC motor scores the best in all criteria. Therefore, it would always win no matter what weight is increased or decreased.

With that in mind, a commercially available motor was selected. Motors from companies that were recommended by the client and by Noth [112] were considered. The companies are Maxon, Minimotor, Portescap, Faulhaber, Strecker, Hacker, Plettenberg and CR Flight. The selection procedure kept in mind the required power that must be provided by the motor to the propeller while aiming for the highest efficiency and lowest mass. Additionally, it was desired that the reduction ratio between the propeller and motor rotational speed was as little as possible since, as seen in Section 6.5, it increases the overall propulsive efficiency. Finally, the chosen motor is NOVA 10 - HP 620/40/A2 S P12 from the company Plettenberg, its specifications can be found in Table 6.6. Where η_{motor} is

[3] https://www.globalspec.com/pfdetail/motors/brushed-dc-motor-working-principle

the motor efficiency for flight conditions at 25 km. Note that the efficiency varies slightly with the required power output.

Table 6.5: Motor Specifications [4]

Variable	Value	Unit
Max Continuous Current	180	A
Voltage	30	V
Peak Power	5.4	kW
Max Torque	7.2	Nm
η_{motor} at h = 25 km	0.875	-
RPM at h = 25 km	6673	RPM
Mass	2.2	kg
Dimension (⌀ x L)	104x110	mm
Quantity	2	-

Table 6.6: Motor Specifications [Plenttenberg, 2024]

Variable	Value	Unit
Peak Power	5.4	kW
Motor Efficiency	0.875	-
Max Continuous Current	180	A
Voltage	30	V

6.4. Design of ESC

The Electronic Speed Controller (ESC) is a critical component in the propulsion sub-system. It serves as the intermediary between the power source and the motor, as can be seen in Figure 6.1, regulating rotational speed and torque. This makes the ESC indispensable for ensuring smooth and efficient motor operation. Selecting the right ESC directly impacts system performance, efficiency, and reliability. The requirement on the ESC is that its maximum continuous power is higher than the motor's maximum power required. On top of that, its burst current shall be higher than the maximum operational current of the motor.

In order to ensure optimal system performance, and compatibility with the NOVA 10 motor selected in Section 6.3, the MST 60-260 from Plettenberg has been chosen. Additionally, Plettenberg allows for tailored ESC solutions, therefore use could be made of this additional feature increasing the compatibility. The ESC properties have been summarised in Table 6.7. Note that the efficiency of the ESC can be assumed to be equal to 1.

Table 6.7: ESC Specifications [5]

Variable	Value	Unit
Max Continuous Power	15.6	kW
Voltage Range	10 - 60	V
Max Continuous Current	260	A
Mass	0.525	kg
Dimensions	123x92x25	mm
Quantity	2	-

6.5. Design of Gearbox

Gearboxes reduce the rotational speed of the motor to reach the desired propeller rotational speed. In this case a fixed-ratio transmission will be used since multiple gear ratios add weight. Additionally, planetary gearboxes were preferred for their higher efficiency [6]. The reduction ratio is defined as the ratio between the motor and propeller rotational speed. The higher this ratio, the lower the efficiency of the gearbox. In this case using the data from Table 6.2 and Table 6.6, the reduction ratio is 4.9. For these values, η_{grb} (gearbox's efficiency) is above 0.9 [112]. The mass of the gearbox depends on the continuous power that it must provide. According to Hall et al [11], its specific power is 1 kW/kg.

[4] https://plettenbergmotors.com/product/nova-10-en/
[5] https://plettenbergmotors.com/product/mst-60-260-en/
[6] https://www.precisionmicrodrives.com/spur-versus-planetary-gear-types

A gearbox from commercially available solutions was chosen. The requirement on the gearbox was that it matches the maximum torque of the motor (7.2 Nm [7]) and the correct reduction ratio. The model chosen is the TG60-G5, its specifications can be found in Table 6.8.

Table 6.8: Gearbox Specifications [8]

Variable	Value	Unit
Reduction Ratio	5:1	-
Max Torque	28	Nm
η_{grb}	0.96	-
Mass	0.94	kg
Quantity	2	-

6.6. Sensitivity Analysis

The sensitivity analysis will consist of quantifying the impact of the assumptions made in the design process by changing parameters with the ultimate goal of demonstrating the robustness of the design. If the change is deemed too significant, new design choices will be made.

International Standard Atmosphere (ISA): To model the atmospheric conditions, the ISA model was used. However, ISA assumes a constant base temperature (standard day), meaning that it does not take into account weather or night/day conditions. On top of that, it does not simulate humidity. To correctly model the atmospheric conditions, weather model predictors should be used. To simulate this error, the density was varied, and its influence on the available thrust and propeller efficiency is shown in Figure 6.5.

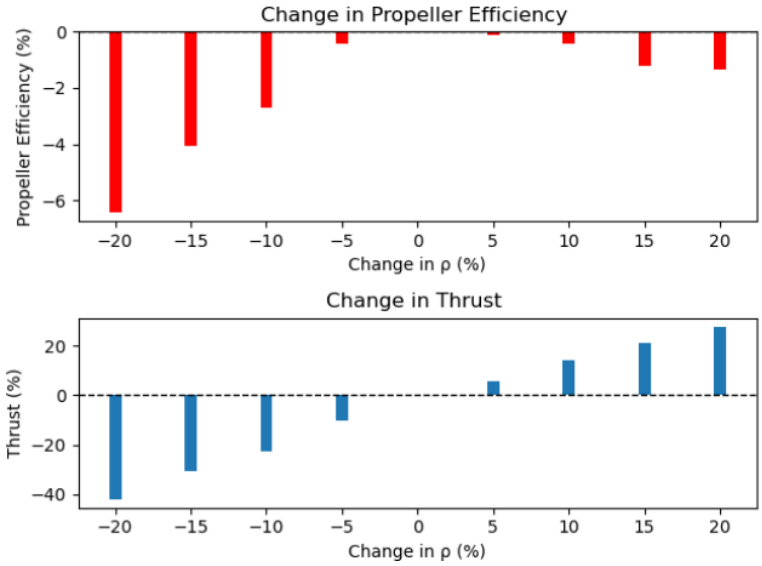

Figure 6.5: Relative Change in η_{prpl} (red) and Available Thrust (blue) for Change in Air Density

The change in air density negatively affects the propeller efficiency. The change is rather small (-6% for a change of density of -20%), therefore it is assumed that the effect of air density on efficiency is negligible. Furthermore, as expected, the available thrust is highly affected by a change in air density (-40% for a change of density of -20%). For a reduction of 40 %, the maximum thrust becomes 103.5 N still higher than the 101 N drag. The conclusions drawn are that a careful measurement of density shall be done with either instruments on board or using advanced meteorological models, fed by remote measurement, to then determine the correct propeller rotational speed needed to generate the required thrust.

Wind speeds: In the stratosphere, winds are less strong than in the troposphere but can still reach 20 m/s [8]. The wind speed increases the drag, as the relative velocity (for headwind) between the flow and the object is bigger. Using Equation 6.14 [9], it is possible to determine the drag in case of headwind.

$$D_{wind} = \frac{1}{2}\rho(V_\infty + V_{wind})^2 S_w C_D \tag{6.14}$$

[7] https://plettenbergmotors.com/product/nova-10-en/
[8] https://www.omc-stepperonline.com/tg-series-60mm-5-1-planetary-gearbox-backlash-10-arc-min-for-servo-motors-tg60-g5
[9] https://x-engineer.org/aerodynamic-drag/

where V_{wind} is the absolute value of headwind. Using the drag coefficient and surface from chapter 4 and chapter 3, the new drag is 294.5 N higher than the maximum thrust (172.5 N) found in section 6.2. To match the wind drag, it is possible to increase the number of blades or propellers. A four-blade per propeller design rotating at 29 rps would work. Four propellers with two blades rotating at 30 rps would also match the drag. With the current design, the maximum tolerable wind speed is 8.63 m/s. Such value is tolerable as the average of winds at 20 km is around 9 m/s [8]. On top of that, HAPS loiter in circles most of the time and therefore, they almost never have a headwind.

Number of Blades: In literature, it was found that increasing the number of blades per propeller would lower the efficiency [96]. This was checked for the considered application by increasing B from 2 to 6. The result is surprising and shows that with increasing blade number efficiency stays almost the same (B=3, $\frac{\Delta\eta_{prpl}}{\eta_{prpl}}$ = -0.1 %; B=4, $\frac{\Delta\eta_{prpl}}{\eta_{prpl}}$ = -0.1 %; B=5, $\frac{\Delta\eta_{prpl}}{\eta_{prpl}}$ = -0.1 %; B=6, $\frac{\Delta\eta_{prpl}}{\eta_{prpl}}$ = -0.2 %). One may think that the optimal rotational speed increases as well. However, this is not the case and stays exactly at 26.24 rps (the same value as the design). Logically, the blade diameter decreases significantly (-71% for 6 blades). This model does not take into account the wake interference of the blades between each other which causes a decrease in efficiency. However, if wake interference is negligible then this result is interesting as it would ease ground operations by reducing the required ground clearance.

Mass Variation: The mass estimate was done by summing the individual subsystem masses. However, the mass estimation may contain errors since the detailed design is not done. An example of one such missing detail is that the length of the required cable is not known. Furthermore, when the mass increases the required lift increases hence the drag since the $\frac{L}{D}$ ratio is constant. Therefore, if the mass is increased by X%, the lift will need to be increased by X% and the drag (and thrust required) will increase by X%. The maximum thrust, hence maximum tolerable drag, that the current design can deliver is 172.5 N. The current drag with the estimated mass is 101 N. The drag can increase by 71 %. Consequently, the mass can be increased by 71 %.

In this section, it was shown that the design can resist a mass increase of 71%, a density decrease of 20 % and a headwind of 8.6 m/s.

6.7. Summary and Recommendations

The goal of this chapter was to maximise the total efficiency of the propulsion system while respecting the requirements generated in section 6.1. Since the components are in series the total propulsive efficiency is given by Equation 6.15 [41].

$$\eta_{prop} = \eta_{prpl}\eta_{grb}\eta_{motor}\eta_{ESC} \tag{6.15}$$

A look back at Figure 6.1 shows that all identified components have been designed, concluding the propulsion system design.
The most important design characteristics along with the mass and cost budgets are shown in Table 6.9. Note that the cost of the ESC and Motor was not provided by the company but components with the similar properties (eg. peak power, burst current, etc..) were used to estimate the price.

Table 6.9: Final Design of Propulsive Sub-System

(a) Relevant Characteristics

Variable	Value
Max Thrust (25 km)	172.5 N
η_{prop}	0.77
Propeller Diameter	2.29 m

(b) Mass Budget

Component	Mass [kg]	%
Propellers	1.36 [5]	15.65
Gearboxes	1.88 [4]	21.63
Motors	4.4 [6]	50.63
ESCs	1.05 [7]	12.08
Total	**8.69**	**100**

(c) Cost Budget

Component	Cost [€] FY24	%
Propellers	80,000 [1]	94.87
Gearboxes	100 [4]	0.12
Motors	3276[2]	3.88
ESCs	952 [3]	1.13
Total	**84328**	**100**

Throughout the design process assumptions had to be made to simplify reality to an allowable extent. Hence, some limitations and recommendations for future design are presented:

[1] See section 12.2
[2] https://www.kit-elec-shop.com/gb/synchronous-motors/4177-synchronous-motor-10kw-golden-motor-liquid-cooling.html
[3] https://wetronic.nl/hobbywing-HW30203101-platinum-pro-260-hv-v5-esc_nl
[4] https://www.omc-stepperonline.com/fr/reducteur-planetaire-serie-tg-60mm-5-1-contrecoup-10-arc-min-pour-servomoteurs-tg60-g5
[5] See section 6.2
[6] https://plettenbergmotors.com/product/nova-10-en/
[7] https://plettenbergmotors.com/product/mst-60-260-en/

- **XFLR5:** The performance of the airfoil was computed using XFLR 5 as this software was taught in the Bachelor and met the limited time available requirement of the project. However, the program struggles to simulate viscous effect that are present at low Re numbers. This leads to significant difference in lift and poor simulation of flow separation [51]. More accurate airfoil performance can be determined with advanced Computational Fluid Dynamic (CFD) software as the one used in Liu and He [96]. Such analysis would yield better results but longer process time. Experimental data could also be used thanks to wind tunnel experiments. This method would however be more costly and take longer.
- **Twist and Chord:** The span-wise distribution of the chord and twist used in this design was taken from Dahal et al. [10]. It was deemed a reasonable choice overall as this shape was optimised for stratospheric used and led to a high propeller efficiency. However, the optimisation was done for a different airfoil than the one used in this report. Further investigation could be about developing an optimiser algorithm being able to find the optimal shape of the blades. Particle swarm optimisation is a suitable candidate.
- **Design Process:** In the presented design process, all components were considered separately. The best design choice for all components was chosen. However, to further improve the propulsive efficiency, the design choices that created the best synergy between the components should be used. Such work is complicated and requires global optimisation algorithms taking into account the propeller, motor, gearbox and ESC selection as a whole. Wall [142] developed such an algorithm in his PhD thesis demonstrating the amount of work it requires. A concrete example of that would be to choose a motor will a lower efficiency but lower rotational speed. Therefore, the reduction ratio is lower increasing the gearbox efficiency and potentially the entire propulsive efficiency.

7. Power

This chapter focuses on the design and optimisation of the power subsystem for the Eurus platform. We start by outlining the critical requirements and constraints that ensure the platform can consistently deliver power to its various subsystems in Section 7.1. Next, in Section 7.2 we provide an in-depth analysis of the electrical system. After which the solar panel design and battery configuration, in Section 7.3 and Section 7.4 respectively. A sensitivity analysis is performed in Section 7.5 to assess the robustness of the power subsystem. In Section 7.6, we summarise the key findings and recommendations to guide future improvements and practical implementation.

7.1. Requirements

In order to provide a frame for the design of the power subsystem, the power subsystem requirements are extended and restated as can be seen in Table 7.1.

Table 7.1: Overview of Power Subsystem Requirements

Power		
ID	**Requirement**	**Derived from**
REQ-TEC-PW-1	The platform shall be capable of delivering the required power to LCT.	Section 1.3
REQ-TEC-PW-2	The platform shall be capable of delivering the required power to the propulsion system.	Section 1.3
REQ-TEC-PW-3	The platform shall be capable of delivering the required power to the sensing system.	Section 1.3
REQ-TEC-PW-4	The platform shall be capable of generating power to an energy storage system from the operating environment equal to that of the drawn power at mission end-of-life.	Section 1.3
REQ-TEC-PW-5	The platform shall be capable of enduring intermittent periods where no power generation is possible.	Section 1.3
REQ-PW-1	The platform shall be capable of delivering the required power to the CDHS subsystem.	Identification of added subsystem
REQ-PW-2	The platform shall be capable of delivering the required power to the communications subsystem.	Identification of added subsystem
REQ-PW-3	The platform shall be capable of delivering the required power to the actuator subsystem.	Identification of added subsystem
REQ-PW-4	The platform shall be capable of reaching 45°N and 45°S throughout the entire year.	Exceed performance of other HAPS vehicles
REQ-PW-5	The platform shall be capable of launching to the minimum operational altitude of 15 km with the use of battery capacity.	Chapter 3

7.2. Electrical System Overview

Before starting the sizing of the power system components, an overview of the system has to be created.

7.2.1. Electrical Block Diagram

To provide an overview of all systems that use and produce power, the electrical block diagram has been created and is shown in Figure 7.1. This provides an overview of all the components in the HAPS vehicle that require power throughout the mission. Two electrical harnesses will be used to ensure each component receives the correct voltage.

In here, it can be seen that use will be made of two low voltage power lines, 12V and 30V. To accommodate this, a step-down voltage converter is required. This has been chosen in order to minimise the size of this converter.

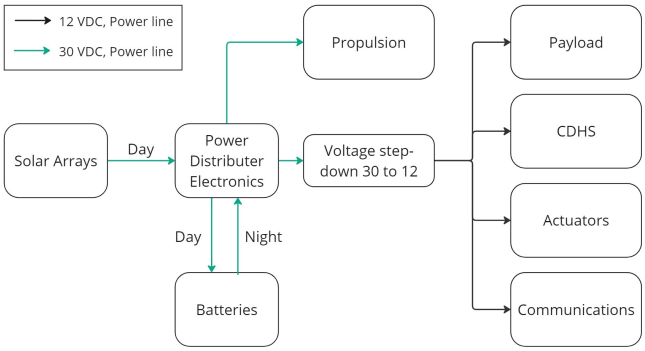

Figure 7.1: Electrical Block Diagram.

7.2.2. Energy Management

Throughout the day and night, the system should maintain an energy equilibrium. This means that the energy produced by the solar arrays during the day should be sufficient to charge the batteries and provide power to all other subsystems, the batteries will then provide the necessary energy during the night which contains a powered descent and a cruise at 15 km altitude as mentioned in Chapter 3. The equilibrium equation is shown in Equation (7.1).

$$P_{elec,climb}t_{climb} + \frac{1}{\eta_{battery}}(P_{elec,cruise}t_{cr} + P_{elec,descent}t_{descent}) = \frac{I_{max}t_{day}}{\pi/2}A_{solar}\eta_{cells}\eta_{camber}\eta_{mppt} \tag{7.1}$$

where $P_{elec,climb}$, $P_{elec,cruise}$ and $P_{elec,descent}$ are the required electrical power by all the subsystems in climb, cruise and descent respectively. The A_{solar} is the solar area, I_{max} is the maximum solar intensity, t_{day} is the duration of the day, t_{climb} is the duration of the climb, t_{cr} is the duration of the cruise, $t_{descent}$ is the duration of the descent and $\eta_{battery}, \eta_{cells}, \eta_{camber}, \eta_{mppt}$ are the efficiencies of the battery, solar cells, camber geometry, and Maximum Power Point Tracking (MPPT), respectively. The $\pi/2$ term originates from an assumption that will be explained in Section 7.3.1. Equation (7.1) originates from an approach taken by A. Noth [112].

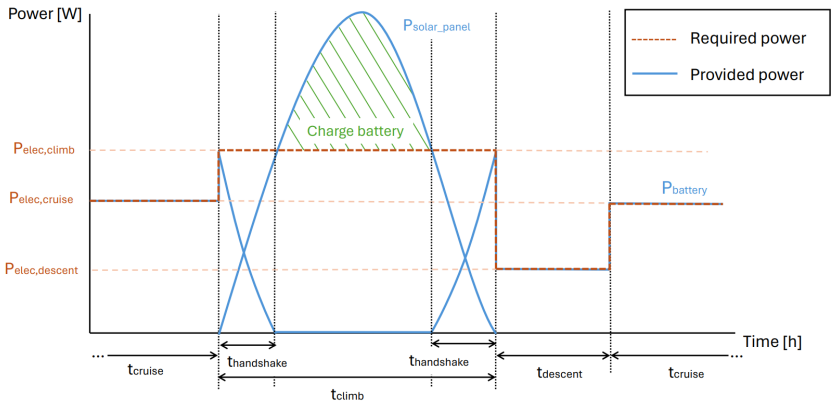

Figure 7.2: Energy Equilibrium Depiction.

This equilibrium equation can be graphically depicted in Figure 7.2. In this figure, one can clearly see the correlation between the battery and solar panel power as well as the required power during the day and night. In this figure $t_{handshake}$ is the duration where the batteries supply additional power to the solar panels in order to meet the required power during the day.

Efficiencies

In order to perform the analysis, attention should be given to the efficiencies of all the components associated with the system. Energy losses, aside from direct consumption, significantly impact the total energy that the

solar panels need to generate. Below is an overview of all the involved efficiencies along with their reasoning.

Type	Symbol	Value	Reasoning
Battery	$\eta_{battery}$	0.64	Will be obtained from the chosen battery in Section 7.4
Camber	η_{camber}	0.9	Originates from the change of incidence angle due to the curvature of the airfoil [112]
Solar cells	η_{cells}		Will be obtained from the chosen solar cell in Section 7.3.2
MPPT	η_{mppt}	0.95	Obtained in Section 7.3.3
Cabling	$\eta_{cabling}$	0.99	Acknowledgement of possible losses due to cabling
ESC	η_{ESC}	1	Obtained from Section 6.4
Motor	η_{motor}	0.885	Obtained from Section 6.3
Gear box	η_{grb}	0.96	Obtained from Section 6.5
Propeller	η_{prpl}	0.91	Obtained from Section 6.2

These efficiencies can be implemented in the electrical system diagram, thereby creating an electrical efficiency diagram as can be seen in Figure 7.3. The actuator, communications, CDHS and payload have no specific efficiencies associated with them since it is assumed that the losses in the systems are included in the required electrical power of the respective subsystems.

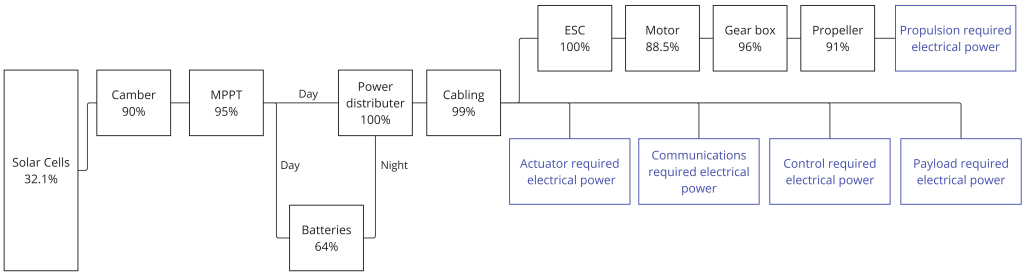

Figure 7.3: Efficiency Block Diagram

7.2.3. Power and Energy Budget

It is important to have an overview of the power and energy consumption of all components during the mission. Therefore, Table 7.2 presents the power budget, showing all the subsystems illustrated in Figure 7.1. The power consumption is based on the limiting operational mode, winter solstice at 45° latitude. To ensure safety, an extra margin of 10% has been added to account for any discrepancies between the expected and actual consumption. The efficiencies presented in Figure 7.3 are not incorporated: the table presents the electrical power required at the final layer of the diagram.

Table 7.2: Power Budget and Total Energy for the Various Modes of Operation

Required Electrical Power	**Take off**		**Nominal mode**		**Landing**
		Climb	**Descent**	**Cruise @ 15 km**	
Duration (h):	4.75	6.91	3.96	13.13	17.84
Subsystem	**Power (W)**	**Power (W)**	**Power (W)**	**Power (W)**	**Power (W)**
Actuators	10	10	10	10	10
Payload	180	180	180	180	180
Propulsion	2571.47	2571.47	0	976.85	0
Communications	15.9	15.9	15.9	15.9	15.9
CDHS	27.1	27.1	27.1	27.1	27.1
Total Required Power (W)	**3078.3**	**3078.3**	**249.7**	**1324.23**	**249.7**
Total Energy (kWh)	**14.62**	**21.27**	**0.99**	**17.39**	**4.45**

7.3. Solar Panel Design

To perform the sizing of the solar panels, use has been made of a Python model which will, using components explained in this subsection, provide the outcome of the solar panel design. An effort has been made from this, to ensure that the iterative process can be done with the highest efficiency.

7.3.1. Modelling Solar Effects

In order to design the solar panel, the solar effects have to be analysed.

Solar Irradiance

Solar irradiance is the amount of solar power per unit area produced by the sun that is received at the HAPS. Direct irradiance is the primary source of solar energy, although diffuse and reflected irradiance can also contribute. Reflected irradiance largely depends on the Earth's albedo, but due to the difficulty in accurately predicting albedo, its contribution has been excluded from this analysis. Furthermore, to harness this type of solar power, panels must be placed on the downward-facing side of the vehicle, which will not be investigated. Therefore, the effect of reflected irradiance is not considered.

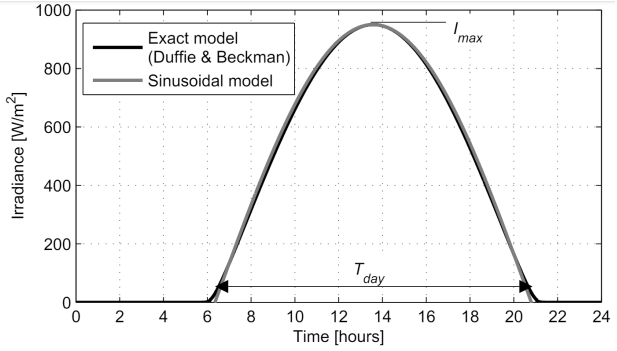

Figure 7.4: Sinusoidal Approximation of Irradiance Throughout One Day [112]

Operating in the stratosphere, the HAPS encounters minimal atmospheric interference. Due to the very low levels of aerosols and water vapour, scattering is negligible. According to a model by Q. Dai and X. Fang [49], diffuse irradiance alters total irradiance by only 0.75% at the HAPS's operating altitude, which is insignificant and thus can be neglected. For the same reason, the solar constant I_{sc}, the standard solar constant at zero air mass, can be assumed to be equal to the $1366 W/m^2$. Also, only the horizontal placement of the solar panels is considered for three reasons. Firstly, the incidence angle between the sun and the vertical surface depends heavily on the direction in which the HAPS is flying and therefore is an unreliable design case. Secondly, in comparison to the horizontal surface, the vertical surface is small, therefor neglecting the vertical surface has a limited effect. Lastly, the vertical surface will mainly be effective when the sun elevation angle is low, where the solar irradiance is lower compared to high sun elevation, as can be seen in Figure 7.4, making them less effective in generating energy.

For further simplicity, the irradiance throughout the day is approximated by a sinusoidal function, as illustrated in Figure 7.4. Which will be used to estimate the amount of energy that is received based on the maximum solar intensity I_{max}.

Maximum Solar Intensity

To find the maximum solar intensity, the Equation (7.2) has been used [88].

$$I_{max} = I_{sc}\left(1 + 0.033\cos\left(\frac{360d}{365}\right)\right) \cdot (\sin(Lat)\sin(\delta) + \cos(Lat)\cos(\delta)) \tag{7.2}$$

Where $I_{sc} = 1366 W/m^2$ is the standard solar constant at zero air mass, δ is the solar declination angle, Lat is the latitude and d is the day of the year. The solar declination angle can be found by using Equation (7.3)[88]:

$$\delta = 0.4093\sin\left(\frac{2\pi(d - 79.75}{365}\right) \tag{7.3}$$

Using Equation (7.2) and Equation (7.3), one can model the maximum solar intensity based on the latitude and the day of the year. From this model, it is evident that during the summer and winter solstices, the maximum solar intensity is limited in the northern and southern latitudes, respectively. This limitation indicates that the operational range of the HAPS will be restricted by the latitude and day of the year.

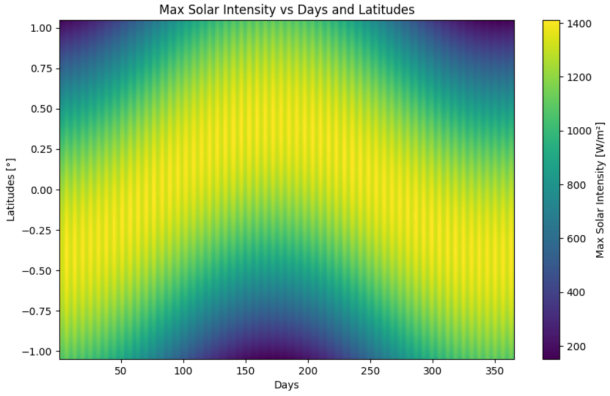

Figure 7.5: Maximum Solar Intensity as a Function of Latitude and Day on the HAPS's Operational Altitude.

Duration of the Day

In order to determine how long the HAPS will experience light, the height, latitude and day in the year should be known. Equation (7.4) can be used to find the amount of daylight in one day [84].

$$T_{day}(Lat, d) = 24\left[1 - \frac{1}{\pi}\arccos(\tan(Lat)\frac{\sin(\epsilon_{obl})\sin(\phi_{sun})}{\sqrt{1-\sin^2(\epsilon_{obl})\sin^2(\phi_{sun})}}\right] \tag{7.4}$$

Where T_{day} is the duration of the day, d is the day in year, ϵ_{obl} is the angle of obliquity which is the axial tilt of the Earth compared to the Sun, and ϕ_{sun} is the azimuth angle of the sun, which can be determined using the following:

$$\phi_{sun}(d) = -1.3411 + M_{anom}(d) + 0.0334 * \sin(M_{anom}(d)) + 0.0003\sin(2M_{anom}(d))$$

where $M_{anom}(d)$ is the mean anomaly of the sun, given by:

$$M_{anom}(d) = -0.041 + 0.017202d$$

7.3.2. Solar Cell Selection

To select the appropriate type of solar cell, extensive studies have been conducted to explore various options available, keeping in mind the rapid advances in solar cell technology [9].

In the aerospace industry, InGaP/InGaAs/Ge triple-junction solar cells and AlInGaP/AlInGaAs/InGaAs/Ge four-junction solar cells, produced by companies such as Azur Space [1], Spectrolab [2] and CESI [3], have become the standard [15]. These cells are favoured for their superior performance compared to other photovoltaic technologies. However, they are generally rigid, heavy, and thick, which limits their application in certain scenarios. It should be noted that thin-film options are researched [20] [15] [9].

Researchers are also interested in Cu(In,Ga)Se2 (CIGS), CdTe and Perovskite solar cells, which show great promise for this application [9][17]. These thin-film solar cells offer advantages such as natural resilience to radiation [56], performance in low temperature and the potential for low-cost production [12]. Additionally, their flexibility makes them suitable for use on curved surfaces. The advances in their performance are increasing significantly. Among these, Perovskite solar cells stand out for their promising performance, however, their operational stability remains a significant challenge [21] [22]. The main disadvantage of these solar cells is the lack of production, companies like Tandem PV [4] and Swift Solar [5] are developing these types of solar cells however they are not commercially available yet. This rapid technological progress has extensively been researched and documented by The National Renewable Energy Laboratory [6].

After investigating the available solar panel technologies, it is time to identify suitable solar cells for the HAPS. Given the high operating altitudes, radiation hardness is a critical consideration. Additionally, the weight of the solar panels must be taken into account. However, the most crucial factor is efficiency, as the amount of energy generated from the available sunlight directly impacts the operational latitudes. The placement of the solar panels on the wings allows for bending relief, making weight less of a concern during the selection process. Operating temperatures at these altitudes can be as low as -60°C, as can be seen inchapter 8. These cold conditions must also be considered.

This combination of factors led to the investigation of III-V multijunction panels produced by the aforementioned companies. According to private conversations with manufacturers, these panels can be placed on curved surfaces if small solar cells are used, particularly the TJ 3G30C model. In addition to these, more sheet-like solar panels produced by Microlink and Sharp were examined.

To ensure confidence in the chosen solar panel, a trade-off analysis was conducted between five possible solar cell types. The panels were evaluated based on four criteria: efficiency, area density, relative cost, and flexibility. Efficiency was given a weight of 60%, as the generated energy is crucial for defining the operating latitudes of the HAPS. Area density was assigned a weight of 10%, recognizing its importance but also considering its potential for providing bending relief. Relative cost, weighted at 10%, was considered important but not the most critical factor due to the functionality of the subsystem. The costs were compared relative to other options, taking into account the design's influence on cost. Lastly, flexibility, with a weight of 20%, was important because the solar panels need to be placed on highly curved surfaces, making some panel types more suitable than others. The trade-off criteria, their weights, and the weighing definitions are summarized in Table 7.3.

[1]URL: https://www.azurspace.com/index.php/en/ [Accessed on 8-06]
[2]URL: https://www.spectrolab.com/index.html [Accessed on 8-06]
[3]URL: https://www.cesi.it/space-solar-cells/[Accessed on 8-06]
[4]URL: https://www.tandempv.com/ [Accessed on 8-06]
[5]URL: https://www.swiftsolar.com/tech/ [Accessed on 8-06]
[6]URL: https://www.nrel.gov/pv/cell-efficiency.html [Accessed on 8-06]

Table 7.3: Solar Cell Trade-off Criteria

Criteria	1: Poor	2: Moderate	3: Nominal	4: Good	5: Excellent
Efficiency [%] (60%)	<22	22 - 24	25 - 27	28 - 30	>30
Area density [g/m2] (10%)	>1000	1000 - 801	800 - 601	600 - 401	<400
Relative cost (10%)	Extremely high	High	Moderate	Low	Extremely low
Flexibility (20%)	Extremely bad	Bad	Moderate	Good	Extremely good

Table 7.4: Performance of Each Solar Cell

	TJ 3G30C[1]	UTJ Spectrolab[2]	TJ CTJ30[3]	ZTJ	Microlink[4]	Sharp TJ[5]
Efficiency [%]	29.7	28	29.5	29.5	27	32.1
Area density [g/m^2]	1300	840	850	840	250	280
Relative cost	High	High	High	High	Low	Low
Flexibility	Good	Bad	Bad	Bad	Extremely good	Extremely good

From research, information can be found on all solar cell types. These have been summarized in Table 7.4. With the definition of the trade-off criteria, their weights and all specifications of the solar cells the selection can be done, as in Table 7.5.

Table 7.5: Solar Cell Trade-off Results

	TJ 3G30C	UTJ Spectrolab	TJ CTJ30	ZTJ	Microlink	Sharp TJ
Efficiency [%]	4	4	4	4	3	5
Area density [g/m2]	1	2	2	2	5	5
Relative cost	2	2	2	2	4	4
Flexibility	4	2	2	2	5	5
Weighted Average	3.5	3.2	3.2	3.2	3.7	**4.9**

From this trade-off, it can be concluded that the Sharp Triple Junction solar sheet is the most suitable solar cell for the mission. Therefore this solar cell has been chosen. In private conversations, Sharp ensured that it was possible to produce this solar panel for the HAPS application. For further information a non-disclosure agreement had to be signed, which has not been done. Some research on this panel has been provided by Sharp [79].

7.3.3. Max Power Point Tracking (MPPT)

For the selected solar cells, implementing an efficient MPPT system is essential to maximise energy harvest. MPPT is a technology used in photovoltaic systems to optimise the power output by continuously adjusting the electrical operating point of the modules. By doing so, the MPPT system ensures that the solar panels operate at their optimal power point regardless of varying environmental conditions such as temperature and irradiance.

The efficiency of the MPPT system plays a crucial role in the overall energy conversion process. For the chosen solar cells, the MPPT system operates with an efficiency of 95% [57] [55]. This high efficiency ensures that almost all the energy generated by the solar panels is effectively converted and utilised, thereby significantly enhancing the overall performance.

7.3.4. Solar Panel Results

Using the information gathered in Section 7.2 and Section 7.3.1 to Section 7.3.3, a model has been made to size the solar panels. Giving the geometry of the vehicle, the possible placement of solar panels, the efficiencies of the components and the solar effects. In this calculation, it is assumed that 90% of the total horizontal surface can be used for the placement of the solar cells [112], this is a result of the presence of actuators and other surfaces which are unsuitable for panel placement. Resulting in a total effective solar panel area of $99m^2$.

[1]URL: https://www.azurspace.com/images/products/0003422-02-02_DB_3G30C.pdf [Accessed on 10-06]
[2]URL: https://www.spectrolab.com/DataSheets/TNJCell/utj3.pdf [Accessed on 10-06]
[3]URL: https://www.cesi.it/app/uploads/2020/03/Datasheet-CTJ30-1.pdf [Accessed on 10-06]
[4]URL: https://www.rocketlabusa.com/assets/Uploads/RL-SolAero-Data-Sheet-ZTJ.pdf [Accessed on 10-06]
[5]URL: https://www.mldevices.co.uk/high-efficiency-flexible-solar-sheets/ [Accessed on 12-06]
[6]URL: https://global.sharp/solar/en/high-efficiency/pdf/datasheet_atmospheric-solar-module.pdf [Accessed on 12-06]

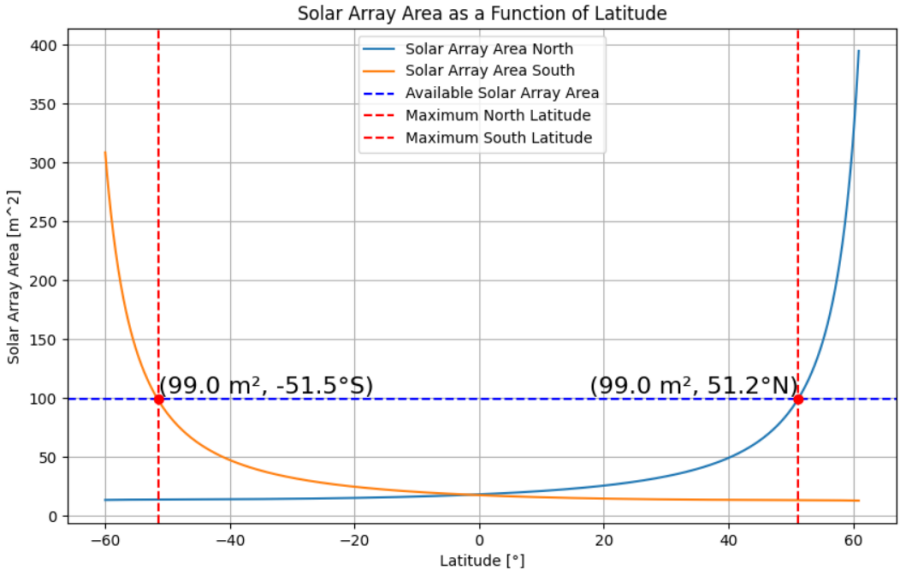

Figure 7.6: Relation Between Required Solar Panel Area and Maximum Latitude Range

A relation between the solar panel area and the operation latitude range throughout the entire year can be found, keeping the limiting summer and winter solstice in mind, which can be seen in Figure 7.6. From this, it can be concluded that the maximum north and south latitudes in which the HAPS can operate throughout the entire year are 51.2 and 51.5 degrees respectively. This 3-degree difference originates from the obliquity of the earth, which is the tilted orientation of the earth with respect to the sun.

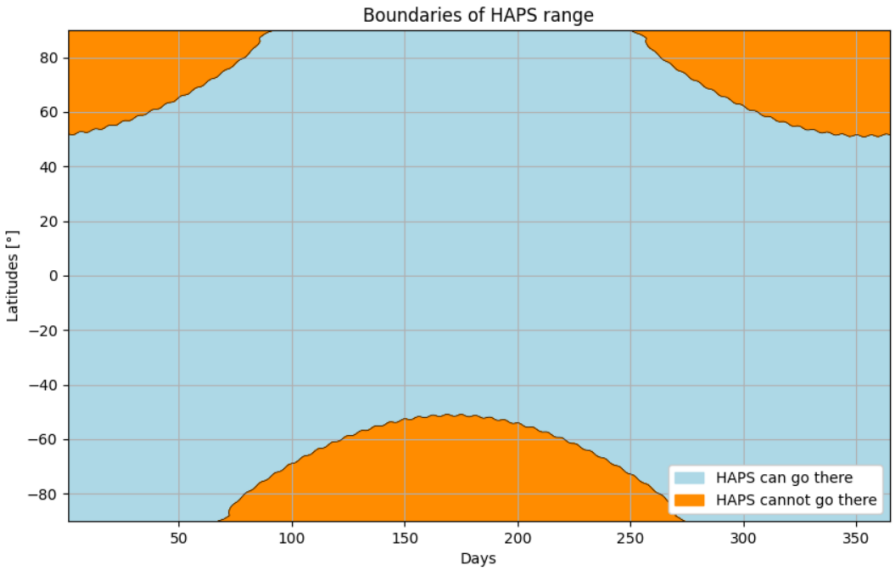

Figure 7.7: Operational Bound of HAPS Depending on Latitude and Day of Year

However, this does not preclude the possibility of operating at greater latitudes depending on the time of year. This is depicted in Figure 7.7, showing that the HAPS can travel further north during the summer solstice and further south during the winter solstice.

These operational ranges greatly exceed the requirements set in REQ-PW-4. This extension accommodates the client's interest in increasing the vehicle's operating range, ensuring a wider area where the vehicle can perform its mission and generate revenue.

Cost Budget

Sharp does not provide the cost of their solar panels, but an estimation can be made based on expert information. According to M. O. Reese [17], a solar panel expert at the National Renewable Energy Laboratory, the cost of solar panels ranges from $10 to $100 per watt. Using the conservative end of this estimate, the solar panel cost is approximately € 307,800 (FY24) using a 0.93 €/$ conversion rate. Table 7.6 summarises the design of the solar panel.

Table 7.6: Solar Panel Design

Characteristic	Value
Solar Panel Type	Sharp Triple Junction
Solar Panel Mass	$27.72kg$
Solar Panel Area	$99m^2$
Solar Cell Efficiency	0.321
Solar Panel Cost	€307,800 (FY24)
Maximum North Latitude	51.2°
Maximum South Latitude	51.5°

7.4. Battery Design

In this section, the Battery Energy Storage System (BESS) for the HAPS platform will be designed. Before delving into battery specifications, it is crucial to consider the operational modes of the HAPS platform and the associated battery capacity. These modes will help identify the most demanding scenarios that the system must accommodate. The design process begins with obtaining the required battery capacity, after which various modern BESS types will be evaluated and their suitability will be compared.

7.4.1. Required Battery Capacity

Given the solar panel design from Section 7.3 ensures sufficient energy capture to power the HAPS during nominal operations, the primary focus here will be on determining the battery capacity needed to store energy which is required during the night. As discussed in Section 7.2.3, the energy consumption of the HAPS platform is primarily influenced by its flight modes: climb, cruise, and descent. This energy demand is closely tied to the energy management system, as illustrated in Figure 7.2. Apart from these nominal operations, take-off must be considered according to REQ-PW-5, as it could impact battery sizing.

Before the required energy storage for the BESS can be calculated an additional consideration needs to be fleshed out: the handshake protocol between the solar array and the batteries. The amount of energy the batteries need to supply to accommodate this handshake can be calculated using Equation (7.5). In this equation, it has been assumed that the generated solar power P_{solar_panel} during this handshake period shows a linear increase and decrease.

$$E_{handshake} = 2 \cdot 0.5 t_{handshake} P_{elec\_cruise} \tag{7.5}$$

In this equation, $t_{handshake}$ represents the time during the day when the battery must provide power to ensure sufficient energy supply to the other subsystems. At the beginning and end of the day, the solar panels produce insufficient power for the other subsystems, and the battery must compensate for this shortfall. This is illustrated in Figure 7.2. Therefore, making use of Table 7.2 and Figure 7.3 and summing the handshake energy, the total energy required to be stored in the BESS is 25.5 kWh.

7.4.2. Battery Type Selection

To select the battery type to be used for the BESS, an overview is presented in Table 7.7. Table 7.7 shows that Lithium-Ion batteries are a clear favourite when optimizing for weight and size.

Table 7.7: Overview of BESS Types, Nazaralizadeh S. et al. [18]

Battery Type	Ni – Cd	Ni – MH	Zn – Br	Li	NaS	NaNiCl
Power Density (W/L)	80 – 600	250 – 1000	60 – 110	1500 – 10,000	140 – 300	150 – 270
Energy Density (Wh/kg)	60 – 150	40 – 80	65 – 75	200 – 400	140 – 300	160 – 275
Energy Efficiency	69 – 90%	75%	80%	80%	90%	95%
Life Cycle	2500	800 – 1200	200 – 400	10,000	5000	3000
Estimated Cost (USD /kWh)	400	100 – 500	170 – 580	200 – 1260	263 – 735	315 – 488

However, there are still several types of Lithium-ion batteries to choose from, as presented in Figure 7.8. Among these, Lithium Nickel Manganese Cobalt Oxide (NMC) and Lithium Nickel Aluminium Cobalt Oxide (NCA) are predominantly used in aerospace applications, however, NMC performs better when considering the cost and safety of sourcing the raw materials during manufacturing[7]. Contrasting this, both the Airbus' Zephyr S

[7] https://nanografi.com/blog/lithiumion-batteries-for-aerospace-applications/

and the BAE PHASA-35 made use high-energy Si/LCO batteries from Amprius[8][9]. Further comparison of LCO and NMC reveals that the former is indeed preferred for higher energy application[10]. With the knowledge that the Zephyr S stayed aloft for almost 24 days while making use of Amprius Technologies' SiMaxx™ batteries and another order was issued in 2024[11], they will be assumed to be trustworthy. They are therefore chosen to be used for the Eurus' design, more specifically their High Energy Design version boasting 500 Wh/Kg energy density and 1300 Wh/L volumetric energy density.

Chemical name	Material	Abbreviation	Notes
Lithium Cobalt Oxide[1]	$LiCoO_2$ (60% Co)	LCO	High capacity; for cell phone laptop, camera
Lithium Manganese Oxide[1]	$LiMn_2O_4$	LMO	Most safe; lower capacity than Li-cobalt but high specific power and long life. Power tools, e-bikes, EV, medical, hobbyist.
Lithium Iron Phosphate[1]	$LiFePO_4$	LFP	
Lithium Nickel Manganese Cobalt Oxide[1]	$LiNiMnCoO_2$ (10–20% Co)	NMC	
Lithium Nickel Cobalt Aluminum Oxide[1]	$LiNiCoAlO_2$ (9% Co)	NCA	Gaining importance in electric powertrain and grid storage
Lithium Titanate[2]	$Li_4Ti_5O_{12}$	LTO	

[1] Cathode material [2] Anode material

Figure 7.8: Overview of Potential Lithium-ion Battery Types for their BESS and their General Application[32]

7.4.3. Battery Results

Sizing the selected lithium-ion cobalt oxide from Amprius for the total required energy stored in the BESS as defined in Section 7.4.1 results in a BESS weight of 51 kg and 19.62 L. An overview of the BESS is presented in Table 7.8.

A bespoke order of batteries can likely be issued, however, assuming the standard size for a similar High Energy battery pack from Amprius that is 4.5 x 50 x 105 mm, 831 batteries would need to be ordered. This is easily fit inside the wing geometry. A final consideration is whether the BESS can charge sufficiently during the minimal daylight hours. As of current the battery's charging performance has been validated at C/10. Such that the battery requires 10 hours to fully charge and discharge for a single cycle, and inferring that maximum (dis)charge power would be 2550 W. While this duration might not seem problematic, the sinusoidal shape of the solar power generated will prove difficult to effectively transfer to the BESS.

A precise cost of the BESS cannot be accurately generated as Amprius does not make the prices of the products known. However, as Amprius' facilities are located in North America and are in high demand [12], the upper bound of the cost in Table 7.7 is used, totalling to k$32,13(FY24). Furthermore, considering the batteries are stated to have 200 cycles at nominal conditions, roughly equal to 6 months, it is assumed that these batteries will be replaced 19 times throughout the HAPS platform's nominal lifetime. This increases the total cost of the BESS during the mission lifetime to k$ 738.99 (FY24).

Based on this sizing, the batteries can store up to 25.5 kWh of energy when fully charged. This capacity ensures that the batteries can provide the necessary 14.62 kWh for takeoff, as detailed in Table 7.2. Following takeoff, the vehicle can cruise for 8.2 hours at an altitude of 15 km. This capability allows the HAPS vehicle to take off during nighttime conditions when solar power is unavailable, provided that the duration until daylight does not exceed 12.9 hours.

[8] https://amprius.com/amprius-silicon-nanowire-lithium-ion-batteries-power-airbus-zephyr-s-haps-solar-aircraft/
[9] https://evtechinsider.com/2024/04/14/amprius-completes-qualification-process-for-simaxx-mass-production-tool-ramping-up-manu
[10] https://amprius.com/wp-content/uploads/2023/02/Amprius_Technologies_10th_Annual_eVTOL-Symposium.pdf
[11] https://www.greencarcongress.com/2024/04/20240420-amprius.html
[12] https://amprius.com/amprius-completes-qualification-process-for-simaxx-mass-production-tool-ramping-up-manufacturing-capacit

Table 7.8: Overview of the BESS

Characteristic	Value
BESS Type	Amprius SIMAXXTM
BESS Mass	51 kg
BESS Volume	19.62 L
Nr. Battery Packs	831
BESS Cost	k$euro 738.99
BESS Efficiency @ EOL	64%
Nominal Nr. Cycles	200
Cost	$ 32,130

7.5. Sensitivity Analysis

In order to show confidence in the model, a sensitivity analysis has been performed.

Influence of the Efficiencies: As seen at the start of this section, there are a lot of efficiencies associated with the system. In this part of the sensitivity analysis, these efficiencies will be lowered until the design does not meet the requirements. In this table, the propulsion efficiency is the product of the ESC, motor, gearbox and propeller efficiency.

Table 7.9: Sensitivity Analysis on the Efficiencies

Type	Real value	Minimum value	Change [%]
Solar Panel Efficiency	0.321	0.207	-35.51
Battery Efficiency	0.64	0.31	-51.56
Camber Efficiency	0.9	0.58	-35.56
MPPT Efficiency	0.95	0.615	-35.26
Propulsion Efficiency	0.773136	0.495	-35.98

Influence of Irradiation Absorption: As has been elaborated on before, it has been assumed that the zero mass solar constant, I_{sc}, is $1366 W/m^2$. This received irradiance can be, according to the performed sensitivity analysis, as low as $880 W/m^2$, without changing the design. In this case, REQ-PW-4, will also still be met. For reference, on sea level solar irradiance of $1000 W/m^2$ can be received on a sunny summer day [102].

Influence of Solar Panel Coverage and Shading: As mentioned previously, it has been assumed that 90 % of the total horizontal surface on the wing and tail can be covered with solar panels. Changing this variable, it can be found that this can be as low as 56 %. One can also imagine that the geometry of the vehicle influences the light that reaches the vehicle. This could cause an area of shade which, as can be seen, will realistically be no more than obtainable coverage.

Influence of Required Electrical Power: The required electrical power of all subsystems, as can be seen in Table 7.2, can be changed. From this, it can be found that the subsystems that use power continuously throughout the day, which are the CDHS, actuator, communications and payload, can accumulatively use $600 W$ of additional power.

Influence of Battery Performance: As previously discussed, the battery efficiency can be as low as 31%, resulting in significant energy losses. However, the solar panels are designed to generate sufficient energy to compensate for these losses. Despite this, the reduced efficiency limits the operational latitudes of the HAPS. Nonetheless, the vehicle still complies with the REQ-PW-4 requirement.

7.6. Summary and Recommendations

This section will provide a summary of what has been discussed in the previous sections.

Design Overview and Performance

The solar panels are a critical component, designed using Sharp Triple Junction solar cells due to their high efficiency (32.1%) and flexibility. The total effective area for the solar panels is calculated to be $99 m^2$, ensuring sufficient energy capture to power the HAPS during daylight operations. The panels are designed to operate efficiently up to latitudes of 51.2° North and 51.5° South, accommodating the seasonal variations in solar irradiance.

The BESS is designed to store energy during the day, enabling continuous operation during the night. As shown in Section 7.4.3 the lithium cobalt oxide BESS was sized such that it could sustain all onboard systems, in the operating condition, for the full duration of the eclipse during winter solstice at 45° latitude, as well as perform

the handshake with the solar array. However, an effective BESS charge and discharge protocol remains outside the scope of this system design.

The overall design ensured that all requirements from Table 7.1 were met. The sensitivity analysis showed confidence in the model, having a lot of room for any discrepancies between expected and real values for efficiencies, solar irradiance, panel coverage, required powers and battery performance.

The importance of the handshake protocol between the solar array and the batteries has been investigated, as shown in Figure 7.2. This protocol ensures a smooth transition of power during sunrise and sunset, preventing any power interruptions. The total energy required for this handshake is calculated to be approximately 2.987 kWh.

Interface

It has been demonstrated that the power subsystem is highly dependent on other subsystems, as illustrated in the electrical block diagram shown in Figure 7.1. Consequently, the design process required numerous iterations due to the fluctuating values from these interdependent subsystems.

Sustainability

As demonstrated, the production of solar panels and batteries involves the use of rare materials such as lithium and various metals. The extraction of these materials is challenging and frequently conducted in unsustainable ways. Additionally, it is important to acknowledge that the batteries will require replacement over the lifespan of the vehicle.

Limitations and Recommendations

During the design process, several assumptions were made and subsequently validated, particularly through sensitivity analysis, demonstrating the design's robustness against varying parameters. However, there are areas for potential improvement:

Irradiance: The current design only considers direct irradiance. It is recommended to also account for reflected and diffuse irradiance. Additionally, placing solar panels on downward and sideward-facing surfaces could increase power generation. A trade-off analysis should be conducted to ensure that the added weight does not outweigh the benefits of the additional power generated.

Connections: Limited consideration was given to power distributors and the current and voltage regulators within the system. This oversight could lead to issues if not addressed. Therefore, it is recommended to conduct a thorough review and optimisation of these components.

Battery Sustainability: Due to battery degradation, replacements will be necessary over the vehicle's lifespan. More extensive research into alternative, more sustainable battery solutions is recommended to improve overall sustainability.

8. Thermal Design and Analysis

The HAPS will be operating in low-temperature conditions [1], where heat will be dissipated into the atmosphere. Therefore, the platform and its subsystems will be subject to significant heat losses unless properly insulated. Furthermore, as many components have minimum operational and storage temperatures below the ambient free stream air temperature that need to be accommodated, the thermal design of the HAPS platform is of significant importance. It is therefore the purpose of this chapter to determine if the HAPS platform shows viable operation within its mission profile. The thermal model identifies several inputs that are taken from Chapter 7 (solar array area), Chapter 9 (spar sizes) and Chapter 4 (wing sizes).

Due to project schedule constraints, the thermal analysis will only be directed at the wing system. The sections following will expand on the methods used for the analysis, presenting the results of the simulations and finally generating conclusions and recommendations for the thermal system of the HAPS platform.

8.1. Requirements

For the thermal system 2 new requirements were derived from REQ-TEC-STR-1.1 throughout its design, shown in Table 8.1. These requirements stem from the analysis of the minimum temperatures for elements inside the wing system.

Table 8.1: Thermal Sub-system Requirements

Code	Description	Derived from

[1] https://www.noaa.gov/jetstream/atmosphere/layers-of-atmosphere

Thermal Requirements		
Structures		
REQ-TEC-STR-1.1	There shall be a structure to provide thermal insulation for internal systems.	-
REQ-THL-1	The thermal subsystem shall keep the energy storage system above -20° throughout the mission lifetime	REQ-TEC-STR-1.1
REQ-THL-2	The thermal subsystem shall direct dissipated heat from the solar arrays to the energy storage system	REQ-TEC-STR-1.1

8.2. Method

In this section, a thermal model is demonstrated for the wing system analysing it for day and night time conditions at an altitude of 25km. The approach for this thermal analysis is similar to the approach by Ortega, Zimmer and Weber [114]. Before the model can be created in the Simulink environment within Matlab, the heat sources need to be identified. Starting with defining these heat sources at the perimeter of the wing system, the wing surface:

- Solar irradiance: the solar intensity incident on the upper surface of the wing. The film and solar panels are treated separately, due to their difference in absorptivity and isolation characteristics. This is further referred to when mentioning $Q_{rad,sun}$.
- Aerodynamic convection: the heat transferred by the passing air over the wing surfaces. This is further referred to when mentioning $Q_{conv,dynamic}$.
- Albedo: the reflected solar irradiance due to the Earth's surface and atmosphere incident on the lower surface of the wing. This is further referred to when mentioning $Q_{rad,albedo}$.
- Planetary radiation: infrared radiation from the Earth's surface. This is further referred to when mentioning $Q_{rad,Earth}$.

Inside the wing system, several components are included: wing skin, solar panels, main spar, and batteries. The thermal model considers convection, conduction and radiation between each pairing of the bodies inside the wing. Note that the LCT, CDHS and Ribs were not included as a component. An overview of the heat transmission is given in Figure 8.1.

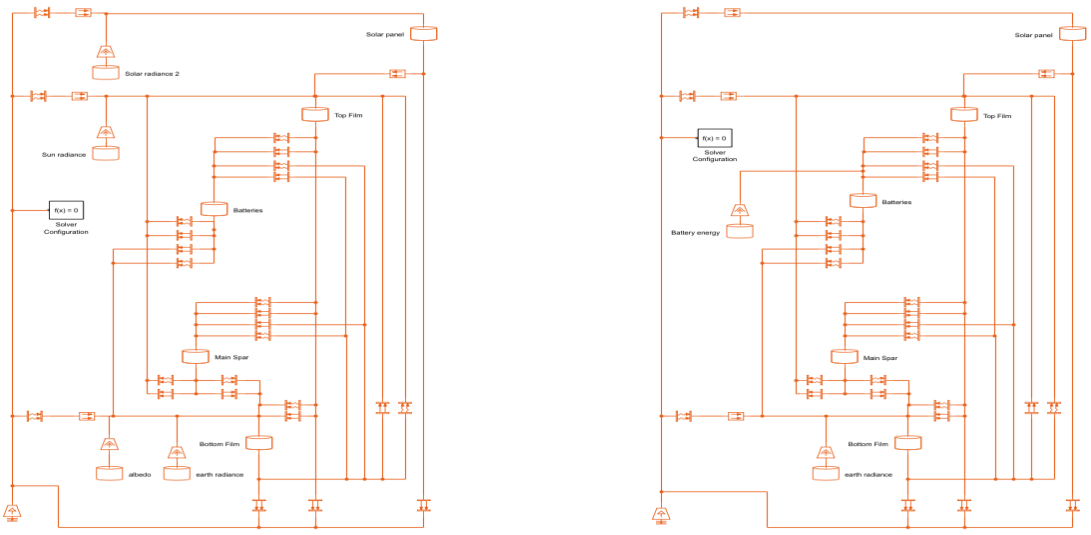

Illuminated conditions

(b) Eclipsed conditions

Figure 8.1: Overview of Simulink Block Diagram of the Wing for Illuminated and Eclipsed Conditions

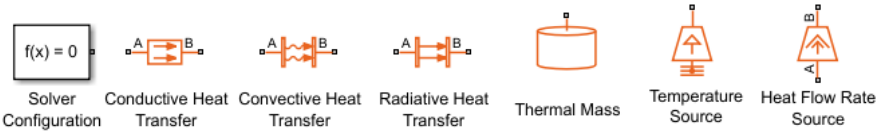

Figure 8.2: Legend for the Icons Used in the Thermal Model

The mathematical representations for these heat processes are defined in Equations (8.1), (8.7) and (8.10) to (8.14).

$$Q_{conv,static} = h_{conv} Ar(T_a - T_f) \tag{8.1}$$

Equation (8.1) represents the heat flow due to convection in a static medium such as the air inside the wing. In Equation (8.1) h is the convection coefficient of the medium defined in Equation (8.2); Ar is the projected heat transfer area, such that the smallest area between two mediums is used; T_a and T_f being the temperature of the body a and f respectively.

$$h_{conv} = \frac{max(\gamma_1, \gamma_2)\gamma_{air} Ar}{t} \tag{8.2}$$

$$\gamma_{gain\_1} = 0.2Gr^{\frac{1}{4}} \tag{8.3}$$

$$\gamma_{gain\_2} = 0.073(GrPr^{1.65})^{\frac{1}{3}} \tag{8.4}$$

Here γ_1 and γ_2 are coefficients representing the dominance of, respectively, natural convection and thermal diffusivity, t_{plate} represents the average distance between two bodies, and in Equations (8.3) and (8.4), Gr and Pr are the Grashof and Prandtl numbers. These are defined in Equations (8.5) and (8.6).

$$Gr = \frac{t_{plate}^{\frac{3}{2}} g\beta(T_a - T_b)}{\nu} \tag{8.5}$$

$$Pr = \frac{\mu c_p}{\gamma_{air}} \tag{8.6}$$

In Equation (8.5) g is the standard gravitational acceleration defined on Earth, β_{therm} is the coefficient of thermal expansion and ν is the kinematic viscosity of the medium. In Equation (8.6) mu is the absolute viscosity and c_p is the specific heat at constant pressure of the medium. Dynamic convection or forced convection[100] is where a fluid is forced over a surface and exchanging heat. In Equation (8.7) w_{char} represents the characteristic length (span) of the wing, Nu is the Nusselt number determined by the airflow regime [100] and λ_{air} is the thermal conductivity of air.

$$Q_{conv,dynamic} = w_{char} Nu \lambda_{air} \tag{8.7}$$

$$Nu = 0.664Re^{\frac{1}{2}}Pr^{\frac{1}{3}} \tag{8.8}$$

$$Nu = 0.037Re^{\frac{4}{5}}Pr^{\frac{1}{3}} \tag{8.9}$$

For completeness, the equation for both laminar (Equation (8.8) and turbulent flow (Equation (8.9) are given. However, due to project schedule constraints, this has remained outside the thermal analysis scope. Both equations make use of the Reynolds number, which is determined by the environmental conditions during flight and set at 100.000. This concludes the convection processes.

Similar to static convection, thermal conduction is defined in much the same way.

$$Q_{cond} = kAr(T_a - T_b) \tag{8.10}$$

Where in Equation (8.10) k is the thermal conductivity at the interface of two mediums. This concludes the thermal conduction processes.

The radiation processes are defined as directed radiation in Equations (8.11) to (8.14).

$$Q_{rad,2bodies} = Ar\sigma\epsilon(T_a^4 - T_b^4) \tag{8.11}$$

$$Q_{rad,albedo} = Ar\alpha_{abs} a_{albedo} S_s \tag{8.12}$$

$$Q_{rad,sun} = Ar\alpha_{abs} S_s \tag{8.13}$$

$$Q_{rad,earth} = 237[W] \cdot Ar\alpha_{abs} \left(\frac{RE}{RE + h}\right)^2 \tag{8.14}$$

In Equation (8.11), representing the heat flow between 2 bodies through radiation, Ar is taken to be the target area of the radiation, σ is the Stefan-Boltzmann constant, and ϵ is the emissivity of the radiating body. In Equation (8.13) α_{abs} represents the absorptivity of the wing surface material and S_s the solar irradiance at the altitude of the HAPS platform. For a_{albedo} in Equation (8.12) is a generic albedo coefficient of Earth. Finally, in Equation (8.14) RE is the radius of the Earth and h is the altitude of the HAPS platform.

With the thermal processes identified and formulated, these processes can be modelled in the Simulink environment with 'Foundation Library' elements from the Simscape Package, as demonstrated in Figure 8.1. Furthermore, the wing subsystems are modelled as either thin boxes (films, solar panels and BESS or as a cylinder (main spar). A special note should be made on the battery energy in Figure 8.1b, representing the heat dissipated when the BESS is delivering power.

An overview of the origin of variables used, and their values where applicable, is presented in Equation 8.2

Component	Temp. Day (° C)	Temp. Night (° C)
Batteries	-44.22	-49.06
Solar Array	-44.08	-49.13
Main Spar	-44.19	-49.10
Top Film	-44.13‘	-49.12
Bottom Film	-44.23	-49.08

Table 8.2: Steady-State Temperatures of Wing Components during Illuminated (Day) and Eclipsed (Night) Conditions

Symbol	Definition	Unit
α_{abs_film}	0.3[2]	[-]
α_{abs_panel}	0.679[3]	[-]
β_{therm}	0.00369[4]	[-]
γ_{air}	1.4[5]	[-]
ϵ_{film}	0.873[6]	[-]
ϵ_{panel}	0.88[113]	[-]
ϵ_{spar}	0.808[6]	[-]
$\epsilon_{batteries}$	0.45[7]	[-]
λ_{air}	24.35[8]	$[WK^{-1}m^{-1}]$
μ	From ISA	$[kgm^{-1}s_{-1}]$
ν	From ISA	$[m^2s^{-1}]$
σ	5.67E-8[9]	$[Wm^{-2}K^{-4}]$

Symbol	Definition	Unit
a_{albedo_Earth}	0.3[67]	[-]
$Ar_{batteries}$	5,25	$[m^2]$
Ar_{film}	30	$[m^2]$
Ar_{panel}	70	$[m^2]$
Ar_{spar}	14,92	$[m^2]$
g	9.82[10]	$[ms^{-2}]$
c_p	1.0045	$[kJkg^{-1}K^{-1}]$
h	25	[km]
k_{film}	0.24[11]	$[WK^{-1}m^{-1}]$
k_{panel}	122,64[44][12]	$[WK^{-1}m^{-1}]$
RE	6371 [13]	[km]
Re	100E3	[-]
S_s	1308	$[Wm^{-2}]$

8.3. Results

Running the model for ISA conditions at 25km altitude for both illuminated and eclipsed conditions, provides results for the steady-state temperature of the wing's components, as demonstrated in Table 8.2.

At an outside temperature of -50 °C for both day and night conditions respectively the thermal systems settle roughly at 5.8 °C and 0.9 °C above free-stream temperature. For both conditions the wing system, as modelled, would require additional insulation and or heating elements. Several systems - most notably the BESS - cannot operate at the shown steady-state temperatures.

A potential solution considered was the incorporation of a conducting body, a heat exchanger, between the solar panels and the BESS and simultaneously insulating the BESS such that it can maintain its temperature for longer. This proposed solution incorporated an insulating housing around the BESS made out of expanded polystyrene and a copper heat exchanger modelled as a plate, alongside a new estimate for the heat transfer due to forced convection of 12 $Wm^{-1}K^{-1}$[58]. This resulted in a local steady-state temperature for the BESS of -38.5° C, 11.5° C above ambient free stream temperature. Further tooling showed that with 7.6mm insulation material around the BESS, it could already retain its minimal temperature of -20° C. The cost associated with this would be a low €50 (FY24).

8.4. Summary

The proposed passive thermal system would not be able to keep the wing subsystems at operable temperatures, using only a passive system, above -20° C [14] for the BESS during illuminated conditions when the solar arrays generate heat (not complying with REQ-THL-1). Yet, the temperature of the BESS could be kept steady at -20° C when assuming this to be its initial condition and disconnecting the proposed copper heat exchange. However, this heat exchanger would be able to direct heat generated from the solar array to the battery energy storage system, complying with REQ-THL-2. It is recommended to consider active heating systems to assist in temperature control during eclipsed conditions. However, the model is not validated nor critically verified, therefore it is earnestly recommended that any further designing of the subsystem should be preceded by verification of the analysis tool through the use of computational fluid dynamics calculations. Ultimately, to optimise the temperature control it is proposed that the CDHS should be located close to the LCTs.

[14] https://www.tycorun.com/blogs/news/comprehensive-and-overall-guide-to-lithium-cobalt-oxide-battery/

9. Structures

To be able to keep your subsystems together, a backbone is needed to support them. This backbone is the structural subsystem of the HAPS. As the flight performance, propulsion and aerodynamic subsystems have already made their first design choices. The structural subsystem can be built upon these choices and can be sized accordingly. To further develop the structures, first, the requirements are set up in section 9.1, then the forces applied are calculated in section 9.2. After which the thought is put into structural decisions associated with the design in section 9.3. Lastly, the structures can be sized in section 9.4.

9.1. Requirements

Most requirements set for the structures can be directly derived from the system, user and stakeholder requirements. The requirements can be split into integration, LCT, reliability and manufacturing requirements. All requirements for the structures are shown in Table 9.1.

Table 9.1: Structural Subsystem Requirements

Structural Requirements		
ID	**Requirement**	**Derived from**
Integration		
REQ-TEC-STR-1.2	There shall be a structure to provide radiation protection for internal systems.	-
REQ-TEC-STR-1.4	There shall be a structure to provide waterproofing for the internal systems.	-
REQ-STR-INT-1	The structure subsystem shall provide humidity-low sectors.	REQ-TEC-STR-1.5
REQ-STR-INT-2	The structure subsystem shall provide structural support to all subsystems.	-
LCT		
REQ-STR-LCT-1	The LCT subsystem shall be detachable from the structure subsystem.	REQ-UR-11
REQ-STR-LCT-2	The structure subsystem shall provide mounting locations for the LCT.	REQ-TEC-OPT-8
REQ-STR-LCT-3	The structure subsystem shall not limit the LCT field of regard to less than 180° for any given plane.	REQ-TEC-LIN1,2,3
Reliability		
REQ-STR-REL-1	The structure subsystem shall be safe-life.	-
REQ-STR-REL-2	The structure subsystem shall withstand a load factor of 3.7g.	REQ-TEC-STR-2.3
REQ-STR-REL-3	The structure subsystem shall have an operational lifetime of 10 years.	REQ-CON-REL-2
REQ-STR-REL-4	The structure subsystem shall sustain a mission length of 6 months.	Stakeholder[1]
REQ-STR-REL-5	The structure subsystem shall sustain flight for the duration of the maintenance interval.	-
REQ-STR-REL-6	The structure subsystem shall not plastically deform during the full operational lifetime.	-
REQ-STR-REL-7	The structure subsystem shall sustain cracks/fractures for the entire maintenance interval.	-
REQ-STR-REL-8	The structure subsystem shall sustain 25 landings.	REQ-TEC-STR-2.1
REQ-STR-REL-9	The structure subsystem shall sustain 25 take-offs.	REQ-TEC-STR-2.1
REQ-STR-REL-10	The structure subsystem shall sustain climbing to mission altitude.	REQ-TEC-STR-2.2
REQ-STR-REL-11	The structure subsystem shall sustain descending to ground altitude.	REQ-TEC-STR-2.2
REQ-STR-REL-12	The structure subsystem shall be accessible for the assembly of all subsystems.	REQ-TEC-MAI-1
REQ-STR-REL-13	The structure subsystem shall be accessible for the maintenance of all subsystems.	REQ-TEC-MAI-2,3
REQ-STR-REL-14	The structure subsystem shall be accessible for the testing of all subsystems.	-
Manufacturing		
REQ-STR-MAN-1	The structure subsystem shall maintain its structural rigidity without fragmentation.	REQ-SR-03
REQ-STR-MAN-2	The structure subsystem shall utilize traditional manufacturing methods.	REQ-SR-07
REQ-STR-MAN-3	The structure subsystem shall be transportable.	REQ-SR-09
REQ-STR-MAN-4	The structure subsystem shall sustain all loads presented before take-off.	-

[1]Private communication

REQ-STR-MAN-5	The structure subsystem shall not utilize hazardous materials.	REQ-SR-04

9.2. Force Simulation

As the design process of the structural subsystem can take off, the first step is determining all forces acting on the system. There are four types of forces applied: Thrust force and torque generated by the propellers, All subsystem weights, Aerodynamic lift and drag forces and the structural weight.

All these forces can be calculated using data provided by all the subsystems. For the propeller-generated forces, the data provided by the propulsion subsystem can be used. The aerodynamic forces can be calculated with the usage of the XFLR5 tool as mentioned in section 4.2. The subsystems' weights can be found in the respective subsystems. At last, the structural mass can be calculated.

All forces are assumed to be point loads with the exception of the aerodynamic loads, these can be calculated by considering them to be a distributed force along the width of the wing. With the force now determined, the wing can be modelled as a rigid beam with a fixed end to calculate all internal forces and necessary structural weights.

9.2.1. Internal Force Calculations

For the modelling of the wing as a rigid beam, the forces need to be in a computable form. To start off the aerodynamic forces need to be found. The XFLR5 tool is able to export all data of the wing airfoil as selected in section 4.2. This data includes the lift coefficient and parasitic drag around the airfoil. These 2D lift coefficients can be extrapolated to the entire wing (C_L) by determining the wing lift slope, using Equation 9.1 [117]. The aspect ratio is denoted with AR. C_{L_α} and, C_{l_α} are the wing and airfoil lift slopes respectively.

$$C_{L_\alpha} = \frac{C_{l_\alpha}}{1 + \frac{C_{l_\alpha}}{\pi AR}} \tag{9.1}$$

Looking at Equation (9.1), it can be seen that the 3D effects are small due to a high aspect ratio wing. As a result, 3D effects are neglected in the determination of the internal forces of the wing. The forces can now be extrapolated over the entire wing using Scipy[2] in Python. These forces can then be used to determine the wing's internal normal, w', and shear loading, w, per unit per spanwise location, y, in Equation 9.2.

$$w'(y) = \cos(\alpha) \times L'(y) + \sin(\alpha) \times D'(y) \tag{9.2}$$

The shear force per unit span $w(y)$ can thus be found by integrating the internal normal force distribution using Numpy[3]. In addition to the shear force distribution of the lift, additional shear forces have to be added for the masses of the separate subsystems on their spanwise location. This results in the shear force over the span, V_s, being Equation 9.3, here W_i is used to note the weights of all subsystems.

$$V_s(y) = \int_0^{\frac{b}{2}} w(y)dy + \sum_{n=i}^{n} \left(W_i(1 - y_i)\right). \tag{9.3}$$

The moment forces generated by the system can be integrated from the shear force distribution. As no coupling moments are assumed using Equation 9.4.

$$M(y) = -\int_0^{\frac{b}{2}} V(y)dy \tag{9.4}$$

The last internal forces that remain are the torques along the wing circumference. Here the airfoil geometry can be used to determine the moment acting in the direction of flight. XFLR5[4] can be used to determine the torque forces themselves. The non-aerodynamic torques also have to be added to the torque determination. These are the weights that are not applied in the geometric centre of the wing as well as the thrust of the propellers. This results in Equation 9.5. Here τ is the torque with τ' is the torques created by the airfoil.

$$\tau(y) = \int_0^{\frac{b}{2}} \tau'(y)dy + T\left(z_{prop}\right)\left(1 - y_{prop}\right) + \sum_{n=i}^{n} \left(W_i x_i(1 - y_i)\right) \tag{9.5}$$

[2]URL: https://scipy.org/ [Accessed on 13-06]
[3]URL: https://numpy.org/ [Accessed on 13-06]
[4]URL: https://www.xflr5.tech/xflr5.htm [Accessed on 13-06]

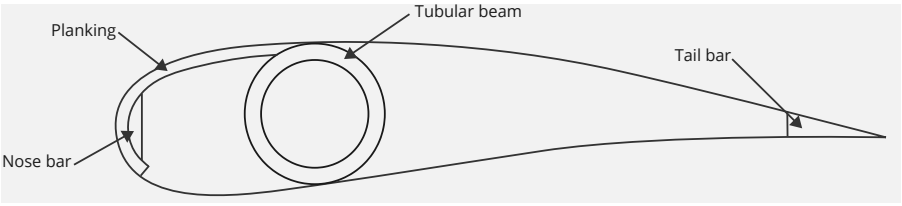

Figure 9.1: Structural layout of the wing

Now the internal shear force, moment and torque can be determined along the entire span. To translate these forces into spar and skin sizing, first the architecture of the wing and materials have to be chosen.

9.3. Structural Decisions

Before the internal forces can be adjusted as stresses inside of the structure, first the skin material and general architecture of the wing needs to be determined.

9.3.1. Architecture Selection

The load distribution inside the wing structure is essential for the sizing of the structural architecture of the wing. This architecture consists of at least the skin, spars and ribs. The setup of these structural elements varies per author. Michael C.Y. Nui [111] describes 3 possible architectures:

1. **Mass boom:** All bending material is located at the spar caps. All shear is transferred using the spar flanges.
2. **Multi-spar:** The bending material is distributed around the circumference of the wing. The multiple spar flanges and part of the skin take the shear loading.
3. **Wingbox:** The skin consists of most of the bending material. The skin will take most of the shear loading together with the structural spars.

As described by Michael C.Y. Nui [111], the torsional wing box architecture is mainly used to create sufficient torsional load resistance. In a case where the wing loading is sufficiently low, the skin used to connect the wing box can become so thin that it doesn't provide any functional buckling resistance, thus resulting in a sub-optimal configuration.[90] Now the multi-spar and concentrated spar caps options remain. The airfoil chosen in subsection 4.2.2 is sufficiently thick to allow for a single-spar option and does not impose a significant shear force loading on the wing, thus the multi-spar option can also be considered sub-optimal. This reasoning is also mentioned by Egbert Torenbeek [141].

The most commonly used configuration for a single-spar structural architecture is either the use of a D-box or I/O-beam with added structural elements on the leading edges [42]. Out of the 2 options, the tubular beam architecture would provide the highest buckling resistance [90]. The circular spar configuration can also be found in other HAPS that have been produced in the past, such as the Zephyr and Helios.[5]. To ensure that the skin keeps its cross-sectional airfoil, the usage of bars on the leading and trailing edges. The resulting geometry is shown in Figure 9.1.

9.3.2. Skin Material Selection

The skin is needed to let the aerodynamic force pressure change into aerodynamic loading on the craft. The skin is also needed to keep the airfoil shape, thus providing the simulated lift and drag as well as possible. To determine which skin material best fits the structural architecture determined earlier, a trade-off needs to be made. This trade-off needs to encompass several subsystems as it heavily influences other design choices for the respective parts. There are also multiple requirements that need to be taken into account such as requirements REQ-TEC-STR-1.2, REQ-TEC-STR- MAN-2 and REQ-STR-REL- 7. This is addressed when selecting the trade-off criteria. The considered materials are as follows[132]:

1. **Aluminium Alloy 7xxx:** High strength over weight ratio. Easy to manipulate.
2. **Fabric:** Low strength over weight ratio. Easy to manipulate and cheap to produce.
3. **Carbon Fibre:** High strength over weight ratio. Hard to manipulate and expensive to produce.
4. **Glass Fibre:** High strength over weight ratio. Hard to manipulate and expensive to produce.
5. **Film:** Low strength over weight ratio. Easy to manipulate.

These materials can now be tried against one another using a trade-off table. The scales of the trade-off criteria are based on the relative properties of the materials, resulting in various numbers. For sustainability and

[5]From URL: https://cdn.arstechnica.net/wp-content/uploads/2016/02/Zephyr_8_under_construction_Airbus_press_pic-980x653.jpg [Accessed on 6-6-2024]

manufacturing, this is not possible. As a result, the manufacturability will be scaled according to the usage of specialist requirements needed to produce the skin of the wing out of the material. The sustainability will be based on the life-cycle effects of the material. The durability of the material is also an important factor as per requirement REQ-STR-REL-3. However, there was insufficient data to determine the scores of all materials. Now the table with all the scales per criteria can be formed in Table 9.2.

Table 9.2: Skin material trade-off criterium scale

Criteria	1: Poor	2: Moderate	3: Nominal	4: Good	5: Excellent
Structural mass $[kgm^{-3}]$	≥ 2000	≤ 2000	≤ 1500	≤ 1000	≤ 500
Thermal conductivity $[Wm^{-1}K^{-1}]$	≥ 100	≤ 100	≤ 10	≤ 1	≤ 0.1
Specific strength $[kNmkg^{-1}]$	≤ 200	≥ 200	≥ 500	≥ 1000	≥ 1500
Cost $[\$kg^{-1}]$ (FY24)	≥ 750	≤ 750	≤ 500	≤ 250	≤ 100
Radiation resistance $[Gy]$	$\leq$ 100k	$\geq$ 100k	$\geq$ 1M	$\geq$ 10M	$\geq$ 100M
Manufacturability	Specialist facility	Specialist equipment	Specialist tool	Specialist training	No specialist
Sustainability	Very low	Low	Medium	High	Very High

All values for the various materials can be determined with the usage of literature. The sustainability and manufacturability scores are based on estimations given by Jos Sinke in his production of aerospace systems course[132]. All trade-off scores can be seen in Table 9.3.

Table 9.3: Skin material trade-off table

Criteria	Film	Aluminium 7xxx	Fabric	CFRP	GFRP
Structural mass (25%)	5 [1]	1 [2]	5 [94]	2 [3]	1 [4]
Thermal conductivity (10%)	2 [5]	1 [148]	5 [86]	4 [129]	5 [131]
Specific strength (20%)	2 [6]	3 [7]	1 [137]	5 [123]	5 [123]
Cost (20%)	1 [6]	3 [8]	2 [9]	1 [10]	1 [11]
Radiation resistance (10%)	4 [139]	2 [145]	1 [138]	3 [78]	5 [139]
Manufacturability (15%)	4	3	4	1	1
Sustainability (10%)	4	5	4	1	1
Weighted Average	3.45	2.4	3.35	2.15	2.20

From Table 9.3, it can be seen that film would be the best option in consideration for the HAPS wing skin. A fabric leads as a close second, but due to the fabric used for the trade-off, the trade-off is slightly skewed. Using a fabric with better radiation resistance to meet the requirement set would result in a lowered structural mass score. The weighted average for the fabric would then become 3.2 instead of 3.35. As a result, the film was chosen to adhere to requirement REQ-TEC-STR-1.2. The film that will be used is the Hostaphan 87220 foil made by the producer Hostaphan[6].

9.4. Structural subsystem Sizing

Using the architecture selected in subsection 9.3.2, the internal forces can be turned into stresses that depend on the cross-sectional area of all materials selected. In this section, all major structural elements are placed and

[1]URL: https://www.kremer-pigmente.com/en/shop/linen-paper-foils/87220-hostaphan-foil-rn-15-roll.html [Accessed on 10-06]
[2]URL: https://www.thyssenkrupp-materials.co.uk/density-of-aluminium.html [Accessed on 10-06]
[3]URL: https://www.chemeurope.com/en/encyclopedia/Carbon_fiber.html [Accessed on 10-06]
[4]URL: https://www.engineeringtoolbox.com/polymer-composite-fibers-d_1226.html [Accessed on 10-06]
[5]URL: https://wkaiglobal.com/blogs/understanding-the-thermal-conductivity-of-pet [Accessed on 10-06]
[6]URL: https://www.kremer-pigmente.com/en/shop/linen-paper-foils/87220-hostaphan-foil-rn-15-roll.html [Accessed on 10-06]
[7]URL: https://www.matweb.com/search/DataSheet.aspx?MatGUID=ab9706916818406b80c22b7f39db0c78&ckck=1 [Accessed on 10-06]
[8]URL: https://www.jagdishmetalindia.com/aluminium-7050-sheet-bar-price-list.html [Accessed on 10-06]
[9]URL: https://www.onlineclothingstudy.com/2011/11/garment-costing-sheet.html [Accessed on 10-06]
[10]URL: https://www.easycomposites.co.uk/high-strength-carbon-fibre-sheet [Accessed on 10-06]
[11]URL: https://www.carbon-composite.com/en/Glass-Fiber-Plate-4.0mm/GP040-1 [Accessed on 10-06]
[6]URL: https://www.kremer-pigmente.com/en/shop/linen-paper-foils/87220-hostaphan-foil-rn-15-roll.html [accessed on 11-06]

sized. Starting from the ribs in subsection 9.4.1 to the spars in subsection 9.4.2 and finishing with the placement of the fuselage and computing the showing the forces in subsection 9.4.3

9.4.1. Rib placement

If a wing does not use stringers as part of its load path, the ribs take the role of the stringers instead. The ribs ensure that the wing is sectional, which creates a load path for the forces applied on the wing and ensures that skin damage cannot extend to other surfaces. The spacing of the ribs can be determined according to the buckling of the skin and literature.

The skin can be assumed to be thin-walled as per the sheet thickness determined in the data sheet[7]. Thus to determine the critical buckling stress, Equation 9.6[75] can be used. Here the critical stress σ_{cr}, is calculated with the usage of a buckling coefficient k_b, the material Young's modulus E, the Poisson's ratio v and the ratio between the length and width of the skin panel $\frac{t}{b}$.

$$\sigma_{cr} = \frac{k_b \pi^2 E}{12\left(1-v^2\right)}\left(\frac{t}{b}\right)^2 \tag{9.6}$$

$$\left(\frac{t}{b}\right)_{cr} = \sqrt{\frac{2\pi^2 E}{\sigma_y}} \tag{9.7}$$

The critical slenderness ratio used for $\frac{t}{b}$ can be determined with the addition of the yield stress in Equation 9.7[75]. Using the equations presented, it can be determined that the skin will fail in buckling unless the ribs are unrealistically spaced. As a result, it is assumed that the spars will take up all compressive loads and the ribs merely hold the skin and keep their damage protection function.

The low wing loading of the HAPS vehicle is comparable to that of a parasail, unfortunately, the rib spacing techniques used in parasail are inapplicable due to the tension on the lines connecting the parasail. Luckily, Mohammad Sakib Hasan[72] presents a manner to space the ribs at 0.5 times the chord length. A chord length of 2 meters results in a spacing of 1 meter. As the skin material provider, Hostaphan provides material reels that exceed the spacing of the ribs,[8] full-size ribs can be used to compartmentalize the wing. These compartmentalized areas can be used to create humidity-low zones as per REQ-STR-INT-1. The compartments can also be maintained separately, thus meeting requirement REQ-STR-REL-13.

9.4.2. Spar sizing

With the ribs, skin and other subsystems in place. The wing spar can be sized to take all the loads necessary. The spar will be made out of carbon fibre material[128] to ensure a high strength-over-weight ratio and can be sized according to the airfoil selected. The spar will be placed according to the architecture in the thickest part of the wing at one-fourth of the chord. The total height of the spar is dictated by being 95% of the total thickness to provide the best structural integrity. The spar can be tapered in accordance with the production capabilities of CFRP, but for modelling the spar is segmented into multiple sections. Within these sections, the maximum stresses can be calculated and the inner diameter needed can be determined by using Equation 9.8[90]. The inner and outer diameter are depicted using D_i and D_o respectively. With the maximum load and spar safety factor presented as M_{max} and n_{spar}.

$$D_i = \sqrt[4]{-\frac{32 M_{max} n_{spar} D_o}{\sigma_{yield}\pi} + D_o^4} \tag{9.8}$$

With a safety factor of 1.5 applied to the spar, the outer diameter is 190 mm across the entire spar with a thickness of 3.5 mm at the root and 0.1 mm at the tip. This thickness may cause difficulties in manufacturing, therefor it minimal manufacturable thickness should be used up to 0.1 mm, which should be further investigated.

9.4.3. Structural forces

As the fuselage has already been sized in section 5.2, now the matter remains of placing the boom. The stability department has determined that the placement of the boom does not affect the stability requirements sufficiently to limit it's positioning. Thus the structural predictability and bending relief can be accounted for when placing the boom. Placing the boom at a spanwise position of one-third of the half-wing span is thus chosen. Placing the boom at 8.25 meters from the centerline of the aircraft.

With all forces and weights now known, the final spar size can be iterated and the structural forces can be computed. The maximum load factor as per requirement REQ-STR-REL-2 can also be applied to ensure that the structures can handle all loadings. Another load factor is added to ensure that the structure is a safe life. The internal force results can be seen Figure 9.2. As can be seen, the dent in the graph is produced by the boom. As the batteries were assumed to span the entire span to not limit their placement, no clear dent is produced by them.

[7]URL: https://www.kremer-pigmente.com/en/shop/linen-paper-foils/87220-hostaphan-foil-rn-15-roll.html [accessed on 11-06]
[8]URL: https://www.kremer-pigmente.com/en/shop/linen-paper-foils/87220-hostaphan-foil-rn-15-roll.html [accessed on 11-06]

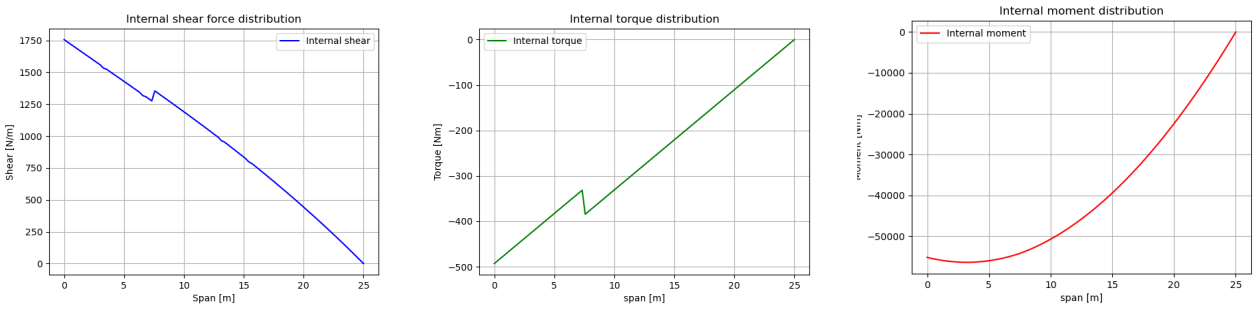

(a) Internal Shear Forces per Unit Span **(b)** Internal Torque Moments per Unit Span **(c)** Internal Moments per Unit Span

Figure 9.2: Internal Forces with Respect to the Spanwise Position

Making use of the final weights of the structural system, the HAPS can be iterated over. The total weight of the aircraft drives the lift generated, thus driving the drag and driving the propulsion system which drives the battery and solar panel sizing. All these changes account for a change in structural system size once again. After multiple iterations, the total weight and structural weight converged for the HAPS and thus final values were found. These are presented in Table 9.4.

The structural wing is modelled in 3DExperience as per all the specifications, including the dihedral. In the model, the leading and trailing edge bars are not shown. The model can be seen in Figure 17.3.

Figure 9.3: Structural Design of the Wing Made in 3DExperience

9.5. Sensitivity Analysis

In the sensitivity analysis, implications given by assumptions and design choices of other sub-departments are quantified. If the implications are significant, the structural subsystem design is to be adjusted.

Flight Performance Assumptions:

In the determination of the initial characteristics of the HAPS, a specific aspect ratio was chosen as well as a load factor. Both these items heavily influence the design of the structural subsystem of the aircraft. Due to the customer's wishes, both these parameters might be adjusted to better suit the network and operation capabilities of the craft. As a result, it is necessary to check if the spar would be sufficiently designed for these adjustments.

A relative change in load factor as well as aspect ratio is determined in Figure 9.4. It is noted that even with a 20% increase in either the load factor or the aspect ratio, due to the safety factor on the spar. The stress would not exceed the yield stress.

Thermal Stress:

Thermal stresses were not accounted for in the stress determination of the spar. This could pose an issue as the outside temperature of the craft could reach - 60°C. Equation 9.9 can be used to determine the thermal stresses posed on the material. α_t depicts the thermal coefficient of the spar material.

$$\sigma = E\alpha_t \Delta T \tag{9.9}$$

The general thermal coefficient of CFRP is generally less than 10^{-5}[52], thus the thermal stresses posed on the material will be around -8 MPa. This thermal stress is significant but does not pose an issue to the spar.

9.6. Summary and Recommendations

The aircraft needs a well-made internal structure to handle all loads posed on the craft and give the possibility for other subsystems to mount and accomplish their requirements. The structural subsystem's architecture

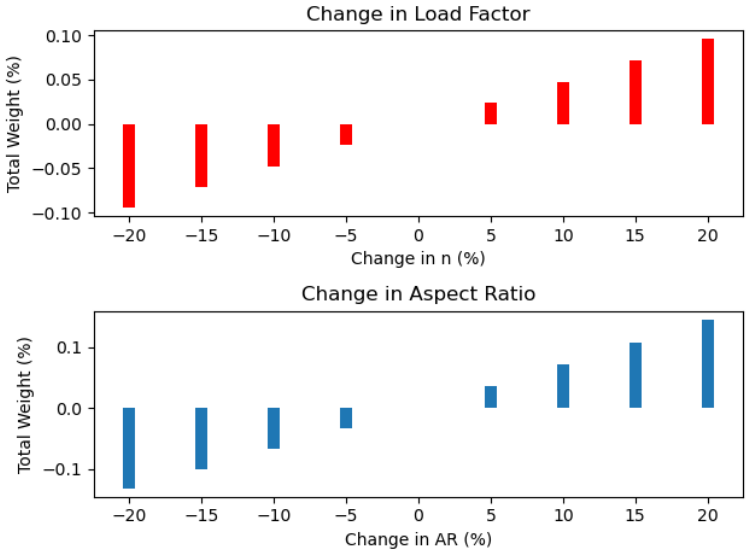

Figure 9.4: Relative Change in Total Weight per Load Factor n (red) and Aspect Ratio AR (blue)

was determined to be a circular single-spar configuration with a skin made of foil. The characteristics of the structural subsystem are as posed in Table 9.4.

The sensitivity analysis shows that there are assumptions present that have an impact of the structural subsystem. These changes however are covered by the safety factors presented, so do not pose an issue. However, the sensitivity analysis does show that changes higher than 15% can heavily influence the full design as the total weight changes by more than 5% as a result. This would mean that the design is robust against minor changes, but not against major ones.

Table 9.4: Structures Characteristics

(a) General Parameters

Structural characteristic	Value	Unit
Spar outer diameter	190	mm
Spar thickness root	6.6	mm
Spar thickness tip	0.2	mm
Rib spacing	1	m
Skin Material	Hostaphan 87220	-

(b) Mass Budget halfwing

Element	Value	Unit
Weight skin	1.04	kg
Weight spar	52.9	kg
Weight Ribs	1.91	kg
Total	**55.9**	**kg**

To further develop the design of the structural subsystem, multiple steps have to be undertaken. First of all, the costs can be computed for the entire system. This is done in chapter 15. The remainder of the necessary actions can be split into analysis and design. The analysis possibilities are as follows:

1. **Finite Element Method Analysis:** The structural model currently used is heavily simplified. As the structure is modelled as a singular beam with all load being transferred using the spar, the model can be expanded. This can either be done by the usage of voxel, surface or truss elements to expand the analysis of the structure further. With a more advanced model, the deflection needed for determining the dihedral position can be refined.
2. **Fatigue Analysis:** Making usage of the methods presented by Niu[111], a fatigue analysis can be done on various parts of the structures. These analyses can pose significant changes needed for the craft to meet the operational lifetime requirement.
3. **Gust loading probability:** By the methods of Danowsky[50], the probability of certain gust loadings within the atmosphere is modelled. These gusts probabilities can be applied to the structure to determine the likelihood of failure over its operational lifetime and thus help in determining the needed load factors for various structural elements.
4. **Thermal Analysis:** The thermal effects on the structure are relatively simple, but they can be modelled to help understand the need of thermal relief on various parts of the craft.

In terms of the design of the structural subsystem, several detailed design steps have to be done to develop the design further.

1. **Lay-up design:** As the craft uses multiple carbon fibre reinforced polymers, each can be optimised for their specific usecase. As an example, Bertrand Kirsch[91] discusses the possibilities of incorporating various materials to reduce the aeroelastic behaviour of the wing and thus reducing the effects of flutter. These and various other selections can be done to further develop the design.
2. **Joints:** The jointing of the various structural elements is of essence to the lifetime and maintainability of the structural subsystem. These various joints have to be designed and incorporated into the design.
3. **Mounting surfaces:** The overall lay-out of the plane has been determined, but the exact mounting points with the various structural elements required are to be designed for all the subsystems.
4. **Rib optimisation:** As can be seen on various HAPS, the ribs are optimised to be a truss-like structure. The current rib design can be adjusted to further incorporate weight savings inside of the wing.
5. **Skin tension:** The structural leading and trailing edge elements have to be designed and tested to ensure that the airfoil is kept up to the spec required for lift generation.

10. Command and Data Handling

The command and data handling architecture of the HAPS, represents the brain of the platform, and the method with which the HAPS conducts operations. The architecture has two main aspects: operating the mission and flying the platform. Each aspect is critical for safe and effective operations. The architecture of the system, as well as both aspects, will be discussed, as well as the system block diagrams.

10.1. Subsystem Requirements

Before the subsystem design can be completed, the subsystem requirements must first be considered.

Table 10.1: Command and Data Handling System Requirements

Command and Data Handling System		
ID	**Requirement**	**Derived from**
REQ-CDH-OPS-1	The CDHS shall be capable of continuous operation for 180 days.	-
REQ-CDH-OPS-2	The CDHS shall be able to operate autonomously.	REQ-TEC-SC-1
REQ-CDH-OPS-3	The CDHS shall ensure resilience against any single failure.	-
REQ-CDH-OPS-4	The CDHS shall regularly collect logging data from all subsystems.	-
REQ-CDH-LCT-1	The CDHS shall provide support for two LCT terminals.	-
REQ-CDH-LCT-2	The CDHS shall ensure LCT communications can be sustained in the event of poor signal.	-
REQ-CDH-APS-1	The CDHS shall ensure the platform will be able to return to base in all operating cases.	-
REQ-CDH-APS-2	The CDHS shall be able to manoeuvre the platform to a given position.	-
REQ-CDH-APS-3	The CHDS shall be able to automatically takeoff.	-
REQ-CDH-APS-4	The CHDS shall be able to automatically land the platform.	-
REQ-CDH-APS-5	The CDHS shall be able to orbit the aircraft around a set point for a set length of time.	-
REQ-CDH-APS-6	The CDHS shall be able to determine aircraft position.	REQ-TEC-SEN-1
REQ-CDH-APS-7	The CDHS shall be able to determine aircraft heading.	REQ-TEC-SEN-1
REQ-CDH-GND-1	The CDHS shall not activate any dangerous component until instructed by operator.	-
REQ-CDH-MC-1	The CDHS shall be able to communicate its status to the ground.	-
REQ-CDH-MC-2	The CDHS shall allow operators to change the mission plan during the mission.	-
REQ-CDH-TTC-1	The CDHS shall provide communication links of 100km.	-
REQ-CDH-TTC-2	The CDHS shall provide an RF data rate of 10 Mb/second.	REQ-MOP-CNW-2
REQ-CDH-TTC-3	The CDHS shall ensure aircraft avoidance broadcasting.	-

10.2. Command System architecture

The twin responsibilities of the command system are operating the payloads and operating the avionics to fly to aircraft. As such, it becomes important to determine the overall architecture that provides the optimal control system. To choose this, primarily satellite CDHS systems were considered, especially drawn from the paper by Gerard Aalbers et al.[5] The two options for the command system discussed in that paper were considered for this application, along with an additional option synthesised from the discussion within the paper. The three options were a single computer star design, a distributed bus design and a split design, with two main

computers each within their own star architecture. The aspects that were relevant to this decision were the redundancy of the system, as well as the required data throughput and handling approach. The single star was disregarded first, as a failure of the computer would then prevent control of the aircraft. Distributed buses would provide this redundancy by allowing the radio to communicate directly to the control surfaces in the event of a computer failure, but sending all avionics data along with LCT transmission data will stress the data bus, and may compromise commanding. As such, a hybrid approach was selected, with two computers being used. A mission computer to handle the LCT data, along with radio data and general mission operations, and a flight computer to handle the avionics suite and the control of the aircraft. Both computers provide redundancy in the other's operation, ensuring that a computer failure will not compromise aircraft flight.

10.3. Mission Computer

The mission computer (abbreviated MC), serves as the processing centre for all tasks that are not related to the flight of the HAPS platform. These tasks include operating the radio, LCT terminals, power system and handling all data. It also serves as the endpoint for operator commands, and the main point for error handling on the platform.

10.3.1. Mission Computer Tasks

The MC serves as the brain of the whole HAPS and acts as the master computer. As such, it is responsible for a large number of main tasks, as well as supporting all subsystems. Firstly, under the star architecture that is in use, the MC serves as the centre point for all data being transferred. This includes processing any radio transmissions, handling the data transfer between LCT terminals during communications, handling subsystem logging and providing routing data for the flight computer. The mission computer has multiple requirements imposed on its performance, as well as a drive to reduce power and mass costs of operation. For this reason, a trade-off was necessary to select the optimal architecture.

10.3.2. Mission Computer Trade Off

To conduct the trade-off, three criteria were determined. These are the power draw of the component, the computational power of the component in terms of raw computing power, as well as the ease of configuration of the component. This criteria indicates how efficiently the component can be integrated into the system, and extended and modified to suit a changing mission. The four options considered for this trade-off were the Intel NUC mini-computer[1], a raspberry pi 3A+[2], an Isispace onboard computer running Free RTOS[3], and a raspberry Pi 0 micro controller[4]. All of these options provide the necessary reliability and lifetime performance to satisfy each requirement but vary in the power draw, computational power and configuration constraints.

Options

The first option considered was the intel NUC. This computer provides the greatest computational power, being equivalent to a regular consumer PC in specs, but this comes at the cost of additional power draw and constraints on the interface. As the NUC does not have standard SPI outputs, converters and supporting components are required to provide connection to critical components such as the radio and power system controller. It does, however, present the greatest computational power, which will ensure rapid processing of high-speed LCT data and may allow for future modifications to the mission profile

The Raspberry PI 3A+ is a smaller mini-PC, with half the power draw of the larger NUC but still effective computational power. It also provides for SPI and U-ART connections, allowing for native connection to peripherals. Like the NUC it operates as a standard computer operating system, both of which are assumed to run Debian 12 as the operating system for the purpose of this trade off. By running a full operating system, configuration, software updates and error handling become far simpler and more robust with the added support from the OS.

The ISIspace onboard computer is a microcontroller running free RTOS, a real-time operating system that provides concurrency and scheduling support. As this is a microcontroller and not a fully-fledged computer, the power draw is an order of magnitude smaller than the previous two options. It retains the interface capabilities of the PI 3A+, but due to the nature of the microcontroller and free RTOS as the OS, more implementation falls on the mission control software including manually scheduling tasks and ensuring concurrency is properly handled. This also limits the software update capability, as it now requires multiple operations and a platform reboot to correctly reload the new software, rather than simply switching which software Debian loads by default.

The final option is the use of a PI-0 microcontroller. Unlike the previous option, this board does provide the capability to operate a Linux operating system as the baseline, providing the support and scaffolding also offered to the larger mini-computers but with a slightly lower power draw due to the form factor. Performance

[1]https://ark.intel.com/content/www/us/en/ark/products/126141/intel-nuc-kit-nuc8i7hnk.html
[2]https://www.raspberrypi.com/products/raspberry-pi-3-model-a-plus/
[3]https://www.isispace.nl/product/on-board-computer/
[4]https://www.raspberrypi.com/products/raspberry-pi-zero/

remains acceptable, with double the capability of the ISISpace board, but still falling far short of the larger mini-computers.

Weights

When considering the options discussed above, it becomes necessary to select appropriate weights for each trade off criterion. All three of the criteria were similar in importance, but preference was given to the power draw of the system as a minimised power draw allows for additional power to be expended on other aspects of the CDHS and the design as a whole. For this reason, the power draw was weighted at 40%, with the remaining two criteria weighted at 30%. The resulting trade-off can be seen below.

Table 10.2: Mission Computer Trade-off table

Criteria	Intel NUC	Pi 3A+	ISIspace OBC	Pi 0
Power Draw (40%)	2	3	5	4
Computational Power (30%)	5	4	2	3
Configuration (30%)	3	5	2	5
Weighted Average	3.2	3.9	3.2	4

Based on the results of the trade-off, the Raspberry Pi 0 was selected as the optimal MC component. This ensures the optimum mix of functionality with a minimised power draw. As can be seen in Table 10.2, the Raspberry Pi 3A+ computer scores very close to the Pi 0, this will be further explored in

10.3.3. Operational Modes

As the platform will operate autonomously, considerations must be made for correct operation in several potential cases. To facilitate this, a number of operational modes for the mission computer will be defined. The flow of modes can be seen in Figure 10.1 with each mode elaborated on below.

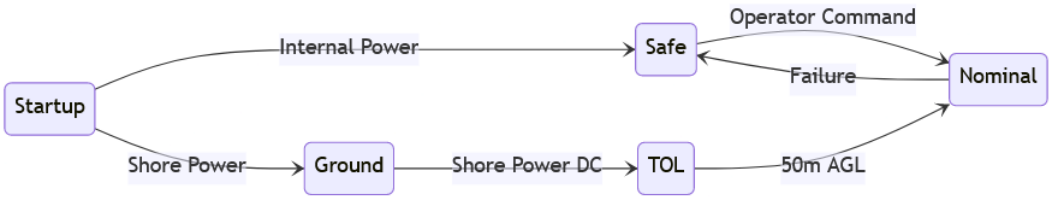

Figure 10.1: State Diagram for the Mission Computer

Startup The startup mode is the initialisation mode of the system, with the mission computer booting into this mode upon receiving power. In this mode, the mission computer first determines the status of each subsystem, as well as the flight computer status. In the event the platform is already in the air, the mission computer then switches to safe mode and begins the safe mode procedure. If the platform is on ground and connected to the ground infrastructure, the mission computer will instead start up non-essential subsystems and then wait for commands from ground to transition mode.

Ground Ground Mode will only be enabled while connected to external power and data, once the mission computer has completed startup. The purpose of this mode is to protect ground personnel from spurious emissions of the radio or LCT and ensure no moving parts of the propulsion system can pose a threat. As this mode is only enabled while ground crews have access to the vehicle, detailed logging will not be stored in the onboard memory, in order to preserve capacity for operations. Once the HAPS is disconnected from ground power and data and is operating on internal power, the mission control system will automatically transition to takeoff and landing mode.

Takeoff and Landing mode The takeoff and landing mode (TOL mode) serves to ensure the vehicle is safe for the ground crew just before launch and after recovery. In this mode, all subsystems apart from the LCT are on, but the Flight Computer is initially disarmed to ensure the propellers do not start unexpectedly. Just before launch, the system will be manually armed to enable the propellers once ground crews are clear. Once takeoff is achieved, the mission computer will automatically transition to nominal mode. On recovery, The mission computer will transition back to the takeoff and landing mode as the aircraft begins its final approach. As the approach is flown unpowered, the propellers will be disarmed and locked in a safe position and the LCT terminals will be set to safe to prevent a spurious emission. The overall landing procedure is discussed in section 3.5 The radio will continue operating until touchdown to ensure connectivity with the ground.

Nominal Mode The first main mission operating mode is nominal operations mode. This mode is the standard mode of the mission computer, and the vast majority of the mission will be flown in this profile. In this mode, all subsystems are powered and operating, and the flight computer has full control of the aircraft. While in this mode, health data is broadcast to the ground at regular intervals to ensure the operating team knows the status of the vehicle. This mode is the only mode where the LCT is operational, and can complete connections. This is done to ensure the LCT will never present a risk to the platform, or its surroundings. Each connection will have its data pre-loaded into the mission computer via the radio, then loaded as needed into the specific LCT terminal to allow for tracking and acquisition.

Safe Mode The other main operations mode is safe mode. In this mode, the mission computer aims to minimise the risk of additional faults or damage to the system while waiting for commands from the ground to recover the system. In this mode, the LCT terminals will be disabled, and the mission computer will stop sending waypoints to the flight computer. This signals to the flight computer that the mission computer is no longer operating in nominal status and allows the flight computer to proceed with its handling procedure. While in safe mode, the rate of beacons is increased, such that the vehicle will continuously beacon while waiting for operator intervention. Once operators have determined the problem has been handled, nominal mode can be restored by operator command.

10.3.4. Error Handling

Another major aspect handled by the mission computer is error detection and handling of the system. This includes software problems, as well as hardware faults in the power system, main bus, radio or LCT faults. The primary handler of avionics faults is the Flight computer, but telemetry data for avionics is also transmitted to the mission computer to ensure redundancy. The majority of failures or faults will be handled either automatically, or by dropping the mission computer to safe mode pending operator involvement. Some key critical failure modes will be elaborated on here, that are of specific interest but additional failure modes should be accounted for as the project continues.

Mission computer Failure In the event of a fatal error in the mission computer, such that the computer shuts down and is unable to restart, total system control will be automatically transferred to the flight computer. This includes automatically re-routing the radio connection, which will then begin broadcasting the mission computer fail code. As the flight computer will not be able to handle all possible commands sent by the operations team, a restricted list of commands, using the MAVlink communications protocol of the flight computer rather than the CCSDS packet radio system normally used. These commands are limited to the operation of the avionics but will be sufficient to return the platform to base and complete basic troubleshooting.

Low Power In the event of a problem in the electrical system restricting the available power of the system, the flight computer will be prioritised, even to the extent of disabling all aspects of the mission computer possible to save power. This may include shutting down the mission computer entirely if needed, at which point the radio will be routed to the flight computer to maintain connection. The flight computer will then, upon losing connection to the mission computer, automatically begin the return to base procedure. This will ensure the flight of the aircraft is not compromised.

Flight Computer Failure In the event of a fatal flight computer failure, the mission computer will assume control of the avionics subsystem. This control will be limited and will remove the capability to continue the mission. Rather, the mission computer will fly directly back to base to minimise the risk imparted by the damaged aircraft.

Radio Failure In the event of a failure in the TT&C subsystem, the LCT will be used as a backup communications link. A failure of the radio is not alone a critical failure necessitating a return to base as the platform will be able to continue operating within a network with commands sent by LCT. In the event the LCT link is lost and the radio remains inoperable, the HAPS will automatically return to the launch site as additional flight routing data are not provided to the system.

Software Updates Software updates for the mission computer will be avoided if possible during a mission but may be required to patch critical problems or implement a workaround for a non-critical fault. This will be completed by first uplinking the new flight software to the platform, confirming it is valid, then copying the flight software to flash memory and rebooting into the new software. In the event an error occurs, the mission computer reboots again, which will cause it to reboot to launch spec, which is known as safe. Once the uploaded new version has been verified to run without failure after testing, it will be set as the default load version and the mission can continue.

10.4. Telemetry, Tracking and Command

The RF radio will be used for operational communications and as a backup communication system to the LCT as required. This sub-subsystem includes both the radio as well as the ADS-B system for collision avoidance.

10.4.1. Operating Band
Before designing the TTC subsystem, the RF band for use must be considered. Based on requirements REQ-CDH-TTC-2 and REQ-CDH-TTC-1, a high data rate long-range communication band is needed, with a megabit/second performance. As such, the S-Band was selected. This is a 2.4GHz frequency band, providing high data rates to extremely long distances. This band is mainly used for space applications, which has similar conditions as the HAPS use case. These conditions more specifically are the long ranges in use, 100km or longer, and the low power available to the transmitter. There is also a large amount of existing infrastructure within this operating band, providing third party ground station support to expand the footprint where the vehicle can be commanded.

10.4.2. Tranceiver and Antenna
With the transmission band selected, a transceiver and antenna must be selected next. When considering the dual considerations of low power and frequent effective broadcasting of large quantities of data. To achieve this, the CTR-S Transceiver from Spaceteq[5] was selected. This transceiver provides 10Mb/s uplink and 100Mb/s downlink capability, with full duplex transmission for only 11W of power draw. Paired to this transceiver is an omnidirectional antenna of at least 3dB gain to be selected later. This ensures connection can be achieved at the requisite 100km link range even with this low power setup at both ends of the link. The use of a higher-performing ground station will increase the link distance, with an expected range in excess of 400km possible with a high-power ground station setup.

10.4.3. Communication Protocol
For communications with the HAPS, the CCSDS packet radio communication protocols will be used[133]. These are a set of communication protocols for each data layer that serve as the standards for space-borne communication. As the HAPS will operate at stratospheric altitudes for extreme mission durations, the use of space communication standards is preferred to standard UAV communication standards. In the event of mission computer failure or the need for an operator to command the avionics directly, the flight computer operates on the MAVLink[6] communications protocol.

10.4.4. ADS-B
In addition to the Radio system, the HAPS also contains an ADS-B transponder for collision avoidance during the period of the flight within commercial airspace, and an ADS-B receiver for use to detect other aircraft, both for collision avoidance as well as potentially to prevent LCT transmissions from intersecting with an aircraft. The ADS-B transponder that was selected is the Ping200X[7] transponder from uAvionix. This is specialised for UAV systems and provides an integrated antenna system to ensure connectivity. The ADS-B receiver is also from UAvionix and is the pingRX[8]. This is also specialised for UAV platforms, with minimal SWaP constraints and strong performance.

10.5. Memory System
In order to store and process the data required for operation, a number of different memory solutions will be used. Table 10.3 Demonstrates an overview of the different responsibilities for each type.

Table 10.3: Memory Components and Stored Data

Flash Memory/FRAM	SD Cards	Operational Memory	LCT Cache
Current Flight Software	Flight plan	Mission schedule	Cached LCT transmissions
Known safe flight software	Flight Recorder	High resolution health data logging	
Home Location	Low resolution logs (each subsystem)	LCT Connection data	
TTC Radio Frequencies			
Encryption Key			

10.5.1. Operational Memory (DRAM)
The most commonly used type is the operational memory or DRAM. This memory is volatile, which implies it will not persist its data across a reboot. Due to this, the primary function of DRAM is to store common relevant data for the moment that does not have a priority for preservation. This includes the high-resolution log files during nominal operation, data supporting the current and next LCT connection including tracking data and

[5]https://satcatalog.s3.amazonaws.com/components/615/SatCatalog_-_Spaceteq_-_CTR-S_Transceiver_-_Datasheet.pdf?lastmod=20210708080920
[6]https://mavlink.io/en/
[7]https://uavionix.com/products/ping200x/
[8]https://uavionix.store/ads-b-receivers/pingrx-pro

linkup information. This also handles storing scheduled mission tasks and upcoming waypoints, as a reboot would almost assuredly invalidate the existing mission profile.

10.5.2. Flash memory (FRAM)

The most mission-critical memory type is flash memory, which also encompasses FRAM. These are non-volatile memory types, which will preserve their data during a reboot. The trade-off for this functionality is limited storage and a constraint on the number of write operations that can be conducted. As this memory is primarily read-focused, it will handle mission-critical data that must remain accessible throughout the mission and be readily available. Flash memory is inherent in the MC, and can be considered the baseline memory of the system, while FRAM is additional memory to expand the capacity.

This component will contain the current flight software, a known safe version of the flight software, normally version 1.0, as well as the home base for return-to-base commands, frequencies, encryption keys and fixed mission parameters.

10.5.3. Operational Storage (SD Cards)

SD cards provide operational storage for the system, allowing for non-volatile storage of large amounts of data, with a penalty to operating performance. The main use of this component is long-duration logging, including storing actual log files as well as coarse-grain telemetry and flight data. In this way the SD cards serve as the storage medium for the flight recorder, ensuring post-mission analysis can be effectively conducted.

Two independent SD cards will be used, in accordance to RAID 1 specification[9]. This system ensures that a failure in any one SD card does not lose any data, as data is written to both cards. For this purpose, a pair of 64Gb SD cards from SanDisk. These provide resilience and the capacity for a high number of read/write options [10].

10.5.4. LCT Cache

In order to support a broken connection during an LCT transmission, incoming data must be first cached on the platform. To support this, a RAID 10 array of 4 SSDs will be used. RAID 10 implies two sets of two drives. Data is written simultaneously to both sets, ensuring if a drive fails the connection can continue. Each set writes data in an alternating form between the two drives, which provides effectively double the rate of read/write operations. The drives selected for this purpose are the Samsung PM9A3[11]. These drives can hold 3.84 TB of data, with a write speed of 4100MB/s. These drives are also rated for 5 years of operation at 1 full drive write per day, or 7000 terabytes of written data before failure.

10.6. Flight Computer

The flight computer or autopilot (abbreviated FC), serves as the control system for the platform and handles the flight tasks during vehicle operation. This includes handling the aircraft sensors, actuating aircraft control surfaces along with handling navigation to a given waypoint or loitering operations.

10.6.1. Autopilot Selection

In order to ensure the autopilot system is as resilient as possible, the usage of an off-the-shelf system open-source system is preferred. The collective development of open source systems and their common use in the field will minimise the risks of the system suffering a software fault.

As the autopilot serves as the safe half of the control system, a priority of robustness is preferred over the potentially expanded role a bespoke autopilot could provide. The impacts of this choice on operations will be discussed in subsection 10.3.4.

From these factors, it follows that the PX4 autopilot software suite[12], developed by ETH Zurich and supported by the Linux Foundation was selected. This open-source software suite is already in use in commercial applications and is open-source. This ensures robustness, as well as allowing for simple modification of the flight logic if needed to suit the particular characteristics of the HAPS platform. This autopilot is integrated into a Pixhawk 6X[13] flight controller, providing the bus for integration into the avionics along with integrated triple redundant IMU, two barometers and a magnetometer to ensure precise position finding.

10.6.2. Flight Logic

The flight procedure is intended to ensure the safe operation of the aircraft while incorporating checks on aircraft health and status. The mission will be divided into 4 separate phases, takeoff, travel, loiter, and landing. These phases will be elaborated on further here.

Takeoff Phase During takeoff, the safety of the ground crew is paramount. For this reason, the flight

[9]https://www.snia.org/sites/default/files/SNIA_DDF_Technical_Position_v2.0.pdf
[10]https://www.dataio.nl/sandisk-64gb-high-endurance-micro-sd-100mb-s-geheugenkaart/#read-more-anchor
[11]https://semiconductor.samsung.com/ssd/datacenter-ssd/pm9a3/mzql23t8hcls-00a07/
[12]https://docs.px4.io/main/en/config/
[13]https://holybro.com/collections/autopilot-flight-controllers/products/pixhawk-6x?variant=43699025641661

computer will remain disarmed, with the propellers locked and disabled, until immediately ready to fly. Upon launch, the vehicle will immediately begin climbing, following a standard pre-planned climb route. Once aloft and the standard climb out complete, the travel phase will begin.

Travel Phase During the travel phase the HAPS moves into the mission area to begin operations. The flight computer will be tasked to follow waypoints fed by the mission computer from a pre-loaded list of waypoints. The flight computer will only have information on the current waypoint, and the waypoint immediately after, and will automatically return to base in the event it reaches the second waypoint and no communication with the mission computer has occurred.

Loiter Phase During the loiter phase, the platform will move around the area of operations while completing LCT communications. In this phase, the flight computer will continue to fly a pre-determined path depending on the relay mode in order to provide the desired link. These flight plans will be loaded from the operations team onto the HAPS, enabling mid-mission changes to the flight plan and the ability to park a HAPS for an extended period between uses.

Landing Phase The landing phase begins once the HAPS begins its descent to land. In this phase, the propellers are locked horizontally in place at the beginning of the descent, with the landing process completed unpowered. This allows the propellers to be locked in a position that protects them from striking the ground on landing. Once over the runway, the aircraft will pitch up to stall before landing on the underbody skids. Once the platform has stopped moving, the flight computer will disarm completely to make it safe for ground crews to approach.

10.6.3. Avionics Sensors

In addition to the 6 integrated sensors in the PixHawk flight controller (3 IMU, 2 Barometers and a magnetometer), additional sensors are used to determine aircraft course and position. The primary additional sensor is a set of GNSS receivers, placed as close to the ends of the wings of the HAPS as possible. These provide an absolute determination of position, immune to the drift that occurs in IMU units. In addition to the GNSS set, two independent pitot-static tube assemblies will also be included in the aircraft to provide the barometric pressure, and hence the altitude and speed of the aircraft. The combination of the GNSS array and the pitot-static tubes is sufficient to determine the aircraft's position and velocity even if the internal IMU and barometric pressure sensors in the flight computer fail.

10.6.4. Error Handling

Non-critical errors in the flight computer will be handled without compromising operations if possible. In the event operations are impossible, efforts will be taken to preserve the flight performance of the vehicle. A number of potential faults and their handling approach will be enumerated here.

HW Faults Hardware problems in the control systems, may occur in the propulsion system, sensors or in the actuators of the control surfaces. In the event of a failure in any of these components, the flight computer will automatically attempt to return to base and inform the mission computer of the fault.

SW Errors In the event of a major software fault in the flight computer, or any component attached the first step is to attempt a reboot of the component. If the flight computer itself suffered the fault and a reboot did not solve the issue, the flight computer will be shut down and the mission computer will take over as detailed in subsection 10.3.4. Other components will be short-circuited and cut out of operation if possible.

10.7. System Diagrams

In order to consider the layout of the entire system a number of diagrams are included. These are the Data flow diagram indicating how data moves through the CDHS, as well as the software and hardware block diagrams demonstrating the overall system architecture. Finally, the functional flow diagram indicates how the HAPS moves through its operation.

10.7.1. Data Flow Diagram

The Data flow through the system is indicated in Figure 10.2. This diagram indicates what components provide data to the two computers, and which connection systems are used. The vast majority of connections to peripherals are made through SPI, or serial peripheral interface, with the Mission computer connected to the flight computer and the LCT connected to the mission computer with high data rate ethernet. SPI is capable of 60Mb/second of data transfer and Ethernet is capable of 10Gb/s.

The coloured linkages serve as backup connections in the event of a computer failure, with the orange links representing the connections between the mission computer and avionics in the event of flight computer failure, and the blue linkages representing the connections between the flight computer and critical data points in the event of mission computer failure.

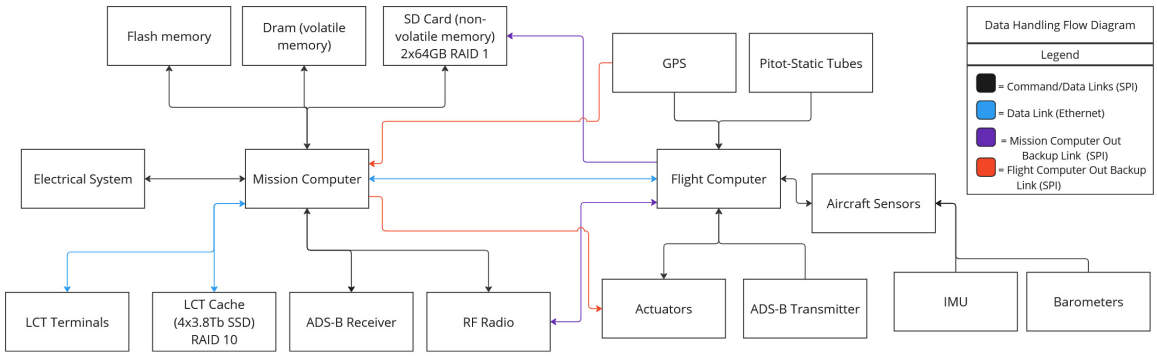

Figure 10.2: Data Handling Flow Diagram

10.7.2. Software Block Diagram

As the software of the flight computer is off the shelf, and thus not the scope of the design the software block diagram only consists of the mission computer subroutines. This software diagram can be seen in Figure 10.3.

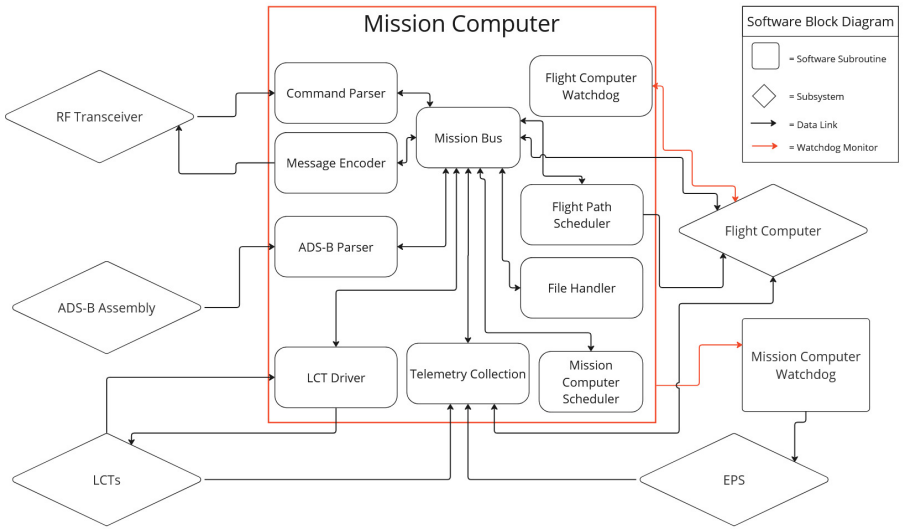

Figure 10.3: Software Block Diagram

The mission computer internally exists within a star architecture, functioning as a publisher/subscriber system. As such, the mission computer has 8 subroutines running asynchronously, each handling a specific aspect of the mission part of the system. These are the command parser, ADS-B parser, LCT Driver, Telemetry collection subroutine, scheduler, flight computer scheduler and file system manager. These all feed into and draw the central message handler or bus of the system, which functions as an extremely lightweight stack. Messages are operated on in a first-in-first-out approach, with the potential for high-priority messages to be flagged to be handled immediately. There is also one subroutine that runs only as needed, the message encoder. This is only used when the Mission computer is ready to transmit data to the ground through the RF radio. Finally, two aspects run independently of the publish/subscribe approach. These are the flight computer watchdog which is the responsibility of the mission computer, and the mission computer watchdog that is offloaded to the EPS software. In the event either watchdog stops receiving commands from its computer, it forces a reboot of the component to ensure they remain active.

10.7.3. Hardware Block Diagram

The hardware layout of the HAPS follows the software design. With the power system providing power to the entire HAPS, and the data links are split between the mission and flight computer. The Backup lines are also visualised here, indicating what subsystems are back-connected in the event of a fault.

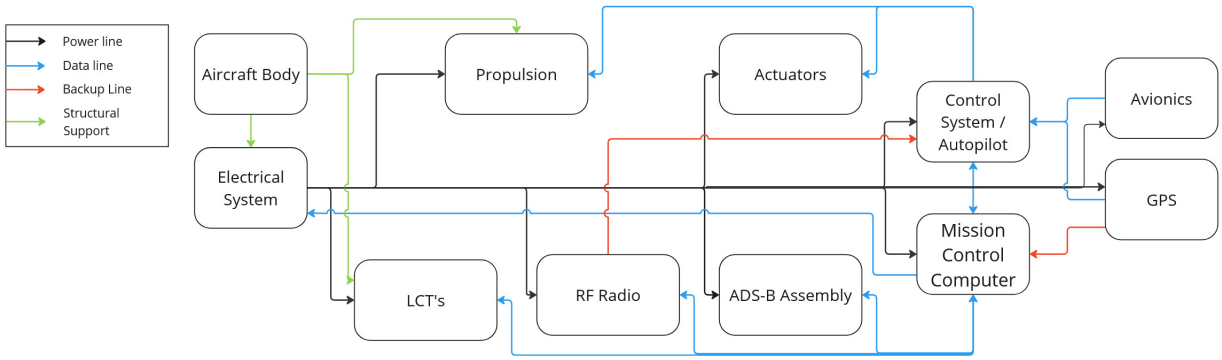

Figure 10.4: Hardware Block Diagram

10.7.4. Functional Flow Diagram

The functional flow diagram of the mission remains similar to the earlier plan, with only minor alterations as the design evolved. It can be seen in Appendix C. The main changes were in the determination of the takeoff and landing phases, and the expansion of the LCT communication handling.

10.7.5. Functional Breakdown Structure

The functional breakdown structure was also developed further as the design continued, with the updated diagram seen in Appendix B. The main aspects updated were in the specification of sub-functions.

10.8. Sensitivity Analysis

When considering the design decisions, varied parameters have the potential to lead to different designs being selected. The primary two aspects that were considered to be sensitive to design changes are the required computing power of the mission computer and the data link capacity of the TT&C. As can be seen in Table 10.2, Both the Raspberry Pi 3A+ and the Pi 0 score very similarly in weighted total. As such, only a small shift in the input parameters would be required to make the 3A+ the preferred choice. The most likely impetus to cause this shift is an increased need for onboard processing, potentially due to network computations being completed on the HAPS. In that case, the greater power of the PI3A+ becomes more appealing, even with the additional power draw.

The second primary aspect is the data link capacity of the TT&C. In the event additional data is required to be uplinked or downlinked, such as due to network concerns requiring more data to be transferred or to provide a redundant link for the LCT, a shift in radio approach would be required, and a different transceiver may be needed.

10.9. Summary and recommendations

In summary, the CDHS subsystem consists of a mission computer that is responsible for processing data from sensors, handling radio communications, supporting LCT operation and providing routing data to the flight computer. This mission computer was selected to be a Raspberry PI 0. The Flight computer is responsible for the avionics and the control of the aircraft, including determining aircraft position and managing its position, with a PixHawk Flight controller selected, running the PX4 autopilot software. Supporting the mission computer, the telemetry, tracking and command sub-subsystem consists of an S-Band radio system the CTR-S, as well as an ADS-B transponder and receiver, enabling the HAPS to both identify other aircraft in the airspace as well as broadcast its own data for avoidance.

Table 10.4: Overview of Components

Component	Mass [g]	Power Draw [w]	Cost [$](FY24)
Mission Computer - Pi 0	9	6	10
Flight Computer - PixHawk	102.8	15	400
Antennas	31	-	100
LCT Cache - Samsung PM9A3	120	4-32	2400
RF Radio - CTRS-S	31	11	10000
GNSS Receiver - Mosaic X5	13	1.1	2000
SD Cards - SanKey 64GB High Endurance Micro-SD	4	-	12.50
ADS-B Receiver - PingRX	50	0.9	453.75
ADS-B Transponder - Ping200X	50	4	5620
FRAM	4	-	5.65

Further development into the design concept must occur in the design of the software itself. As part of the continuing design process, further effort must be taken to explore how the software design integrates and develops with the remaining HAPS aspects and what other subroutines and interfaces are required to support network establishment and sustained operations.

11. RAMS Analysis

Performing an analysis on Reliability, Availability, Maintainability and Safety is necessary in any engineering design. It allows to prove requirements compliance, improve the design, schedule maintenance and solidify the overall design. Reliability will be presented in section 11.1, Maintainability in section 11.2, Availability in section 11.3 and Safety in section 11.4.

11.1. Reliability

The reliability analysis is done by determining the probability of critical failure for the entire HAPS/LCT system. The calculation starts by constructing Figure 11.1, which presents each unit prone to failure. On top of that, it shows, in case of failure of one unit, if the entire system fails or not. In other words, it represents whether the components are in series or in parallel. Note that the order and colour are arbitrary.

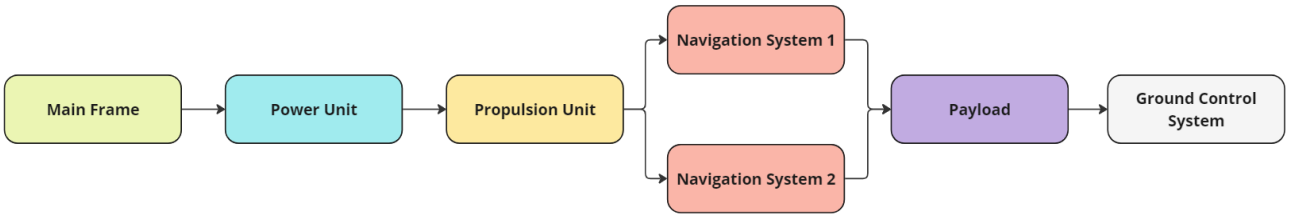

Figure 11.1: Series-Parallel of HAPS system

The reliability of a system in series as the one presented can be computed with Equation 11.1 [23]. Where R is the system reliability, n is the number of components, t is the mission duration (6 months) and $MTBCF_i$ is the Mean Time Between Critical Failure (MTBCF) of the i-th component. Critical failure refers to the case where the system can not perform its intended function but may still return home. For units in parallel, where the failure of one unit does not lead to system failure, Equation 11.2 holds[1].

$$R_{series} = \prod_{i=1}^{n} e^{\frac{t}{MTBCF_i}} \tag{11.1}$$

$$R_{parallel} = 1 - \prod_{i=1}^{n} (1 - e^{\frac{t}{MTBCF_i}}) \tag{11.2}$$

The potential critical failure modes of each unit are briefly explained along with their MTBCF. Note that this list is not exhaustive but presents the most common cases of failure.

- **Main Frame:** The main frame unit encompasses the structures and aerodynamics sub-systems. Structural components are connected through adhesive bonding which may fail resulting in structural failure. However, they present a long lifetime [132]. Additionally, due to the HAPS' long wings typical failure may be caused by excess wing deflection as the Helios [2]. Typical values of MTBCF for HALE's main frame is in the range of $2.77 \cdot 10^6$ hours [53].
- **Power Unit:** The power sub-system may cause critical failure of the system in case of a solar array or battery failure. If stored at the correct temperature, electronic components present a long lifetime. However, under the harsh conditions of the stratosphere and the high usage, the power sub-system is prone to failure. Cables and battery redundancy may be implemented but add considerable weight [23]. No data was found on the failure rate of the power subsystem for HAPS. Therefore, data from spacecraft was used as they present similar power architecture (solar arrays and batteries). Typical MTBCF values are in the order of $3 \cdot 10^6$ hours [13].
- **Propulsion Unit:** BLDC motors are prone to overheating[1], especially in this particular application as they need to rotate at large RPMs. Propellers may structurally fail due to the high loads generated by the rotational speeds. The two engines can not be treated in parallel as one motor is not sufficient to propel the aircraft. Motors and propellers have respectively MTBCF of $0.07 \cdot 10^6$ and $0.1 \cdot 10^6$ hours [62].

[1] https://www.youtube.com/watch?v=k74WXpGqPhg&t=97s

[2] https://www.nasa.gov/news-release/nasa-dryden-flight-research-center-news-room-news-releases-nasa-releases-helios-prototype-aircraft-mishap-report/

- **Navigation System:** Redundancy was used for the navigation system as they are cheap, lightweight and more prone to failure compared to other parts (see chapter 10 for more details). Therefore, the system is in parallel, increasing the overall reliability. The MTBCF is $7.39 \cdot 10^6$ hours for military drones [53]. Similarly, to the power the data for HAPS was not found and it was decided that HAPS application required a highly reliable navigation system as military drones.
- **Payload:** Estimating the payload reliability was not possible as using historical data as before is inaccurate since UAVs carry various payloads. A more thorough analysis was not performed due to limited manpower.
- **Ground Control System:** Ground Control System (GCS) presents a high failure rate but is easy to implement redundant systems. Therefore, the MTBCF for HAPS is in the order of $14.6 \cdot 10^6$ hours [53].

With the MTBCF of each component, it was possible to determine the individual and system reliability shown in Table 11.1.

Table 11.1: MTBCF and Reliability of the System and Individual Units

Units	MTBCF [10^6 hours]	Reliability
Main Frame	2.77	0.99844
Power Unit	3.0	0.99856
Propulsion Unit	0.021	0.819
Navigation System	7.39	0.99999
Payload	-	-
GCS	14.6	0.9999
Total	**0.014**	**0.817**

The system reliability is 0.817 meaning that on average a critical failure occurs every 30 months for a 6 months mission. This result violates REQ-CON-REL-1. The biggest contributor to the low reliability is the propulsion system. To solve this issue it would be advised to use more than two motors or increase their diameter in order to create a redundant system. Having a redundant dual propeller would increase the reliability to 0.98. It was also advised by the client to use a redundant coil increasing the overall redundancy. After a discussion with the client, it was decided that the reliability of 0.817 is sufficient. Therefore, REQ-CON-REL-1 is changed to: The system shall operate at least with 80% reliability within its operational lifetime. On top of that, the reliability of the LCT is not calculated as it requires significantly more work by investigating the reliability of each component. After a discussion with the client, this was deemed to be satisfactory. If the LCT reliability is a driving factor, effort should be made to increase the propulsive reliability.

11.2. Maintainability

Scheduled aircraft maintenance is divided into four categories namely: A, B, C and D checks that are done respectively every month, 6-8 months, 18-24 months and 6 years[3]. Even though these checks are done for commercial aircraft and have strict safety regulations, the same logic will be applied to the HAPS since reliability (and redundancy) in telecommunications is critical and drives the business case. Further substantiating this, several components and systems were identified to require this maintenance approach (eg. batteries and the caching system) for the sake of replacing components. Each check requires different maintenance times namely 10 hours, 1-3 days, 2 weeks and 5 weeks. For all subsystems, it is possible to schedule maintenance activities as seen in Figure 11.2. As the mission duration is 6 months, check A are out of the question.

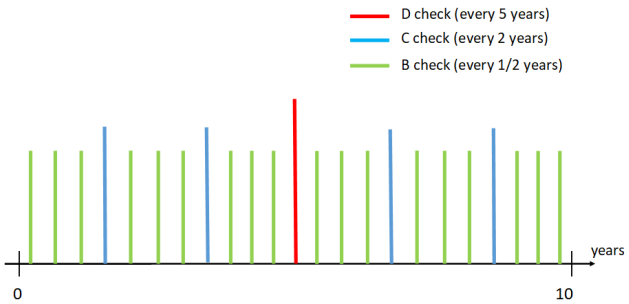

Figure 11.2: Scheduled Maintenance throughout the Operational Lifetime (10 years)

[1]https://www.ato.com/bldc-motor-overheating-troubleshooting#:text=What%20Causes%20a%20BLDC%20Motor,power%20supply%20department%20for%20solutions

[3]https://www.naa.edu/types-of-aviation-maintenance-checks/

- **Propulsion:** As seen in section 11.1, the propulsion system is the most prone to failure. Therefore, regular maintenance must be performed. Checks B, C and D will be used for the propulsion system. At check B, the propeller will be checked for cracks and damage using visual inspection and fluorescent liquid. Due to the landing, dust may be present on the propeller which should be wiped. For motors, the maintenance in check B will consist of bearing lubrication and checking the commutator and brushes. On top of the B checks, every 24 months (4 mission cycles), a C check will be done. They will consist of test armature windings, check electrical connections and test field coils. [4]. On top of that, the thrust of the propulsion system and efficiency will be measured to check for any performance degradation. Check D will be done every 5 years (along with B and C). Therefore, only once in the operational lifetime of the HAPS (10 years). At check D, the entire motors will be replaced as their MTBCF was found to be 8.9 years (section 11.1), therefore they would most likely not survive one HAPS operational lifetime. Propellers will be tested for structural integrity and only if they are found to be weak they will be changed.
- **Power:** The battery chosen in section 7.4 is designed for 200 cycles [5]. Therefore, at check B the battery shall be changed as it would not survive another operational cycle. Regarding, the solar arrays at every check the dust will be wiped away since it decreases efficiency.
- **Aerodynamics Surfaces:** The rough environment of the stratosphere and the change of conditions that the aircraft will face may cause degradation of the wing surface (reducing aerodynamic performance). Therefore, at B check, a visual inspection will be done on the aerodynamic surfaces, on top of the wiping. At check D (every 5 years), the plane should be equipped with measuring equipment to check for the aerodynamic performance of the wing.
- **Structures:** During check B, Non-Destructing Testing (NDT) methods will be used to check for structural integrity. Radiography and fluorescent liquid will be used. As adhesive bonding is used, maintenance is harder. Nonetheless, it is possible to dismantle the entire structure at D checks to check for internal damage.
- **Thermal:** As there are no physical components (apart from the structures) in the thermal subsystem, no maintenance is needed.
- **CD&H:** The hard drive responsible for the LCT caching was found to have an operational lifetime of 6 months therefore at every B check it shall be changed. At D check, the radio should also be changed as it can only last 7 years.

11.3. Availability

Availability refers to the percentage of time that the HAPS can perform its intended purpose. After a system failure, repair has to be done to use the system again. Availability relates to the MTBCF and Mean Time To Repair (MTTR), its relation is shown in Equation 11.3 [16].

$$A = \frac{MTBCF}{MTBCF + MTTR} \tag{11.3}$$

The availability of the network is intended to be 100 % as in case of a single HAPS failure it can be immediately replaced. Regarding a single platform, estimating the availability requires the calculation of the MTTR. To calculate the MTTR, Figure 11.2 must be considered. Figure 11.2 shows that 18 B checks, 4 C checks and 1 D check are performed throughout the 10 years. The MTTR can be computed as the weighted average of the repair time for all the checks. The value is 53 hours. Therefore, the availability becomes 99.6 %. Note that this number does not take into account unexpected maintenance.

11.4. Safety

Safety has been extensively addressed in the Midterm Report [3]. But with the detailed design done, it becomes possible to dive deeper into safety considerations.

Legislation for Safety Considerations: The stratospheric layer where the HAPS operates is under national sovereignty [147]. Consequently, it must respect the specific country's aircraft regulations. However, the problem is that legislation on HAPS usage is still limited and varies significantly per country [82]. Current legislation does not cover part of the stratosphere. In Europe for instance air traffic regulations go up to 14 km [101]. Using UAV regulations is not always possible as the altitude and weight limit ($\approx$ 250 m and 150 kg) is considerably below the HAPS [135]. Nonetheless, the technology has many similar aspects, hence the regulations can be extended to HAPS. The main aspect as mentioned before is respecting national sovereignty and on this point, the International Civil Aviation Organisation (ICAO) established legislation: "No aircraft

[4] https://www.gohispeed.com/the-importance-of-dc-motor-maintenance/
[5] https://amprius.com/products/

capable of being flown without a pilot shall be flown without a pilot over the territory of a contracting State without special authorization by that State and in accordance with the terms of such authorization." [92]. The intended operation of the network was globally posing real legal and bureaucratic issues as authorisation needed to be granted to the country.

Close-to-ground operations pose safety and regulatory concerns. The size of the aircraft is considerable with a span of 50 m (for reference a B747-400 has a span of 64 m[6]). The intended ground operations are explained in chapter 13. Take-off and landing are particularly critical moments. Regulations imposed on UAVs that in case of loss of communication between the craft and the ground, the UAVs shall be able to autonomously return home [101]. Authorities advise the use of redundancy which was used in our design where a double redundant return system was implemented (see chapter 10).

Safety Design Considerations: Li-Ion batteries are susceptible to overheating. The increase in temperature generates more overheating creating a disastrous spiral.[7] Overheating may cause fire on a board of the HAPS. To address this issue, non-flammable materials were used on board the HAPS (film and CFRP) so that in case of fire there is enough time to return home. The problem remains to detect the fire. Due to their long wing typical HAPS failure may be caused by excess wing deflection as the Helios [8]. In chapter 9, a fail safe philosophy was used where a rod inside of the wing was placed so that in case of failure the number of debris is lowered. When doing air-to-ground and air-to-air links, there is a chance that another object is in line of sight of the laser posing safety concerns. Air-to-space links are also susceptible to interference but the probability is lower. To address this issue the use of Automatic Dependent Surveillance–Broadcast (ADS-B) systems was considered. ADS-B determines the position of the aircraft via satellite navigation and shares its position with air traffic control which in return shares it with other airborne vehicles [9]. ADS-B would allow the HAPS to know the position of the surrounding aircraft to then determine whether the link is feasible or not.

12. Manufacturing, Assembly & Integration Plan

To realize the Eurus HAPS platform the production processes leading up to its first launch should be considered and well documented. To this extent, this chapter shall first discuss the requirements relevant to these processes, and proceed by documenting a general outline of the manufacturing, assembly and integration processes.

12.1. Requirements

The relevant requirements are restated in Table 12.1 for Manufacturing, Assembly and integration. These requirements shall be taken into account when defining the production process.

Table 12.1: Requirements Relevant to Manufacturing, Assembly and Integration of the HAPS Platform and its Subsystems.

Maintenance		
ID	**Requirement**	**Derived from**
REQ-TEC-MAI-1	The system, including all components, shall be smartly positioned in the design to ensure ease of access for (dis)assembly.	Section 1.3
REQ-TEC-MAI-2	The system shall be designed to allow for efficient repair of components in case of failure.	Section 1.3
REQ-TEC-MAI-3	The system shall provide inspection capabilities to facilitate routine checks.	Section 1.3
Use of Resources		
REQ-CON-RSC-1	The LCT shall utilise Off-the-shelf components when possible and not in conflict with cost and standardization requirements.	Section 1.3
REQ-CON-RSC-2	Materials used shall be sustainably procured when possible.	Section 1.3
REQ-CON-RSC-3	Recycle material shall be used when possible.	Section 1.3
REQ-CON-RSC-4	Design effort shall be made to use TRLs better than 5.	Section 1.3

[6] https://www.cargolux.com/fleet-equipment/aircraft/747-400f-specifications/

[7] https://www.unsw.edu.au/newsroom/news/2023/03/seven-things-you-need-to-know-about-lithium-ion-battery-safety#::text=Overheating%20is%20one%20of%20the,and%20cause%20it%20to%20fail.

[8] https://www.nasa.gov/news-release/nasa-dryden-flight-research-center-news-room-news-releases-nasa-releases-helios-prototype-

[9] https://www.airservicesaustralia.com/about-us/projects/ads-b/how-ads-b-works/

12.2. Manufacturing

The first step in the production process is the acquisition and fabrication of parts to be assembled in a later stage. Throughout the design process, efforts were made to incorporate off-the-shelf and, where applicable, more sustainably procurable components. In this section, the fabrication of parts that could not be sourced will be deliberated on.

Spars and Booms

The first challenge encountered is manufacturing single structural elements made from carbon fibre-reinforced polymers (CFRP). The largest element is the wing spar. One of the largest single-shot CFRP manufacturing facilities is operated by GKN Aerospace in Western Approach, UK[1], allowing for single-shot CFRP elements up to 17 meters. As this development was initiated as part of Airbus' Wing of Tomorrow program it is assumed that the production of the Eurus, in cooperation with Airbus, will be able to make use of this facility. This facility produces these elements by employing Automated Fibre Placement (ATP) and is applicable for the main spar of a HAPS platform. A cost breakdown of ATP shows that for the wing-skin of a horizontal stabiliser, a majority (77,5%) of the costs associated with manufacturing are due to the material costs [35]. This cost estimation was based on the material surface area of 8.26 m^2 and required a total area of 334,18 due to the part being wrapped 10 times in 4 orientations (-45°, 0°, 45°, 90°). The thickness of the fibre tows was not mentioned, a value of 0.2 mm, [2] will be used. The thickness of the main spar in the wing was reduced by 0,256 mm per meter span. Therefore, for this cost analysis, the thickness will remain constant every 0.758 meters, such that one less wrap is required every half meter. For the spar, the total required area is then 495 m^2, as defined by Equation (12.1). This leads to a material cost for the spar of €17987 and a total cost, assuming the material cost is 77.5% of the total manufacturing cost, of €23209. Similarly, the booms cost €245.27 using 6.75 m^2. The previous assumption is likely underestimating the true manufacturing cost. For such smaller parts, the manufacturing cost will be dominated by the fixed cost per part. Therefore, the fixed cost of €3028 is used to supplement the material cost, totalling €3273 (FY24).

$$A_{tot} = \sum_{i=1}^{n} N_{wraps_i} \cdot A_{avg_i} \tag{12.1}$$

In Equation (12.1) A_{avgi} is the average area of the cylinder according to Equation (12.2).

$$S_{part} = \frac{\pi(R_o - \frac{t}{2})l}{4} \tag{12.2}$$

In Equation 12.2, R_o stands for the outer radius of the spar, t is the thickness of the CFRP wrapping, and l is the part length requiring the same number of wrappings.

Ribs

The custom ribs for the HAPS platform are key structural elements for the aerodynamic performance of the craft and shall be designed to a low tolerance. For the ribs, it was opted to again go for CFRP, as defined in Chapter 9. Among the fabrication processes for fibre-reinforced polymers, resin transfer moulding (RTM) is capable of producing good surface finishes and is suitable for parts that require high dimensional accuracy[116]. A comparison of RTM and its usual competitor, autoclave curing, shows that they "tend to be preferred over autoclave technology as they reduce manufacturing and assembly costs" [36, p. 1]. Here too a rudimentary cost estimate is performed. In a paper by Baskaran M. et al. the total production of a car sunroof, with a projected area of 1.72 m^2, cost €18.97 per part[37]. As this paper accounts for high throughput, 90000 parts per year, the cost per part is doubled for lower throughput quantity for the HAPS platform[74]. As the main wing requires 51 ribs, spaced 1 meter apart, fabrication costs for the ribs total €1935 (FY24).

Wing skin

The wing skin shall not need to be fabricated as an off-the-shelf product was found in Section 9.3.2. However, for completeness sake a cost estimate shall be given for this product. The HOSTAPHAN foil RN 15 costs €53.55 per roll, consisting of 70 m^2. Therefore for the main wing, a minimum of 6 rolls are required, totalling €321.3 (FY24).

Empennage

The material and fabrication process for the parts required for the empennage (horizontal and vertical tails) shall be identical to that of the main wing, such that identical facilities and equipment can be used to improve both financial and environmental sustainability. To this extent, the cost associated with these parts will be related to the costs calculated prior using a ratio of surface area. The total surface area of the horizontal and vertical

[1] https://www.compositesworld.com/articles/one-piece-one-shot-17-meter-wing-spar-for-high-rate-aircraft-manufacture
[2] https://www.easycomposites.co.uk/6k-carbon-fibre-tow

tails was 17.73 m^2 as presented in Sections 5.2 and 5.2.2. Hence, a cost estimate, using the ratio $\frac{17.73}{100}$, for the empennage is €4515 (FY24).

Propeller
One other component that will have to be custom fabricated is the propellers. In Section 6.2 the material for the propeller was not yet defined, but for weight optimization, a composite propeller is a promising candidate. This would enable the propellers to be made using RTM and make use of identical facilities and equipment as was done for other components. An analogous estimation for the propeller blades resulted in a cost of €40000 (FY24), roughly doubling the price of a pre-existing propeller by Hartzell[3].

12.3. Assembly

Post fabrication, the HAPS platform's components need to be assembled. With a wing span of 50 meters and a length of 10.3 meters, the aircraft could fit in most airliner manufacturing halls. Costs related to the assembly are generally unavailable, a very rough estimate of €100000 (FY24) is taken, as the complexity of assembly of the craft is assumed to be similar to that of the Icon A5[127], where it is further assumed that the assembly is not more than 1/2 half of the development cost. This would probably overestimate the cost of assembly, but that is deemed acceptable.

Several processes still need to be considered more in-depth: the method of joining the wing system and booms; joining the tail surfaces to the booms; incorporating the LCTs inside the wing; and incorporating the CDHS inside the wing. This will be done in the remainder of this section. It was proposed in Chapter 8 to group the CDHS and LCT optical assemblies such that they can be more effectively heated and insulated. This infers that the wing should incorporate a rigid mounting surface for these assemblies. This mounting surface could be a reinforced plate spanning between two adjacent ribs. Furthermore, the two booms connecting the tail surfaces are sufficiently separated that two separate jigs are required to connect these parts to the middle spar. These components were not designed and are assumed to impact the development costs minimally. For the two tails, a similar jig shall be required.

From the above discussion on manufacturing of the spars, a minimum of three separate spars would need to be joined. With three spars, this would infer joining the spars at 8.5 meters off the centre axis, and incur a maximum axial stress on the surface of 43.76 MPa. It is proposed that these spars be joined with an external sleeve that is riveted to both parts, such that the connection is not prone to loosening due to vibration.

12.4. Integration

Integrating the subsystems into the final HAPS platform is normally split into separate integration stages. This section gives a short description of what these stages entail. The cost of this stage would be too speculative to include and therefore remains as a recommendation for further studies.

Pre-Integration Preparation
Before the integration process begins, it is essential to ensure that all subsystems are thoroughly pre-tested and verified this stage is discussed in Chapter 18. Verification reports should be compiled, documenting that each subsystem meets the predefined specifications and is ready for integration.

Initial Integration
The integration process starts with the assembly of the core structural components. This involves constructing (sub)assemblies that are tested at multiple stages, such as a maximum stress test of the empty wing structure.

Electrical Integration
Following the installation of the structural components the electrical system including the electric motors. This involves connecting the power system, which includes solar panels, batteries, and power distribution units, to the various subsystems. Proper wiring and grounding are critical to prevent electrical interference and ensure a stable power supply. The electrical integration process also includes the installation of power management systems that regulate power distribution and battery charging.

Communication and Control Integration
Once the power system is in place, the communication and control systems are installed and configured. This step involves setting up antennas, transceivers, data processing units, GPS modules, and autopilot systems. The communication system must be calibrated to ensure reliable data transmission and reception. The navigation and control systems are also tested and configured to ensure accurate positioning and stable flight control.

Final Assembly
In the final assembly phase, the mission-specific payload is integrated into the HAPS platform. This could include sensors, cameras, or scientific instruments. The payload integration is followed by a complete system

[3] https://taturbo.com/hartzelltrailblazer.html

integration, where all subsystems are connected and tested together. This phase ensures that the entire system functions as a cohesive unit. Any discrepancies or integration issues identified are resolved before proceeding to testing and validation, such as flight tests.

13. Operations and Logistic Concept Description

The Operational and logistical concept of the design is of critical importance, as it dictates the network structure, the number of HAPS required for effective operations, and what operational performance can be achieved through the use of these HAPS platforms. As the HAPS operates primarily above controlled airspace, the operational flow is more similar to a space vehicle as opposed to an aircraft, and as such has been designed along these lines.

13.1. Network Concept Design

In order to effectively leverage the long range of the air-to-air link performance of the LCT terminals, and the extended mission time of the HAPS platform, the use of multiple interconnected HAPS as a network can provide significant benefits to operational performance. These network options include concepts such as the use of a single HAPS to extend the range of ground station coverage, the use of a chain of HAPS to bridge long distances such as the Atlantic Ocean, as well as the usage of parking orbits to ensure rapid response times of a connected HAPS to a new mission objective.

13.1.1. Ground Station Support

The use of a supplementary HAPS platform in combination with an LCT ground station provides an out-sized return on the initial investment. A ground-to-HAPS link is limited to a range of approximately 40 km and is highly weather-dependent to achieve that range. This can be further seen in Figure 2.2. A ground station-HAPS direct link provides a significant constraint on the operational domain. By including a supplementary HAPS positioned directly over the ground station's position, the improved air-to-air data link connection with a 400 km range as well as significantly minimised impact of weather on the link, can be leveraged.

This expands the operational domain significantly, with a Ground link using only two HAPS now able to reach a maximum effective distance of 480 km, and even with significant visibility constraints a range of 400 km would remain achievable. In the single HAPS case, an 80 km effective distance is the ideal maximum, with a potential bad weather case removing the benefits of the HAPS entirely. The drawback of this design choice is the supplementary HAPS can only support one connection at a time, as each HAPS platform only contains two LCT terminals. Thus, if a single ground station is supporting multiple simultaneous missions, several supplementary HAPS may be needed.

13.1.2. Multi-HAPS Links

The logical development from the ground station supplementary HAPS concept is the use of several HAPS platforms to extend the operating domain without the requirement of an additional ground station for support. This can provide the greatest benefits when the HAPS is called upon in a remote environment, or if other external factors limit the location of a potential ground station installation.

As HAPS can maintain communication even in the event of intermittent outages through the use of caching, as discussed in subsection 10.5.4, a multi-HAPS chain can remain viable. Without the caching capability, a loss of a single link anywhere in the chain would interrupt the entire chain's communication, which may cause extreme slowdowns in data transfer in long networks. With the caching implemented, an arbitrarily long link can be sustained, with signal loss at any point being absorbed by the preceding HAPS, allowing data to be transferred in an optimised manner.

13.1.3. Network Merging

By combining aspects of the two previous concepts, a more robust operational concept can be developed. This concept consists of a HAPS-supported ground station acting as the base of a HAPS chain, that extends towards the area of interest. In order to support multiple possible areas of interest, the HAPS chain can be branched, with each branch consisting of its own HAPS chain. This operational concept provides a number of potential benefits but comes with some of the downsides implicit in the previous two concepts. The major downside is the throughput constraint. As these chains still end with a single HAPS above the ground station, the entire chain is limited in throughput to the performance of a single HAPS. This means sub-chains are limited to $\frac{1}{n}$ of nominal performance, where n is the number of operating sub-chains.

This downside can be mitigated however, by adding an additional HAPS chain to a different ground station. This

increases the throughput again by allowing communications to path to either ground station chain, providing a maximal per chain performance of $\frac{g}{n}$, with g being the number of ground stations and n being the number of chains. This formulation does imply any given HAPS sub-chain can effectively path to any ground station node. The problem of optimising this network would fall into the domain of graph theory and can hence be optimised for an ideal layout of HAPS chains for maximum throughput. This distributed network would not be required for all operations, as this system would require an extremely high number of HAPS platforms airborne at once, but after the adoption of the platform becomes widespread will ensure optimal utilisation of the aircraft.

The other advantage of this system is new areas of operation can be quickly brought online as needed by simply connecting them to the network, and additional ground station capacity can be added to the network overall, rather than requiring a specific ground station per mission. Additional ground station capacity could also be more easily added through the incorporation of multiple terminals at a single ground station site, and hence placing more supplemental HAPS above. In the full network case, these additional terminals can be quickly connected and brought online without requiring a full additional HAPS chain, but if the network is not yet saturated with nodes the additional terminals may not be able to be leveraged to their fullest potential.

Further research should be conducted to also consider that missions may not be constantly transferring data, and hence what the minimum required number of ground station nodes would hence be with certain duty cycles.

13.1.4. Communication Block Diagram

The total set of connections can be visualised in a communication block diagram. This diagram can be seen in Figure 13.1. The diagram intends to show all possible connection types, thus it does not represent a true HAPS network layout. In a real HAPS network, far more Network HAPS will be used, with a variety of connection types. In addition, HAPS in the middle of a chain will only be able to sustain 2 connections, unlike the effective 3 connections of the middle network HAPS.

Data flow is indicated by the red lines and can flow in either direction. This supports the client satellite to the client ground station, the client satellite to own ground station for that data to be transferred later, as well as the client ground station to own ground station.

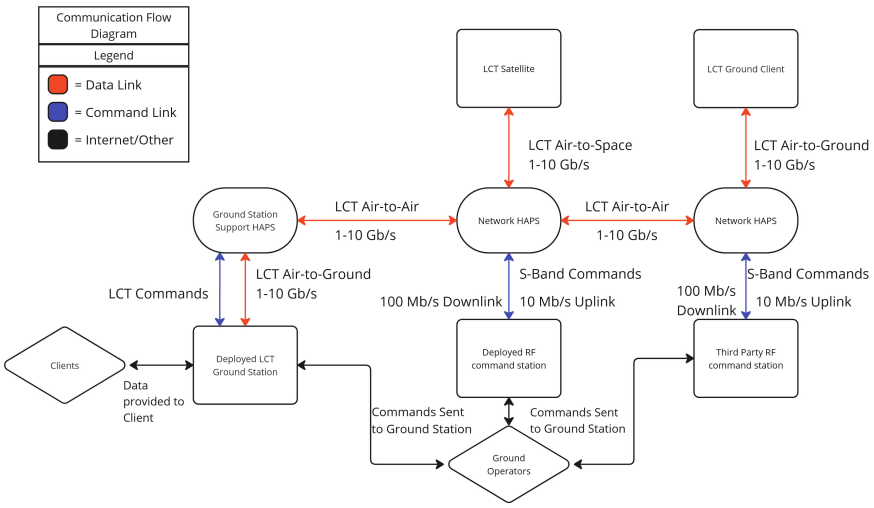

Figure 13.1: Communication Block Diagram

13.2. Logistics

Another critical consideration in the HAPS operational life-cycle is the logistical concerns of the platform. These include the logistics of ground station deployment, HAPS deployment and launch, HAPS recovery and maintenance, as well as the rapid response case for HAPS use.

13.2.1. Ground Station Deployment

As discussed in section 13.1 above, the number and position of ground stations in the network have a significant impact on the throughput of the network as a whole. In addition, before the full network has been established with a sufficient HAPS fleet, dedicated ground stations will be necessary to support individual mission operations. These ground stations must hence be easily transportable and temporary, until such a time that the network provides for established permanent stations. The preliminary terminals must contain both LCT and S-band transceivers but do not require operators to be present on site. This allows a set of operators to manage an increasing number of ground stations without necessitating additional teams.

13.2.2. HAPS Deployment

The deployment of the HAPS consists of transporting the HAPS to the launch site, preparing it for launch, launch, and post-launch travel to the operations area. In order to prepare, launch and command the HAPS during the deployment phase, a team of technicians and operators will need to be deployed along with the HAPS for integration. The HAPS will first be assembled from the packed state into the flight condition. Next, testing of the control surfaces, propulsion and avionics will be completed to ensure the HAPS remains functional even after transport. Once the functionality is confirmed, the flight configuration will be loaded and checked by the ground crew, and the vehicle will conduct its own pre-flight checks.

Once all the checks are complete, the vehicle will be put on the runway, the Pogo wheels will be inserted and the vehicle will be disconnected from ground power and begin the takeoff process. The takeoff itself is explained in section 3.5. This procedure should take less than 24 hours to ensure compliance with the deployment requirements. In order to optimize the climb performance of the vehicle, Takeoff will be conducted before dawn on battery power. This ensures the HAPS reaches 15km as the sun rises, beginning its operational cycle with the expected drained batteries.

Due to this launch approach, HAPS can be launched at a variety of times of day, ensuring a quick response time of the platform, and with the quick launch tempo and quick climb, HAPS should be able to be at altitude and operating within 36h of arrival to the launch site.

13.2.3. Landing and maintenance

Once the HAPS itself is on the ground, it will first disable all rotors as it switches to ground operations mode. The ground crew will then download the logs of the HAPS and shut it down. Once the HAPS is unpowered, disassembly will begin to prepare the HAPS for transport. All maintenance will be done at one of the permanent maintenance sites, so once a HAPS has landed, it will then be disassembled and transported back to the manufacturing base for refurbishment. The centralized maintenance approach is preferred due to the extensive maintenance required after each mission, and the long mission duration. After a mission, a HAPS will be fully refurbished, then re-deployed to the next relevant position. A central maintenance system provides a lower cost basis, and the increased refurbishement time and transport time has minimal impact due to the operating regime.

13.3. Platform Operators

In order to ensure the HAPS platform has oversight in operations, and to support the missions undertaken by the platform a team of operations engineers will be required. These engineers will be tasked with communicating with each platform, handling mission data and LCT communications data uploads, monitoring of telemetry, and any troubleshooting that may be required during the operation of the HAPS platforms. As the HAPS may be deployed in remote areas, and potentially globally, operations shall be conducted from a central location, with commands and data transferred to the local ground station or a partner ground station as required.

Thanks to the extended range of the RF communications link to the ground, as well as the increased number of commercially available ground stations for use within the transmitting band, more HAPS will be directly accessible to the operations team than would be from the LCT. This ensures monitoring and support can be rendered to the majority of the fleet, and provides for rapid response in the event of a fatal error on the platform.

14. Risk

During the more detailed design of subsystems, there are new and more detailed risks that present themselves. In this chapter, these risks are identified per subsystem in section 14.1 and then mitigation actions are set up accordingly in section 14.2. Finally, the effects of the mitigating actions is visualised in risk tables in section 14.3 and the results are discussed.

14.1. Risk Identification

Quantifying risks is not always easy and is only possible to a certain extent. To make this process easier, each risk is identified in terms of likelihood and impact. Then, after identification, every risk is placed on the scales as accurately as possible before and after mitigation. The scale for likelihood can be found in Table 14.1 and the scale for impact in Table 14.2. In the process of estimating likelihood a scale of 5 was enough, but the impact seemed to vary more so for that case a 7-step scale is used. To fit in the tables, likelihood will be shortened with LLH and impact with IM.

Table 14.1: Likelihood Scale

Scale	1	2	3	4	5
Likelihood	Negligible	Minute	Small	Moderate	High

Table 14.2: Impact Scale

Scale	1	2	3	4	5	6	7
Impact	Negligible	Low	Modest	Medium	High	Huge	Extreme

Now that the scales for likelihood and impact are set, the risks and their consequences can be described and are divided into risks for each subsystem of the HAPS. The risks are listed in Table 14.3.

Table 14.3: Risk Description

Risk ID	Description	Consequence	LLH	IM
Risk Description				
Aerodynamics				
RSK-AE-01	Significant density variation from ISA model	Degradation of aerodynamic performance due to Reynolds number decrease	2	3
RSK-AE-02	Wing profile is not manufactured to tolerance required	Unpredictable aerodynamic performance, i.e. unexpected separation or decreased endurance values	4	4
RSK-AE-03	Thermal effects change effective airfoil and wing geometry	Unpredictable aerodynamic performance, i.e. unexpected separation or change in minimum flight velocity	2	3
RSK-AE-04	Wing torsion during flight changes effective angle of attack	Lift becomes more inefficient as a consequence of either the tips or the root flying at a sub-optimal angle of attack	3	3
RSK-AE-05	Propeller interference effects are stronger than expected	Degradation of aerodynamic performance	2	4
Flight Performance				
RSK-FP-01	Unexpected higher-than-maximum gust loading	Loss of HAPS control	4	6
RSK-FP-02	Unexpected over banking turn	Loss of altitude	2	5
RSK-FP-03	Improper take-off procedure	Repeat take-off procedure	5	3
RSK-FP-04	Improper landing procedure	Landing Failure	3	7
Structures				
RSK-STR-01	Incorrect production of structural spar	Structural failure of structural system	3	7
RSK-STR-02	Incorrect production of structural rib	Structural failure of rib	3	5
RSK-STR-03	Adhesive unevenly applied	Skin ribbed off or failure	4	4
RSK-STR-04	Maintenance inspection incorrectly done	Structural failure of structural element	4	6
RSK-STR-05	Skin incorrectly placed back after maintenance	Breach of humidity-low zones, failure of skin	3	5
RSK-STR-06	Unexpected higher-than-maximum gust loading	Structural failure	2	6
LCT				
RSK-LCT-01	Optical focus lost	Performance degraded	4	5
RSK-LCT-02	Available power reduced	Performance degraded	3	5
RSK-LCT-03	Aeroplane in the optical path	Pilot not able to see / disoriented	4	5
RSK-LCT-04	Drive failure	CPA cannot move	3	6
RSK-LCT-05	FSM Shortage/Discontinued	Critical component shortage	3	6
Propulsion				
RSK-PRO-01	Motor over-heating	Decrease in performance, risk of fire, risk of HAPS failure	5	6
RSK-PRO-02	Electromagnetic Interference	Mal-functioning of near by electronics (ESC, cables)	3	5
RSK-PRO-03	Permanent magnets shortage	Motor not available	2	7
RSK-PRO-04	Structural failure of one blade due to crack propagation	One of out two motors can not be used, damage on structure from debris	3	6
RSK-PRO-05	Dust and granulate inside motor	Reduction in motor performance, risk of deacrease in HAPS's altitude	2	4
Power				

RSK-PW-01	Overheating of batteries causing a thermal runaway condition	Battery is prone to catch fire or explode	2	5
RSK-PW-02	Overcharging the batteries	Degrades lifespan of the batteries	2	2
RSK-PW-03	Deep discharge of battery cells	Reduce capacity and operational life of batteries	1	2
RSK-PW-04	Defunct solar cells	Energy capacity drops, maximum latitude decreases and minimum altitude increases	4	3
RSK-PW-05	Physical damage from debris, birdstrike or weather on solar array during take off	Reduces solar array's performance	4	2
Stability and Control				
RSK-SC-01	Horizontal tail volume is too small	Dynamic or static longitudinal instability	3	6
RSK-SC-02	Vertical tail volume is too small	Inadequate directional stability	2	4
RSK-SC-03	Wing moment coefficient is larger than expected	Higher nominal trim drag	2	3
RSK-SC-04	Failure of a sensor part of a control loop	Potentially unstable eigenmode	3	3
RSK-SC-05	C.g. is more aft than estimated	Dynamic longitudinal instability	4	5
Thermal				
RSK-THL-01	Hole in insulation	BESS capacity and power delivery drops	2	5
RSK-THL-02	Extended period of wind gusts	thermal insulation will not be sufficient and critical components fall below operating temperature	1	5
RSK-THL-03	Extensive solar irradiance	thermal insulation will cause components to exceed operating temperature	1	5
CDHS				
RSK-CDH-01	Loss of Connection	Unable to command the HAPS	5	2
RSK-CDH-02	Bug in flight software	Unexpected action by the HAPS	2	4
RSK-CDH-03	Software crash	HAPS uncontrolled	1	6
RSK-CDH-04	Memory System Failure	Unable to record logging data	3	3
RSK-CDH-05	Positioning Loss	HAPS becomes unable to determine position	4	4

14.2. Risk Mitigation

For each risk it is important that they are mitigated and these mitigating actions linked to the risk-id are listed in Table 14.4. After mitigating action the likelihood and impact will be reduced to the reduced likelihood (RLLH) and reduced impact (RIM) as will also be indicated in Table 14.4.

Table 14.4: Risk Mitigation

Risk ID	LLH	IM	Mitigating action	RLLH	RIM
Risk Mitigation					
Aerodynamics					
RSK-AE-01	2	3	Margin in minimum Reynolds number for desired aerodynamic performance and the use of more complex atmospheric models	1	3
RSK-AE-02	4	4	Rib design takes into account solar panel thickness	3	4
RSK-AE-03	2	3	Thermal effects on structures are modelled and the optimal flight velocity is found for the new geometry	2	2
RSK-AE-04	3	3	Structural deflections are modelled and an intermediate angle of attack is found	3	2
RSK-AE-05	2	4	Perform wind tunnel interference tests under various simulated flight conditions	2	3
Flight Performance					
RSK-FP-01	4	6	Make proper use of control surfaces and systems	1	2
RSK-FP-02	2	5	Make proper use of control surfaces and systems	1	2
RSK-FP-03	5	3	Perform pre-flight checks	2	3
RSK-FP-04	3	7	Take careful flight procedures before and during landing	2	3
Structures					
RSK-STR-01	3	7	Spars quality controlled during production process	1	7
RSK-STR-02	3	5	Ribs quality controlled during production process	1	5
RSK-STR-03	4	4	Adhesive quality controlled after appliance	1	4
RSK-STR-04	4	6	Maintenance routines standardised and verified after completion	1	6
RSK-STR-05	3	5	Use fracture detection techniques (such as applying water) to verify placement	1	5

RSK-STR-06	2	6	Incorporate atmospheric measurement equipment	1	6
LCT					
RSK-LCT-01	4	5	Implementation of validated thermal control system, FEC implemented to increase link margin.	1	3
RSK-LCT-02	2	6	FEC Implemented to increase link margin	2	3
RSK-LCT-03	4	5	ADSB data available so that aeroplane interference is prevented	1	5
RSK-LCT-04	3	6	Drive validation, implementation of lubrication system and maintenance plan.	1	6
RSK-LCT-05	3	6	In-house FSM developed/commissioned or intellectual rights ensured.	3	2
Propulsion					
RSK-PRO-01	5	6	Placing air duct, to create air stream towards coils, states and rotor	2	6
RSK-PRO-02	3	5	Placing ESC far enough from motor	1	5
RSK-PRO-03	2	7	Buying motors in bulk (also reducing unit price)	2	3
RSK-PRO-04	3	6	Visual Inspection and Maintenance on propeller blades	1	6
RSK-PRO-05	2	4	Wiping dust from motor and blades	1	4
Power					
RSK-PW-01	5	2	Implement robust thermal management systems and ensure proper ventilation and cooling	3	1
RSK-PW-02	2	2	Use advanced battery management systems	2	1
RSK-PW-03	1	2	Prevent discharge below a safe threshold with battery management systems	1	1
RSK-PW-04	4	3	Considerations in take off conditions and cleaning	3	3
RSK-PW-05	4	2	Use protective coatings and robust manufacturing	3	2
Stability and Control					
RSK-SC-01	3	6	Test prototype and resize	1	6
RSK-SC-02	2	4	Test prototype and resize	1	4
RSK-SC-03	2	3	Move c.g. further forward	2	2
RSK-SC-04	3	3	Implement redundant sensors for each controller	2	3
RSK-SC-05	4	5	Implement an increased safety margin on c.g. estimation	2	5
Thermal					
RSK-THL-01	2	5	Extensive isolation testing	1	5
RSK-THL-02	1	5	Design thermal heater with extra redundancy	1	5
RSK-THL-03	1	5	Design for most extreme case of solar irradiance	1	2
CDHS					
RSK-CDH-01	4	2	Redundant communication through LCT	2	1
RSK-CDH-02	2	4	All flight software will first be tested on a simulated environment to ensure bugs are detected	1	4
RSK-CDH-03	1	6	Software is first tested on simulated environment	1	4
RSK-CDH-04	3	3	Redundant SD cards are included in the design, arranged in a RAID 1 layout	3	2
RSK-CDH-05	4	4	Positioning can be transmitted by RF or LCT if needed, based on radar location or ADS-B data.	4	2

14.3. Risk Visualisation and Results

To visualise all risks a risk table can be made. In this table, the severity of the risk is shown by colour and is determined by the combination of impact and likelihood. The correlated risk severity by colour is shown in Table 14.5. To make the risk tables more clear, the RSK part of the ID of the risk is left out. The risk before mitigation action can be seen in Table 14.6 and the risk after mitigation can be seen in Table 14.7. The mitigating actions clearly reduced the severity of each risk to an acceptable level with RSK-STR-01 and RSK-PRO-01 being the only medium severity risks only based on their critical function as the motor of the propellor is quite critical as is one of the spars. For both of these parts, it is recommended to perform extra maintenance to further minimise chances of these event occurring.

Table 14.5: Risk Severity by Colour

Colour	Risk Severity
	Very high
	High
	Medium
	Low
	Minimal

Finally, it is important that to ensure mitigation of the risk, the responsible engineer for each subsystems is also set responsible for mitigation of these risks.

Table 14.6: Risk Table Before Mitigation

Impact					
7		PRO-03	FP-04,STR-01		
6	CDH-03	STR-06	LCT-04,LCT-05,PRO-04,SC-01	FP-01,STR-04	PRO-01
5	THL-02, THL-03	FP-02,PW-01,THL-01	STR-02,STR-05,LCT-02,PRO-02	LCT-01,LCT-03,SC-05	
4		AE-05,PRO-05,SC-02, CDH-02		AE-02,STR-03,CDH-05	
3		AE-01, AE-03,SC-03	AE-04,SC-04,CDH-04	PW-04	FP-03
2	PW-03	PW-02		PW-05	CDH-01
1					
	1	2	3	4	5
	Likelihood				

Table 14.7: Risk Table After Mitigation

Im-pact					
7	STR-01				
6	STR-04,STR-06,LCT-04,PRO-04,SC-01	PRO-01			
5	STR-02,STR-05LCT-03,PRO-02,THL-01,THL-02	SC-05			
4	STR-03,PRO-05,SC-02,CDH-02,CDH-03		AE-02		
3	AE-01,LCT-01	AE-05,FP-03,FP-04,LCT-02,PRO-03,SC-04	PW-04		
2	FP-01,FP-02,THL-03	AE-03,SC-03	AE-04,LCT-05,PW-05,CDH-04	CDH-05	
1	PW-03	PW-02,CDH-01	PW-01		
	1	2	3	4	5
	Likelihood				

15. Financial Analysis

In this chapter, a market analysis is presented together with a revenue estimation and cost breakdown structure. These can be found respectively in section 15.1 to 15.4. Together these sections are meant to give a clear image of the financial feasibility of project Eurus for the stakeholders, and in particular the client Airbus.

15.1. SWOT Analysis

To assess the market opportunities, a SWOT analysis is performed in this section. A SWOT analysis consists of an assessment of the strengths, weaknesses, opportunities and threats. Together these internal, external, positive and negative aspects give a clear view of the important factors that determine the potential revenue when entering certain markets. More in-depth information on the SWOT analysis can be found in the baseline report [1].

Table 15.1: SWOT Analysis for HAPS using Laser Communication

Aspect	Internal Factors (Strengths & Weaknesses)	External Factors (Opportunities & Threats)
Positive	**Strengths** • Operating altitude in the Stratosphere • Emerging market • Long Endurance • Secure communication • High data rates • Environmental sustainability • Several profitable use cases	**Opportunities** • Small direct competition • Areas without cable communication • Potential military applications • Increasing need for faster communication • The market position of Airbus
Negative	**Weaknesses** • Direct line of sight required • Limited payload mass • Sensitive to atmospheric conditions • Cost • Limited reference data of HAPS systems operating with an LCT	**Threats** • Bargaining power of suppliers • Powerful potential buyers • Development of 5G networks • Competition from large companies

15.2. Identified Business Cases

The SWOT analysis performed in section 15.1 now gives a clear start to identify the business cases with the highest potential revenue for Airbus. After identifying them, all business cases were filtered for feasibility after which a trade-off was made based on revenue potential, required investment and market saturation. These criteria together describe the attractiveness of a business case resulting in three winning business cases that will be used as design drivers.

Disaster Relief

The first of three final business cases is Eurus, which functions as a high-capacity network access for disaster relief. Telecommunication infrastructures are relatively vulnerable to natural disasters, with such events leading to network power losses, physical infrastructure damage, and over-saturation resulting in partial or complete failure of communications services [140]. Here the HAPS with integrated LCT will be able to provide disaster response services with reliable, high-capacity communication allowing organisations and governments to keep communicating and reacting more organised and effective.

Radio-silent Communication

The second business case is Eurus providing radio-silent communication for multiple applications. The ability to communicate in private and securely has always been desired, this too holds true for wireless communication. The commonly used radio-frequency (RF) communication has issues with being able to be intercepted, decrypted and interfered with. Luckily, laser communication offers the solution by being untraceable and undetectable. The sender, receiver and the data itself are protected. Eurus is well suited to be deployed for this application with potential uses for the government, military and even corporations.

Provide SmallSat and CubeSat Communication Coverage and Support

The third business case is that Eurus provides communication coverage and support for SmallSats and CubeSats. For every satellite, it is required to have some sort of ground station infrastructure available to communicate with the satellite. This infrastructure is expensive and complicated. For large companies with the option to create this infrastructure themselves, this is no problem. However, for small companies that only operate individual SmallSats or CubeSats the cost of ground station operations quickly becomes unfeasible. Using the HAPS, Airbus will be able to offer small companies contact time with the EURUS ground stations by having their satellites communicate through the HAPS vehicles.

15.3. Revenue Estimation

In section 15.2, the business cases with the highest potential revenue have been identified. In this section, the markets they are involved in, the total market size and Airbus' potential revenue will be estimated and discussed.

15.3.1. Global Disaster Preparedness Market

In the first business case, the HAPS functioning as a high-capacity network access for disaster relief finds its potential revenue in the global disaster preparedness market. This market ranges from evacuation services to disaster predictive technology and in our business case, providing network in times of disaster.

Market Size and Region

In 2023, it was estimated that the market size of the global disaster preparedness market was around USD 180 billion. This is a rounded average based on three market analysis reports by DMR (Dimension Market Research)[1], Precedence Research[2] and Acumen[3] which all present similar market sizes.

Similarly, the estimated market size for 2030 is predicted in these analyses resulting in a rounded average market size prediction of USD 315 billion, describing a growth of 75% of this market in 7 years.

Precedence Research also estimates that the emergency response radars segment captured about 30% of the revenue share in 2022, this market segment is relevant for this business case application. They also described the market share per region as can be seen in Figure 15.1.

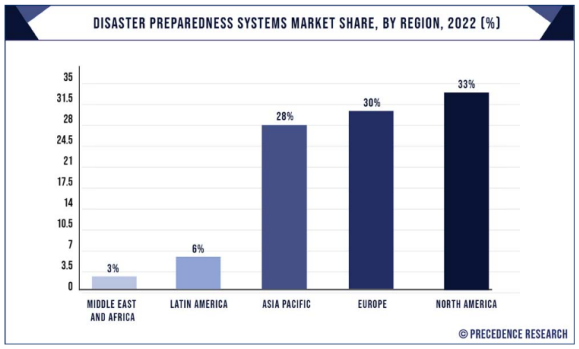

Figure 15.1: Market Share per Region Described by Precedence Research

The largest market share is for North America at the moment. They are currently leading the innovation, but Europe also has quite a large share. The share of Asia-Pacific is predicted to be growing the most thanks to upcoming innovations.

Potential Revenue for Airbus

In this subsection, the total addressable market (TAM) will be discussed, as will be the equally important serviceable addressable market (SAM) relevant to the deployment of the HAPS in this market. It was identified in subsection 15.3.1 that 30% of the market is serviceable and addressable leading to USD 54 billion in 2023 and an estimated USD 94.5 billion in 2030.

Finally, the serviceable obtainable market (SOM) will include the actual market share of Airbus of the SAM. Each per cent of the market share here will result in USD 540 million revenue in 2023 and about USD 945 million revenue in 2030.

15.3.2. Global Communication Intelligence Market

The second business case, exploiting the HAPS for its radio-silent communication capabilities, finds its potential revenue in the global communication intelligence market (GCOMINT). This global communication intelligence market quite accurately describes this specific application of the HAPS.

Market Size and Region

The market size for GCOMINT in 2023 was estimated to be around USD 8.0 billion. This is a rounded average based on three market analyses performed by ResearchDive [119], KBV Research [118] and MMR [108] as all present similar market sizes. The estimated market size for 2030 is predicted to be a rounded average of USD 12.0 billion, describing a 50% growth in 7 years. It should be mentioned that the analysis of KBV only runs until 2028. The 2030 estimate is thus generated by extrapolating with the same CAGR (Compound Annual Growth Rate). The extrapolation leads to similar results as the other two analyses and thus it is judged to be a valid estimation.

ResearchDive [119], similarly to MMR [108], reports a market share in 2021 of about 30% for airborne vehicles similar to our HAPS as can be seen in Figure 15.2.

[1]Dimension Market Research Market Analysis
[2]Precedence Research Market Analysis
[3]Acumen Research Market Analysis

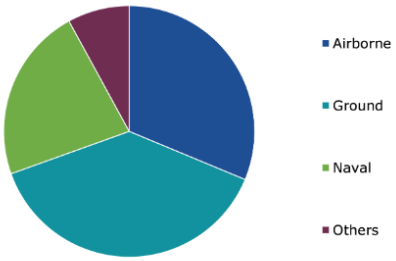

Figure 15.2: Market Share Estimation of Airborne Vehicles in GCOMINT Market by ResearchDive [119]

Then ResearchDive also analysed and described the market share per region for the GCOMINT market. This is depicted in Figure 15.3.

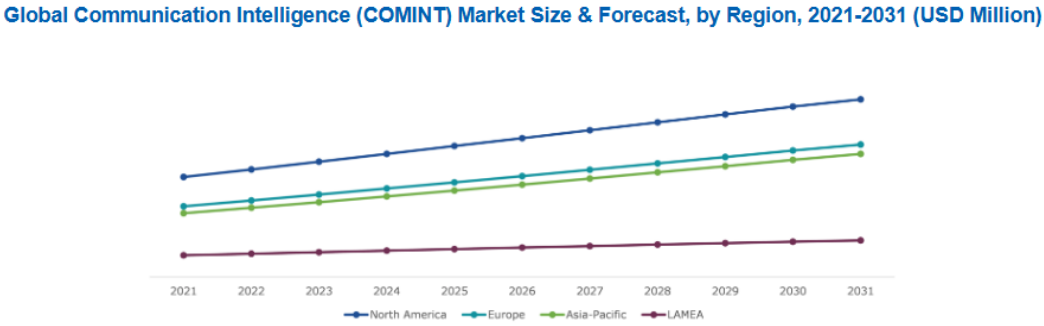

Figure 15.3: The Estimated Global GCOMINT Market Share per Region by ResearchDive [119]

In Figure 15.3, North America has the largest market share in 2023 and is also predicted to have the largest growth up to 2030. Europe and Asia-Pacific have similar market shares and are also predicted to have similar growth up to 2030, growing significantly more than LAMEA (Latin America, Middle East and Africa) but less than North America.

Potential Revenue for Airbus

In this subsection the TAM has been discussed, but it is important to calculate the SAM relevant for deployment of the HAPS in this market. It was identified in subsection 15.3.2 that 30% of the market is part of this SAM leading to a SAM of USD 2.4 billion in 2023 and an estimated USD 3.6 billion in 2030.

Finally, the serviceable obtainable market (SOM) will include the actual market share of Airbus of the SAM. Each per cent of the market share here will result in USD 24 million revenue in 2023 and about USD 36 million revenue in 2030.

15.3.3. Global Small Satellite Market

In the last business case, the HAPS is used to provide communication coverage and support for small satellites, it is less straightforward to determine the market from which to extract potential revenue figures. It was determined that it will be possible to find revenue in the market for small satellites. The HAPS will create value with a supporting role and is not directly competing with satellite operators, but this market will give an image of potential revenue for this business case.

Market Size and Region

We have estimated the market size in 2023 of the small satellite market to be around USD 3.7 billion. This is a rounded average based on three market analysis reports of Fortune Business Insights [80], Spherical Insights [81] and Market Research Future [63] all presenting similar market sizes. Similarly, the estimated market size for 2030 is predicted in these analyses resulting in a rounded average market size prediction of USD 9.3 billion, describing a growth of about 150% of this market in 7 years. Between the three analyses, there were quite large differences with the estimations being in a range of USD 5.8 billion by Fortune Business Insights to USD 12.3 billion by Research Future. This indicates that the growth of this market is still uncertain, which makes sense since an increase of 150% is a lot and the market will thus be changing rapidly in the coming years.

The HAPS will partly be communicating earth observation data, which has about 60% share of the market according to Fortune Business Insights as is also depicted in Figure 15.4.

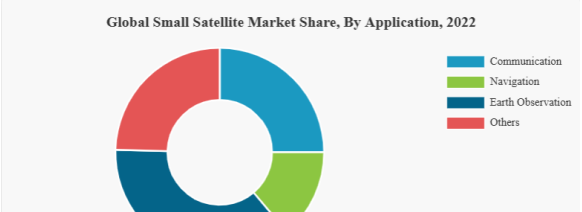

Naturally, this requires that satellites have optical communication to be able to communicate with the HAPS, which seems to be a promising trend [4]

Then looking into the regional market share, Spherical Insights [81] discusses that North America dominates the market with a market share of about 35%. Market Research Future [63] also made an estimation of the rest of the shares for the other regions as can be seen in Figure 15.5. They predict that the share of North America will remain

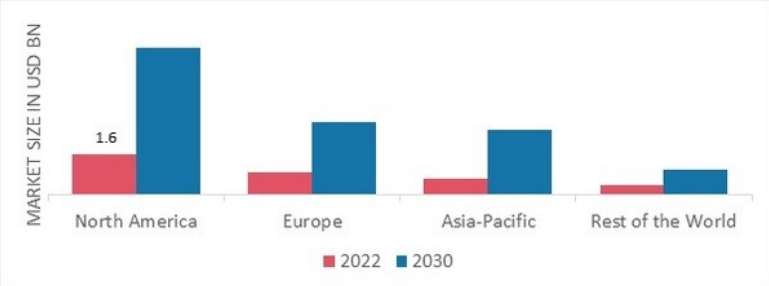

Figure 15.5: SmallSat Market Share Estimation per Region by Market Research Future [63]

dominant as large growth is expected, but the Asia-Pacific
size will increase with the highest estimated CAGR and is thus interesting to watch. The share of Europe will stay steady and is expected to still have the second largest share after North America.

Potential Revenue for Airbus

In this subsection the TAM will be discussed, as well as the SAM. It was identified in subsection 15.3.3 that 6% of the market is part of this SAM leading to a SAM of USD 220 million in 2023 and an estimated USD 232.5 million in 2030.

Finally, the serviceable obtainable market (SOM) will include the actual market share of Airbus of the SAM. Each percent of the market share here will result in USD 2.2 million revenue in 2023 and about USD 5.58 million revenue in 2030.

15.3.4. Final Revenue Estimation and Market Opportunities

To be able to make an accurate estimation of the potential revenue of Airbus, the SOM must be determined. Doing so requires extra knowledge about the market position, the key competitors, and also Airbus' involvement within the market. Entering a market can be difficult and existing competitors can experience advantages in terms of being settled in, one of them being the economies of scale. To overcome a cold start within a market, a strategy must be formed, which can be something like cooperation with existing players in the market or with other smaller companies trying to enter the market.

To summarize the key points and opportunities: The highest potential revenue lies in the global disaster preparedness market. Here just 1% of SAM will result in an estimated revenue of USD 540 million revenue in 2023 and a potential revenue of USD 945 million in 2030. Regional, North America has the largest share at the moment, however, Asia-Pacific's share is expected to have the largest CAGR in the coming 7 years.

In the global communication intelligence market 1% of SAM will result in an estimated revenue of USD 24 million and a potential revenue of USD 36 million in 2030. Regional, North America is leading this market share by quite much and is also expected to be growing. This market will present a large amount of extra potential revenue when an event happens leading to an increased demand for defence and military in general. Establishing that this is a growing market where North America proves to be especially interesting.

Finally, in the global small satellite market, the way of entering is very interesting. The HAPS will support and improve the services of existing competitors and is therefore not in direct competition as in the previous two markets. Airbus also has a significant market share meaning it will not be bothered by phenomena such as the cold start problem. Cooperation and exploitation of the current market position will thus be key in this market. Just 1% of SAM will result in an estimated revenue of USD 2.2 million and for this market enormous growth is predicted. This growth of 150% means that the potential revenue in 2030 for 1% SAM will be USD 5.58 million. Similar to the global preparedness market, North America is the largest force in this market and is expected to stay that with Asia-Pacific showing the largest expected CAGR.

[4] https://www.photonicsonline.com/doc/optical-communication-unleashes-new-era-for-satellites

15.4. Cost Breakdown Structure

A cost breakdown was performed to prove compliance with the cost requirement (REQ-CON-CST-1 and REQ-CON-CST-2) and to consolidate the design overall. The costs of the HAPS platform comprise the development, manufacturing, operations and maintenance. These costs are presented in Tables 15.2 and 15.4 to 15.6. The total cost is then finally presented in Table 15.7. For the non-recurring cost per HAPS, a disposal cost of 1% of the total life cycle cost is added[120], this includes the maintenance, development and production costs. For a modest fleet of locally 20 deployed HAPS, the total mission cost would be €299,848,000. For the LCT the costs comprise development and manufacturing. Operational costs associated with network infrastructure development and maintenance are considered outside of the scope of this report, as the inclusion of the LCT in this report was product design-oriented. The total cost for the theoretical first unit is €400,000. Both final costs have an added 20% to account for uncertainties presented by the state of the design. These percentages reflect the results shown in the sensitivity analyses provided by the subsystems.

The values in Table 15.2 for the HAPS were calculated using Equations (15.1) to (15.6). Zhaodong, Rongxuan and Jing proposed these cost estimate relations providing the cost in dollars (FY14)[149]. These costs were converted to euros in FY24 using a 2% yearly interest rate and a conversion rate of 0.93 EUR/USD. In Equations (15.1) to (15.6) e is Euler's number, W is the weight of the HAPS platform, V the cruise velocity, Q the quantity of HAPS platforms to be manufactured, E is the effectiveness of the design. The inclusion of FTA was not properly defined, however, the paper gives an example value of 2 to 6. For the following calculations, 2 was used.

$$\text{Engineering Construction:} \quad H_E = e^{3.08} W^{0.588} V^{0.962} Q^{0.236} E^{0.018} \tag{15.1}$$

$$\text{Manufacturing Hours:} \quad H_M = e^{11.8} W^{0.063} V^{0.022} Q^{0.627} E^{0.432} \tag{15.2}$$

$$\text{Quality Control:} \quad H_Q = 0.133 H_M \tag{15.3}$$

$$\text{Development Support Costs:} \quad C_D = e^{9.32} W^{0.084} V^{1.13} E^{0.186} \tag{15.4}$$

$$\text{Flight Test fee:} \quad C_F = e^{4.31} W^{0.114} V^{1.39} FTA^{0.129} E^{1.004} \tag{15.5}$$

$$\text{The manufacturing cost of materials:} \quad C_M = e^{9.032} W^{0.092} V^{0.559} Q^{1.031} E^{0.18} \tag{15.6}$$

Table 15.3 presents a breakdown of the manufacturing cost of the materials for the components of each subsystem assimilated throughout this report. The data in Tables 15.2 and 15.5 was taken from the Business Case Report [2]. The maintenance costs per HAPS per year in Table 15.6 are based on the specified expenses per subsystem and their maintenance cycle as presented in Section 11.2, the hangar rental is also based on the Business Case Report [2]. For more information on these costs please refer to that report.

Furthermore, for Table 15.2, 15.4 and 15.6 the costs were calculated using the average wage cost for a mechanic in the Netherlands of €30.2. [5]

In Table 15.8, the assembly cost was estimated using Equation (15.7), where C_{HW_LCT} is the cost for all the components used in the LCT [127]. The design cost of the LCT was calculated using Equation (15.8), where the hourly wage of a designer was estimated at 150 €/hr (FY24), n_{dept_LCT} the members within the LCT development department (an average of 3 people) and t_{dev} the development time (280 hours). Additionally, the testing cost is estimated to be 50% of the design cost.

$$C_{assembly\_LCT} = 27\% \cdot C_{HW\_LCT} \tag{15.7}$$

$$C_{design\_LCT} = 150[N/hr] \cdot n_{dept\_LCT} \cdot t_{dev} \tag{15.8}$$

[5] Accesssed on 20-6-2024:https://www.salaryexpert.com/salary/job/aircraft-mechanic/netherlands

Table 15.2: Development Costs of HAPS Platform for Theoretical First Unit to Nearest k€ (FY24)

Cost Description	Cost in €
Airframe Engineering and Design Cost	3,026,000
Prototype Manufacturing	1,481,000
Development Support and Testing Cost	1,267,000
Total Development Cost	**5,773,000**
Total Wage Costs	4,416,000
Fixed Development cost	1,357,000

Table 15.3: Material Manufacturing Cost Breakdown of HAPS Platform to Nearest k€(FY24)

Cost Description	Cost in €	Relative Cost in %
Propulsion	84,000	14.6%
Structures	130,000	22.5%
Power	340,000	58.9%
CDHS	21,000	3.6%
Control & Stability	2,000	0.3% [1]
Total Material Manufacturing Cost	**577,000**	**100%**

Table 15.4: Production Cost Breakdown per HAPS Platform Taking into Account Assembly and Integration for Fleet Size 20 to Nearest k€(FY24)

Cost Description	Cost in €
Manufacturing	€2,236,000
Development Support and Testing Cost	€317,000
Total Production Cost	**2,553,000**

Table 15.5: Operations Costs of HAPS Platform to Nearest k€ (FY24)

Cost Description	Cost in €
Command Center Costs	100,000
Ground Personnel Costs	134,000
Total Operations Cost	**234,000**

Table 15.6: Maintenance Costs of HAPS Platform to Nearest k€ (FY24)

Cost description	Cost in €
Total Cost per Year per HAPS	213,000
Hangar Rental	14,600,000
Total Fixed Maintenance Cost per Year	**14,813,000**

Table 15.7: HAPS Platform Mission Costs to Nearest k€ (FY24): Recurring, non-Recurring and Total Fleet Mission cost

Cost Description	Cost in €
Recurring costs	
Per HAPS	213,000
Fixed	14,834,000
Non-Recurring Costs	
Per HAPS	2,658,000
Development	5,773,000
20 HAPS for 10 years	**249,873,000**
Including Margin of 20%	**299,848,000**

Table 15.8: LCT Development and Manufacturing Costs to Nearest k€ (FY24)

Cost Description	Cost in €
Development Costs	
Design Cost	126,000
Testing Cost	63,000
Manufacturing Costs	
Component Cost	113,000
Assembly Cost	31,000
Theoretical First Unit Cost	**333,000**
Including Margin of 20%	**400,000**

15.4.1. Product Price

As the costs for the HAPS are now determined, the product price for the HAPS can be found. Using the recurring costs over 10 years together with the initial non-recurring costs as per Table 15.7, the product price per bought HAPS can be determined by identifying the amount of HAPS sold over 10 years. This is shown in Figure 15.6. For 20 bought HAPS, this results in a product price of 12.5 M€ (FY24). An additional profit margin can be used to improve the investment return for possible business partners. In comparison to the Microsoft ground station pricing[6], this would result in a decrease in ground station operation expense by a factor of 4, whilst increasing the possible data transferred by a factor of a thousand.

16. Sustainable Development Strategy

In this chapter, the sustainable development strategy of the EURUS is discussed. This chapter will discuss and elaborate on all design considerations made in the design process so far related to and implementing sustainability. For more detailed parts of the design out of the scope of this project, recommendations are given to reach maximum sustainability. There are different kinds of sustainability and over the sections, they will

[6]URL: https://azure.microsoft.com/en-us/pricing/details/orbital/ [Accessed on 19-06]

Figure 15.6: Product Prices per HAPS Varying with the Amount of HAPS Bought

be split up in social sustainability, environmental sustainability and economic sustainability. The concept of sustainability explore in this chapter is based on treaties such as United Nations Conference on Sustainable Development, Rio+20 [1]

16.1. Social Sustainability

To promote social sustainability community participation is encouraged. The full accounting cost of the life cycle of products cradle-to-grave, including associated social costs, are planned to be measured. Furthermore, improvements in social organisation systems and community well-being over measurable economic benefits are to be promoted. Natural and recyclable materials are to be used in a way that increases impartiality and fairness and reduces societal disturbances. Lastly; funds, know-how, and technology should be properly transferred to those who need them and this is thus recommended to be taken into account in the further design stages [109].

For the EURUS project, social sustainability very much depends on the internal relations of the team. Sustainable contact with the coaches, the client Airbus and other external influences is important and has therefore had sufficient attention throughout the whole project. One team member was assigned to external communications, which helped with clear and sustainable contact with all external parties. Important factors determining social sustainability in this way are mainly communication, attitude and respect.

Clear rules helped avoid conflicts between team members and together with a professional attitude at the needed times this increased social sustainability. Multiple team-building activities took place to enhance the engagement of all team members and built a stronger bond. This resulted in better cooperation between team members and increased the efficiency of the team as a whole [85].

Furthermore, acquiring resources of certain parts of the design can also have large social influences. In the current design of the HAPS, the batteries are for example made from lithium and cobalt. Both of these resources are often mined in inhuman conditions where the local population are close to being enslaved [2]. Therefore it is very important to pay thorough attention to the supplier it will used to procure batteries from sustainable and social sources in further development stages. This logic is also applicable to many other materials on the HAPS such as composite or solar cells.

16.2. Environmental Sustainability

In this section, the environmental sustainability of project EURUS is described by discussing the research and development, the production sustainability, operational sustainability and finally the decommissioning of dead platforms.

16.2.1. Research and Development

The business cases discussed in chapter 15 all have supporting functions generating more use per satellite orbiting in LEO. This means that by deploying a HAPS or even a network of HAPS, it is possible to significantly reduce the amount of space debris launched into space. Even though more vehicles will be occupying the atmosphere, there is now the possibility to bring them back to Earth and be able to reuse the parts for future HAPS systems or the repair of other HAPS systems. This also plays nicely into the shortage of the natural resources of Earth by not sending them out of the atmosphere and waste them.

[1] https://sustainabledevelopment.un.org/index.php?menu=122
[2] https://www.globalwitness.org/en/campaigns/natural-resource-governance/lithium-rush-africa/

16.2.2. Production Sustainability

Material selection plays a big role in sustainability. In the case of these HAPS systems, it is not worth it to set up a whole recycling pipeline since potential recycling would not happen that frequently. Then to minimise the environmental impact it is important to make sure that HAPS systems are brought back to the ground station so that all functioning parts can be reused. The selection of carbon fibre reinforced polymer from chapter 9 aligns quite well with this vision with carbon fibre having a very long lifetime resulting in good opportunities to reuse parts. A disadvantage of this reuse strategy is that it will in the end result in waste in the form of broken parts of which the material will not be recycled.

The manufacturing process also has a big influence on sustainability. Automated fibre placement is used and this will lead to a minimisation of scrap with it being only about 6% [98]. This manufacturing process consumes a lot of energy, so it is important that the potential energy efficiency this process can offer is maximised. There also needs to be a focus on sustainable sources to generate the energy used in these processes.

Then resin transfer moulding (RTM) is also used, which can be done at room temperature to minimise energy usage. It is decided in chapter 12 that RTM is used for multiple parts of the design to decrease the amount of machines required for the manufacturing of EURUS and also make minimising the environmental impact of the logistics easier.

The required solar array area, as determined in chapter 7 is very large and there are thus a lot of solar panels needed for the EURUS. The selected Sharp TJ solar panel needs to be produced in very controlled and high-temperature conditions leading to a large environmental impact. The long lifetime of the panels combined with high efficiency will need to compensate for this high energy consumption.

Logistics often play a big role in the sustainability of a design too. It is very sustainably inefficient to be moving parts of whole countries or even continents. The sustainability will increase significantly if as many parts as possible are manufactured in a sustainable manufacturing chain, with the EURUS only using two main manufacturing methods also allowing for minimal travel of parts. It is also possible and recommended in further design to make sure the whole system obtains a sustainability certification, such as ISO 14001 certification. This will then again also increase the image of EURUS and thus the social sustainability.

16.2.3. Operational Sustainability

The impact of the EURUS in operation also needs consideration. The system will need constant energy to be able to keep operating since it is still in the atmosphere. All power for the EURUS will be generated with the solar panels present on the wing surfaces of the HAPS at will then generate and store enough energy to have enough energy left for the night-time. In this way, EURUS will be able to operate on sustainable solar energy.

Next to the generation of required power, it is also possible to increase the sustainability of the HAPS systems by increasing the sustainability of the whole communication network they are part of. There has e.g. been research on cell-switching technology with which energy consumption of the cellular network as a whole can be significantly decreased. Here the HAPS systems play a crucial role by extending coverage, enhancing capacity and allocate resources in an intelligent way [25]. It is recommended to keep this into account in further design stages and look into the feasibility and application context of this concept.

Another important part of operational sustainability is the length of one operational cycle and the total lifetime of a HAPS system. Designing complex systems as this one always has fixed costs in terms of money, but also in terms of sustainability. Designing to increase the operational lifetime of one HAPS system by sacrificing a bit of the direct material sustainability for example has been taken into account during the material selection.

Finally, another aspect of operational sustainability is ensuring sustainable maintenance practices, allowing a system to operate for an extended period before decommissioning. This factor has an impact both at the design level, ensuring parts can be accessed and replaced without causing damage to the system, as well as during the operational phase directly by considering the procedures for maintenance. Ensuring components are designed to minimise material waste during maintenance, especially toxic material waste, ensures a sustainable design continues to be sustainable through its life cycle. This design of the EURUS has not reached this level of detail yet, but this is highly recommended to take into account for future more detailed design.

16.2.4. Decommissioning

The final phase concerned with sustainability is the decommissioning of the system. In this phase, the system will be deconstructed and taken out of service. This has the potential to introduce significant environmental concerns, as the components and elements of the system are discarded. Designing for reuse of components will help minimise the impact of the vehicle at the end of its life. The main goal here should be to ensure that decommissioned systems can be used as parts donors for other functioning systems, minimising the lost material and parts through decommissioning.

16.3. Economic Sustainability

During the design of the EURUS three business cases have been used as design drivers, leading to design decisions based on functioning in attractive markets with lots of revenue, or profit, potential. These business cases have been thoroughly analysed: The markets, specifically the relevant part of the market, they will enter have been determined and potential revenue has been determined and reported to the client Airbus. In chapter 15 a cost breakdown structure is made and these factors combined give a clear view of the economic sustainability of EURUS.

16.4. Sub-system Sustainability Considerations

To create more awareness on the sustainability implications of the design of each subsystem, the relevant subsystems are discussed in this section expanding on previously discussed parts and adding more detailed considerations.

LCT: When considering the sustainability of the LCT, one positive aspect of using laser communication is that it helps prevent further crowding of the RF spectrum for communication. This efficient use of the communication spectrum reduces the need for additional infrastructure and energy consumption, contributing to overall sustainability. Furthermore, the next point to consider for the LCT is the main material used for manufacturing it, namely Titanium TI 6AL-4V. This material is used for the big part of the LCT, which is used for the gimbal and the housing of the telescope. Even though Titanium is an exceptionally environmentally friendly material that does not pose any risk to human health or the ecosystem [3], the same can not be said about the mentioned alloy. This is mainly due to the highly energy-intensive process involved in its production that has a significant environmental impact which poses challenges to its sustainability. Efforts to improve efficiency of these processes and to reduce emissions are continuously evolving, making the process more sustainable but it remains a energy intensive production. However, despite the aforementioned point, it should be noted that this material is still relatively sustainable due to its long lifespan and recyclability and its footprint is mitigated by these.

Aerodynamics: In the design of the aerodynamics subsystem it is mainly the aerodynamic efficiency that impacts sustainability. In this case, the required lift is not limiting in terms of wing surface area, so mainly the drag and endurance performance of the subsystem is important here. During the airfoil selection the FX 63-137 was selected, but this airfoil still has quite a high C_L leading to more induced drag. While still optimising for ${C_L}^3/{C_D}^2$, maximum endurance, it would possible to reduce these lift properties when combining it with reduced drag properties for the wing. Less drag means less thrust needed leading to lower power required, which again would decrease the wing surface and decrease drag. The optimisation between minimum drag and maximum endurance is thus the leading force contributing to the sustainability of the aerodynamics subsystem.

Power: Within the power subsystem, the sourcing of materials inside the electronic components presents difficulties, as a high proportion of these materials used are scarce or sourced under unethical conditions (i.e. cobalt mining). However, for the solar array, the Sharp Triple Junction cell is manufactured using InGaP/GaAs/InGaAs. According to a report by Mohr N. J. et al. the production of the metals inside the proposed solar cells has a high material efficiency and similar environmental impacts as silicon-based cells[110]. For the BESS, lithium cobalt oxide (LCO) creates less CO2 emissions when compared to the considered lithium nickel manganese oxide and lithium manganese oxide. Furthermore, when considering resource depletion, LCO batteries require fewer resources all across the board [68].

Propulsion: BLDC use permanent magnets to rotate the rotor. Such magnets use rare-Earth metals that pose many sustainability-related problems. Their mining is highly polluting. Additionally, as their name suggests, they risk running out. Neodymium is often used for such applications, it was reported that its price has increased by 312% between 2020 and 2022 and is expected to rise. [4]. Therefore, solutions need to be found to ensure the existence of the technology in the future. Highly compressed aluminium is now used to replace ever more rare copper coils [5] but more research needs to be done. Companies such as Advanced Electric Machines (AEM) are leaders in the field.

Structures: For the structural subsystem, the main considerations are the materials used. Composites are currently the market leaders in making stiff lightweight structures.[6]. These light-weight structures together with the new production techniques allow for new possibilities within the structures subsystem that can save on energy usage compared to metals[99]. By not using an autoclave within the production process, the energy per unit saved is reduced by a factor of 4[99]. Additional energy savings might present themselves in the future with the further development of composite materials and their production. As the spar is designed to be safe life, the structural integrity of the spar is still present when the HAPS is decommissioned. This severely increases the

[3] https://keitheurope.com/en/blogs/nos-articles/the-positive-environmental-impact-of-titanium-products
[4] https://advancedelectricmachines.com/how-do-we-make-electric-vehicles-genuinely-sustainable/
[5] https://www.cnbc.com/2023/02/07/there-isnt-enough-copper-in-the-world-shortage-could-last-until-2030.html
[6] URL: https://online-engineering.case.edu/blog/advancements-in-materials-science [Accessed on 18-06]

possible end-of-life use cases for the spar. The end-of-life use-cases for the other structural elements are less fortunate. CFRP is not that reusable in case parts are broken or damaged, these elements will most likely be put into a landfill.

Thermal: For the thermal subsystem, it was recommended to insulate the BESS using expanded polystyrene. This material was chosen as it not only has excellent insulation properties but can also be implemented with little environmental impact as it can be made from recycled plastics at great efficiencies[43].

CDHS: For the CDHS, the material cost of the components is low but the most impactful consideration of the environmental and economic sustainability of the subsystem is the wear-out rate of the LCT Cache. As the array of SSD storage devices may fail after a single mission of use and hence replacement of the 4-drive array is required after each mission. This is both expensive and inefficient, requiring 4 new SSDs to be manufactured and purchased, as well as produce 4 unusable hard drives as waste, that cannot be easily recycled into its raw components. This may be mitigated in the future with advanced RAM chips being developed, that would provide the needed capacity without the write constraints [7] but this technology is not as of yet available.

17. Final Design

In this chapter, the final design of the HAPS will be presented. In section 17.1, the aircraft configuration will be presented. After which the placement of the LCT is analysed in section 17.2. Finally, in section 17.3, the summarised relevant characteristics of the HAPS will be presented.

17.1. Configuration

From chapter 4 to 10, all separate subsystems have been designed. In this section, the integration, placement and configuration of these subsystems will be presented. Important considerations will also be analysed.

As can be seen in Figure 17.1, an overview of the final configuration has been created.

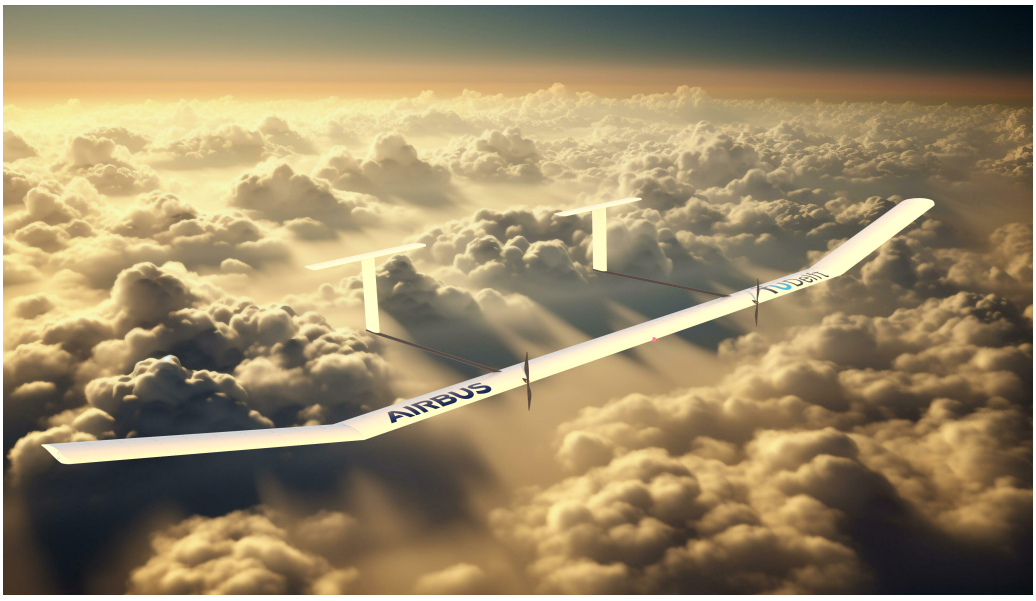

Figure 17.1: Render of HAPS verhicle

17.2. LCT Placement Considerations

The placement of the LCT is paramount for its functionality. As has been elaborated on in section 2.6, its placement has a huge influence on the field of regard as well as the stability of the link. Each HAPS should allow for three fundamental relay modes (depicted in Figure 17.2) as a consequence of the geometric constraints associated with a two LCT payload.

Fortunately, these relay modes allow for the fulfilment of any end-to-end link (within link-distance) with just two HAPS. However, they require that the field of regard of the LCTs when integrated into the platform be at least 180 degrees. A more involved discussion of how the business cases lead to these links and their consequences

[7] https://semiconductor.samsung.com/dram/ddr/ddr5/

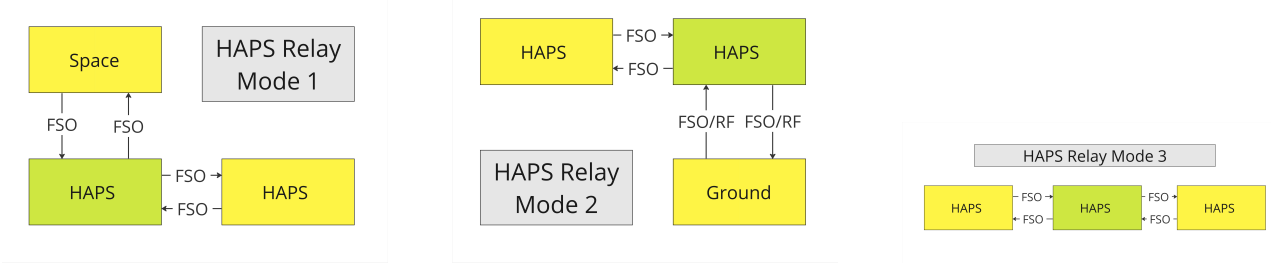

(a) Relay Mode 1 **(b)** Relay Mode 2 **(c)** Relay Mode 3

Figure 17.2: Required HAPS Relay Modes

on the placement of the LCTs is presented in the Midterm report [3]. Figure 17.3 presents the placement of the subsystems within the main wing of the HAPS, including that of the LCTs. Heavy components, like the batteries, have been placed in such a way that they provide bending relief for the wings. Also, solar panels, even though they are lightweight, can provide bending relief in this manner. One of the LCTs is placed facing forward on the leading edge of the plane at the centre line. The other LCT is placed facing downwards, also on the centre line but longitudinally slightly behind the main-wing spar. The placement of the LCTs in these positions is as mentioned before due to geometric constraints on the link-formation. These effects are mainly related to the manoeuvring of the aircraft in order to stay within the link distance or to avoid breaking the line of sight in general. Generally, the front LCT is used for links to any of the three receivers (ground, space or HAPS), whereas the bottom LCT is usually used for HAPS links. In subsection 17.2.1 and subsection 17.2.2 the reasoning behind these choices in conjunction with the field of regard of each LCT is discussed particularly in the context of allowing for the three fundamental relay modes presented in Figure 17.2.

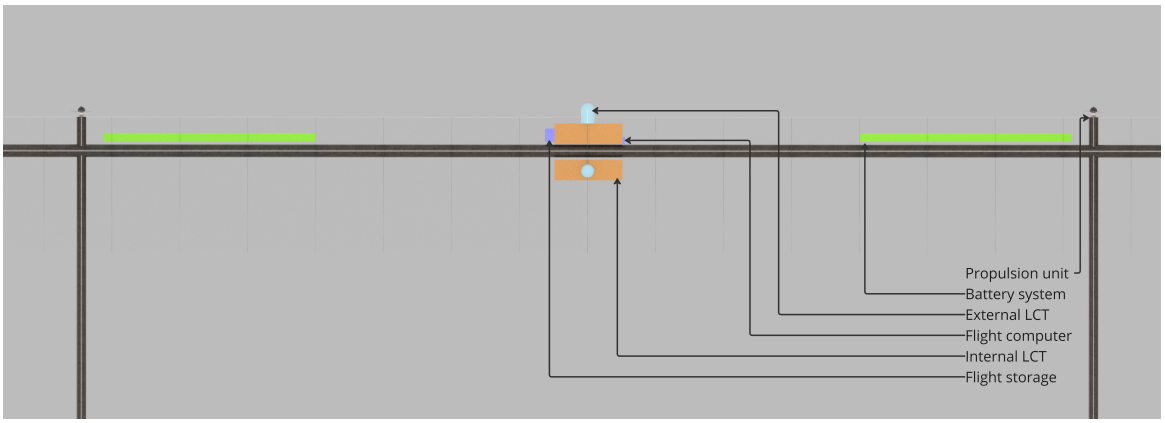

Figure 17.3: System Layout

17.2.1. Bottom LCT

It was discussed in section 17.2 that the field of regard of each LCT would be at least 180° to fulfil the specified relay modes. Here this statement is clarified further since the field of regard is a cut out of a sphere originating at the point the optical signal leaves the LCT so the 180° measure by itself does not specify in what direction the measure applies. The spherical field of regard is divided into three circular cross-sections in Figure 17.4, these three cross-sections correspond to a front view as in Figure 17.4a, a side view as in Figure 17.4b, and a top-down view as in Figure 17.4c.

For the bottom LCT, which is largely responsible for inter-HAPS communication, the 180° criterion applies to two of these sections, effectively reducing the full sphere field of regard to slightly more than a hemisphere. A quick look at Figure 17.5c shows the cross section for which the circle is nearly complete (the two small gaps will be discussed after the placement presentation is complete). The remaining two cross-sections, autoreffig:bottom-side-view and Figure 17.4a, have their field of regard restricted by the aircraft itself. The front view is limited by the wings of the craft with an exception for their dihedral. As the LCT sticks out and the wing structurally deflects during operation a value of more than 180°, namely 182.2°, is ensured. The side-view is limited by the leading edge of the main wing, and off-axis by the tails of the aircraft which also will deflect upwards during flight due to their producing a pitch-down moment for nominal longitudinal stability conditions. Once again this leaves the angle at more than 180° namely 198.9°. Now with regard to the aforementioned gaps, they are as a result of the propellers, which may partially block the laser if the target is directly in that direction. However, the FOR coverage of these gaps is small enough, and the relay modes

involve large movements in the targets (satellite or HAPS) and in the main HAPS itself, such that while the data transmission may be interrupted the alignment is not lost. This allows transmission to resume when the target is out of the gap.

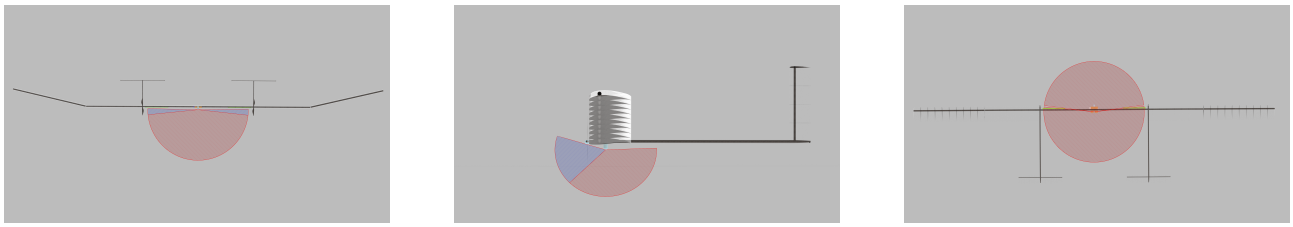

(a) Front View **(b)** Side View **(c)** Top-Down View

Figure 17.4: Different FOR Cross-Sections of the Bottom LCT

17.2.2. Front LCT

Moving on to the front LCT, which is largely responsible for ground and space links. The spherical FOR is divided into three circular cross-sections in Figure 17.5, these three cross-sections correspond to a front view in Figure 17.5a, a side view in Figure 17.5b, and a top-down view in Figure 17.5c.

The 180° criterion applies to two of these sections, also reducing the full sphere field of regard to slightly more than a hemisphere. A quick look at Figure 17.5a shows the front view for which the circle is complete. The remaining two cross-sections, the side and top-down views, (Figure 17.5b and Figure 17.5c respectively) have their field of regard restricted by the aircraft itself. The side view is limited by the wings of the craft (the front of the airfoil in particular) this is depicted by the circle including the blue regions. The blue regions represent the blockage of the FOR by the propellers if the LCT were to be directly in front of them. This corresponds to the worst-case view blocking if the LCT is pointed in the direction of the propellers but as can be seen, this is still more than 180° namely 192.2°. The top-down view is limited by the leading edge of the tips of the main wing. However, since the signal output is positioned slightly forward this leaves the angle at slightly more than 180° namely 180.8°.

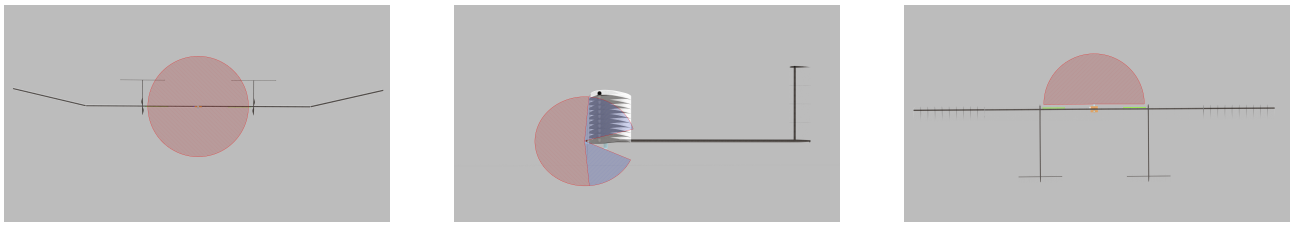

(a) Front View **(b)** Side View **(c)** Top-Down View

Figure 17.5: Different FOR Cross-Sections of the Front LCT

17.3. Performance Analysis

During the design process, multiple iteration processes have taken place where a few important parameters as the required power and the mass are continuously iterated between the flight performance, power, propulsion, aerodynamics and structures subsystems. In further design stages, one could combine the code of all the subsystems and optimise these parameters where for these parameters a snowball effect will take place. The snowball effect for mass is well known in aircraft design, but a similar process will take place for the power. Less required power leads to a smaller wing area leading to smaller drag. When there is less drag, less thrust is required and thus less power is required to continue this loop.

After all iterations that took place, the values of the main parameters converged to the final parameter values of the HAPS which are shown in Table 17.1.

Table 17.1: HAPS Final Design and Mass Budget

Category	Parameters	Value	Unit
Mission Characteristics	Operational Latitude	± 51.2	[deg]
	Operational Ceiling	25	[km]
	Reliability	0.817	[-]
	Operational Life Time	10	[years]
	Availability	99.6	[%]
Flight Performance	Stall IAS	4.66	[m/s]
	Climb Duration[1]	6.91	[hours]
	Descent Duration[1]	3.96	[hours]
	Cruise Duration[1]	13.13	[hours]
	Max Load Factor	3.70	[-]
	Max Power Required	2561	[W]
Aerodynamics	Wing Area	111.4	$[m^2]$
	Wing Span	50	[m]
	Wing Airfoil	FX 63-137	[-]
	Re Range	$1.5\text{-}7{\cdot}10^5$	[-]
	$\frac{C_L}{C_D}$ at 25km	24.25	[-]
Propulsion	Propulsive Efficiency	0.77	[-]
	Number of Engines	2	[-]
	Propeller Diameter	2.29	[m]
	Max Thrust (25 km)	172.5	[N]
Power	Cell Type	Sharp TJ	[-]
	Solar Array Area	99	$[m^2]$
	Battery Type	$LiCoO_2$	[-]
	Battery Energy	25.5	[kWh]
LCT	Optical Power	5	[W]
	Air-to-Air Link	428	[km]
	Air-to-Ground Link	25	[km]
	Air-to-Space Link	2000	[km]
	Data Rate	1-10	[Gbits]
Control & Stability	V-Tail Area	6.40	$[m^2]$
	H-Tail Area	11.4	$[m^2]$
	Fuselage Length	7.9	[m]
Thermal	Type of Control	Passive	[-]
	$T_{out} - T_{inside}$ (day)	11	[°C]
	$T_{out} - T_{inside}$ (night)	1	[°C]
CDHS	Data Rate Up	10	[Mbits]
	Data Rate Down	100	[Mbits]
Structure	Skin Material	Hostaphan 87220	[-]
	Spar Outer Diameter	190	[mm]
	Spar Thickness Root-Tip	0.2-6.6	[mm]
	Rib Spacing	1	[m]
Mass Budget	Propulsion	8.69	[kg]
	Structures	126.15	[kg]
	Power	78.72	[kg]
	LCT	16.30	[kg]
	CDHS	0.411	[kg]
	Control & Stability	28.33	[kg]
	Total	**258.6**	[kg]

18. Verification & Validation

Verification and Validation (V&V) are critical components of any engineering project, ensuring that the system meets its requirements and performs as expected. Verification involves checking that the system correctly

[1]For Winter Solstice

implements the specified requirements, whilst validation ensures that the system fulfils its intended purpose in the real-world scenario. This section outlines the structured approach to V&V, detailing the procedures and methodologies employed to ensure the integrity and reliability of the design.

18.1. Verification Procedures

In the design process, models have been created to support the design. This ensured that, through an iterative process, the optimal design could be found with the help of these models. To verify these models, verification procedures were implemented.

18.1.1. Code Verification

Code verification focuses on ensuring that the computational models correctly implement the intended algorithms without errors. This involves a series of tests to detect and correct any discrepancies between the code and the specifications. Methods to ensure this are the following which have been performed continuously throughout the design process.

- **Static Analysis**: Conduct a thorough review of the code to identify syntax errors and logic errors.
- **Unit Testing**: Perform unit tests on individual modules to ensure that each part functions correctly.
- **Integration Testing**: Test the interaction between units to identify if any issues arise.

18.1.2. Calculation Verification

Calculation verification ensures that the numerical solutions provided by the computational models are accurate. This process involves comparing the model outputs with analytical solutions. The following methods are used:

- **Convergence Testing**: Perform tests to ensure that the numerical solution converges as the mesh is refined or as time steps are reduced.
- **Sensitivity Analysis**: Analyze how sensitive results are to changes in inputs to ensure robustness.

The importance of the sensitivity analysis has been further accentuated by providing a dedicated section for each subsystem.

18.1.3. Product Verification

Product verification must be done to prove that the design meets the requirements. The compliance matrix has been constructed to prove that the design complies with the requirements. Technical requirements are shown in Table 18.1, Operational requirements in Table 18.2, Constraint requirements in Table 18.3, Organisational requirement in Table 18.4 and Sub-system requirements in Table 18.5. The first column shows the requirement ID. The second presents the relevant value if applicable. Additionally, a colour code was used to distinguish between met, not met and not yet checkable requirements, namely: green the requirement is met, red the requirement is not met and blue signifies that the requirement can not be checked but is most likely met. The last column indicates in what part of the report the proof of the requirement can be found and the method used to verify it. An effort was made to be as specific as possible. However, in some cases, an entire chapter proved the compliance of the requirement. To prove the requirements, 4 methods were used primarily:

- **Inspection (I):** Verification by inspection and performing measurements.
- **Analysis (A):** Verification by mathematical analysis, including simulation.
- **Demonstration (D):** Verification by demonstrating the product capabilities.
- **Test (T):** Verification by testing the end product in real-life conditions.

Note that at this stage only Analysis can be done as Inspection, Demonstration and Test would require real-life work.

Table 18.1: Technical Requirement Compliance Matrix

Requirement	Value	Proof (Method)	Requirement	Value	Proof (Method)
REC-TEC-MAI-1		Section 17.1 (I)	REC-TEC-OPT-5	$\leq 60sec$	Section 2.4.3 (T)
REC-TEC-MAI-2		Chapter 9 (I)	REC-TEC-OPT-6	360, 190 deg	Section 2.5.4 (A,T)
REC-TEC-MAI-3		Chapter 9 (I)	REC-TEC-OPT-7	0.3 deg	Section 2.5.3 (A,T)
REC-TEC-LIN-1	$\geq 25km$	Section 2.2 (A,T)	REC-TEC-OPT-8		Section 17.2 (A,D)
REC-TEC-LIN-2	428 km	Section 2.2 (A,T)	REC-TEC-SEN-1		Section 10.6.3 (A,T)
REC-TEC-LIN-3	$\geq 2000km$	Section 2.2 (A,T)	REC-TEC-SEN-2		Section 10.6.3 (A,T)
REC-TEC-DAP-1	$\geq 1Gbps$	Section 2.2 (A,T)	REC-TEC-SEN-3		Section 10.6.3 (A,D)
REC-TEC-DAP-2		Section 2.3.1 (A,D)	REC-TEC-SEN-4		Section 10.6.3 (A,D)
REC-TEC-DAP-3		Section 2.3.1 (A,D)	REC-TEC-SEN-5	2 (1σ) m	Section 2.4.4 (A,D)
REC-TEC-DAP-4		Section 2.1 (A,T)	REC-TEC-PRO-1.1		Section 6.2 (A,T)
REC-TEC-DAP-5	$\geq 1Gbaud$	Section 2.2 (A,T)	REC-TEC-PRO-1.2		Section 6.2 (A,T)
REC-TEC-DAP-6	FPGA	Section 2.1 (A,D)	REC-TEC-PRO-2		Section 6.2 (A,T)

REC-TEC-DAP-7	FPGA	Section 2.1 (A,D)	REC-TEC-STR-1.1		Section 8.3 (A,D)
REC-TEC-INT-1	$\leq 0.5N$	Section 2.5.6 (A,T)	REC-TEC-STR-1.2		Section 9.3.2 (A,D)
REC-TEC-INT-2		Section 2.3.2 (A)	REC-TEC-STR-1.3		(A,D)
REC-TEC-LSN-1		Section 2.1 (A,T)	REC-TEC-STR-1.4		Section 9.3.2 (A,D)
REC-TEC-LSN-2	-56.1 dBm	Section 2.3.1 (A,T)	REC-TEC-STR-1.5		Section 9.3.2 (A,D)
REC-TEC-LSN-3	1.37 mV	Section 2.3.1 (A,T)	REC-TEC-STR-2.1		Section 9.4.2 (A,D)
REC-TEC-LSN-4		Section 2.3.1 (A,T)	REC-TEC-STR-2.2		Section 9.4.2 (A,D)
REC-TEC-LSN-5	10 Gsps	Section 2.3.1 (A,T)	REC-TEC-STR-2.3		Section 9.4.2 (A,T)
REC-TEC-LSN-6	1525-1575nm	Section 2.3.1 (A,I)	REC-TEC-AE-1		Section 4.2 and 4.4 (A,D)
REC-TEC-LSR-1		Section 2.1 (A)	REC-TEC-AE-2		Section 4.4 (A,D)
REC-TEC-LSR-2	$\leq 5W$	Section 2.3.1 (A,D)	REC-TEC-AE-3		Section 4.2.1 (A,T)
REC-TEC-LSR-3	≤ 1.1	Section 2.3.1 and 2.5.3 (A,T)	REC-TEC-SC-1	Level 5	Section 10.6 (A,D)
REC-TEC-LSR-4	$\geq 26\mu rad$	Section 2.5.3 (A,D)	REC-TEC-SC-2.1		Figure 5.3 (A,T)
REC-TEC-LSR-5	80 ps	Section 2.3.1 (A,D)	REC-TEC-SC-2.2		Section 5.2.2 and 5.3.2 (A,T)
REC-TEC-LSR-6	6.4 $\mu W/m^2$	Section 2.2 (A,T)	REC-TEC-PW-1		Section 7.3 and 7.4 (A,T)
REC-TEC-LSR-7	1535-1565nm	Section 2.1 and 2.3.1 (A,I)	REC-TEC-PW-2		Section 7.3 and 7.4 (A,T)
REC-TEC-OPT-1	360n, 190 deg	Section 2.5.4 (A,D)	REC-TEC-PW-3		Section 7.3 and 7.4 (A,T)
REC-TEC-OPT-2	18 deg/s	Section 2.5.5 (A,D)	REC-TEC-PW-4		Section 7.3 and 7.4 (A,T)
REC-TEC-OPT-3		Chapter 2 (A,D)	REC-TEC-PW-5		Section 7.4 (A,D)
REC-TEC-OPT-4		Section 2.4.2 (A,D)	REC-TEC-SEN-6	0.03 (1σ) deg	Section 2.4.4 (A,T)

Table 18.2: Operational Requirement Compliance Matrix

Requirement	Value	Proof (Method)	Requirement	Value	Proof (Method)
REQ-MOP-NWR-1		Section 13.1 (A,D)	REQ-MOP-COV-3.2		(A,I)
REQ-MOP-NWR-2		Section 13.2 (I)	REQ-MOP-CNW-1.1		Section 10.3 (I)
REQ-MOP-NWR-3		Section 13.2 (A,D)	REQ-MOP-CNW-1.2		Section 10.3 (I)
REQ-MOP-NWR-4		Section 10.3 (I)	REQ-MOP-CNW-1.3.1		Section 13.2 (I)
REQ-MOP-DEP-1		Section 13.2.2 (A)	REQ-MOP-CNW-1.3.2		Section 13.3 (I)
REQ-MOP-DEP-2		Section 13.2.2 (D)	REQ-MOP-CNW-1.3.3		Section 13.3 (I)
REQ-MOP-COV-1.1		(A,T)	REQ-MOP-CNW-2		(T)
REQ-MOP-COV-1.2		(T)	REQ-MOP-CNW-3		Section 13.1 (I)
REQ-MOP-COV-2		(T)	REQ-MOP-CNW-4		Section 13.1 (I)
REQ-MOP-COV-3.1		Section 13.1 (A,I)	REQ-MOP-CNW-5		Section 10.3 (I)

Table 18.3: Constraint Requirement Compliance Matrix

Requirement	Value	Proof (Method)	Requirement	Value	Proof (Method)
REQ-CON-CST-1	2 million € (FY24)	Table 15.7 (A)	REQ-CON-SFT-2		Chapter 19 (I)
REQ-CON-CST-3	135 Keuro	Section 2.1 (A)	REQ-CON-SFT-3		Chapter 19 (I)
REQ-CON-CST-4		Table 15.8(A)	REQ-CON-CMP-1		Chapter 9 (A,T)
REQ-CON-LGL-1		Chapter 19 (I)	REQ-CON-CMP-2		Section 10.3 (A,D)
REQ-CON-LGL-2		Chapter 2 (I)	REQ-CON-CMP-3		Section 10.4 (A,I)
REQ-CON-LGL-3		Chapter 19 (I)	REQ-CON-CMP-4		Section 10.4 (A,I)
REQ-CON-LGL-4		Chapter 19 (I)	REQ-CON-ENB-1	150x 300x 900 mm^3	Section 2.3.2 (A,I)
REQ-CON-LGL-5		Chapter 19 (I)	REQ-CON-ENB-2	8 kg	Section 2.1 (A,I)
REQ-CON-RSC-1		Chapter 2 (I)	REQ-CON-ENB-3	90 W	Section 2.1 (A,I)
REQ-CON-RSC-2		Section 9.3.2 (I)	REQ-CON-REL-1	0.817	Section 11.1 (A,T)
REQ-CON-RSC-3		Section 9.3.2 (I)	REQ-CON-REL-2		Section 11.2 and 11.1 (D)
REQ-CON-RSC-4		Chapter 2-10 (I)	REQ-CON-REL-3		(D)
REQ-CON-SFT-1		Section 11.4 and 11.1 (I)			

Table 18.4: Organisation Requirement Compliance Matrix

Requirement	Value	Proof (Method)	Requirement	Value	Proof (Method)
REQ-CON-SCL-1		(D)	REQ-CON-SCL-3		(D)
REQ-CON-SCL-2		(D)			

Table 18.5: Sub-system Requirement Compliance Matrix

Requirement	Value	Proof (Method)	Requirement	Value	Proof (Method)
REQ-PRO-1	172.5 N	Table 6.2 (A,T)	REQ-STR-REL-6		(T)
REQ-PRO-2	4.9 kW	Table 6.2 (A,T)	REQ-STR-REL-7		(T)
REQ-AE-1	111.4 m^2	Table 4.5 and 5.2 (A,D)	REQ-STR-REL-8		(T)
REQ-AE-2		Section 4.4 (I)	REQ-STR-REL-9		(T)
REQ-SC-1		Figure 5.3 (A,T)	REQ-STR-REL-10		Section 9.4.3 (A,T)
REQ-SC-2		Section 5.3.1 (T)	REQ-STR-REL-11		Section 9.4.3 (A,T)
REQ-SC-3		Section 5.3.1 (T)	REQ-STR-REL-12		Section 9.4.1 (A,I)
REQ-SC-4		Section 5.3.1 (T)	REQ-STR-REL-13		Section 9.4.1 (A,D)
REQ-SC-5		Section 5.4 (I)	REQ-STR-REL-14		Section 9.4.1 (A,D)
REQ-PW-1		Section 7.3 and 7.4 (A,T)	REQ-STR-MAN-1		(T)
REQ-PW-2		Section 7.3 and 7.4 (A,T)	REQ-STR-MAN-2		Section 12.2 (D)
REQ-PW-3		Section 7.3 and 7.4 (A,T)	REQ-STR-MAN-3		Section 12.2 (D)
REQ-PW-4	-45 to 45 deg	Figure 7.6 and Section 7.4 (A,T)	REQ-STR-MAN-4		Section 9.4.3 (A,T)
REQ-PW-5	15 km	Section 7.4.1 (A,T)	REQ-STR-MAN-5		Section 12.2 (D)
REQ-FP-1		Chapter 3 (A,T)	REQ-CDH-OPS-1		Chapter 10 (A,T)
REQ-FP-2		Chapter 3 (A,T)	REQ-CDH-OPS-2		Chapter 10 (D)
REQ-FP-3		Chapter 3 (A,T)	REQ-CDH-OPS-3		Section 10.3.4 (A)
REQ-FP-4		Chapter 7 (A,T)	REQ-CDH-OPS-4		Section 10.3 (I)
REQ-FP-5		Section 3.5 (A,T)	REQ-CDH-LCT-1		Section 10.3(I)
REQ-FP-6		Section 3.5 (A,T)	REQ-CDH-LCT-2		Section 10.5.4 (T)
REQ-FP-7		Section 3.4 (A,T)	REQ-CDH-APS-1		Section 10.3.4 (T)
REQ-FP-8		Section 3.2 (A,T)	REQ-CDH-APS-2		Section 10.6 (T)
REQ-THL-1	-20 °C	Section 8.4 (A,T)	REQ-CDH-APS-3		Section 10.6 (I)
REQ-THL-2		Section 8.4 (A,T)	REQ-CDH-APS-4		Section 10.6 (I)
REQ-STR-INT-1		Section 9.4.1 (A,T)	REQ-CDH-APS-5		Section 10.6 (A,T)
REQ-STR-INT-2		Section 9.4.3 (A,T)	REQ-CDH-APS-6		Section 10.6 (D)
REQ-STR-LCT-1		(T)	REQ-CDH-APS-7		Section 10.6 (D)
REQ-STR-LCT-2		Section 9.4.3 (A,T)	REQ-CDH-GND-1		Section 10.3.3 (T)
REQ-STR-LCT-3		Section 17.2 (A,I)	REQ-CDH-OBC-1		Section 10.3 (D)
REQ-STR-REL-1		Section 9.4.3 (A,D)	REQ-CDH-OBC-2		Section 10.3 (T)
REQ-STR-REL-2		Section 9.4.3 (A,T)	REQ-CDH-TTC-1		Section 10.4 (A,T)
REQ-STR-REL-3		(T)	REQ-CDH-TTC-2		Section 10.4 (A,T)
REQ-STR-REL-4		(T)	REQ-CDH-TTC-3		Section 10.4 (A,T)
REQ-STR-REL-5		(T)			

The requirement that are not met (red) and not checkable yet (light blue) are discussed here. **Non-met Requirements**
On June 13th 2024, the group had a meeting with the client, where some requirements that were not met were discussed. More explanation is provided here:

- REQ-TEC-LIN-2: This requirement was deemed by the client too ambitious as it would require more optical power (bigger laser). It was established with the client that 438 km was satisfactory.
- REQ-TEC-STR-1.3: This requirement was deemed to not be relevant. Anti-icing techniques are not necessary.
- REQ-MOP-COV-1.1: The network philosophy is locally placed not the entire world. This requirement is therefore discarded.
- REQ-MOP-COV-2: It is not possible to determine the coverage as the group was assigned multiple business cases where the needed coverage varies.
- REQ-MOP-CNW-2: This requirement is wrongly phrased. The individual platform should be operated by RF link but not the network since each platform is too far from each other for RF links.

- REQ-CON-CST-3: The FSM represents 50 % of the cost. After discussion with the supplier company, it arose that a discount may be given if the components are purchased in quantities. On top of that, the client did not mind the increase in cost.
- REQ-CON-ENB-2 & 3: After discussion with the client, it was deemed ok if the power and mass of the LCT are over budget as long as the HAPS can sustain it (which is the case). The mass requirement may be met if customised components are used.
- REQ-CON-REL-1: After discussion with the client, it was decided that the reliability of 0.817 is sufficient.

Non-checkable Requirements

- REC-TEC-OPT-3: To meet the tracking requirements effort was put into selecting PSDs with high accuracy and FSM with low jitter and high resolution. The combined effects of positional accuracy and actuator resolution could not easily be modelled at this time due to the lack of access to professional grade tools and time limitations. Further analysis should be conducted and the performance of the tracking systems should be demonstrated in order to ensure compliance with the requirement.
- REQ-TEC-SC-2.2: Effort was made to make the plane laterally statically stable by using a dihedral angle on the wing. The actual proof would require the determination of stability coefficients that requires lots of time and are inaccurate (see Section 5.6).
- REQ-MOP-COV-1.2: User connectivity does not depend on the network. Therefore, it is hard to fully say that user connectivity is possible but the network was designed to do so.
- REQ-MOP-COV-3.2: The design is intended to respect this requirement. However, a part is also dependent on the satellite that is not controlled by the LCT.
- REQ-CON-LGL-1,3,4 and 5 and REQ-CON-SFT-2 and 3: All requirements are about certifications. The goal of the design was to meet these requirements and the group is confident that they are met. However, the real proof is only provided by actually doing the certification process that for obvious reasons was not performed. However, for the future of the project it is planned to do so (see Chapter 19)
- REQ-CON-REL-3: The operational lifetime of the LCT was not analysed (in agreement with the client) as it requires significant work. On top of that, the components of the LCT were chosen with this requirement in mind. But hard proof that the assembly has an operational lifetime of 5 years is not existent.
- REQ-SC-2,3,4 and 5: The actual proof would require the determination of stability coefficients that requires lots of time and are inaccurate (see Section 5.6).
- REQ-STR-REL-3,4,5,6,7,8,9 and REQ-STR-MAN-1: To verify this requirement a fatigue analysis should be performed. No time was left to perform such an analysis. However, a safe life philosophy was used therefore, the group is confident that they should resist fatigue.

18.2. Validation Procedures

Validation involves demonstrating that the computational models accurately represent the real-world scenarios they are intended to simulate. This can be achieved by experimental validation and real-world testing. To perform validation one needs to have a clear definition of the model's intended use and perform the verification. The project objective defines the intended use, it being: "Identify viable business cases for free-space laser communication networks with the use of high-altitude pseudo-satellites and design the necessary components to bring them to the market.".

Experimental Validation: To create controlled experiments, one can develop an experiment that closely replicates the conditions and parameters of the computational models. For example, one could use a balloon to get an LCT to the stratosphere where it could be tested. Data could be collected on this experiment and compared to the model, after which the errors can be analysed.
Real-World Testing: When the whole system has been designed, one can start real-world testing. The integrated HAPS and LCT system can be deployed in real-world conditions to observe its performance and gather empirical data. Ensuring that the system works as intended in the operating environment and that the performance meets the required standards. Due to the state of the design, performing these methods of validation is not yet possible for the current design configuration. However, it is possible to edit the model's input parameters to be similar to already existing HAPS missions and validate it with those missions. In chapter 19, the development logic of the succeeding phase has been elaborated on. Specifically, as can be seen in Figure 19.1, in 2.1.3 these activities can be performed.

18.3. Verification & Validation Recommendations

In future work, which could not been done due to time and resource constraints, the verification & validation

of the design can be further enhanced. This should be done by using the Zephyr, produced by Airbus, as an input to the models created in this work. One can than verify if the model outputs the same performance as the real-world product.

19. To Be Continued

As the DSE comes to a close, it is only natural to consider the steps that would be taken to achieve the underlying ambitions behind the project mission statement: *Identify viable business cases for free-space laser communication networks with the use of high-altitude pseudo-satellites and design the necessary components to bring them to the market.* These steps are explored in this chapter, first through a description of the development logic including a corresponding flow-chart in Figure 19.1, the associated Gantt chart is included in Appendix D.

While the mission statement clearly lays out the design-limited scope of the project, the full mission will clearly involve more than just design. This is nicely evidenced by the subtitle on the original project guide for this exercise, namely, "Revolutionizing communication with laser tech aboard HAPS platforms". Such a goal will involve important considerations that follow after the design, such as, regulatory approval, producing the vehicle and terminal, the actual operations of these and finally the end-of-life plan for the system.

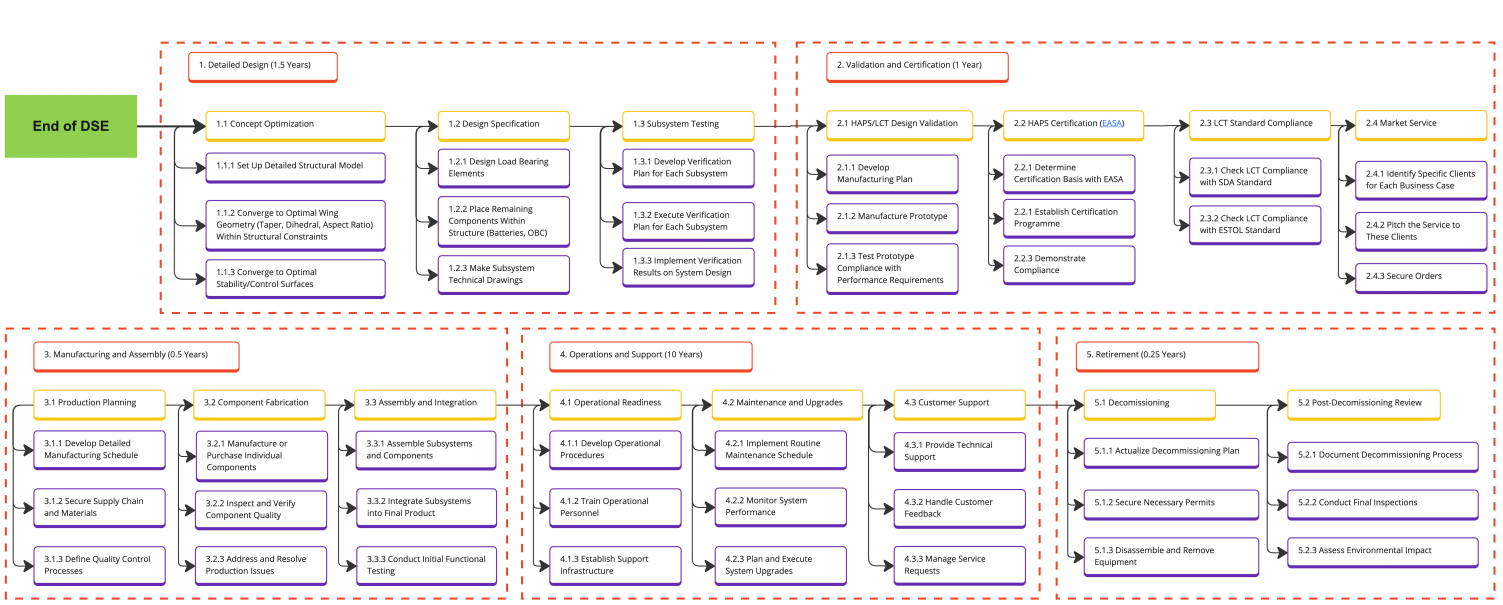

Figure 19.1: Development Logic Plan

Figure 19.1, presents a high-level overview of the phases previously described as well as providing a rough estimate for the scheduling of these. The development logic begins with the completion of the detailed design of the system, noting in particular the subsystems where final touches are needed as well as the implementation of rigorous subsystem testing. In particular, the LCT should further be designed by considering the thermal control and detailed aerodynamic impact analysis. This phase is expected to take 1.5 years to complete and likely involves a degree of non-linearity with revisions made to subsystems as results from the testing clarify some limitations of the design.

The validation and certification phases which follow consist of the internal validation efforts for the complete design, including the testing of a prototype, initially for flight performance considerations but also once these have been met, crucially for LCT integration performance. Once the design has been shown to perform to the established performance specifications the regulatory approval process can begin which is fundamental to beginning commercial operations with the system. Since the HAPS certification will likely be significantly more time constraining than that of the LCT there is either room to extend the LCT development in search for more performance or to apply the design of the LCT to alternative commercial applications.

Once the designs are approved and orders are secured, the scaling up of production can take place to meet the demand for the product, ensuring the benefits of larger production volumes while maintaining a high level of quality control. Depending on the business case that the HAPS-LCT combination is applied to, the details regarding the following phase, "Operations and Support" will vary. However, the fundamentals such as,

ensuring the system is set up and available as agreed, that it can be maintained or improved for the length of the contract, and that any issues on the side of the customer are handled, will largely be present for all cases. As per the requirements (see Table 1.1), the operational lifetime of the HAPS is 10 years whereas that of the LCT is 5 years.

When it becomes time to retire the vehicle (or LCT) the goal is to ensure that this is done in as sustainable a manner as is reasonably practicable as established by REQ-CON-RSC-5 on the reusability of certain parts, shown in Table 1.1. To ensure that the decommissioning of a system has aimed to meet this requirement, a post decommissioning review will be carried out, assessing the environmental impact of the vehicle throughout its life. These activities are scheduled based on a Gantt chart that can be found in Appendix D.

20. Conclusion

The primary objective of this report was to design a High Altitude Pseudo-Satellite (HAPS) integrated with a Laser Communication Terminal (LCT), suitable to fulfil viable business cases. The project objective was defined as follows: "Within 10 weeks, design a HAPS system that provides improved optical communication capabilities within 10 million euros, ensuring seamless integration within the Airbus environment."The analysis conducted has led to significant findings and actionable recommendations that could further enhance the system's performance.

Key Findings

This section highlights the key findings of the design process relevant to stakeholder interests. More detailed information can be found in the report.

LCT

The designed LCT can sustain three types of links at different distances: air-to-air at 428 km, air-to-ground at 25 km, and air-to-space at 2000 km. The system provides data rates ranging from 1-10 Gbps. The laser gimbal is optimized for high altitudes with minimal drag. The LCT is capable of 360° azimuth and 190° elevation pointing, allowing it to point slightly further than parallel to its plane. Each HAPS will be equipped with two LCTs, working in unison to provide network connections. The front LCT can utilise the full 190° elevation and 360° azimuth, whilst the bottom LCT can utilise part of the 360° azimuth.

HAPS

The HAPS was designed with safety and sustainability in mind, resulting in a 258-kilogram twin boom vehicle with a 50-meter wingspan. It exceeds the client's requirement by operating at latitudes exceeding ±45°, achieving over ±51.2° latitude depending on the time of year. Outperforming all other HAPS. The HAPS operates at altitudes between 15 and 25 km throughout its mission and is capable of launching in both day and night conditions. Extensive research has been put into the flight performance, aerodynamics, propulsion, stability & control, power, thermals, structures and command & data handling of the vehicle. Together, these subsystems form the basis of the design.

Cost and Revenue

Extensive market analysis has concluded that high revenues can be obtained depending on three different types of business cases. The highest potential revenue, projected at 925 million USD in 2030, involves the HAPS functioning as a critical component in providing a mobile and fast data transfer system for disaster relief applications, showcasing the vehicle's financial potential.

The cost analysis revealed that the total yearly recurring cost includes a fixed cost of 14,900,000 € for creating a network of HAPS, with each additional HAPS adding 1,217,000 €. The non-recurring cost is estimated at 747,000 €, with each additional HAPS contributing 556,000 € to this total (FY24).

Requirements

The design fulfils all specified requirements. Any requirements that were not initially met were either removed due to feasibility concerns or discussed with the client and mutually agreed upon modifications were made. For instance, the air-to-air link specifications were revised based on client feedback, ensuring alignment with practical needs.

Recommendations

The following recommendations aim to enhance the overall performance of the system. These recommendations can be used to further develop the design in future studies.

- **Concept Optimization**: Allocate dedicated resources to further optimize the design. This involves iterative testing, simulation and validation to achieve an even more robust and efficient design.
- **Develop Relay Mode Flightpath**: Create a line-of-sight connection simulation for the HAPS and LCT to

ensure that the connection is maintained for the required data transfer time.

- **Network Integration**: Conduct a comprehensive study on how the HAPS network can be optimized for a specific business case. This includes defining the functioning of the network for each separate business case and establishing protocols to ensure optimal functionality.
- **Enhance Reliability**: Conduct a thorough investigation into the integration of additional redundancies and more reliable components. This initiative aims to increase system reliability beyond the current 81.6% over a 6-month operational period.
- **Component Validation**: Develop a detailed plan for prototyping and validation testing of all HAPS (sub)systems. This will ensure that the design meets performance expectations in real operational conditions.
- **Certification**: Initiate the certification process for the HAPS. Ensure compliance with industry standards and obtain necessary certifications to facilitate manufacturing and deployment. This step is crucial for market readiness and operational legitimacy.
- **Client Acquisition**: Launch a targeted marketing campaign to attract additional clients. This will involve identifying potential markets, understanding their needs, and adapting the HAPS design specifications. Expanding the client base will increase potential revenue and enhance the project's viability.

Limitations

The project encountered several limitations, which are discussed in this section. These limitations are presented at both the design and system levels. More detailed information on subsystem-specific limitations can be found in the report.

- **HAPS Quantity and Coverage**: The performance of the HAPS network is limited when operating with a small number of units. Due to the range and type of connections required, a viable business model necessitates deploying a large number of HAPS to ensure adequate coverage and connectivity.
- **Limited Connection Capacity**: Each HAPS is designed to support only two connections simultaneously. This limitation creates a bottleneck, restricting the total amount of data that can be transmitted through a single HAPS, thereby impacting overall network performance.
- **Use of Simplifications**: The report employs various simplifications in the design and analysis stages. These simplifications, while necessary due to time constraints, limit the reliability and accuracy of the design. Real-world performance may differ from the simulated outcomes, necessitating further validation and refinement.
- **Limited Engineering Timeframe**: The research's origin constrained the available time for design and analysis. Additional time would have allowed for more in-depth analyses and refinement of the design to potentially enhance performance and reliability further.

Final Thoughts

The design and analysis that have been undertaken demonstrate the potential of the HAPS to provide robust communication solutions for various commercial applications. The recommendations outlined will guide further improvements, ensuring that the system meets the highest standards of reliability and performance.

Looking ahead, the successful deployment of HAPS with LCTs promises to revolutionize communication systems, offering scalable and flexible solutions to meet the demands of modern connectivity. By addressing the recommendations and overcoming the identified limitations, future iterations of this design will undoubtedly achieve great success.

Bibliography

[1] Design Synthesis Exercise Group 22. *Baseline Report: Breaking Barriers with LCT and HAPS*. Tech. rep. May 2024.

[2] Design Synthesis Exercise Group 22. *Business Case Report: Breaking Barriers with LCTs and HAPS*. Tech. rep. TU Delft, May 2024.

[3] Design Synthesis Exercise Group 22. *Midterm Report: Breaking Barriers with LCTs and HAPS*. Tech. rep. May 2024.

[4] Flow 5. *Stability analyses*. 2020. URL: https://flow5.tech/docs/flow5_doc/Tutorials/Stability.html#sanity_check (visited on 06/13/2024).

[5] Gerard Aalbers, Georgi N. Gaydadijev, and Rouzbeh Amini. "CDHS Design for a university nano-satellite". In: *57th International Astronautical Congress*. DOI: 10.2514/6.IAC-06-B5.7.05.

[6] A. Adibekyan et al. "Review of PTB Measurements on Emissivity, Reflectivity and Transmissivity of Semitransparent Fiber-Reinforced Plastic Composites". In: *International Journal of Thermophysics* 40 (Mar. 2019). DOI: 10.1007/s10765-019-2498-0.

[7] European Aviation Safety Agency. *Certification Specifications for Very Light Aeroplanes*. Nov. 2003.

[8] A. García-Gutiérrez et al. "Aerodynamic optimization of propellers for High Altitude Pseudo-Satellites". In: *Elsevier* (2020).

[9] A. M. Oni et al. "A comprehensive evaluation of solar cell technologies, associated loss mechanisms, and efficiency enhancement strategies for photovoltaic cells". In: *Energy Reports* 11 (2024), pp. 3345–3366. DOI: 10.1016/j.egyr.2024.03.007.

[10] C. Dahal et al. "Design and Analysis of Propeller for High-Altitude Search and Rescue Unmanned Aerial Vehicle". In: *Hindawi* (2020).

[11] D. W. Hall et al. "Preliminary Study of Solar Powered Aircraft and Associated Power Trains". In: *NASA CR 3699* (1983).

[12] H. Afshari et al. "The role of metastability and concentration on the performance of CIGS solar cells under Low-Intensity-Low-Temperature conditions". In: *Solar Energy Materials and Solar Cells* 212 (2020), p. 110571. ISSN: 0927-0248. DOI: 10.1016/j.solmat.2020.110571.

[13] Ir. B.T.C. Zandbergen et al. *AE1222-II: Aerospace Design Systems Engineering Elements I, Part: Spacecraft (bus/platform) design and sizing*. Delft University Press, 2022.

[14] J. Gonzalo et al. "On the capabilities and limitations of high altitude pseudo-satellites". In: *Elsevier* (2018).

[15] Li J. et al. "A Brief Review of High Efficiency III-V Solar Cells for Space Application". In: *Frontiers in Physics* 8 (2021). DOI: 10.3389/fphy.2020.631925.

[16] M. Lazzaroni et al. *Reliability Engineering*. Springer, 2011.

[17] M. O. Reese et al. "Increasing markets and decreasing package weight for high-specific-power photovoltaics". In: *Nature Energy* (2018).

[18] N. Solmaz et al. "Battery Energy Storage Systems: A Review of Energy Management Systems and Health Metrics". In: *Energies* 17.5 (2024). ISSN: 1996-1073. DOI: 10.3390/en17051250.

[19] S. Panigrahi et al. "Design, Analysis, and Testing of a Hybrid VTOL Tilt-Rotor UAV for Increased Endurance". In: *MDPI* (2021).

[20] T. Haggren et al. "III–V Thin Films for Flexible, Cost-Effective, and Emerging Applications in Optoelectronics and Photonics". In: *ACS Publications* (2013).

[21] V. Romano et al. "Advances in Perovskites for PhotovoltaicApplications in Space". In: *ACS Energy Letters* (2022).

[22] Y. Tu et al. "Perovskite Solar Cells for Space Applications: Progress and Challenges". In: *Wiley Online Library* (2021).

[23] Z. GORAJ et al. "High altitude long endurance unmanned aerial vehicle of a new generation – a design challenge for a low cost, reliable and high performance aircraft". In: (2004).

[24] G. Witvoet et al. "Performance validation of a high-bandwidth fine steering mirror for optical communications". In: *International Conference on Space Optics — ICSO 2018* (2018).

[25] G.B. Koc et al. "HAPS-Enabled Sustainability Provision in Cellular Networks through Cell-Switching". In: *IEEE* 24 (July 2023). DOI: 10.1109/BlackSeaCom58138.2023.10299797.

[26] J. Kimmons et al. "Aerodynamic effects of surface deformities aerofoils for low-speed stratospheric flight". In: *J Aerospace Engineering* (2023). DOI: 10.1177/09544100221093210.

[27] M. Sakib HASAN et al. "OPTIMAL AIRFOIL DESIGN AND WING ANALYSIS FOR SOLAR-POWERED HIGH ALTITUDE PLATFORM STATION". In: *THERMAL SCIENCE* (2022). DOI: 10.2298/TSCI210419241S.

[28] M.S. Selig et al. "High-Lift Low Reynolds Number Airfoil Design". In: *JOURNAL OF AIRCRAFT* (1997).

[29] R. Ma et al. "MULTI-OBJECTIVE OPTIMIZATION DESIGN OF LOWREYNOLDS-NUMBER AIRFOILS S1223". In: *27TH INTERNATIONAL CONGRESS OF THE AERONAUTICAL SCIENCES* (2010).

[30] Y. J. Hasan et al. "Flight mechanical analysis of a solar-powered high-altitude platform". In: *CEAS Aeronautical Journal* (2023). DOI: 10.1007/s13272-022-00621-2.

[31] J.D. Anderson. *Fundamentals of Aerodynamics*. McGraw-Hill series in aeronautical and aerospace engineering. McGraw-Hill Education, 2017. ISBN: 9781259251344.

[32] Suratsawadee Anuphappharadorn et al. "Comparison the Economic Analysis of the Battery between Lithium-ion and Lead-acid in PV Stand-alone Application". In: *Energy Procedia* 56 (Dec. 2014), pp. 352–358. DOI: 10.1016/j.egypro.2014.07.167.

[33] Masayuki Anyoji and Daiki Hamada. "High-performance airfoil with low reynolds-number dependence on aerodynamic characteristics". In: *Fluid Mechanics Research International Journal* (2019). DOI: 10.15406/fmrij.2019.03.00055.

[34] Masayuki Anyoji et al. "Computational and Experimental Analysis of a High-Performance Airfoil Under Low-Reynolds-Number Flow Condition". In: *Journal of Aircraft* 51 (May 2014), pp. 1864–1872. DOI: 10.2514/1.C032553.

[35] I. Ribeiro B. A. R. Soares E. Henriques and M. Freitas. "Cost analysis of alternative automated technologies for composite parts production". In: *International Journal of Production Research* 57.6 (2019), pp. 1797–1810. DOI: 10.1080/00207543.2018.1508903.

[36] Wael Ballout et al. "Quantitative characterization of interdiffusion at the resin-resin and resin-prepreg interphases of epoxy systems processed by model SQ-RTM". In: *Polymer Engineering Science* 56 (May 2016). DOI: 10.1002/pen.24338.

[37] Maider Baskaran Razkin et al. "Manufacturing cost comparison of RTM, HP-RTM and CRTM for an automotive roof". In: *16th European Conference on Composite Materials, ECCM 2014* (Jan. 2014).

[38] Yiming Bian et al. "Free-space to single-mode fiber coupling efficiency with optical system aberration and fiber positioning error under atmospheric turbulence". In: *Journal of Optics* 24.2 (Jan. 2022), p. 025703. DOI: 10.1088/2040-8986/ac3f8f.

[39] L. M. M. Boermans and Arne van Garrel. "Design and Windtunnel Test Results of a Flapped Laminar Flow Airfoil For High-Performance Sailplane Applications". In: *Technical Soaring* 21 (1997), pp. 11–17.

[40] Remco Den Breeje et al. "Prototype test results of a High-Altitude Pseudo-Satellite laser communication terminal". In: *2023 IEEE International Conference on Space Optical Systems and Applications (ICSOS)*. 2023, pp. 36–41. DOI: 10.1109/ICSOS59710.2023.10491216.

[41] Prof. Ir. Jos P. van Buijtenen et al. *Gas Turbines: Propulsion and Power AE 2203*. Delft University Press, 2011.

[42] Ashwin Candade, Maximilian Ranneberg, and Roland Schmehl. "Structural analysis and optimization of a tethered swept wing for airborne wind energy generation". In: *Wind Energy* 23 (Jan. 2020). DOI: 10.1002/we.2469.

[43] Jaworski C Capricho et al. "Upcycling polystyrene". en. In: *Polymers (Basel)* 14.22 (Nov. 2022), p. 5010.

[44] Ali Chamkha and Fatih Selimefendigil. "Numerical Analysis for Thermal Performance of a Photovoltaic Thermal Solar Collector with SiO2-Water Nanofluid". In: *Applied Sciences* 8 (Nov. 2018), p. 2223. DOI: 10.3390/app8112223.

[45] G. M. Cole and T. J. Mueller. "Experimental Measurements of the Laminar Separation Bubble on an Eppler 387 Airfoil at Low Reynolds Number". In: *NASA* (1990).

[46] A. Colozza. "High Altitude Propeller Design and Analysis Overview". In: *Federal Data Systems* (1998).

[47] McDonnell Douglas Astronautics Company. *THE USAF STABILITY AND CONTROL DATCOM*. 1979.

[48] M.V. Cook. *Flight Dynamics principles*. Elsevier Aerospace Engineering Series, 2007.

[49] Q. Dai and X. Fang. *A simple model to predict solar radiation under clear sky conditions*. Tech. rep. Nanjing University of Aeronautics and Astronautics, 2014.

[50] Brian Danowsky et al. "A Structural Design Methodology for Highly Flexible HAPS Aircraft". In: Jan. 2024. DOI: 10.2514/6.2024-1733.

[51] A. Deperrois. *Part IV: Theoretical Limiations and Shortcomings*. June 2019.

[52] Chengzhi Dong et al. "Evaluation of thermal expansion coefficient of carbon fiber reinforced composites using electronic speckle interferometry". In: *Opt. Express* 26.1 (Jan. 2018), pp. 531–543. DOI: 10.1364/OE.26.000531.

[53] F. Leccese E. Petritoli and L. Ciani. "Reliability and Maintenance Analysis of Unmanned Aerial Vehicles". In: (2018).

[54] ESA and Industry of ESA member states. *ESA SPECIFICATION FOR TERABIT/SEC OPTICAL LINKS (ESTOL)*. 1.0. Reference ESA-CSC-T-SP-0001. July 2023.

[55] C. Larbes F. Belhachat. *A review of global maximum power point tracking techniques of photovoltaic system under partial shading conditions*. Tech. rep. Renew Sustain Energy Rev, 2018.

[56] et al. F. Lang. "Proton-Radiation Tolerant All-Perovskite Multijunction Solar Cells". In: *Wiley Online Library* (2021).

[57] Hassan M. Hussein Farh et al. "Global research trends on photovoltaic maximum power extraction: Systematic and scientometric analysis". In: *Sustainable Energy Technologies and Assessments* 61 (2024), p. 103585. ISSN: 2213-1388. DOI: 10.1016/j.seta.2023.103585.

[58] Alejandro Fernández-Soler et al. "Ascent phase convective heat transfer of a stratospheric-balloon-borne payload". In: *Advances in Space Research* 72.2 (2023), pp. 503–517. ISSN: 0273-1177. DOI: 10.1016/j.asr.2023.04.010.

[59] Tim Flohrer, Holger Krag, and H. Klinkrad. "Assessment and Categorization of TLE Orbit Errors for the US SSN Catalogue". In: (Jan. 2008), pp. 53–.

[60] Space Development Agency United States Space Force. *Optical Communication Terminal (OCT) Standard*. 3.1.0. Document ID: 9100-001-05. Aug. 2021.

[61] D. L. Fried. "Statistics of a Geometric Representation of Wavefront Distortion". In: *J. Opt. Soc. Am.* 55.11 (Nov. 1965), pp. 1427–1435. DOI: 10.1364/JOSA.55.001427.

[62] G Frulla. "Preliminary reliability design of a solar-powered high-altitude very long endurance unmanned air vehicle". In: *Proceedings of the Institution of Mechanical Engineers, Part G: Journal of Aerospace Engineering* 216.4 (2002), pp. 189–196. DOI: 10.1243/0954410260369722.

[63] Market Research Future. *Small Satellite Market*. 2024. URL: https://www.marketresearchfuture.com/reports/small-satellite-market-6007 (visited on 05/24/2024).

[64] Dirk Giggenbach and Hennes Henniger. "Fading-loss assessment in atmospheric free-space optical communication links with on-off keying". In: *Optical Engineering* 47 (Apr. 2008), pp. 046001–1. DOI: 10.1117/1.2951952.

[65] P. Giguère and M. Selig. "New airfoils for small horizontal axis wind turbines". In: *Solar Energ Eng* (1998).

[66] H. Glaubert. "The Elements of Aerofoil and Airscrew Theory". In: *Cambridge* (1947).

[67] P. R. Goode et al. "Earthshine observations of the Earth's reflectance". In: *Geophysical Research Letters* 28.9 (2001), pp. 1671–1674. DOI: 10.1029/2000GL012580.

[68] Bjørn Grimsmo. *Life Cycle Assessment of Li-ion Batteries for Electric Vehicles*. eng. 2014. URL: http://hdl.handle.net/11250/2400819.

[69] Snorri Gudmundsson. "Chapter 8 - The Anatomy of the Airfoil". In: *General Aviation Aircraft Design*. Ed. by Snorri Gudmundsson. Boston: Butterworth-Heinemann, 2014, pp. 235–297. ISBN: 978-0-12-397308-5. DOI: 10.1016/B978-0-12-397308-5.00008-8.

[70] Remco Hageman. *Rudder Incorporated Winglet Design for Blended Wing Body Aircraft*. 2016. URL: https://api.semanticscholar.org/CorpusID:114107278.

[71] Xuan Han et al. "Point-ahead demonstration of a transmitting antenna for satellite quantum communication". In: *Opt. Express* 26.13 (June 2018), pp. 17044–17055. DOI: 10.1364/OE.26.017044.

[72] Mohammad Sakib Hasan et al. "Conceptual Design and Fluid Structure Interaction Analysis of a Solar Powered High-Altitude Pseudo-Satellite (HAPS) UAV Wing Model". In: Oct. 2020, pp. 93–105. ISBN: 978-3-030-62784-3. DOI: 10.1007/978-3-030-62784-3_8.

[73] Yasim J. Hasan et al. "Flight mechanical analysis of a solar-powered high-altitude platform". In: *CEAS Aeronautical Journal* 14 (1 Jan. 2023), pp. 201–223. ISSN: 1869-5582. DOI: 10.1007/s13272-022-00621-2.

[74] Elsa Henriques et al. "Concurrent Engineering–A Case Study involving University and Industry". In: (Jan. 2008).

[75] R.C. Hibbeler and K.B. Yap. *Mechanics of materials Tenth edition in SI units*. 10th ed. England: Pearson Education, 2018.

[76] C.W. Hindman and B.S. Engberg. "Atmospheric and platform jitter effects on laser acquisition patterns". In: *2006 IEEE Aerospace Conference*. 2006. DOI: 10.1109/AERO.2006.1655993.

[77] S. F. Hoerner. *Fluid Dynamic Drag*. Bakersfield, CA, USA: Hoerner Fluid Dynamics, 1965, pp. 3-14 - 3–17.

[78] E.N. Hoffman and T.E. Skidmore. "Radiation effects on epoxy/carbon-fiber composite". In: *Journal of Nuclear Materials* 392.2 (2009). Nuclear Fuels and Structural Materials 2, pp. 371–378. ISSN: 0022-3115. DOI: 10.1016/j.jnucmat.2009.03.027.

[79] M. et al. Imaizumi. *Qualification test results of IMM triple-junction solar cells, space solar sheets, and lightweight compact solar paddle*. Tech. rep. 2017.

[80] Fortune Business Insights. *Small Satellite Market*. 2024. URL: https://www.fortunebusinessinsights.com/industry-reports/small-satellite-market-101917 (visited on 05/24/2024).

[81] Spherical Insights. *Global Small Satellite Market*. 2024. URL: https://www.sphericalinsights.com/reports/small-satellite-market (visited on 05/24/2024).

[82] Pelton J. "High Altitude Platform Systems (HAPS) and Unmanned Aerial Vehicles (UAV) as an Alternative to Small Satellites". In: *International Association for the Advancement of Space Safety (IAASS)* (2020).

[83] John Jasa et al. "Large-Scale Path-Dependent Optimization of Supersonic Aircraft". In: *Aerospace* 7 (Oct. 2020), p. 152. DOI: 10.3390/aerospace7100152.

[84] A. Jenkins. "The Sun's position in the sky". In: *European Journal of Physics* (2013).

[85] B. Jha and A. Kumar. "Employee Engagement: A Strategic Tool to Enhance Performance". In: *Journal for Contemporary Research in Management* 1 (2016).

[86] Ozlem Ipek Kalaoglu-Altan, Burcak Karaguzel Kayaoglu, and Levent Trabzon. "Improving thermal conductivities of textile materials by Nanohybrid approaches". In: *iScience* 25.3 (Mar. 2022), p. 103825. DOI: 10.1016/j.isci.2022.103825.

[87] K. Kallstrom. "Exploring Airfoil Table Generation using XFOIL and OVERFLOW". In: *VFS Aeromechanics for Advanced Vertical Flight Technical Meeting* (2022).

[88] S. Kalogirou. *Solar Engergy Engineering: Process and Systems*. Elsevier, 2009.

[89] Hemani Kaushal, Vk Jain, and Subrat Kar. "Acquisition, Tracking, and Pointing". In: Jan. 2017, pp. 119–137. ISBN: 978-81-322-3689-4. DOI: 10.1007/978-81-322-3691-7_4.

[90] B. Keidel. "Auslegung und Simulation von hochfliegenden dauerhaft stationierbaren Solardrohnen". PhD thesis. Technische Universität München, 2000.

[91] Bertrand Kirsch and Olivier Montagnier. "Towards the Advent of High-Altitude Pseudo-Satellites (HAPS)". In: July 2019, pp. 181–201. ISBN: 9781786304490. DOI: 10.1002/9781119644569.ch9.

[92] Tomaszycki Marek Krawczyk Jacek. "The Exploration of the Content of CFRB in Composite Strengthening Material". In: (2019), pp. 1–14. DOI: 10.37055/pno/125474.

[93] S. Kuiper et al. "HIGH-BANDWIDTH AND COMPACT FINE STEERING MIRROR DEVELOPMENT FOR LASER COMMUNICATIONS". In: Sept. 2017.

[94] Jela Legerská and Pavol Lizák. "Evaluation of the Specific Physiological Properties for the Selected Assortment of Work Clothes". In: *Procedia Engineering* 136 (Dec. 2016), pp. 227–232. DOI: 10.1016/j.proeng.2016.01.202.

[95] Dongkang Li and Yanmei Zhang. "Research on factors influencing the positioning accuracy of four-quadrant detector". In: *Journal of Physics: Conference Series* 1983 (July 2021), p. 012087. DOI: 10.1088/1742-6596/1983/1/012087.

[96] X. LIU and W. HE. "Performance Calculation and Design of Stratospheric Propeller". In: *IEEE* (2017).

[97] E. H. Lockwood. *Book of Curves*. Cambridge University Press, 1961.

[98] Dirk H.-J.A. Lukaszewicz, Carwyn Ward, and Kevin D. Potter. "The engineering aspects of automated prepreg layup: History, present and future". In: *Composites Part B: Engineering* 43.3 (2012), pp. 997–1009. ISSN: 1359-8368. DOI: 10.1016/j.compositesb.2011.12.003.

[99] Vincenzo Lunetto et al. "Sustainability in the manufacturing of composite materials: A literature review and directions for future research". In: *Journal of Manufacturing Processes* 85 (2023), pp. 858–874. ISSN: 1526-6125. DOI: 10.1016/j.jmapro.2022.12.020.

[100] Bahrami M. *Forced Convection Heat Transfer*. Lecture Notes. 2015.

[101] T. Tozer M. Pent and J.A. Delgado-Penín. "HAPs for Telecommunications and Surveillance Applications". In: (Nov. 2015).

[102] Amos Madhlopa. *Solar Receivers for Thermal Power Generation*. 2022.

[103] James F. Marchman. *Aerodynamics and Aircraft Performance, 3rd Edition*. Virginia Tech Libraries, 2004. ISBN: 9781949373639.

[104] Mathworks. *Pole placement design*. 2020. URL: https://nl.mathworks.com/help/control/ref/place.html (visited on 06/13/2024).

[105] Bento Silva de Mattos, Ney Rafael Secco, and Eduardo Francisco Salles. "Optimal design of a high-altitude solar-powered unmanned airplane". In: *Journal of Aerospace Technology and Management* 5.3 (2013). Cited by: 28; All Open Access, Gold Open Access, Green Open Access, pp. 349–361. DOI: 10.5028/jatm.v5i3.223.

[106] B. S. de Mattos1 et al. "Optimal Design of a High-Altitude SolarPowered Unmanned Airplane". In: *Journal of Aerospace Technology and Management* (2013). DOI: 10.5028/jatm.v5i3.223.

[107] Martynas Milaševičius and Laurynas Mačiulis. "A Review of Mechanical Fine-Pointing Actuators for Free-Space Optical Communication". In: *Aerospace 2024, Vol. 11, Page 5* 11 (1 Dec. 2023), p. 24. ISSN: 2226-4310. DOI: 10.3390/AEROSPACE11010005.

[108] MMR. *Communication Intelligence Market: Global Size, Dynamics, Regional Insights and Market Segment Analysis*. 2024. URL: https://www.maximizemarketresearch.com/market-report/communication-intelligence-market/169975/#:~:text=The%20global%20communication%20intelligence%20(COMINT,as%20per%20the%20research%20study. (visited on 05/24/2024).

[109] Evan K. Paleologos Abdel-Mohsen O. Mohamed. *Pollution Assessment for Sustainable Practices in Applied Sciences and Engineering*. Elsevier, 2021. ISBN: 9780128095829. DOI: 10.1016/C2015-0-06451-6.

[110] N. J. Mohr et al. "Life cycle assessment of thin-film GaAs and GaInP/GaAs solar modules". In: *Progress in Photovoltaics: Research and Applications* 15.2 (2007), pp. 163–179. DOI: 10.1002/pip.735.

[111] M.C.Y. Niu. *Airframe Structural Design*. Hong Kong Commilit Press LTD., 1988.

[112] A. Noth. *Design of Solar Powered Airplanes for Continuous Flight*. Tech. rep. Eidgenössische Technische Hochschule Zürich, Sept. 2006.

[113] Gilles Notton et al. "Performances and numerical optimization of a novel thermal solar collector for residential building". In: *Renewable and Sustainable Energy Reviews* 33 (2014), pp. 60–73. ISSN: 1364-0321. DOI: 10.1016/j.rser.2014.01.061.

[114] Cristina Beneitez Ortega, Dirk Zimmer, and Patrick Weber. "Thermal analysis of a high-altitude solar platform". In: *CEAS aeronautical journal* 14 (Jan. 2023), pp. 243–254. DOI: 10.1007/s13272-022-00636-9.

[115] Nicolas Perlot. "Evaluation of the scintillation loss for optical communication systems with direct detection". In: *Optical Engineering* 46.2 (2007), p. 025003. DOI: 10.1117/1.2436866.

[116] Dipen Kumar Rajak, Pratiksha H Wagh, and Emanoil Linul. "Manufacturing technologies of carbon/glass Fiber-Reinforced Polymer composites and their properties: A review". In: *Polymers (Basel)* 13.21 (Oct. 2021).

[117] Daniel P Raymer. *Aircraft design: A conceptual approach*. 4. ed. AIAA education series. Reston, Va.: American Institute of Aeronautics and Astronautics, 2006. ISBN: 1563478293.

[118] KBV Reseaarch. *Communication Intelligence Market*. 2024. URL: https://www.kbvresearch.com/communication-intelligence-market/ (visited on 05/24/2024).

[119] RESEARCHDIVE. *Global Communication Intelligence (COMINT) Market Synopsis*. 2024. URL: https://www.researchdive.com/8420/communication-intelligence-comint-market (visited on 05/24/2024).

[120] J. Roskam. *Airplane Design VIII Airplane Cost Estimation: Design, development, manufacturing and operating. DARcorporation.Optical Fiber Telecommunications*. DARcorporation, 2015.

[121] Roberto Sabatini et al. "Airborne Laser Systems for Atmospheric Sounding in the Near Infrared". In: *Proc SPIE* (May 2012), pp. 33–. DOI: 10.1117/12.915718.

[122] S. Sakama. "Trends of Motors Characteristics". In: *Scholarly Community Encyclopedia* (2022).

[123] Jennifer Schmidt. "Building a Lightweight Future for American Transportation". In: (June 2008).

[124] Michael Selig and Bryan McGranahan. "Wind Tunnel Aerodynamic Tests of Six Airfoils for Use on Small Wind Turbines". In: *42nd AIAA Aerospace Sciences Meeting and Exhibit*. Oct. 2003. DOI: 10.2514/6.2004-1188.

[125] Michael S. Selig. *Low Reynolds Number Airfoil Design Lecture Notes*. Oct. 2003.

[126] M. Sessarego and D. Wood. "Multi-dimensional optimization of small wind turbine blades". In: *Springer* (2015).

[127] Ali Shahriar et al. "Predicting the unpredictable: General Aviation (GA) aircraft cost estimation evaluation". In: *Journal of Air Transport Management* 102 (2022), p. 102221. ISSN: 0969-6997. DOI: 10.1016/j.jairtraman.2022.102221.

[128] Liao Shao-huai and Lu Yi-yan. "The Exploration of the Content of CFRB in Composite Strengthening Material". In: (Dec. 2012). DOI: 10.2991/mems.2012.69.

[129] Gyu Jin Shin et al. "Enhancing vertical thermal conductivity of carbon fiber reinforced polymer composites using cauliflower-shaped copper particles". In: *Materials Today Communications* 35 (2023), p. 105792. DOI: 10.1016/j.mtcomm.2023.105792.

[130] P. Shin and K. Kim. "Aerodynamic performance prediction of SG6043 airfoil for a horizontal axis small wind turbine". In: *Journal of Physics: Conference Series* (2020). DOI: 10.1088/1742-6596/1452/1/012018.

[131] Keisuke Shinozaki et al. "Thermal Property Measurements of Critical Materials for SPICA Payload Module". In: *Physics Procedia* 67 (Dec. 2015), pp. 270–275. DOI: 10.1016/j.phpro.2015.06.086.

[132] J. Sinke. *Reader 2023-2024. Production of Aerospace Systems*. 2023.

[133] "Space Packet Protocol. Recommendation for Space Data System Standards". In: *CCSDS Standards* (June 2020).

[134] Uwe Sterr, Mark Gregory, and Frank Heine. "Beaconless acquisition for ISL and SGL, summary of 3 years operation in space and on ground". In: *2011 International Conference on Space Optical Systems and Applications (ICSOS)*. 2011, pp. 38–43. DOI: 10.1109/ICSOS.2011.5783704.

[135] Claudia Stöcker et al. "Review of the Current State of UAV Regulations". In: *Remote Sensing* 9.5 (2017). ISSN: 2072-4292. DOI: 10.3390/rs9050459.

[136] J. Sunil and Rathinam Maheswaran. "Influence on Nanofluids in Worm Gearbox Efficiency-An overview". In: Apr. 2015.

[137] Maggie Tang et al. "Effect of softener and wetting agent on improving the flammability, comfort, and mechanical properties of flame-retardant finished cotton fabric". In: *Cellulose* 24 (June 2017). DOI: 10.1007/s10570-017-1268-z.

[138] M. Tavlet, A. Fontaine, and H. Schönbacher. "COMPILATION OF RADIATION DAMAGE TEST DATA". In: (Mar. 1998).

[139] Marc Tavlet and Helmut Schönbacher. "Radiation resistance of insulators and structural materials". In: *Large Hadron Collider Workshop* (Oct. 4–9, 1990). Ed. by G. Jarlskog and D. Rein. Aachen, 1990, pp. 743–748.

[140] The GFDRR The World Bank. *Post-disaster needs assessments guidelines: Volume B - Disaster risk reduction*. 2012.
[141] Egbert Torenbeek. *Synthesis of subsonic airplane design*. Delft University Press, 1982.
[142] D. L. Wall. "Optimum Propeller Design for Electric UAVs". In: (2012).
[143] Xuan Wang et al. "A Method for Improving the Detection Accuracy of the Spot Position of the Four-Quadrant Detector in a Free Space Optical Communication System". In: *Sensors* 20.24 (2020). ISSN: 1424-8220. DOI: 10.3390/s20247164.
[144] Y. Wang and R. Feng. "A Feasibility Research for Sustainable General Aviation". In: *IOP Conf. Series: Earth and Environmental Science* (2020).
[145] Patrick Willenshofer et al. "Radiation-resistant aluminium alloy for space missions in the extreme environment of the solar system". In: (Oct. 2022). DOI: 10.48550/arXiv.2210.03397.
[146] Justin Winslow et al. "Basic Understanding of Airfoil Characteristics at Low Reynolds Numbers (104–105)". In: *Journal of Aircraft* 55.3 (2018), pp. 1050–1061. DOI: 10.2514/1.C034415.
[147] D. Yuniarti. "Regulatory Challenges of Broadband Communication Services from High Altitude Platforms (HAPs)". In: *International Conference on Information and Communications Technology (ICOIACT)* (2018).
[148] Ailing Zhang and Yanxiang Li. "Thermal conductivity of aluminum alloys—a review". In: *Materials* 16.8 (Apr. 2023), p. 2972. DOI: 10.3390/ma16082972.
[149] Huang Zhaodong, Luo Rongxuan, and Jin Jing. "Development and Production Costs Estimating for Aviation Equipment Based on Uncertainty Design". In: *Procedia Engineering* 99 (2015). 2014 Asia-Pacific International Symposium on Aerospace Technology, APISAT2014 September 24-26, 2014 Shanghai, China, pp. 143–149. ISSN: 1877-7058. DOI: https://doi.org/10.1016/j.proeng.2014.12.518. URL: https://www.sciencedirect.com/science/article/pii/S1877705814036327.

A. Group Organization

Table A.1 denotes the authorship of each section of this report. Sections denoted with a number followed by an x indicate every section in the chapter was (co)written by that author. When someone contributed to a section without writing, their name is listed in the contributed section. Proofreading and providing feedback is not considered as contributing to a section and is thus omitted.

Table A.1: Section authorship table

Name	Wrote Sections	Contributed Sections
Alexander Groen	10.x, 12.x, FBS, FFD	2.2,
Andrea Poirier	EO, 6.x, 11.x, 17.3, 18.1	7.3, 14.x, 16.4
Christos Margaritis	2.1-5, 2.8, 2.10, Appendix D	2.x 18.1
Jasper Lapidaire	PF, 1.x, 3.x	PF, 1.x, 3.x
Joris Lans	9.x, 3DExperience	EO, 15.x, 17.x
Martijn Oortwijn	7.x, 18.x, 20.x, FBS, FFD	2.3, 6.4, 6.5, 14.x, 17.x
Mateo Rancaño Martinez	4.1-5, 5.1 5.2, 5.5, 17.2 , 19.x	4.x, 5.x, 17.2 , 19.x
Mohammad Ebrahimi	2.3, 2.5-2.9, LCT CAD	2.x
Tiago Stomp	7.4, 8.x, 13.x, 16.1, 16.2, 16.3, 17.x	2.1, 7.6, 14.x
Tim Veerman	4.2, 4.4-4.6 5.1, 5.3, 5.4, 5.6, 14.x, 15.1-15.3, 16.x	2.7, 4.x, 6.x, 14.x, 15.x, 16.x

B. Functional Breakdown Structure

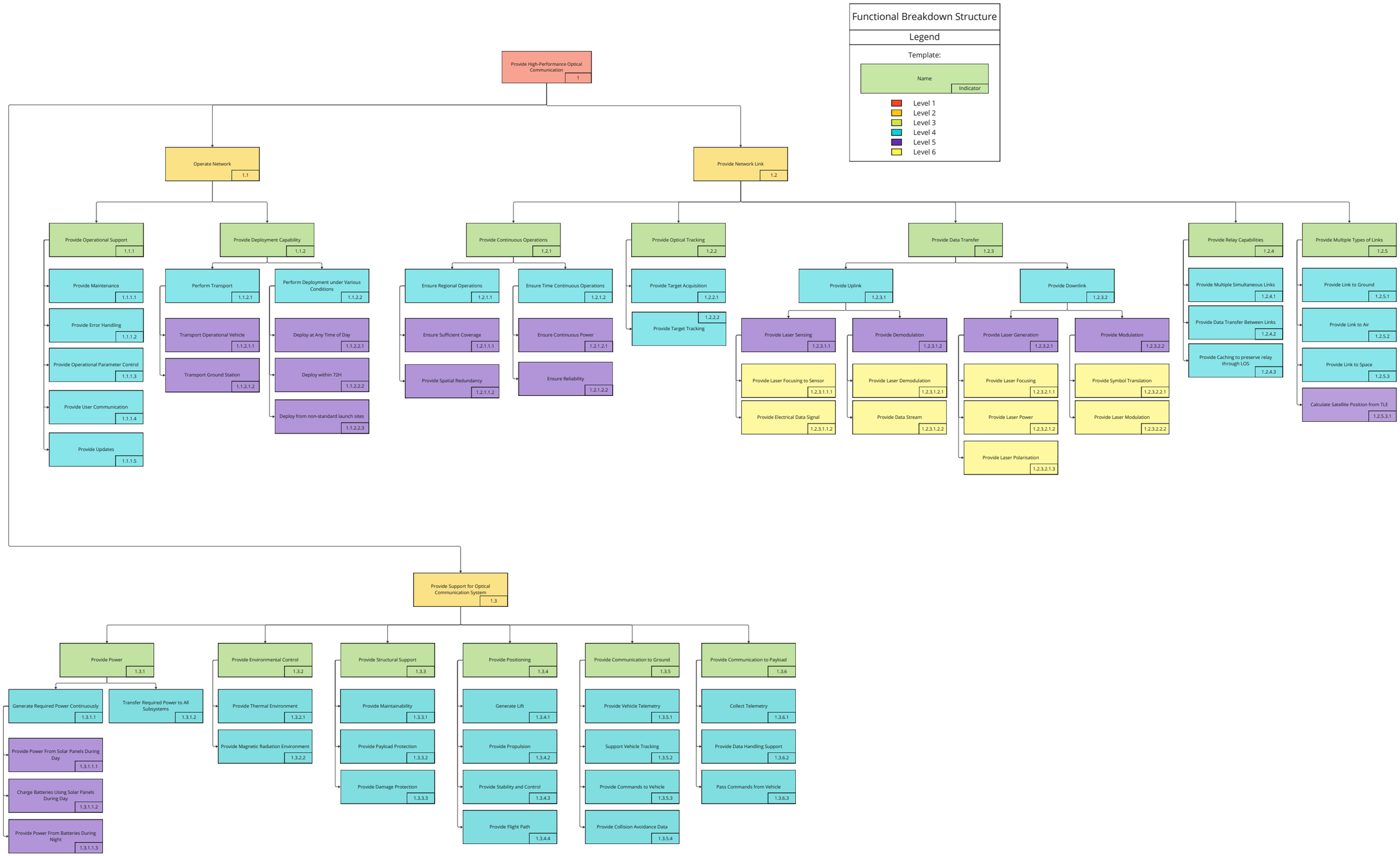

C. Functional Flow Diagram

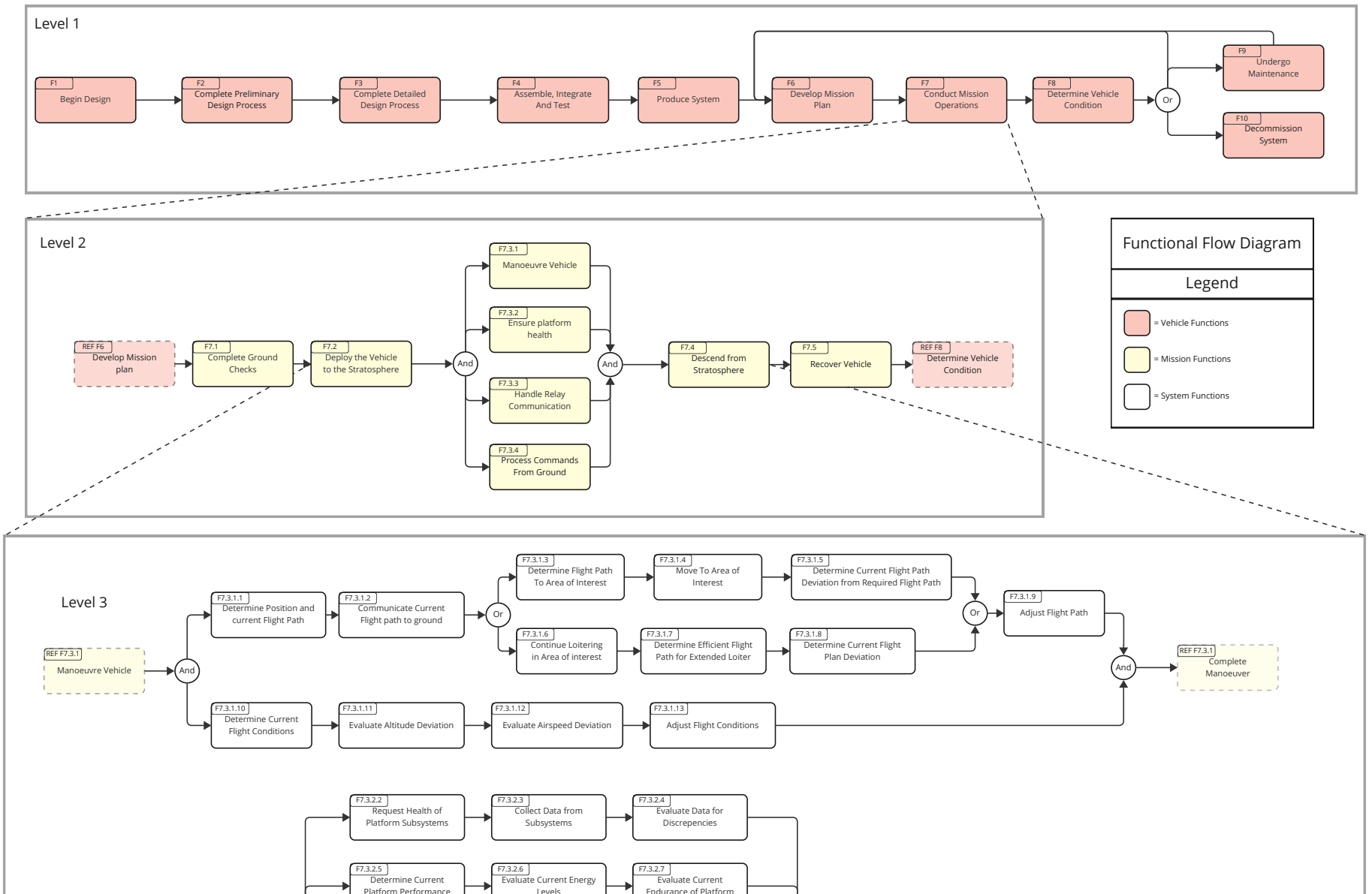

D. Post DSE Gantt Chart

ID	Task Mode	Task Name	Duration	Start	Finish
1		**1. Detailed Design**	**360 days**	**Tue 6/18/24**	**Mon 11/3/25**
2		**1.1 Concept Optimization**	**80 days**	**Tue 6/18/24**	**Mon 10/7/24**
3		1.1.1 Set Up Detailed Structural Model	2 mons	Tue 6/18/24	Mon 8/12/24
4		1.1.2 Converge to Optimal Wing Geometry	2 mons	Tue 8/13/24	Mon 10/7/24
5		1.1.3 Converge to Optimal Stability/Control Surfaces	4 mons	Tue 6/18/24	Mon 10/7/24
6		**1.2 Design Specification**	**80 days**	**Tue 8/13/24**	**Mon 12/2/24**
7		1.2.1 Design Load Bearing Elements	1 mon	Tue 8/13/24	Mon 9/9/24
8		1.2.2 Place Remaining Components Within Structure	1 mon	Tue 10/8/24	Mon 11/4/24
9		1.2.3 Make Subsystem Technical Drawings	1 mon	Tue 11/5/24	Mon 12/2/24
10		**1.3 Subsystem Testing**	**240 days**	**Tue 12/3/24**	**Mon 11/3/25**
11		1.3.1 Refine Verification Plan for Each Subsystem	2 mons	Tue 12/3/24	Mon 1/27/25
12		1.3.2 Execute Verification Plan for Each Subsystem	6 mons	Tue 1/28/25	Mon 7/14/25
13		1.3.3 Implement Verification Results on System Design	4 mons	Tue 7/15/25	Mon 11/3/25
14		Design Phase Completed	0 days	Mon 11/3/25	Mon 11/3/25
15		**2. Validation and Verification**	**280 days**	**Tue 11/4/25**	**Mon 11/30/26**
16		**2.1 HAPS/LCT Design Validation**	**200 days**	**Tue 11/4/25**	**Mon 8/10/26**
17		2.1.1 Refine Manufacturing Plan	1 mon	Tue 11/4/25	Mon 12/1/25
18		2.1.2 Manufacture Prototype	3 mons	Tue 12/2/25	Mon 2/23/26
19		2.1.3 Perform Validation Procedures on Prototype	6 mons	Tue 2/24/26	Mon 8/10/26
20		**2.2 HAPS Certification**	**180 days**	**Tue 2/24/26**	**Mon 11/2/26**
21		2.2.1 Determine Certification Basis with EASA	3 mons	Tue 2/24/26	Mon 5/18/26
22		2.2.1 Establish Certification Programme	3 mons	Tue 5/19/26	Mon 8/10/26
23		2.2.3 Demonstrate Compliance	3 mons	Tue 8/11/26	Mon 11/2/26
24		**2.3 LCT Standard Compliance**	**60 days**	**Tue 8/11/26**	**Mon 11/2/26**
25		2.3.1 Check LCT Compliance with SDA Standard	3 mons	Tue 8/11/26	Mon 11/2/26
26		2.3.2 Check LCT Compliance with ESTOL Standard	3 mons	Tue 8/11/26	Mon 11/2/26
27		**2.4 Market Service**	**80 days**	**Tue 8/11/26**	**Mon 11/30/26**
28		2.4.1 Identify Specific Clients for Each Business Case	1 mon	Tue 8/11/26	Mon 9/7/26
29		2.4.2 Pitch the Service to These Clients	1 mon	Tue 9/8/26	Mon 10/5/26
30		2.4.3 Secure Orders	2 mons	Tue 10/6/26	Mon 11/30/26
31		V&V Phase Completed	0 days	Mon 11/2/26	Mon 11/2/26
32		Orders Secured	0 days	Mon 11/30/26	Mon 11/30/26
33		**3. Manufacturing and Assembly**	**140 days**	**Tue 8/11/26**	**Mon 2/22/27**
34		**3.1 Production Planning**	**40 days**	**Tue 8/11/26**	**Mon 10/5/26**
35		3.1.1 Develop Detailed Manufacturing Schedule	1 mon	Tue 8/11/26	Mon 9/7/26
36		3.1.2 Secure Supply Chain and Materials	1 mon	Tue 9/8/26	Mon 10/5/26
37		3.1.3 Define Quality Control Processes	1 mon	Tue 9/8/26	Mon 10/5/26
38		**3.2 Component Fabrication**	**20 days**	**Tue 12/1/26**	**Mon 12/28/26**
39		3.2.1 Manufacture or Purchase Individual Components	1 mon	Tue 12/1/26	Mon 12/28/26
40		3.2.2 Inspect and Verify Component Quality	1 mon	Tue 12/1/26	Mon 12/28/26
41		3.2.3 Address and Resolve Production Issues	1 mon	Tue 12/1/26	Mon 12/28/26
42		**3.3 Assembly and Integration**	**40 days**	**Tue 12/29/26**	**Mon 2/22/27**
43		3.3.1 Assemble Subsystems and Components	1 mon	Tue 12/29/26	Mon 1/25/27
44		3.3.2 Integrate Subsystems into Final Product	1 mon	Tue 12/29/26	Mon 1/25/27
45		3.3.3 Conduct Initial Functional Testing	1 mon	Tue 1/26/27	Mon 2/22/27
46		Product Ready for Operation	0 days	Mon 2/22/27	Mon 2/22/27
47		**4. Operations and Support**	**2500 days**	**Tue 2/23/27**	**Mon 9/22/36**
48		**4.1 Operational Readiness**	**80 days**	**Tue 2/23/27**	**Mon 6/14/27**
49		4.1.1 Develop Operational Procedures	2 mons	Tue 2/23/27	Mon 4/19/27
50		4.1.2 Train Operational Personnel	2 mons	Tue 4/20/27	Mon 6/14/27
51		4.1.3 Establish Support Infrastructure	2 mons	Tue 4/20/27	Mon 6/14/27
52		**4.2 Maintenance and Upgrades**	**2420 days**	**Tue 6/15/27**	**Mon 9/22/36**
53		4.2.1 Implement Routine Maintenance Schedule	1 mon	Tue 6/15/27	Mon 7/12/27
54		4.2.2 Monitor System Performance	120 mons	Tue 7/13/27	Mon 9/22/36
55		4.2.3 Plan and Execute System Upgrades	120 mons	Tue 7/13/27	Mon 9/22/36
56		**4.3 Customer Support**	**2400 days**	**Tue 6/15/27**	**Mon 8/25/36**
57		4.3.1 Provide Technical Support	120 mons	Tue 6/15/27	Mon 8/25/36
58		4.3.2 Handle Customer Feedback	120 mons	Tue 6/15/27	Mon 8/25/36
59		4.3.3 Manage Service Requests	120 mons	Tue 6/15/27	Mon 8/25/36
60		Product Operational Phase Completed	0 days	Mon 8/25/36	Mon 8/25/36
61		**5. Retirement**	**70 days**	**Tue 8/26/36**	**Mon 12/1/36**
62		**5.1 Decommissioning**	**30 days**	**Tue 8/26/36**	**Mon 10/6/36**
63		5.1.1 Actualize Decommissioning Plan	0.5 mons	Tue 8/26/36	Mon 9/8/36
64		5.1.2 Secure Necessary Permits	0.5 mons	Tue 9/9/36	Mon 9/22/36
65		5.1.3 Disassemble and Remove Equipment	0.5 mons	Tue 9/23/36	Mon 10/6/36
66		**5.2 Post-Decommissioning Review**	**40 days**	**Tue 10/7/36**	**Mon 12/1/36**
67		5.2.1 Document Decommissioning Process	1 mon	Tue 10/7/36	Mon 11/3/36
68		5.2.2 Conduct Final Inspections	1 mon	Tue 11/4/36	Mon 12/1/36
69		5.2.3 Assess Environmental Impact	1 mon	Tue 11/4/36	Mon 12/1/36
70		Product Lifecycle Completed	0 days	Mon 12/1/36	Mon 12/1/36

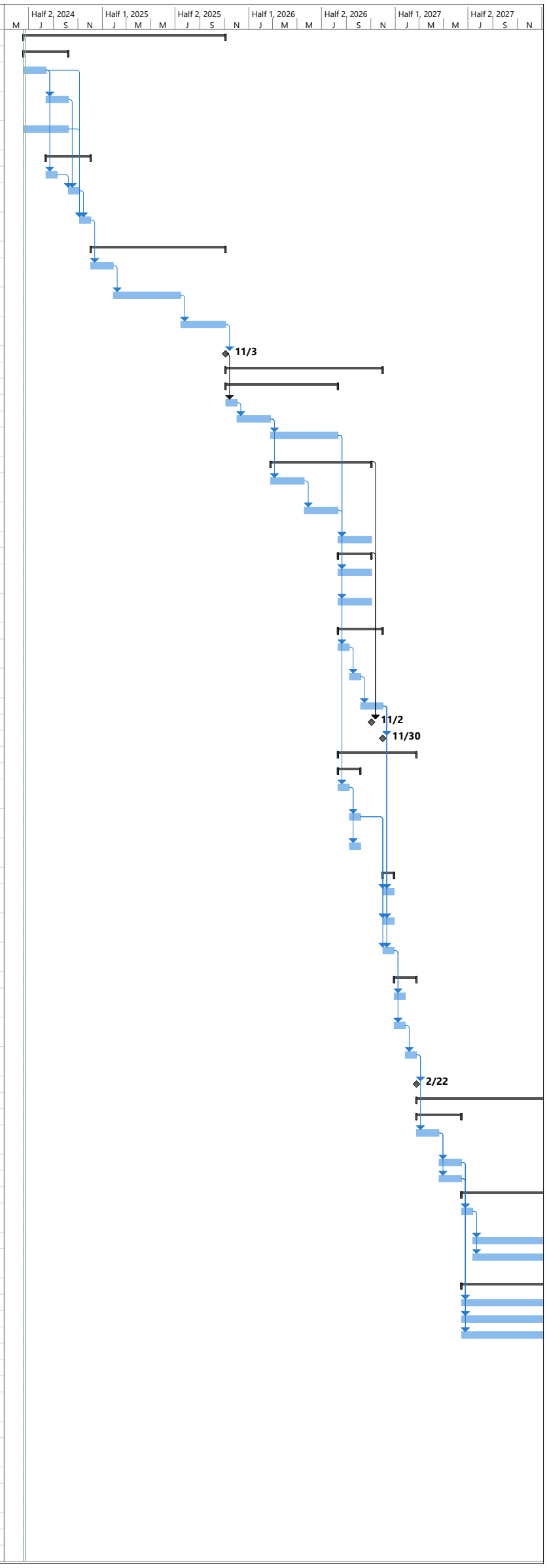

ID	Task Mode	Task Name	Duration	Start	Finish
1		**1. Detailed Design**	**360 days**	**Tue 6/18/24**	**Mon 11/3/25**
2		**1.1 Concept Optimization**	**80 days**	**Tue 6/18/24**	**Mon 10/7/24**
3		1.1.1 Set Up Detailed Structural Model	2 mons	Tue 6/18/24	Mon 8/12/24
4		1.1.2 Converge to Optimal Wing Geometry	2 mons	Tue 8/13/24	Mon 10/7/24
5		1.1.3 Converge to Optimal Stability/Control Surfaces	4 mons	Tue 6/18/24	Mon 10/7/24
6		**1.2 Design Specification**	**80 days**	**Tue 8/13/24**	**Mon 12/2/24**
7		1.2.1 Design Load Bearing Elements	1 mon	Tue 8/13/24	Mon 9/9/24
8		1.2.2 Place Remaining Components Within Structure	1 mon	Tue 10/8/24	Mon 11/4/24
9		1.2.3 Make Subsystem Technical Drawings	1 mon	Tue 11/5/24	Mon 12/2/24
10		**1.3 Subsystem Testing**	**240 days**	**Tue 12/3/24**	**Mon 11/3/25**
11		1.3.1 Refine Verification Plan for Each Subsystem	2 mons	Tue 12/3/24	Mon 1/27/25
12		1.3.2 Execute Verification Plan for Each Subsystem	6 mons	Tue 1/28/25	Mon 7/14/25
13		1.3.3 Implement Verification Results on System Design	4 mons	Tue 7/15/25	Mon 11/3/25
14		Design Phase Completed	0 days	Mon 11/3/25	Mon 11/3/25
15		**2. Validation and Verification**	**280 days**	**Tue 11/4/25**	**Mon 11/30/26**
16		**2.1 HAPS/LCT Design Validation**	**200 days**	**Tue 11/4/25**	**Mon 8/10/26**
17		2.1.1 Refine Manufacturing Plan	1 mon	Tue 11/4/25	Mon 12/1/25
18		2.1.2 Manufacture Prototype	3 mons	Tue 12/2/25	Mon 2/23/26
19		2.1.3 Perform Validation Procedures on Prototype	6 mons	Tue 2/24/26	Mon 8/10/26
20		**2.2 HAPS Certification**	**180 days**	**Tue 2/24/26**	**Mon 11/2/26**
21		2.2.1 Determine Certification Basis with EASA	3 mons	Tue 2/24/26	Mon 5/18/26
22		2.2.1 Establish Certification Programme	3 mons	Tue 5/19/26	Mon 8/10/26
23		2.2.3 Demonstrate Compliance	3 mons	Tue 8/11/26	Mon 11/2/26
24		**2.3 LCT Standard Compliance**	**60 days**	**Tue 8/11/26**	**Mon 11/2/26**
25		2.3.1 Check LCT Compliance with SDA Standard	3 mons	Tue 8/11/26	Mon 11/2/26
26		2.3.2 Check LCT Compliance with ESTOL Standard	3 mons	Tue 8/11/26	Mon 11/2/26
27		**2.4 Market Service**	**80 days**	**Tue 8/11/26**	**Mon 11/30/26**
28		2.4.1 Identify Specific Clients for Each Business Case	1 mon	Tue 8/11/26	Mon 9/7/26
29		2.4.2 Pitch the Service to These Clients	1 mon	Tue 9/8/26	Mon 10/5/26
30		2.4.3 Secure Orders	2 mons	Tue 10/6/26	Mon 11/30/26
31		V&V Phase Completed	0 days	Mon 11/2/26	Mon 11/2/26
32		Orders Secured	0 days	Mon 11/30/26	Mon 11/30/26
33		**3. Manufacturing and Assembly**	**140 days**	**Tue 8/11/26**	**Mon 2/22/27**
34		**3.1 Production Planning**	**40 days**	**Tue 8/11/26**	**Mon 10/5/26**
35		3.1.1 Develop Detailed Manufacturing Schedule	1 mon	Tue 8/11/26	Mon 9/7/26
36		3.1.2 Secure Supply Chain and Materials	1 mon	Tue 9/8/26	Mon 10/5/26
37		3.1.3 Define Quality Control Processes	1 mon	Tue 9/8/26	Mon 10/5/26
38		**3.2 Component Fabrication**	**20 days**	**Tue 12/1/26**	**Mon 12/28/26**
39		3.2.1 Manufacture or Purchase Individual Components	1 mon	Tue 12/1/26	Mon 12/28/26
40		3.2.2 Inspect and Verify Component Quality	1 mon	Tue 12/1/26	Mon 12/28/26
41		3.2.3 Address and Resolve Production Issues	1 mon	Tue 12/1/26	Mon 12/28/26
42		**3.3 Assembly and Integration**	**40 days**	**Tue 12/29/26**	**Mon 2/22/27**
43		3.3.1 Assemble Subsystems and Components	1 mon	Tue 12/29/26	Mon 1/25/27
44		3.3.2 Integrate Subsystems into Final Product	1 mon	Tue 12/29/26	Mon 1/25/27
45		3.3.3 Conduct Initial Functional Testing	1 mon	Tue 1/26/27	Mon 2/22/27
46		Product Ready for Operation	0 days	Mon 2/22/27	Mon 2/22/27
47		**4. Operations and Support**	**2500 days**	**Tue 2/23/27**	**Mon 9/22/36**
48		**4.1 Operational Readiness**	**80 days**	**Tue 2/23/27**	**Mon 6/14/27**
49		4.1.1 Develop Operational Procedures	2 mons	Tue 2/23/27	Mon 4/19/27
50		4.1.2 Train Operational Personnel	2 mons	Tue 4/20/27	Mon 6/14/27
51		4.1.3 Establish Support Infrastructure	2 mons	Tue 4/20/27	Mon 6/14/27
52		**4.2 Maintenance and Upgrades**	**2420 days**	**Tue 6/15/27**	**Mon 9/22/36**
53		4.2.1 Implement Routine Maintenance Schedule	1 mon	Tue 6/15/27	Mon 7/12/27
54		4.2.2 Monitor System Performance	120 mons	Tue 7/13/27	Mon 9/22/36
55		4.2.3 Plan and Execute System Upgrades	120 mons	Tue 7/13/27	Mon 9/22/36
56		**4.3 Customer Support**	**2400 days**	**Tue 6/15/27**	**Mon 8/25/36**
57		4.3.1 Provide Technical Support	120 mons	Tue 6/15/27	Mon 8/25/36
58		4.3.2 Handle Customer Feedback	120 mons	Tue 6/15/27	Mon 8/25/36
59		4.3.3 Manage Service Requests	120 mons	Tue 6/15/27	Mon 8/25/36
60		Product Operational Phase Completed	0 days	Mon 8/25/36	Mon 8/25/36
61		**5. Retirement**	**70 days**	**Tue 8/26/36**	**Mon 12/1/36**
62		**5.1 Decommissioning**	**30 days**	**Tue 8/26/36**	**Mon 10/6/36**
63		5.1.1 Actualize Decommissioning Plan	0.5 mons	Tue 8/26/36	Mon 9/8/36
64		5.1.2 Secure Necessary Permits	0.5 mons	Tue 9/9/36	Mon 9/22/36
65		5.1.3 Disassemble and Remove Equipment	0.5 mons	Tue 9/23/36	Mon 10/6/36
66		**5.2 Post-Decommissioning Review**	**40 days**	**Tue 10/7/36**	**Mon 12/1/36**
67		5.2.1 Document Decommissioning Process	1 mon	Tue 10/7/36	Mon 11/3/36
68		5.2.2 Conduct Final Inspections	1 mon	Tue 11/4/36	Mon 12/1/36
69		5.2.3 Assess Environmental Impact	1 mon	Tue 11/4/36	Mon 12/1/36
70		Product Lifecycle Completed	0 days	Mon 12/1/36	Mon 12/1/36